Quantitative ultrasound imaging of human cortical bone

Amadou Sall Dia

Sorbonne Université

École doctorale
Sciences Mécaniques, Acoustique, Électronique et Robotique de Paris

Laboratoire d'Imagerie Biomédicale LIB

Thèse de doctorat d'**Acoustique physique**

Quantitative ultrasound imaging of human cortical bone

Imagerie ultrasonore quantitative de l'os cortical

Présentée par **Amadou S. DIA**

Dirigée par M. Quentin GRIMAL et M. Guillaume RENAUD

Présentée et soutenue publiquement le 24 Juin 2024

Devant un jury composé de :

M.	Jean-Luc GENNISSON	Directeur de recherche, CNRS	Président de Jury
Mme	Isabelle QUIDU	Maîtresse de conférences, ENSTA Bretagne	Rapporteure
M.	Alain LHÉMERY	Directeur de recherche, CEA-LIST	Rapporteur
M.	François OLLIVIER	Maître de conférences, Sorbonne Université	Examinateur
M.	Arnaud DERODE	Professeur, Université Paris-Cité	Examinateur
M.	Quentin GRIMAL	Professeur, Sorbonne Université	Co-directeur de thèse
M.	Guillaume RENAUD	Chargé de recherche, CNRS	Co-directeur de thèse

Abstract

Osteoporosis is a disease characterized by a decrease in bone mass and an increase in bone porosity. It weakens bones and can lead to fragility fractures. Worldwide, 1/3 of women over the age of 50 and 1/5 of men aged over 50 will experience an osteoporosis fracture, resulting in more than 8.9 million fractures each year. These fractures can be prevented if detected and treated early enough. Several techniques have been developed to assess bone quality, with ultrasound emerging as a cheap, portable, and safe option that provides informations on the mechanical strength of bone. Ultrasound imaging of the cortex of long bones enables the assessment of cortical thickness and ultrasonic wave speeds. However, challenges arise with increased cortical porosity in osteoporotic bone, making difficult the detection of the inner surface of the cortex (endosteum) and limiting image quality. In osteoporotic bone, cortical pores are heterogeneously distributed, with large pores more prevalent at the inner interface, creating a porosity gradient. The objective of this work was to improve our understanding of factors influencing image quality (porosity, pore size, pore distribution, etc.) and to propose an original image reconstruction technique to improve image quality. To achieve this, synthetic and experimental ultrasound datasets were used. Our results demonstrate the ability to estimate cortical thickness and ultrasound wave speed from ultrasound imaging for homogeneous cortical bone. However, for degraded bones, increased cortical porosity and vascular pore size create strong speckle that obscures the visibility of the endosteal interface. A novel model-based beamforming algorithm tailored to the physics of specular reflection and refraction was proposed to improve the visibility of the endosteal interface. Application of this algorithm to both *ex vivo* and *in vivo* datasets revealed enhanced visibility compared to traditional Delay-and-Sum (DAS) beamforming. Overall, this thesis demonstrated that ultrasound imaging can be used to estimate cortical thickness and wave speed in bones with low to moderate porosities typically below 12% and moderate microstructure heterogeneity with pores typically smaller than 250 µm. The precision with which the radial and axial wave speeds are assessed is less than 3%. This is sufficient to identify individuals with low cortical bone mechanical quality at risk of osteoporotic fracture. Furthermore, accounting for the physics of specular reflection, intracortical images with enhanced interface visibility can be obtained.

Keywords

Ultrasound imaging, Cortical bone, beamforming, delay-and-sum, specular beamforming, refraction, specular reflection,

Résumé

L'ostéoporose est une maladie caractérisée par une diminution de la masse osseuse et une augmentation de la porosité des os. Elle affaiblit l'os et peut entraîner des fractures de fragilité. Dans le monde, 1/3 des femmes de plus de 50 ans et 1/5 des hommes de plus de 50 ans subiront une fracture due à l'ostéoporose, ce qui représente plus de 8,9 millions de fractures chaque année. Ces fractures peuvent être évitées si elles sont détectées et traitées suffisamment tôt. Plusieurs techniques ont été mises au point pour évaluer la qualité de l'os, l'échographie apparaissant comme une option bon marché, portable et sûre qui fournit des informations sur la résistance mécanique de l'os. L'imagerie ultrasonore du cortex des os longs permet d'évaluer l'épaisseur corticale et la vitesse des ondes ultrasonores. Cependant, des défis se posent avec l'augmentation de la porosité dans l'os ostéoporotique, rendant difficile la détection de la surface interne du cortex (endoste) et détériorant ainsi la qualité de l'image. Dans l'os ostéoporotique, les pores corticaux sont répartis de manière hétérogène, les grands pores étant plus fréquents à l'interface interne, ce qui crée un gradient de porosité. L'objectif de ce travail de thèse était d'améliorer notre compréhension des facteurs déterminants la qualité de l'image (porosité, taille des pores, distribution des pores, etc.) et de proposer une technique originale de reconstruction d'image pouvant améliorer la qualité de l'image. Pour ce faire, des données échographiques synthétiques et expérimentales ont été utilisés. Nos résultats montrent qu'avec l'imagerie par échographie, il est possible d'estimer l'épaisseur corticale et la vitesse ultrasonore pour un os cortical homogène. Cependant, pour des os dégradés, l'augmentation de la porosité corticale et de la taille des pores créent du speckle qui détériore la visibilité de l'interface endostéale. Un nouvel algorithme de beamforming basé sur un modèle adapté à la physique de la réflexion et de la réfraction spéculaires a été proposé pour améliorer la visibilité de l'interface endostéale. L'application de cet algorithme à la fois aux données *ex vivo* et *in vivo* a montré une meilleure visibilité de l'endoste par rapport à l'algorithme traditionnel de *delay-and-sum* (DAS). Dans l'ensemble, cette thèse a démontré que l'imagerie par ultrasons peut être utilisée pour estimer l'épaisseur corticale et la vitesse des ondes dans des os présentant des porosités faibles à modérées, généralement inférieures à 12 %, et une hétérogénéité modérée de la microstructure, avec des pores généralement inférieurs à 250 µm. La précision avec laquelle les vitesses ultrasonores radiales et axiales sont évaluées est inférieure à 3 %. Cette précision est suffisante pour identifier les individus dont la qualité mécanique de l'os cortical est faible et qui présentent un risque de fracture ostéoporotique. En outre, en tenant compte de la physique de la réflexion spéculaire, il est possible d'obtenir des images intracorticales avec une meilleure visibilité de l'interface.

Remerciements

Hadha min fadli Rabbi, li yablouani aachkourou am akfour
"*Ce n'est pas la hauteur du sommet que l'on atteint qui compte, mais la manière dont on y parvient.*" Sans le concours de plusieurs personnes, ce sommet n'aurait jamais été atteint. Je tiens à exprimer ma profonde gratitude à toutes celles et ceux qui ont contribué à la réalisation de cette thèse.

Comme l'a si bien exprimé Albert Einstein, "*Il n'y a que deux façons de vivre sa vie : l'une en faisant comme si rien n'était un miracle, l'autre en faisant comme si tout était un miracle*". Ces quatre années de thèse ont été une période riche en découvertes et en apprentissages, où j'ai eu le privilège de vivre de véritables miracles à travers tous les échanges, les personnes et les rencontres qui ont jalonné ce parcours.

Je remercie chaleureusement mon co-directeur de thèse, le Professeur Quentin Grimal, pour sa patience, ses conseils avisés et son soutien constant tout au long de ce travail, tant sur le plan professionnel que personnel. Ses encouragements, sa rigueur scientifique et ses commentaires constructifs ont été une source d'inspiration et de motivation. Son expertise m'a formé et a grandement façonné ce travail de thèse.

Je suis également très reconnaissant envers Guillaume Renaud, mon autre co-directeur de thèse, pour ses suggestions précieuses et son soutien tout au long de ce projet. Sa grande rigueur scientifique et sa disponibilité ont été extrêmement bénéfiques. Malgré la distance, il a toujours été là chaque fois que le besoin se faisait sentir.

Je souhaite également exprimer ma gratitude envers l'ensemble des membres du jury, présidé par le Dr Jean-Luc Gennisson, d'avoir accepté d'examiner mon travail. Je remercie particulièrement mes deux rapporteurs de thèse, le Dr Isabelle Quidu et le Dr Alain Lhemery, pour avoir pris le temps d'évaluer mes travaux et pour leurs suggestions précieuses qui ont considérablement amélioré la qualité de ce manuscrit. Un grand merci aussi aux membres de mon comité de suivi, le Professeur Arnaud Derode et le Dr François Ollivier, pour leur aide et leur suivi tout au long de ce projet. Leurs commentaires constructifs et leur expertise ont enrichi ce travail de manière significative.

Je suis profondément reconnaissant envers Maryline Talmant, Aida Hejazi et Pascal Dargent pour leur collaboration et leur contribution précieuse au sein de l'équipe.

Un merci particulier à Catherine Dion, pour tout, mais surtout pour nos moments de discussion autour du 'Bonjour' matinal. Merci pour ta bonne humeur. Merci pour ton accueil chaleureux et surtout merci pour ta bienveillance envers moi et ma famille.

Merci à Patrick, Mélanie et Benoît pour leur disponibilité et leur soutien tout au long de cette aventure.

Je tiens également à remercier les amis du groupe 'Pas de souss' et 'Pas le time' avec qui j'ai partagé mon (nouveau) bureau, pour leur amitié et leur convivialité.

Un grand merci à tous mes collègues doctorants et post-doctorants, anciens et nouveaux, jeunes et moins jeunes (clin d'œil à François l'inventeur). Je ne vous cite pas tous ici par peur d'en oublier ou de mal écrire vos noms, mais vous avez tous contribué à rendre cette expérience de recherche plus agréable.

Un grand merci à tous mes collègues et amis du LIB (Laboratoire d'Imagerie Biomédicale), pour leur soutien, leurs discussions enrichissantes et les moments de convivialité partagés. Leur camaraderie a été une source de joie durant cette expérience de recherche.

Enfin, je souhaite exprimer ma gratitude à ma très grande famille (Doukoure, Diallo, Camara, Dia, Thiam) et à mes amis proches (CAMER, Promo 07, JZ, ENSTA), pour leur amour, leur patience et leur soutien indéfectible. Leur présence m'a donné la force nécessaire pour persévérer dans les moments difficiles.

À toutes ces personnes, ainsi qu'à toutes celles que je n'ai pas mentionnées mais qui ont contribué de près ou de loin à la réalisation de cette thèse, je dis un grand merci.

Rabbi awzi'ni an ashkura ni'mataka allati an'amta 'alayya ...

Dédicaces

Ce travail est dédié à tous ceux qui contemplent cette vie avec émerveillement et gratitude.

À mon bien-aimé Mouhamed, qui a apporté la lumière et la joie dans mon cœur. Que la paix et les bénédictions te suivent éternellement.

Avant toute chose, **je dédie ce travail ainsi que tout mon parcours à mon oncle Lassana**, le véritable artisan de ce voyage académique. Tu m'as accueilli, conseillé et intégré comme ton fils. Ton soutien inébranlable et tes conseils précieux ont été une source constante de force et d'inspiration. Ta confiance en moi s'est manifestée dès ma première année et m'a poussé à poursuivre mes objectifs avec détermination et persévérance.

À la prunelle de mes yeux, ma très chère mère, Rokhaya, dont l'amour et la sagesse ont été les guides de mon parcours. Tu as su voir les miracles dans les choses simples et tu m'as appris à en faire de même. Avec toute ma gratitude, ce travail est pour toi.

À mon père bien-aimé, dont la mémoire m'a accompagné dans les épreuves et les triomphes. Ce travail est dédié à toi, avec tout l'amour et la gratitude que j'ai pour toi.

À ma maman-france, Deguene, dont l'affection a enrichi mon quotidien et m'a offert un soutien constant. Tout ce que je porte de beau vient de toi. Ta présence bienveillante a été une source de réconfort et d'encouragement.

À mon beau-père Samba Diallo pour son support et sa considération depuis le début.

À ma tendre épouse, Fatima, dont l'amour et la compréhension ont été un pilier constant durant ces années de thèse. Ta force tranquille et ta présence douce ont été des sources de réconfort et de motivation. Merci d'avoir partagé ce chemin à mes côtés et d'avoir soutenu mes efforts avec tant de générosité et d'affection.

À toute ma famille Doukouré, Diallo et Camara, pour votre accueil chaleureux et votre profonde considération. Votre confiance en moi m'a donné la force de toujours aller plus loin et de poursuivre mes rêves avec détermination. **À Mariama Camara** que j'admire et respecte énormément.

À ma grande sœur Marie Faye (la daronne), **à mes grands** frères Amadou (le daron), Abdou (Ustaz), Adama (Beuri Fans) et **à mes petits frères** Salayna, Ibrahim, Samba et Bakary. C'est mon nom qui est sur le diplôme, mais cette thèse est la vôtre. Je vous dédie ce travail avec tout mon amour et ma reconnaissance.

À mes frères et soeurs (Ndiabou, Mamadou, Mami, Yama, Mallet, Boubou, Mbaye, Fatma).

Un hommage particulier à ceux qui ont partagé avec moi les hauts et les bas de cette aventure académique. Vous avez été des compagnons précieux, parfois un peu exaspérés, mais toujours présents : **Bathily**, **Amade** (wala Mouhamed), Baay **Maps**, **Milkou** Sombi, **Lamine** le Dormeur, **ElNdonguisto**, **Macodou** l'Invisible, **Bass** le Clairvoyant et **Elhadj** Gueye Borom Boules Yi

Je n'oublie pas **Ngoné** Mu Sell Mi et **Nabou** Baye Zale. Vous avez fait un pot gravé dans les mémoires du LIB.

Dédicaces à la Team CAMER, mes promos ingénieurs de l'ENSTA : **Jordane le Génie**, **Cédric** (le Money Maker), **Yvan** (le Money Seeker), **Jorès** le CF et Maman **Maurelle**.

À Herr Doctor **Amade NDIAYE**, Seydi Dr **Mouhamadou DIALOUNKE** et **Mariama KA**, qui ont inspiré ce parcours.

Last and definitely not least, je n'oserais pas oublier bien sûr les frères d'armes, la Team 07.

La famille est l'endroit où la vie commence et où l'amour ne finit jamais.

List of publications and communications

Publications

- Amadou S. DIA, Guillaume RENAUD, Aidia H. NOOGHABI, Quentin GRIMAL. " *The influence of intra-cortical microstructure on the contrast in ultrasound images of the cortex of long bones: a 2D simulation study*, Ultrasonics, DOI: 10.1016/j.ultras.2022.106831

Communications

1. *Specular beamforming and refraction correction improve ultrasound imaging of the bone cortex geometry in vivo*
   Amadou S. DIA, Guillaume RENAUD, Christine CHAPPARD, Quentin GRIMAL
   Conférence: IEEE, International Ultrasonic Symposium, Vancouver, Canada, September 2023 ,(oral)

2. *Quantitative ultrasound imaging of human cortical bone: influence of microstructure on image quality and speed of sound determination*
   Amadou S. DIA, Guillaume RENAUD, Christine CHAPPARD, Quentin GRIMAL
   Conférence: International Congress on Ultrasonics (ICU), Beijing, China, September 2023, (oral)

3. *Estimation of thickness and wave speed in cortical bone using ultrasound imaging: an ex vivo study*
   Amadou S. DIA, Guillaume RENAUD, Christine CHAPPARD, Quentin GRIMAL
   Conférence: IEEE, International Ultrasonic Symposium, Venise, Italie, October 2022, (poster)

4. *Ultrasound Imaging of bone cortex: beamforming optimization for osteoporotic bones*
   Amadou S. DIA, Guillaume RENAUD, Quentin GRIMAL
   Conférence: Congress of the European Society of Biomechanics, Porto, Portugal, June 2022, (oral)

5. *The influence of cortical microstructure on ultrasound images of the bone cortex: a numerical study*
   Amadou S. DIA, Guillaume RENAUD, Quentin GRIMAL
   Conférence: Quantitative Musculoskeletal Imaging (QMSKI) in conjuctionc with the International Symposium on Ultrasonic Characterization of Bone (ISUCB), Noordwick, Netherlands, 2022, (poster)

6. *Assessing the performance of ultrasound imaging of the cortex in osteoporotic bones*
   Amadou S. DIA, Guillaume RENAUD, Christine Chappard, Quentin GRIMAL
   Conférence: Quantitative Musculoskeletal Imaging (QMSKI) in conjuctionc with the International Symposium on Ultrasonic Characterization of Bone (ISUCB), Noordwick, Netherlands, 2022, (oral)

7. *The influence of intra-cortical microstructure on the contrast in ultrasound images of the bone cortex*
   Amadou S. DIA, Guillaume RENAUD, Quentin GRIMAL
   Conférence: IEEE, International Ultrasonic Symposium, Online, 2021 (oral)

Contents

Chapter 1

General introduction

Contents

1.1 Medical context

Bone mechanical structure. At the macroscopic scale, two types of bone tissue exist: dense cortical bone and spongy trabecular bone (Figure 1.1). Cortical bone constitutes the majority of the human skeleton's mass, accounting for approximately 80%. It is primarily found in the shafts (diaphyses) of long bones, where it forms a compact tube surrounding the bone marrow cavity (medullary cavity). Additionally, the outer shell of other bone types is made of cortical bone tissue, such as short and flat bones, or the skull. Cortical bone has low porosity, typically lower than 15% [1]. Trabecular bone, on the other hand, is highly porous, with porosity larger than 70%. It is primarily found in short and flat bones, such as the vertebrae, and at the extremities of long bones (Figure 1.1)

Below the millimeter scale, cortical bone can be seen as a composite material made of two main components. Firstly, there is a dense mineralized matrix consisting of hydroxyapatite crystals and collagen fibers. This matrix provides the bone with its strength and rigidity, contributing to its overall mechanical properties. Secondly, within this matrix, there is a network of interconnected cavities. These cavities, or pores, contain vessels and nerves (see Figure 1.2). The mineralized collagen fibers and the Haversian canals (cylindrical pores roughly 100 µm in diameter) are nearly parallel to the long bone axis (see Figure 1.2), resulting in elastic anisotropy at the milimeter scale and above [3].

Cortical bone remodeling and bone loss. Remodeling of the mineralized matrix plays a vital role in maintaining the mechanical and metabolic functions of bones. This process involves replacing old bone tissue with new one, with approximately 5 to 10% of the skeleton undergoing remodeling annually during adulthood. Each remodeling cycle begins with a bone resorption phase followed by a formation phase. Functional remodeling units (or basic multicellular units BMUs), typically around 100 µm in size, operate independently in terms of location and activation. Osteoclasts in the BMU are responsible for destroying and removing bone tissue

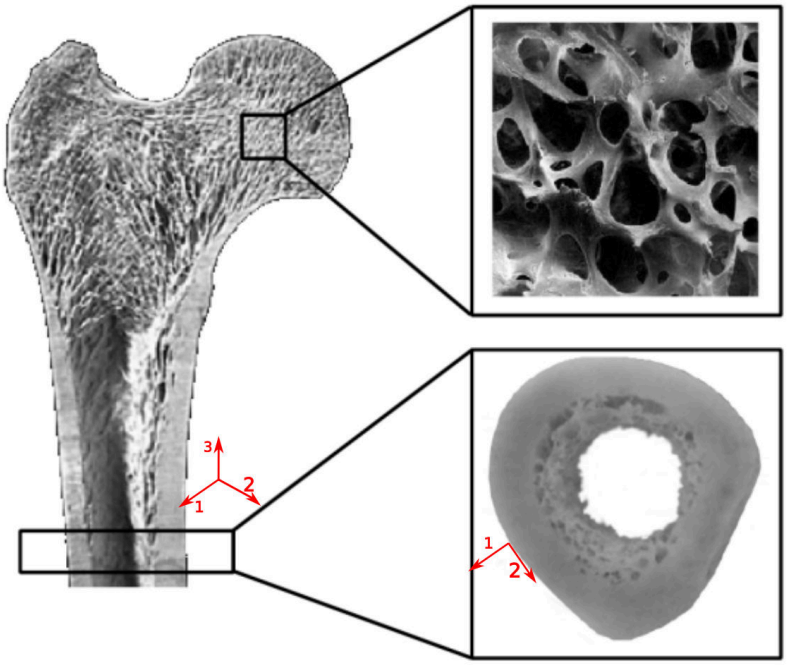

Figure 1.1: Illustration of the structure of both types of bone tissue in a femur: trabecular bone (top) is highly porous and present at the extremities and cortical bone (bottom) is the central part of long bones. Reproduced from Granke [2].

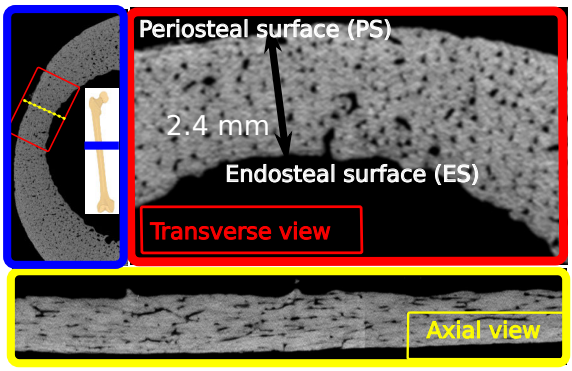

Figure 1.2: Microstructure of human cortical bone in transverse (1-2) and axial plane (1,3). Cortical bone is composed of a dense mineralized matrix and a network of interconnected cavities (pores). Images obtained at the human femoral mid-shaft from microcomputed tomography with a voxel size of 8.8 µm.

during the resorption phase, creating a resorption cavitity observed as large pores (diameter larger than about 80 microns) in post-mortem bone cross-sections. These holes are then partially filled by new bone tissue synthetized by osteoblasts during the formation phase.

Until approximately the age of 35, there exists a balance between bone formation and resorption, resulting in low cortical porosity (<5%). At this age, the peak bone mass is achieved and maintained until the age of approcimately 50. However, beyond this age, bone resorption begins to outpace formation, leading to bone loss [4]. Cortical bone which is the primary focus of this thesis, undergoes significant changes during this process.

Remodeling enlarges canals, causing adjacent ones to merge and creating larger pores (Figure 1.3). Resorption is more pronounced at the internal bone surface (endosteal surface), resulting in reduced thickness, increased cortical porosity, and

changes in endosteal structure: the initially smooth bone surface becomes rougher.

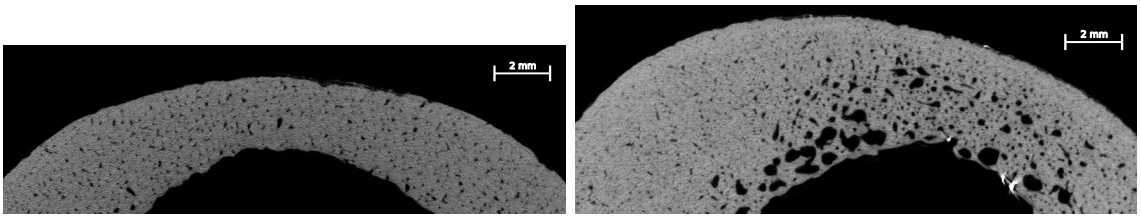

Figure 1.3: Illustration of the increase of pore size in cortical bone. In a healthy bone, the size of the pores is homogeneous in the cortex (left) but for degraded bones the adjacent pores merge to create large pores more present in the endosteal surface (right). Images are obtained from microcomputed tomography with a voxel size of 8.8 µm (see Chapter 4).

Osteoporosis. Osteoporosis is a systemic disease of the skeleton which essentially magnifies this natural bone aging process [5]. Factors like poor nutrition, sedentary lifestyles, or underlying health issues can exacerbate bone loss. In women, bone density decline accelerates post-menopause due to estrogen level drops [6]. Typically, women lose about 0.5% of bone mass annually from their thirties, with a faster loss of 2% to 5% per year in the initial 5 to 10 years post-menopause [7] and a part of this loss of bone is loss of cortical bone through reduction of cortical thickness and increase of cortical porosity.

The primary clinical consequence of osteoporosis is bone fractures. Globally, one in three women over the age of 50 and one in five men aged over 50 will experience osteoporosis fractures, contributing to more than 8.9 million fractures annually worldwide. The economic and human impact of these fractures is significant. For instance, in 2019, approximately 22% of European women aged over 50 were estimated to have osteoporosis, resulting in a cost of around 30 billion euros [1]. Additionally, osteoporosis is an asymptomatic disease, meaning that there are no apparent symptoms until a fracture occurs. Individuals who suffer from fractures are also at an increased risk of developing other illnesses, leading to higher mortality rates.

To tackle these economic and human costs, reliable prediction of fracture risk is essential for the diagnosis of osteoporosis and to initiate therapy.

Bone densitometry. The current gold standard technique for diagnosing osteoporosis and predicting fracture risk is dual-energy X-ray absorptiometry (DXA). It measures bone mineral density (BMD) by transmitting low-dose X-rays through bones. The T-score quantifies the deviation between this measured BMD and the average BMD observed in young adults (aged 30 to 40 years), expressed in number of standard deviations. If the T-score is less than -2.5, meaning the measured density is more than 2.5 standard deviations below the reference of the population, then the patient is diagnosed with osteoporosis. DXA provides precise measurements of BMD at various skeletal sites, typically the hip and spine. However, studies have revealed that BMD alone cannot reliably identify all individuals at risk of fracture [5]. For instance, research has shown that a significant proportion of non-vertebral fractures occur in individuals with normal BMD. This highlights the limitation of BMD in assessing bone strength, as it primarily reflects bone quantity rather than mechanical quality. Bone quality, which encompasses factors beyond BMD such as microstructure, bone matrix constituents, and tissue mechanical properties, plays

[1] https://www.osteoporosis.foundation/facts-statistics/key-statistic-for-europe

a crucial role in determining bone strength and fracture risk. Furthermore, DXA, being a 2D (projection) imaging technique, it only measures the combined loss of cortical and trabecular bone.

Recent advancements have introduced a 3D X-ray imaging technique known as High-resolution peripheral computed tomography (HR-pQCT), which stands as the most advanced imaging method currently available. With a physical resolution of approximately 100 µm, HR-pQCT enables quantitative analysis of both cortical and trabecular bone, providing estimates of bone density, microarchitecture, and geometry. It allows for the measurement of cortical thickness and, to some extent, cortical porosity (large pores only) at the distal radius and tibia. However, due to its high cost and the use of ionizing radiation, HR-pQCT is unlikely to become a clinical diagnostic tool for osteoporosis, thus remaining primarily confined to clinical research.

1.2 Role of cortical porosity and cortical thickness in bone strength

As cortical bone primarily bears the load and contributes to bone strength, the cortical thickness correlates with both mechanical strength. For instance, a study has demonstrated a correlation (r = 0.88) between cortical bone thickness and fracture load at the distal radius [8].

Cortical porosity is also an important determinant of bone mechanical quality and is recognized as a biomarker of fracture risk [9, 10, 11, 12]. Various studies have reported correlations between porosity and elastic moduli. Granke et al. [13] and Cai et al. [14] reported R^2 values (Pearson's linear coefficient of determination) ranging from 0.70 to 0.84 between all stiffness coefficients and cortical porosity. They demonstrated that the Haversian porosity is the primary factor determining the elasticity of cortical bone at the millimeter scale. Furthermore, cortical porosity has been observed *in vivo* with HR-pQCT to rise with age [1], as well as with the advancement of osteoporosis [15]. Studies have shown correlations between cortical porosity and the occurrence of vertebral and non-vertebral fractures [16, 17].

Moreover, increased porosity can lead to the trabecularization of the internal (endosteal) surface of cortical bone and thinning of the cortex, which further diminishes bone strength and exposes it to an increased risk of osteoporotic fractures [18]. Consequently, cortical porosity, along with cortical thickness, plays a major role in determining bone mechanical strength.

Therefore, there is a pressing need to develop alternative diagnostic approaches to DXA capable of providing a comprehensive assessment of bone strength. Specifically, one objective is to assess porosity and thickness of cortical bone.

1.3 QUS for the characterisation of cortical bone

An alternative to X-ray techniques, proposed for about more than 30 years, involves the use of quantitative ultrasound techniques (QUS), which have the advantage of being non-ionizing and less costly. Ultrasound (mechanical waves) is intrinsically sensitive to the mechanical properties that contribute to the overall strength of bone. In cortical bone, variations in ultrasonic properties (speed of sound, attenuation) within and between individuals primarily stem from differences in bone

micro-architecture, in particular the porosity. Also, because ultrasound waves are strongly reflected at interfaces between bone and soft tissues, wave propagation can be leveraged to measure cortical thickness.

1.3.1 US wave speeds reflect the strength and porosity of cortical bone

Due to the limitations in resolution, QUS can not directly evaluate cortical porosity. Wavelength is typically larger than 1 mm, hence, US probe apparent material properties. Indirect measurements of properties sensitive to changes in porosity are used. Numerous studies have demonstrated a significant correlation between propagating wave speed and cortical bone porosity [19, 20, 21, 22].

Furthermore, Peralta et al. have shown that wave speeds, measured in various directions and polarizations (shear or longitudinal wave), reflect bone strength and porosity [23]. Higher wave speeds typically indicate denser bone with lower porosity, associated with greater strength and stiffness. Conversely, lower wave speeds often correlate with increased porosity, reduced bone density, and compromised mechanical strength.

Consequently, ultrasonic wave speeds may serve as indirect biomarkers for assessing bone strength and understanding the structural characteristics of cortical bone to help predict fracture risk [24].

1.3.2 Elastic anisotropy of cortical bone

In figure 1.1 and 1.4, the radial direction corresponds to direction 1, the circumferential direction corresponds to direction 2, and the axial direction corresponds to direction 3. Human cortical bone elasticity is often characterized by a model of transverse isotropy [13, 25]. More precisely, cortical bone can be considered isotropic (independent of direction) in the (1-2) plane perpendicular to the bone axis 3 (which is the material symmetry axis), and anisotropic in other planes. In elastic materials,

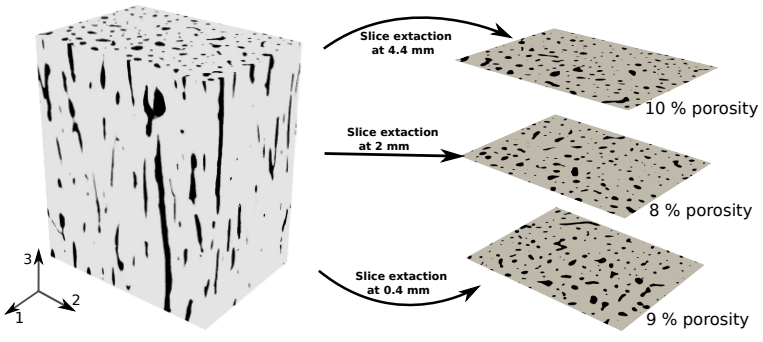

Figure 1.4: Binarized Synchroton Radiation microcomputed tomography (SR-µCT) image of a cortical bone specimen of nominal dimensions $3 \times 4 \times 5$ mm^3 (original voxel size 6.5 µm). Black: vascular pores; light gray: mineralized matrix. Axis 1 corresponds to radial direction, axis 2 to the circumferential direction and axis 3 to the axial direction. For illustration, 3 slices extracted from the 3D volume are shown. 2D porosity values are given for each slice, illustrating the variable porosity in a 3D volume.

two types of ultrasonic waves propagate: compressional and shear waves. This thesis focuses only on the propagation of compressional waves. For elastic materials, the speed of sound is defined as the square root of the ratio of elasticity to mass density ρ. Using Voigt notation, the elasticity law is expressed as $\sigma_i = C_{ij}\varepsilon_j$ with i, j = 1..3, where σ_i and ε_j represent components of the stress and strain vectors, respectively, and C_{ij} is the stiffness matrix. The stiffness constants C_{ii} correspond to compressional loadings along different anatomical directions. Given that the (1-2) plane is the plane of isotropy, $C_{11} = C_{22}$. The longitudinal speed of sound in the radial and axial directions are given respectively by $V^{\text{radial}} = \sqrt{\frac{C_{11}}{\rho}}$ and $V^{\text{axial}} = \sqrt{\frac{C_{33}}{\rho}}$. The reported anisotropy ratio C_{33}/C_{11} of human cortical bone *ex vivo* , ranges between 1.3 and 2.5 [25, 12].

1.3.3 Developed QUS techniques for assessing cortical porosity and cortical thickness

Developed QUS methods can be categorized into two types: pulse-echo and axial transmission techniques [24].

Axial transmission. These methods exploit the fact that cortical bone acts as a waveguide.

Most of the existing devices that exploit the principle of axial transmission for measuring cortical bone properties measure the velocity of the First Arriving Signal (FAS). Among these devices are SoundScan (Myriad Ultrasound Systems Ltd., Israel), Omnisense (Sunlight Ultrasound Technologies Ltd., Rehovot, Israel), and Sono (Oscare Medical Oy, Vantaa, Finland). Physically, the FAS is associated with the head wave (lateral wave) and Lamb waves guided by the cortical thickness; it correlates with a combination of material properties and cortical thickness (for Lamb waves only). However, these devices provide only one ultrasound parameter, which cannot be used as a proxy for a structural or material bone property. They do not provide in real time the anatomy of the bone. For further details on these devices and the axial transmission method, readers are encouraged to refer to [24], particularly chapters 3, 4, and 5.

Another approach, BDAT (Azalée, Paris, France), uses the Bidirectional Axial Transmission. From a multimode guided waves approach and a dedicated signal processing, BDAT is capable of estimating both cortical thickness and an index of cortical porosity [26, 27]. The device has undergone validation both *in vivo* and *ex vivo* [28, 29, 30]. However, a major limitation of this device is the assumption that bone behaves as a perfect waveguide (i.e. a plate made of homogeneous material and with constant thickness), which is only the case for healthy or moderately altered bones.

Pulse-echo methods. Some devices using the pulse-echo techniques use a single-element focused transducer to send a short pulse and record the specular echoes from external and internal bone interface. From the delay between the reflections, cortical thickness is deduced. The device has undergone clinical validations and proof-of-concept studies [31]. However, this technique has at least two principal limitations: (i) the cortical thickness is not accurately measured since a fixed ultrasonic wave speed of 3565 m/s is assumed for all individuals [32] and (ii) the alignment of the transducer and the bone axis is not based on a real-time image of the cortex but only on the raw received RF echoes.

Limitations of current QUS techniques. While the methods mentioned above give estimates of cortical thickness or relevant material properties for discriminating osteoporotic individuals, simultaneously retrieving multiple bone characteristics, such as geometry (e.g., cortical thickness or cortical area) and material properties (e.g., ultrasonic wave speed or cortical porosity), poses a significant challenge. BDAT, the only clinical device capable of providing a combined estimation of cortical thickness and an index of cortical porosity assumes that bone behaves as a perfect wave guide, which is not the case for many individuals in practice.

Furthermore, despite using advanced ultrasound physics, none of these clinical devices are capable of producing an anatomical image of the cortex, as is typically done in most ultrasound devices for soft tissues.

Emerging techniques. Recently, various approaches have been proposed for obtaining an ultrasound image of the cortex [33, 34, 35, 36, 37].

A tomography setup has been proposed to provide a quantitative image of cortical bone in the transverse plane [38, 33]. From the image, an estimate of the cortical thickness is provided. However, this method requires highly specialized ultrasound equipment such a circular array and no *in vivo* data is available yet as far as we are aware.

Another imaging method was developed using refraction-corrected multifocus imaging to provide an estimate of the cortical thickness and the wave speed in the radial direction of bone [37]. The method has been tested and validated *ex vivo* [39]. However, the method does not provide a real-time image of bone anatomy and is limited to the transverse plane meaning that the anisotropy of the cortex can not be evaluated.

The imaging approach initiated at the Laboratoire d'Imagerie Biomédicale (LIB, Sorbonne Université, Paris) by Renaud et al. (2018) [35] provides real-time anatomical images of cortical bone in both the transverse (1-2) and longitudinal planes (2-3). It enables the estimation of cortical thickness and material properties by measuring wave speeds in all anatomical directions. This thesis focuses on exploring this approach which is briefly presented in the next section. An extensive description of the technique can be found in [40].

1.4 Bone ultrasound imaging

1.4.1 General principle to obtain an image of the cortex

The primary reason conventional echographs fail to image the interior of cortical bone is due to significant refraction [35]. Indeed the speed of sound in cortical bone is notably higher, ranging from 2800 to 4200 m/s [13], compared to soft tissues, which typically have speeds ranging from 1400 to 1700 m/s [41].

Therefore, the main assumption that a ray propagates in a straight line used for soft-tissues imaging is not applicable to bone imaging. In this imaging approach, the medium to be imaged is considered as composed of three distinct homogeneous layers (silicone layer of the ultrasound probe, cutaneous tissue and cortical bone). Refraction is accounted for at each boundary. The steps to obtain an image of the cortex can be summarized as follows:

- First, an image of the cutaneous tissue is obtained using a delay-and-sum (DAS) beamforming algorithm (see section 1.4.2).

- Second, from the image of the cutaneous tissue, the boundary between the cutaneous tissue and the cortical bone is segmented. The segmentation is achieved by searching for the shortest path extending along the entire lateral length of the image with maximal intensity, using Dijkstra's algorithm. Afterwards, the segmented interface is fitted to a parabola.

- Using this fitted parabola as the external boundary of the cortex, an image of the cortex is obtained with the DAS beamforming algorithm accounting for refraction between soft tissues and bone.

- Finally, from the image of the cortex, the boundary between cortical bone and the marrow (medullary cavity) is segmented using a Dijkstra's algorithm. Note that the approach can be extended to image also the cortex opposite to the medullary cavity.

After image reconstruction, two types of anatomical image are obtained depending on the configuration: an image in the transverse plane (1-2) (Figure 1.5a and 1.5c) and an image in the longitudinal plane (1-3) (Figure 1.5b and 1.5d).

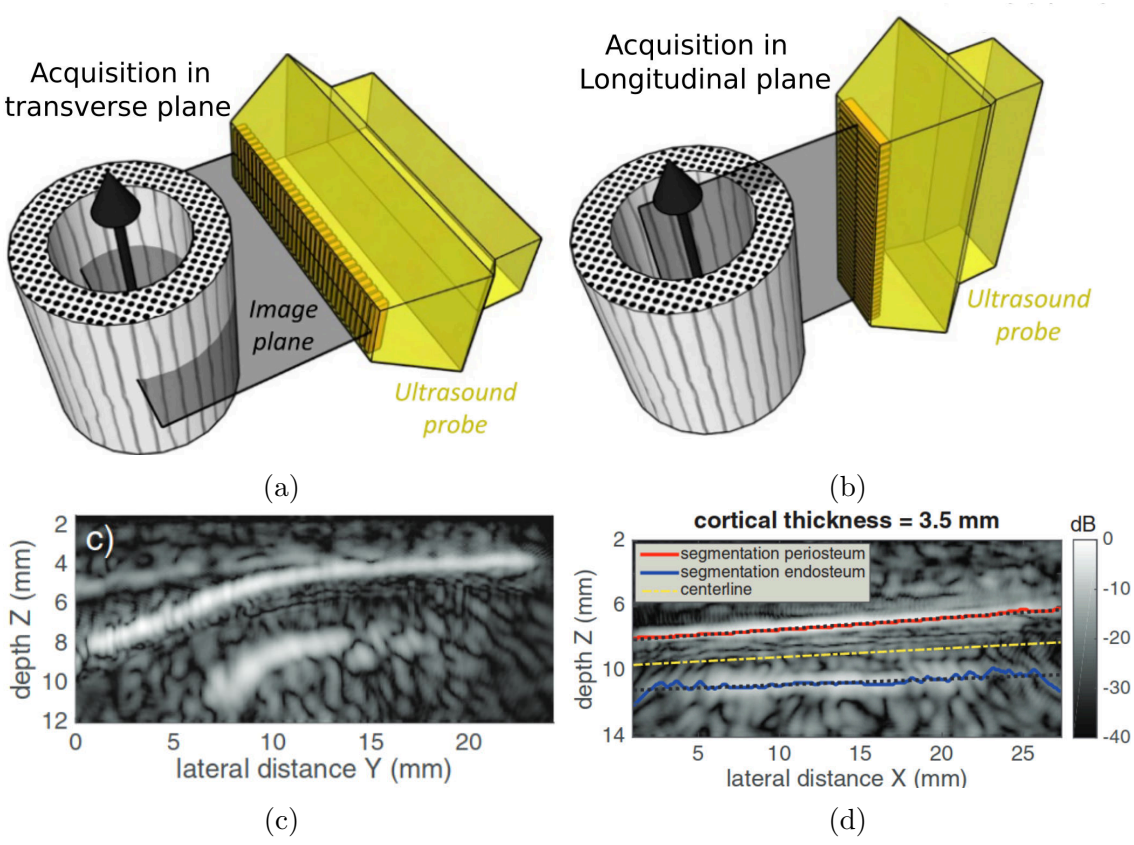

Figure 1.5: Illustration of the two imaging configurations *in vivo* : a transverse configuration (a) to obtain an *in vivo* image of cortical bone in the transverse plane (c) and a longitudinal configuration (b) to obtain an *in vivo* image of cortical bone in the longitudinal plane (d). Images are reproduced and adapted from [35, 42].

From these images and the segmented outer (periosteal) and inner (endosteal) surface of the cortex, the cortical thickness is estimated (Figure 1.5d). In the transverse plane (1-2), there exists only one longitudinal wave speed for all directions: V^{radial}. However, in the axial plane, the wave speed varies depending on the propagation direction due to anisotropy. We denote V^{axial} the wave speed in the direction parallel to the axis. More details on the velocity model are given in Chapter 2.

1.4.2 Principle of image reconstruction

A synthetic Aperture (SA) transmission technique [43] is used: each element of the probe sequentially transmits an unfocused beam, and all elements of the probe record the back-scattered echoes. A low-resolution image is reconstructed for each transmit. Coherently combining the low-resolution images yields a high-resolution image. The signals recorded by the elements are stored in the 3D matrix $\mathbf{S}(t, iR, iT)$ where iT and iR are the emitting and receiving element numbers respectively.

Image reconstruction of each layer (lens, cutaneous tissues, bone cortex) is performed using a delay-and-sum (DAS) beamforming algorithm. In DAS algorithms, each image pixel represents a hypothetical scattering point within the medium. Thus, the fundamental principle of all DAS-based methods involves delaying all received signals originating from a specific point in the medium (corresponding to the pixel to be reconstructed) based on their respective time-of-flight. These delayed signals are then summed to generate an estimate of the reflectivity, corresponding to the intensity $I(P)$ of pixel P. The intensity of an image pixel is thus given by:

$$I(P) = \sum_{iT}^{N_T} \sum_{iR}^{N_R} \mathbf{S}\left(t = \tau_T(iT, P) + \tau_R(iR, P), iT, iR\right), \tag{1.1}$$

where τ_T and τ_R are the transmit and receive travel times of the wave.

τ_T and τ_R are determined by calculating the travel time along a transmit ray path from the emitting element iT to the point of interest P and a receive ray path from the point P to the receiving element iR (Figure 1.6). These ray paths are computed using Snell's law of refraction.

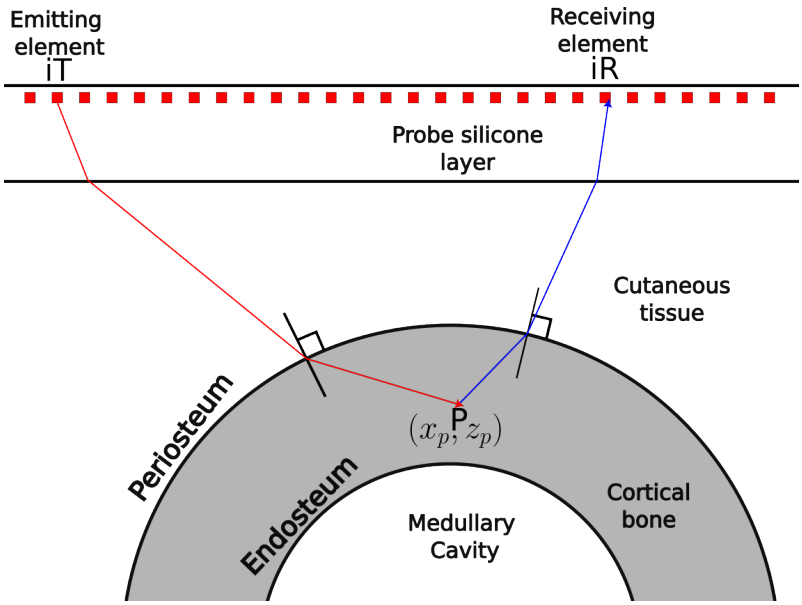

Figure 1.6: Illustration of the transmit ray path from transmit element iT to pixel P and the receive ray path from pixel P to receive element iR for a medium with four homogeneous layers: the silicone front layer of the probe, cutaneous tissue, cortical bone, and the marrow. Refraction is considered at each boundary between two layers.

To compute the travel time, the speed of sound in each medium must be known. The wave speed and characteristics of the silicone layer of the probe are fixed. However, the wave speeds in cutaneous tissues and cortical bone are individual-specific. Therefore, before each reconstruction, these wave speeds are calculated

using a model that considers bone anisotropy. More details on their determination are given in Chapter 2. For real-time imaging, a fixed 'reasonable' value of these wave speed is sufficient to reconstruct the image. However, accurate determination of these individual-specific material properties are required to measure cortical thickness.

1.5 Scope and Objectives of the Thesis

In 2020, before the start of this thesis, anatomical images of cortical bone were only obtained for two healthy volunteers with the method presented above. Given the variability in bone geometry and microstructure composition among individuals, data from two healthy individuals is insufficient to assess the potential of the technique. Furthermore, the different factors that affect the quality of an ultrasound image of the bone are unknown. Finally, the algorithm relies on the Delay-and-Sum (DAS) beamforming to obtain cortex images; however, DAS is primarily optimized for diffuse scattering, whereas reflections occurring at external and internal interfaces are more likely to be specular rather than diffuse.

The purpose of this thesis was to achieve three main objectives:

- Improve our understanding of the factors influencing the quality of bone ultrasound images, in particular the role of pores acting as scatterers and creating speckle.
- Complement the validation of the technique to measure cortical thickness and material properties of bones of healthy subjects but also bones of older individuals.
- Explore the added value of using image reconstruction techniques tailored to the physics of wave propagation in bone, enhancing specular reflections at bone interfaces to improve contrast.

For these purposes, we used synthetic data generated with a numerical wave solver, *ex vivo* data and *in vivo* data.

1.6 Outline of the thesis

Chapter 2 presents the first *in vivo* assessment of wave speed precision in bone tissues using ultrasound imaging, providing wave speed values in both radial and axial directions of the human tibia, along with the anisotropy form parameter. The study involved 11 healthy male individuals and contributes to the validation of the technique to measure wave speed and its anisotropy for healthy subjects. This chapter includes a detailed description of the estimation of the ultrasound wave speed and its anisotropy.

Chapter 3 presents a published study [44] that quantifies the impact of microstructure on the contrast of bone ultrasound images. Through simulations of ultrasound propagation in realistic cortical microstructures where the geometry of the bone is controlled, the chapter investigates the influence of variables of microstructures such as porosity and pore size on ultrasound image quality.

Chapter 4 presents the first *ex vivo* ultrasound images of femur specimens from elderly human donors. In this chapter, wave speed and cortical thickness are estimated and US images are compared to reference micro-computed tomography

(μCT) images (high resolution). This chapter not only contributes to the validation of cortical thickness estimation in transverse ultrasound images but also enhances our understanding of the determinants of ultrasound image quality in specimens exhibiting moderate to high cortical porosity. It further examines a relationship between wave speed estimated from ultrasound images and cortical porosity.

In Chapter 5, we present an adapted specular beamforming algorithm initially proposed to better image specular reflectors in soft tissue. The algorithm is adapted to consider bone curvature and account for both wave refraction and specular reflection physics with the aim to enhance the contrast of bone surfaces and reduce speckle from intracortical pores. In this chapter, the method is presented and tested on simulated bone datasets designed to replicate cortical bone with varying microstructures.

Finally, in Chapter 6, we apply the specular beamforming algorithm discussed earlier to both the *in vivo* (Chapter 2) and *ex vivo* (Chapter 4) datasets. Its performance is compared with the DAS algorithm.

Bibliography

[1] Valérie Bousson, Alain Meunier, Catherine Bergot, Éric Vicaut, Maria Augusta Rocha, Maria Helena Morais, Anne-Marie Laval-Jeantet, and Jean-Denis Laredo. Distribution of Intracortical Porosity in Human Midfemoral Cortex by Age and Gender. *Journal of Bone and Mineral Research*, 16(7):1308–1317, 2001.

[2] Mathilde Granke. *Evaluation multi-échelle de la qualité osseuse par ultrasons*. These de doctorat, Paris 7, January 2012.

[3] Xiran Cai, Laura Peralta, Renald Brenner, Gianluca Iori, Didier Cassereau, Kay Raum, Pascal Laugier, and Quentin Grimal. Anisotropic elastic properties of human cortical bone tissue inferred from inverse homogenization and resonant ultrasound spectroscopy. *Materialia*, 11:100730, June 2020.

[4] Usha Kini and B. N. Nandeesh. Physiology of Bone Formation, Remodeling, and Metabolism. In Ignac Fogelman, Gopinath Gnanasegaran, and Hans van der Wall, editors, *Radionuclide and Hybrid Bone Imaging*, pages 29–57. Springer, Berlin, Heidelberg, 2012.

[5] Ethel S. Siris, Ya-Ting Chen, Thomas A. Abbott, Elizabeth Barrett-Connor, Paul D. Miller, Lois E. Wehren, and Marc L. Berger. Bone Mineral Density Thresholds for Pharmacological Intervention to Prevent Fractures. *Archives of Internal Medicine*, 164(10):1108–1112, May 2004.

[6] B. Lawrence Riggs, Sundeep Khosla, and L. Joseph Melton, III. Sex Steroids and the Construction and Conservation of the Adult Skeleton. *Endocrine Reviews*, 23(3):279–302, June 2002.

[7] Matthew B Dobbs, Joseph Buckwalter, and Charles Saltzman. Osteoporosis. *The Iowa Orthopaedic Journal*, 19:43–52, 1999.

[8] P. Augat, H. Reeb, and L. E. Claes. Prediction of fracture load at different skeletal sites by geometric properties of the cortical shell. *Journal of Bone and Mineral Research*, 11(9):1356–1363, September 1996.

[9] Yohann Bala, Roger Zebaze, and Ego Seeman. Role of cortical bone in bone fragility. *Current Opinion in Rheumatology*, 27(4):406–413, July 2015.

[10] Roger Zebaze, Cesar Libanati, Michael R McClung, José R Zanchetta, David L Kendler, Arne Høiseth, Andrea Wang, Ali Ghasem-Zadeh, and Ego Seeman. Denosumab Reduces Cortical Porosity of the Proximal Femoral Shaft in Postmenopausal Women With Osteoporosis. *Journal of Bone and Mineral Research*, 31(10):1827–1834, October 2016.

[11] L. A. Ahmed, R. Shigdel, R. M. Joakimsen, O. P. Eldevik, E. F. Eriksen, A. Ghasem-Zadeh, Y. Bala, R. Zebaze, E. Seeman, and Å. Bjørnerem. Measurement of cortical porosity of the proximal femur improves identification of women with nonvertebral fragility fractures. *Osteoporosis International*, 26(8):2137–2146, August 2015.

[12] Q. Grimal and P. Laugier. Quantitative Ultrasound Assessment of Cortical Bone Properties Beyond Bone Mineral Density. *IRBM*, 40(1):16–24, February 2019.

[13] Mathilde Granke, Quentin Grimal, Amena Saïed, Pierre Nauleau, Françoise Peyrin, and Pascal Laugier. Change in porosity is the major determinant of the variation of cortical bone elasticity at the millimeter scale in aged women. *Bone*, 49(5):1020–1026, November 2011.

[14] Xiran Cai, Hélène Follet, Laura Peralta, Marc Gardegaront, Delphine Farlay, Rémy Gauthier, Boliang Yu, Evelyne Gineyts, Cécile Olivier, Max Langer, Aurelien Gourrier, David Mitton, Françoise Peyrin, Quentin Grimal, and Pascal Laugier. Anisotropic elastic properties of human femoral cortical bone and relationships with composition and microstructure in elderly. *Acta Biomaterialia*, 90:254–266, May 2019.

[15] Kyle K Nishiyama, Heather M Macdonald, Helen R Buie, David A Hanley, and Steven K Boyd. Postmenopausal women with osteopenia have higher cortical porosity and thinner cortices at the distal radius and tibia than women with normal aBMD: An in vivo HR-pQCT study. *Journal of Bone and Mineral Research*, 25(4):882–890, April 2010.

[16] Agnès Ostertag, Martine Cohen-Solal, Maurice Audran, Erick Legrand, Caroline Marty, Daniel Chappard, and Marie-Christine de Vernejoul. Vertebral fractures are associated with increased cortical porosity in iliac crest bone biopsy of men with idiopathic osteoporosis. *Bone*, 44(3):413–417, March 2009.

[17] K. L Bell, N Loveridge, J Power, N Garrahan, B. F Meggitt, and J Reeve. Regional differences in cortical porosity in the fractured femoral neck. *Bone*, 24(1):57–64, January 1999.

[18] Roger MD Zebaze, Ali Ghasem-Zadeh, Ann Bohte, Sandra Iuliano-Burns, Michiko Mirams, Roger Ian Price, Eleanor J Mackie, and Ego Seeman. Intracortical remodelling and porosity in the distal radius and post-mortem femurs of women: a cross-sectional study. *The Lancet*, 375(9727):1729–1736, May 2010.

[19] Kay Raum, Ingrid Leguerney, Florent Chandelier, Emmanuel Bossy, Maryline Talmant, Amena Saïed, Françoise Peyrin, and Pascal Laugier. Bone microstructure and elastic tissue properties are reflected in QUS axial transmission measurements. *Ultrasound in Medicine & Biology*, 31(9):1225–1235, September 2005.

[20] Julien Grondin, Quentin Grimal, Kazufumi Yamamoto, Mami Matsukawa, Amena Saïed, and Pascal Laugier. Relative contributions of porosity and mineralized matrix properties to the bulk axial ultrasonic wave velocity in human cortical bone. *Ultrasonics*, 52(4):467–471, April 2012.

[21] Vincent Mathieu, Christine Chappard, Romain Vayron, Adrien Michel, and Guillaume Haïat. Radial Anatomic Variation of Ultrasonic Velocity in Human Cortical Bone. *Ultrasound in Medicine & Biology*, 39(11):2185–2193, November 2013.

[22] C. T. M. Eneh, M. K. H. Malo, J. P. Karjalainen, J. Liukkonen, J. Töyräs, and J. S. Jurvelin. Effect of porosity, tissue density, and mechanical properties on radial sound speed in human cortical bone. *Medical Physics*, 43(5):2030–2039, 2016. _eprint: https://onlinelibrary.wiley.com/doi/pdf/10.1118/1.4942808.

[23] Laura Peralta, Juan Deyo Maeztu Redin, Fan Fan, Xiran Cai, Pascal Laugier, Johannes Schneider, Kay Raum, and Quentin Grimal. Bulk wave velocities in cortical bone reflect porosity and compression strength. *Ultrasound in Medicine & Biology*, 47(3):799–808, 2021.

[24] Pascal Laugier and Quentin Grimal. *Bone Quantitative Ultrasound: New Horizons*. Number 1364 in Advances in Experimental Medicine and Biology. Springer International Publishing, 1st ed. 2022 edition, April 2022.

[25] Simon Bernard, Joannes Schneider, Peter Varga, Pascal Laugier, Kay Raum, and Quentin Grimal. Elasticity–density and viscoelasticity–density relationships at the tibia mid-diaphysis assessed from resonant ultrasound spectroscopy measurements. *Biomechanics and Modeling in Mechanobiology*, 15(1):97–109, February 2016.

[26] J. G. Minonzio, N. Bochud, Q. Vallet, Y. Bala, D. Ramiandrisoa, H. Follet, D. Mitton, and P. Laugier. Bone cortical thickness and porosity assessment using ultrasound guided waves: An ex vivo validation study. *Bone*, 116:111–119, November 2018.

[27] Quentin Vallet, Nicolas Bochud, Christine Chappard, Pascal Laugier, and Jean-Gabriel Minonzio. In Vivo Characterization of Cortical Bone Using Guided Waves Measured by Axial Transmission. *IEEE Transactions on Ultrasonics, Ferroelectrics, and Frequency Control*, 63(9):1361–1371, September 2016. Conference Name: IEEE Transactions on Ultrasonics, Ferroelectrics, and Frequency Control.

[28] J-G Minonzio, N Bochud, Q Vallet, D Ramiandrisoa, A Etcheto, K Briot, S Kolta, C Roux, and P Laugier. Ultrasound-Based Estimates of Cortical Bone Thickness and Porosity Are Associated With Nontraumatic Fractures in Postmenopausal Women: A Pilot Study. *Journal of Bone and Mineral Research*, 34(9):1585–1596, September 2019.

[29] Johannes Schneider, Donatien Ramiandrisoa, Gabriele Armbrecht, Zully Ritter, Dieter Felsenberg, Kay Raum, and Jean-Gabriel Minonzio. *In Vivo* Measurements of Cortical Thickness and Porosity at the Proximal Third of the Tibia Using Guided Waves: Comparison with Site-Matched Peripheral Quantitative Computed Tomography and Distal High-Resolution Peripheral Quantitative Computed Tomography. *Ultrasound in Medicine & Biology*, 45(5):1234–1242, May 2019.

[30] Johannes Schneider, Gianluca Iori, Donatien Ramiandrisoa, Maroua Hammami, Melanie Gräsel, Christine Chappard, Reinhard Barkmann, Pascal Laugier, Quentin Grimal, Jean-Gabriel Minonzio, and Kay Raum. Ex vivo cortical porosity and thickness predictions at the tibia using full-spectrum ultrasonic guided-wave analysis. *Archives of Osteoporosis*, 14(1):21, February 2019.

[31] J. P. Karjalainen, O. Riekkinen, and H. Kröger. Pulse-echo ultrasound method for detection of post-menopausal women with osteoporotic BMD. *Osteoporosis International*, 29(5):1193–1199, May 2018.

[32] Janne Karjalainen, Ossi Riekkinen, Juha Toyras, Heikki Kroger, and Jukka Jurvelin. Ultrasonic assessment of cortical bone thickness in vitro and in

vivo. *IEEE Transactions on Ultrasonics, Ferroelectrics, and Frequency Control*, 55(10):2191–2197, October 2008. Conference Name: IEEE Transactions on Ultrasonics, Ferroelectrics, and Frequency Control.

[33] Rui Zheng, Lawrence H. Le, Mauricio D. Sacchi, and Edmond Lou. Imaging Internal Structure of Long Bones Using Wave Scattering Theory. *Ultrasound in Medicine & Biology*, 41(11):2955–2965, November 2015.

[34] Simon Bernard, Vadim Monteiller, Dimitri Komatitsch, and Philippe Lasaygues. Ultrasonic computed tomography based on full-waveform inversion for bone quantitative imaging. *Physics in Medicine & Biology*, 62(17):7011, August 2017. Publisher: IOP Publishing.

[35] Guillaume Renaud, Pieter Kruizinga, Didier Cassereau, and Pascal Laugier. In vivo ultrasound imaging of the bone cortex. *Physics in Medicine & Biology*, 63(12):125010, June 2018. Publisher: IOP Publishing.

[36] Yunqing Li, Kailiang Xu, Chen Jiang, Ying Li, Chengcheng Liu, Jianqiu Zhang, Bo Hu, and Dean Ta. Cortical Bone Fracture Imaging using Velocity Model Based Multistatic Synthetic Aperture Ultrasound. In *2019 IEEE International Ultrasonics Symposium (IUS)*, pages 2348–2350, October 2019. ISSN: 1948-5727.

[37] Huong Nguyen Minh, Juan Du, and Kay Raum. Estimation of Thickness and Speed of Sound in Cortical Bone Using Multifocus Pulse-Echo Ultrasound. *IEEE transactions on ultrasonics, ferroelectrics, and frequency control*, 67(3):568–579, 2020.

[38] Philippe Lasaygues, Edgard Ouedraogo, Jean-Pierre Lefebvre, Marcel Gindre, Marilyne Talmant, and Pascal Laugier. Progress towards in vitro quantitative imaging of human femur using compound quantitative ultrasonic tomography. *Physics in Medicine & Biology*, 50(11):2633, May 2005.

[39] Huong Nguyen Minh, Marie Muller, and Kay Raum. Estimation of Thickness and Speed of Sound for Transverse Cortical Bone Imaging Using Phase Aberration Correction Methods: An In Silico and Ex Vivo Validation Study. *Applied Sciences*, 12(10):5283, January 2022. Number: 10 Publisher: Multidisciplinary Digital Publishing Institute.

[40] Guillaume Renaud and Sébastien Salles. Single-Sided Ultrasound Imaging of the Bone Cortex: Anatomy, Tissue Characterization and Blood Flow. In Pascal Laugier and Quentin Grimal, editors, *Bone Quantitative Ultrasound: New Horizons*, Advances in Experimental Medicine and Biology, pages 197–225. Springer International Publishing, Cham, 2022.

[41] K. Kirk Shung. *Diagnostic Ultrasound: Imaging and Blood Flow Measurements, Second Edition*. CRC Press, Boca Raton, 2 edition, April 2015.

[42] Guillaume Renaud, Pierre Clouzet, Didier Cassereau, and Maryline Talmant. Measuring anisotropy of elastic wave velocity with ultrasound imaging and an autofocus method: application to cortical bone. *Physics in Medicine & Biology*, 65(23):235016, November 2020.

[43] Jørgen Arendt Jensen, Svetoslav Ivanov Nikolov, Kim Løkke Gammelmark, and Morten Høgholm Pedersen. Synthetic aperture ultrasound imaging. *Ultrasonics*, 44:e5–e15, December 2006.

[44] Amadou Sall Dia, Guillaume Renaud, Aida Hejazi Nooghabi, and Quentin Grimal. The influence of intra-cortical microstructure on the contrast in ultrasound images of the cortex of long bones: A 2D simulation study. *Ultrasonics*, 127:106831, January 2023.

Chapter 2

In vivo assessment of speed of sound in cortical bone using ultrasound imaging: precision analysis

Contents

2.1 Introduction

Bone exhibits anisotropic properties, enabling the extraction of independent measures indicating its mechanical characteristics. Previously, Renaud et al. introduced the estimation of three parameters linked to elastic coefficients: wave speed in axial (V^{axial}) and radial (V^{radial}) directions, along with an anisotropy parameter (ξ). Potentially, the combination of these different material properties may emphasize different microstructural changes and provide a more complete analysis into alterations in the mechanical quality and fragility of the cortex.

The ultrasonic wave speed of an osteoporotic bone differs from that of a healthy bone. Peralta et al. (2021) reported that an increase in cortical porosity of 5% (corresponding to a loss of 10% of strength) is associated with a decrease in bulk wave speed of 100 m/s. This corresponds to a relative variation of around 3.3% of mean radial wave speed and around 2.6% of mean axial wave speed [1]. Therefore, for a QUS device to discriminate osteoporotic from healthy patients, it should have a precision error smaller than 3%.

As highlighted in Chapter 1, most of the current clinical QUS devices including BDAT, Omnisense, Soundscan and BDAT measure the ultrasonic wave speed in the cortex of different skeletal sites [2]. The precision of these devices has undergone extensive validation and testing in both clinical and research settings. Other quantitative ultrasound devices have been proposed to probe the wave speed in the transverse direction [3]. However, all of these approaches only estimate the properties of the bone along one direction.

This study presents the first *in vivo* assessment of wave speed precision in bone tissues using ultrasound imaging, providing wave speed values in both radial and axial directions of the human tibia, along with the anisotropy form parameter.

In the next section, we introduce the subjects involved in the study and describe the technique used for estimating the wave speed and its anisotropy parameter. In section 3, we present the results of the estimated wave speed in the cutaneous tissues

and the wave speed in cortical bone, and precision. Furthermore, we analyze the differences in measured wave speed between two measurement locations. In section 4, we discuss the results.

2.2 Subjects & methods

2.2.1 Experimental protocol

Human subjects. This study was part of a study involving healthy subjects aimed at measuring intra-osseous blood flow in the tibia using ultrasound similar to [4]. The research included eleven healthy male participants aged between 24 and 31 years old, with an average age of 28. Prior to participation, informed written consent was obtained from each participant for research purposes, in compliance with the legal requirements outlined in the French Code of Public Health approved by Ethics Committee and French Health Authorities (NO IDRCB: 2019-A02589-48, ClinicalTrials ID: NCT04396288).

Ultrasound data acquisition. The measurements were conducted using a fully programmable ultrasound system (Vantage, Verasonics Inc., Redmond, WA, USA). The scanning protocol utilized a synthetic aperture technique [5, 6], where each element in the ultrasound array was sequentially activated, followed by recording the full array of received echo signals. A complete ultrasound acquisition generated a total of 96×96 pulse-echo signals. A phased-array ultrasound transducer with 96 elements, operating at a central frequency of 2.5 MHz (P4-1 ATL/Philips, Bothell, WA, USA; pitch 0.295 mm), was used by two trained operators. The emitted pulse had a bandwidth of 80%.

Ultrasound acquisitions were performed perpendicular to the bone axis in transverse planes (Figure 2.1a) and parallel to the bone axis in longitudinal planes (Figure 2.1b). An example of received RF signals by all elements for emitting elements number 1 and 48 in the longitudinal plane is shown in Figure 2.2. The measurement sites were located at the middle of the tibia (mid-diaphysis) and proximal one-third of the tibia (proximal third). The length of the tibia was defined as the distance between the apex of the medial malleolus and the distal patellar apex. A pencil mark was made at each measurement site by the operators. Acquisitions were repeated five times at each site and for each measurement plane with repositioning, guided by real-time visualization. The probe alignment was confirmed when the ultrasound image presented bright external and internal interfaces.

2.2.2 Measurement of wave speed in cutaneous and bone tissues

As discussed in the first chapter, the region of interest will be considered as a medium with three homogeneous layers: the silicone front layer of the ultrasound probe, a layer of cutaneous tissue, and a layer of cortical bone tissue. Image reconstruction is performed sequentially for each layer. Following Renaud et al. 2018 [7], the estimation of the wave speed parameters is performed sequentially for each layer. The wave speed and thickness of the silicone layer for the P4-1 probe are 970 m/s and 1.3 mm respectively [7]. In the cutaneous and bone layers, the wave speed are estimated.

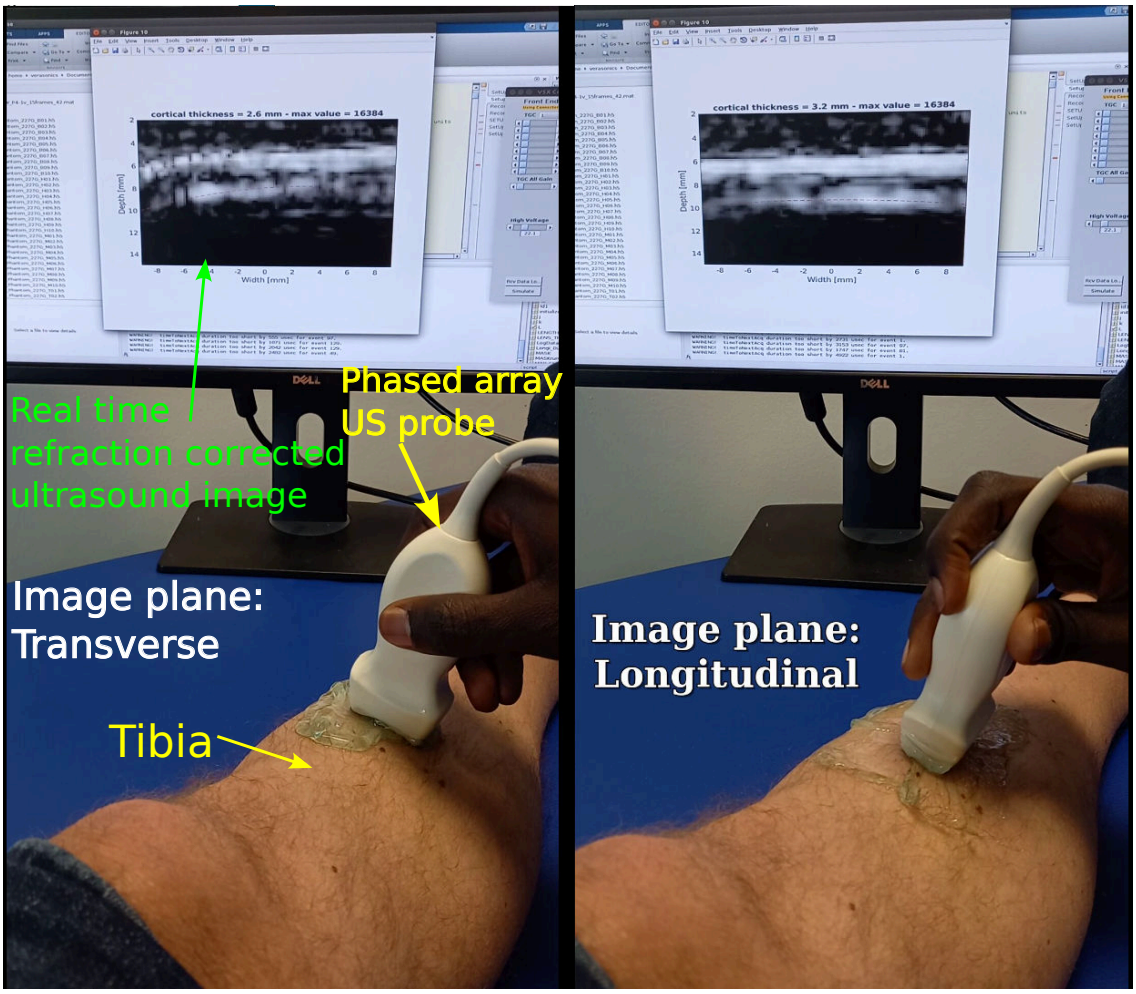

(a) (b)

Figure 2.1: Configuration for acquisition of ultrasound data. Panel (a): probe is placed perpendicular to bone axis (transverse). Panel (b): probe is place along bone axis (longitudinal).

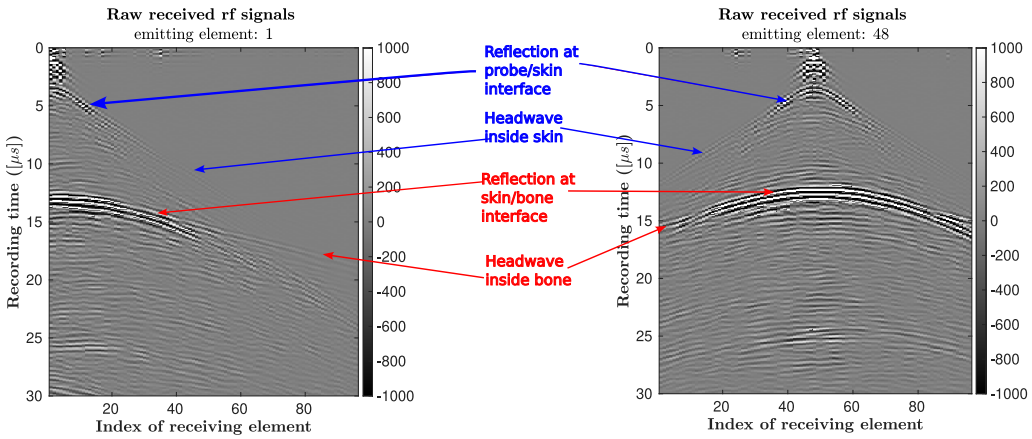

Figure 2.2: *In vivo* Received RF signals by all elements when element 1 is emitting (left panel) and when element 48 is emitting (right panel) in a longitudinal configuration.

2.2.2.1 Estimation of wave speed using autofocus approach

The autofocus approach asserts that the best image quality in terms of sharpness and intensity is achieved with the wave speed closest to the true wave speed. Following

references [7, 8, 9], we use the mean image intensity μ as an intensity metric, and the normalized variance S_{nv}, and Brenner's sharpness S_{br} as sharpness metrics. They are defined as follows:

$$\mu = \frac{1}{N_{px}} \sum_{i,j} I_{i,j}, \tag{2.1}$$

$$S_{nv} = \frac{1}{\mu} \sum_{i,j} (I_{i,j} - \mu)^2, \tag{2.2}$$

$$S_{br} = \sum_{i,j} (I_{i+2,j} - I_{i,j})^2 + (I_{i,j+2} - I_{i,j})^2, \tag{2.3}$$

where $I_{i,j}$ is the intensity of the reconstructed image at pixel (i, j) and N_{px} is the total number of pixels. In the autofocus approach, these metrics are calculated for several candidate wave speed values. The entire image of the layer is considered when computing the metrics. The wave speed V_m that maximizes the sum of the three normalized metrics with their max value is considered as an estimate of the wave speed of the medium:

$$V_m = \max_{V_i} \left(\frac{\mu(V_i)}{\mu^{max}} + \frac{S_{nv}(V_i)}{S_{nv}^{max}} + \frac{S_{br}(V_i)}{S_{br}^{max}} \right), \tag{2.4}$$

where V_i denotes each wave speed candidate and terms μ^{max}, S_{nv}^{max} and S_{br}^{max} are the maximum values of each respective metric across all wave speed candidates.

2.2.2.2 Cutaneous tissues

wave speed. For the estimation of wave speed in cutaneous tissues, 21 wave speed candidates ranging from 1400 to 1700 m/s are considered. Image reconstruction of the cutaneous layer is conducted for each wave speed candidate, and the three metrics are computed for each reconstructed image. Figure 2.3 illustrates an example of autofocus in cutaneous tissues applied *in vivo*.

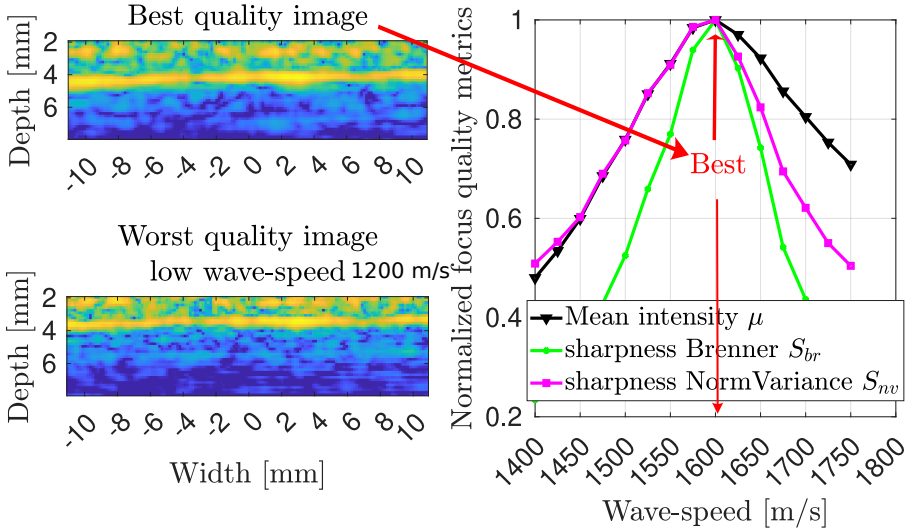

Figure 2.3: Illustration of autofocus for a longitudinal acquisition in cutaneous tissue on the specular reflection from the external bone interface

We denote V_0 the optimal wave speed for cutaneous tissues.

Segmentation of the external interface of the cortex. Using the wave speed V_0, the segmentation of the external interface of the cortex is performed using Dijkstra's algorithm. The algorithm searches for the shortest path extending across the whole lateral width of the ultrasound image that has the maximal intensity (see Figure 2.4). For the purpose of refraction computations, the segmented interface is

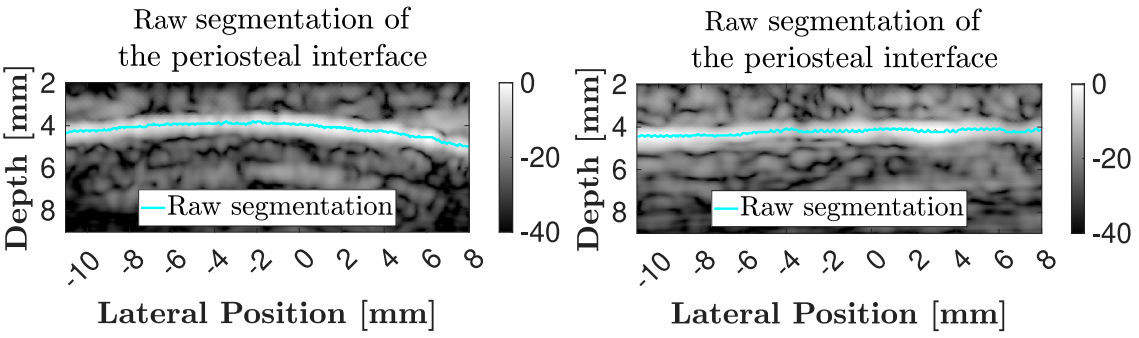

Figure 2.4: Illustration of fine segmentation of the external interface of the cortex using Dijkstra's algorithm. The line in cyan blue is the segmented interface and corresponds to the shortest path that maximizes intensity. Panel (a): segmentation in the transverse plane and panel (b): segmentation in the logitudinal plane

subsequently fitted to a parabola.

2.2.2.3 Bone cortex

wave speed anisotropy. As discussed in [10], the elastic anisotropy of cortical bone is well-described by transverse isotropy [11, 12]. Renaud et al. suggested in [7, 8, 10] to use a model of weak transverse isotropy introduced in seismology by Leon Thomsen [13]. The equation that describes how the compressional group velocity V varies with the angle (ϕ) relative to the normal of bone axis, taking into account the anisotropy of cortical bone is given by:

$$V(\phi) = V^{\text{axial}} - (V^{\text{axial}} - V^{\text{radial}}) \times \left[\xi \sin^2(\phi)\cos^2(\phi) + \cos^4(\phi)\right], \qquad (2.5)$$

where V^{axial} is the propagating wave speed in the direction parallel to the bone axis (axis 3 in Figure 1.1 and 1.4), V^{radial} is the propagating wave speed in the direction perpendicular to the bone axis (axis 1 in Figure 1.1 and 1.4) and ξ is an anisotropy form parameter.

Wave speed in the axial direction, V^{axial}. Due to the higher wave speed in cortical bone compared to cutaneous tissues, a critical angle α_c (given by Snell's law $\sin(\alpha_c) = \frac{V_0}{V^{\text{axial}}}$) is observed. At this critical angle, a head-wave propagates at the external bone interface (see Figure 2.5). In the longitudinal plane, where the propagation direction of the head-wave is parallel to the bone axis ($\phi = \frac{\pi}{2}$), the head-wave travels at the wave speed V^{axial} [14]. In this scenario, where flat interfaces are assumed for the cortex, if the probe is oriented parallel to the bone axis, the delay τ_h for receiver iR to record the head-wave emitted by element iT is given by:

$$\tau_h(iT, iR) = \frac{1}{V_0}\frac{z}{\cos(\alpha_c)} + \frac{x - 2d\tan(\alpha_c)}{V^{\text{axial}}} + \frac{1}{V_0}\frac{z}{\cos(\alpha_c)}, \qquad (2.6)$$

where d is the distance between the probe and the external interface of the bone, x is the distance between emitting iT and receiving iR elements. Developing the

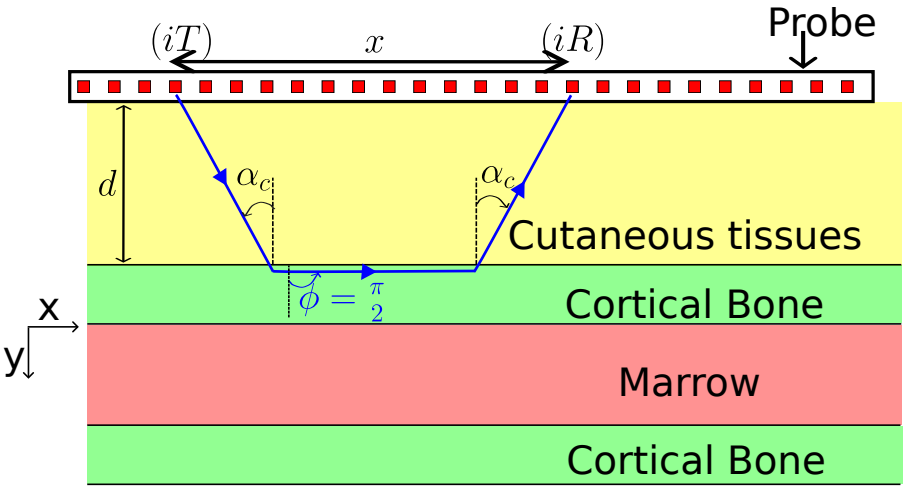

Figure 2.5: Schematic description of the propagation of a head-wave at the surface of the bone cortex along the bone axis

relationship above and using the law of Snell, equation 2.6 becomes:

$$\tau_h(iT, iR) = \frac{1}{V^{\text{axial}}} x + 2\frac{d}{V_0 V^{\text{axial}}} \cos(\alpha_c). \tag{2.7}$$

This implies that the record-time of the head-wave by the receivers is a line of slope $\frac{1}{V^{\text{axial}}}$ and of intercept time $2\frac{d}{V_0 V^{\text{axial}}} \cos(\alpha_c)$. The parameter d is obtained from the segmented periosteal interface, making $\frac{1}{V^{\text{axial}}}$ the only unknown parameter. By calculating the similarity of the signals along the lines described by Equation 2.7 for different values of the wave speed $\frac{1}{V^{\text{axial}}}$, a wave speed spectrum can be obtained. Following previous works by [7] and [8], we use semblance as a metric of similarity. It is defined as :

$$C_{iT} = \frac{\int_{-\frac{T}{2}}^{\frac{T}{2}} \left[\sum_{iR} \mathbf{S}(t - \tau_h(iT, iR), iR, iT)\right]^2}{\int_{-\frac{T}{2}}^{\frac{T}{2}} \sum_{iR} \mathbf{S}(t - \tau_h(iT, iR), iR, iT)^2}, \tag{2.8}$$

where T is the time window, S is the matrix of 96×96 recorded pulse-echo signals from Synthetic Aperture acquisitions protocol. This metric quantifies the coherence of the received signals along lines τ_h corresponding to different candidate values of V^{axial} for a specific emission. The wave speed that maximizes C_{iT} is the estimated wave speed.

If the probe is tilted of θ with respect to the the bone interface, Equations 2.6 and 2.7 yield an apparent wave speed that differs from the true wave speed. A wave speed estimated when the first element is emitting ($iT = 1$) will give a wave speed V_1^{axial} different from the one estimated when the last element of the probe is emitting ($iT = 96$) V_{96}^{axial}. According to Telford [14], the true wave speed is given by the relationship, as cited by Renaud et al. [8]:

$$V^{\text{axial}} = \frac{2V_1^{\text{axial}} V_{96}^{\text{axial}} \cos(\theta)}{V_1^{\text{axial}} + V_{96}^{\text{axial}}}. \tag{2.9}$$

Figure 2.6 illustrates the estimation of V^{axial} using maximum semblance of head-wave.

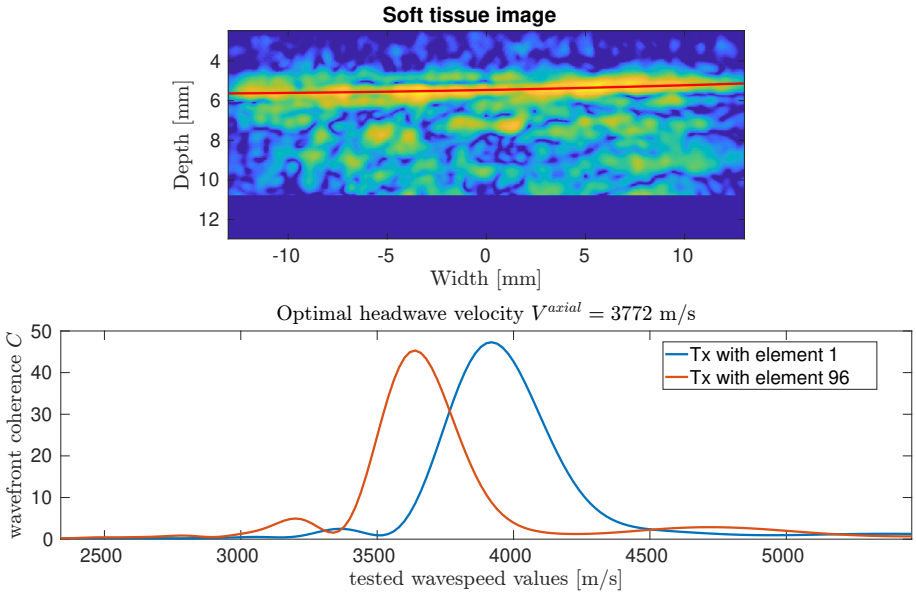

Figure 2.6: Illustration of estimation of V^{axial}. In the top panel, the image of the cutaneous tissue is given and the red line is the periosteal interface. The bottom panel is the computation of Equation 2.8 when the first (blue line) and last element (red line) of the probe is emitting

Wave speed in radial direction V^{radial}. The radial direction is the plane of isotropy. In the transverse configuration, the cortical layer is assumed to be homogeneous with a uniform wave speed V^{radial}. The same autofocus principle presented in section 2.2.2.1 is applied to determine V^{radial}. Using the wave speed determined for the cutaneous tissues V_0 and the segmentation of the periosteal interface done in the previous steps, refraction is accounted for at the probe-cutaneous tissue interface and at the cutaneous-bone tissue interface. Wave speed candidates ranging from 2500 to 3500 m/s [11, 15] with an increment of 25 m/s [16] are considered (Figure 2.7). For each wave speed candidate, a refraction-corrected delay-and-sum algorithm is utilized to reconstruct the image of the cortex, and the metrics defined by Equations 2.1, 2.2, and 2.3 are computed. The wave speed that maximizes the sum of the metrics is considered as the estimate of V^{radial}.

Anisotropy form parameter ξ. In the longitudinal plane, the wave speed depends on the direction of propagation of the incident ray. Therefore, Equation 2.5 must be used for image reconstruction. After determining V^{axial} and V^{radial} previously, the only remaining parameter for Equation 2.5 is the anisotropy form parameter ξ. We once again apply the autofocus principle to search for the anisotropy form parameter among 21 candidates ranging from 0.5 to 2.5 [11, 15]. This search aims to maximize the sharpness metrics of the longitudinal image reconstructed using Equation 2.5.

2.2.3 Statistical analysis

Comparison of wave speed groups at two anatomical sites, for 11 volunteers. To compare wave speed across measurement locations (mid-diaphysis and proximal third) or probe positions (longitudinal or transverse), we conducted Kolmogorov-Smirnov tests at a significance level of 5% between two sets of measured wave speed. Each set comprised all estimated wave speed obtained from all repetitions for all subjects within a specific measurement location and probe posi-

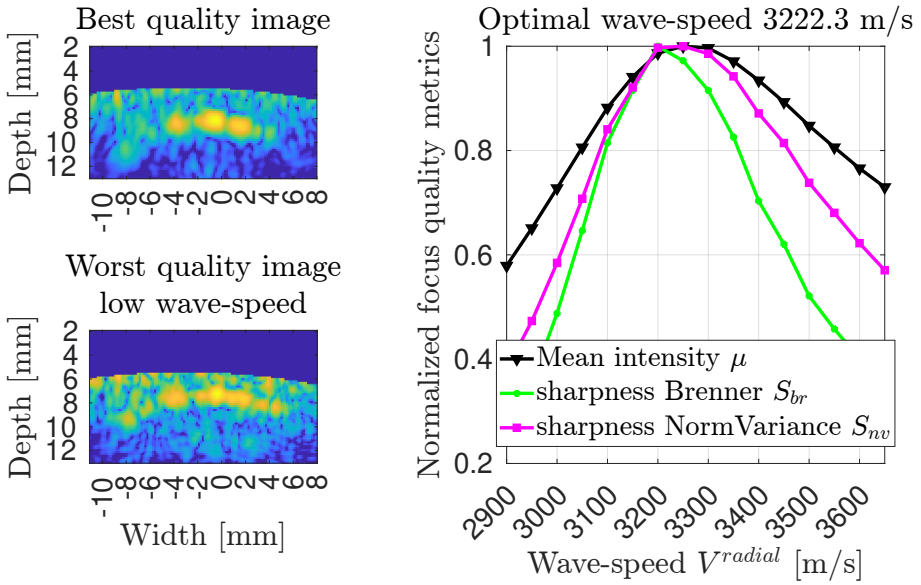

Figure 2.7: Illustration of autofocus in the cortex in the transverse plane. The wave speed V^{radial} that maximizes specular reflection from the endosteal surface is 3222.3 m/s

tion, resulting in a total set of 55 (5×11) wave speed. The Kolmogorov-Smirnov test evaluated if the wave speed originated from the same distribution. The test was performed on all measured wave speeds for each location and each probe orientation.

To determine if the measured wave speed in the mid-diaphysis was significantly higher (or lower) than that estimated in the proximal one-third diaphysis, we conducted the non-parametric Wilcoxon signed-rank test between two sets of mean wave speeds. Each set of mean wave speeds comprised the mean wave speed over the five repetitions from all subjects within a specific measurement location. The Wilcoxon signed-rank test evaluated whether the difference between the medians of samples from the two sets was significant.

For both tests, a result of "1" suggested a significant difference between the two compared sets, while a result of "0" implied no significant difference.

Additionally, for each view, if an estimated value (of wave speed or anisotropy form parameter) was more than three standard deviations from the mean, it was removed. Only one value of axial wave speed fell into this category across all the data, and it was subsequently removed for the rest of the analysis.

Precision errors on wave speed estimation. We computed the absolute precision error σ_i [17] of each individual i by using the standard deviation over the five repeated measurements of each variable:

$$\sigma_i = \sqrt{\frac{1}{N_i - 1} \sum_{j=1}^{N_i} \left(\zeta_{i,j} - \bar{\zeta}_i\right)^2}, \tag{2.10}$$

where ζ can be either V_0, V^{axial}, V^{radial} or ξ, N_i is the number of repetitions considered for subject i and $\bar{\zeta}_i = \frac{1}{N_i} \sum_{j=1}^{N_i} \zeta_{i,j}$ is the mean. The corresponding relative precision (Coefficient of Variation CV)is given by

$$CV_i = \frac{\sigma_i}{\bar{\zeta}_i} \times 100. \tag{2.11}$$

The absolute precision of the technique σ [17] is given by:

$$\sigma = \sqrt{\frac{1}{df}\sum_{i=1}^{M}\sum_{j=1}^{N_j}\left(\zeta_{i,j} - \bar{\zeta}_i\right)^2}, \tag{2.12}$$

where M is the total number of subjects $M = 11$ and df is the number of degree of freedom

$$df = \sum_{i=1}^{M} N_i - 1. \tag{2.13}$$

The corresponding relative precision of the technique is given by

$$CV = \frac{\sigma}{\bar{\zeta}} \times 100, \tag{2.14}$$

where $\bar{\zeta} = \frac{1}{M}\sum_{i=1}^{M}\bar{\zeta}_i$.

The confidence interval of the estimated precision is provided with a confidence level of 95%, derived from the chi-square distribution using the total degrees of freedom (df) as a parameter for the distribution.

2.3 Results

2.3.1 Estimated wave speed and bone anisotropy form parameters

Estimated wave speed in cutaneous tissues. Table 2.1 presents estimated wave speeds in cutaneous tissues for different subjects and measurement locations and Figure 2.8 visualizes the results. The subjects are identified by a number. For each location, the table provides the wave speeds in meters per second (m/s) estimated from acquisitions in the transverse and longitudinal planes for each subject.

In Table 2.2, the results of the Kolmogorov-Smirnov tests are presented.

Overall, the table suggests that estimated wave speed in cutaneous tissues from the same probe orientation at different measurement sites (proximal third and mid-diaphysis) can be combined for both the transverse and longitudinal views. This indicates, as expected, that the wave speed estimated in cutaneous tissues does not depend significantly on the measurement site. However, there might be a slight but significant dependency on the propagating direction of the waves. In the rest of the chapter we will not combine estimated wave speed in the cutaneous tissues.

Estimated axial and radial wave speed in bone tissues. Table 2.3 summarizes the estimated wave speed in the radial (V^{radial}) and axial (V^{axial}) directions of the bone. As predicted by Equation 2.5, values in the axial direction (corresponding to $\phi = \frac{\pi}{2}$) are greater than values in the radial direction (corresponding to $\phi = 0$) for each subject. This difference in wave speed can exceed 800 m/s for some individuals, highlighting the dependence of wave speed on the direction of propagation.

In Table 2.4, the results of Kolmogorov-Smirnov test for radial and axial wave speed in bone tissues across different measurement locations are presented. The results indicate that there are significant differences in the wave speed estimated along the axial direction V^{axial} between the mid-diaphysis and the proximal third locations. However, wave speed estimated along the radial direction V^{radial} does not

	Mid-diaphysis		Third proximal	
	Transverse	Longitudinal	Transverse	Longitudinal
Subject 1	1584	1590	1559	1548
Subject 2	1540	1512	1547	1553
Subject 3	1526	1519	1522	1495
Subject 4	1550	1548	1560	1570
Subject 5	1588	1607	1538	1548
Subject 6	1540	1532	1560	1542
Subject 7	1545	1519	1585	1506
Subject 8	1591	1581	1570	1538
Subject 9	1564	1547	1564	1517
Subject 10	1578	1534	1589	1578
Subject 11	1526	1511	1512	1490
MIN	1526	1511	1512	1490
MAX	1591	1607	1589	1578
Average	1558	1548	1554	1535

Table 2.1: Estimated wave speed V_0 in m/s in cutaneous tissues for different measurement locations and probe orientations. The minimum, maximum and average values across the five repetitions are also provided

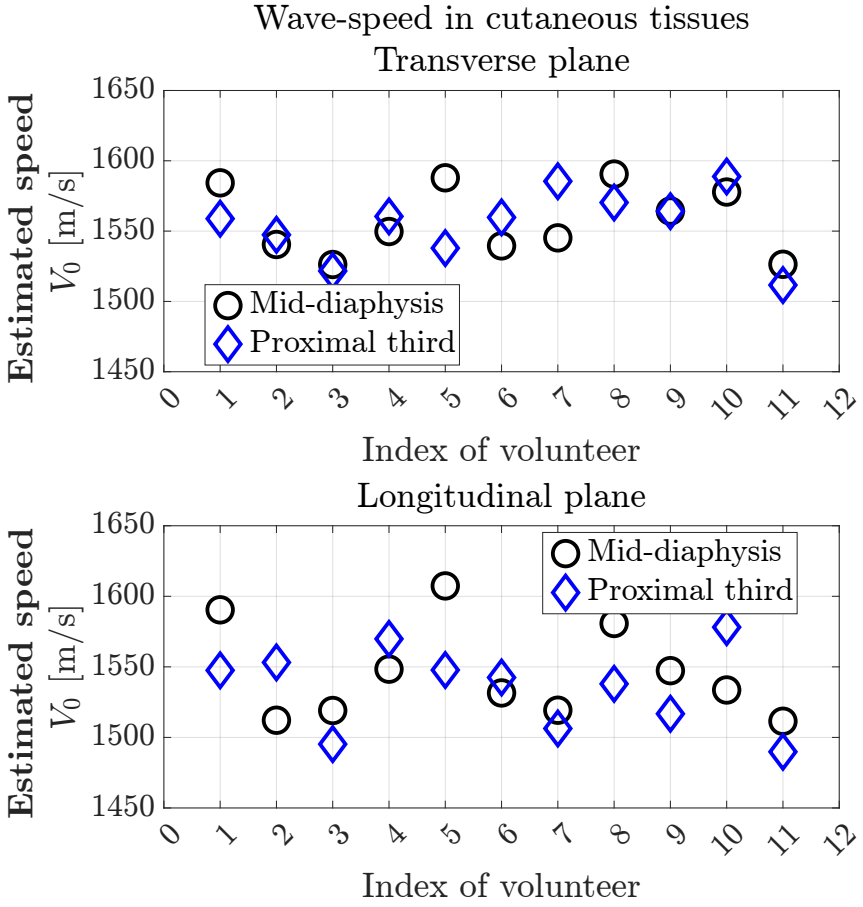

Figure 2.8: Estimated wave speed V_0 in cutaneous tissues of the different measurement sites. Each subject corresponds to a number. Top: measurement in the transverse plane. Bottom: measurement in the longitudinal plane

	Mid-transv	Mid-longi	Proxi-transv	Proxi-longi
Mid-transv	-	-	-	-
Mid-longi	1	-	-	-
Proxi-transv	0	1	-	-
Proxi-longi	1	0	1	-

Table 2.2: Null-hypothesis rejection analysis of wave speed in cutaneous tissues comparisons across measurement locations using the Kolmogorov-Smirnov test at a significance level of 5%

	Mid-diaphysis				Third proximal			
	V^{radial}	V^{axial}	$\left(\frac{V^{\text{axial}}}{V^{\text{radial}}}\right)^2$	ξ	V^{radial}	V^{axial}	$\left(\frac{V^{\text{axial}}}{V^{\text{radial}}}\right)^2$	ξ
Subject 1	2941	3762	1.6	1.2	3057	3764	1.5	1.2
Subject 2	3220	3911	1.5	1.5	3178	4080	1.6	1.8
Subject 3	3275	3897	1.4	1.1	3121	3907	1.6	1.6
Subject 4	3234	3944	1.5	1.6	3115	4015	1.7	1.4
Subject 5	3033	3869	1.6	1.2	3154	3954	1.6	1.3
Subject 6	3190	3936	1.5	1.3	3232	4000	1.5	1.8
Subject 7	3246	3788	1.4	1.1	3118	3843	1.5	1.3
Subject 8	3180	3866	1.5	1.3	3225	3845	1.4	1.0
Subject 9	3360	3967	1.4	1.4	3319	3973	1.4	1.3
Subject 10	3149	3944	1.6	1.4	3244	3979	1.5	1.2
Subject 11	3172	4067	1.6	1.8	3258	3966	1.5	1.3
MIN	2941	3762	1.4	1.1	3057	3764	1.4	1.0
MAX	3360	4067	1.6	1.8	3319	4080	1.7	1.8
Average	3177	3906	1.5	1.4	3184	3936	1.5	1.4

Table 2.3: Mean radial and axial wave speed (V^{radial} and V^{axial} expressed in m/s) and anisotropy form parameter ξ across the repetitions in bone tissues for different measurement locations. The anisotropy ratio $\left(\frac{V^{\text{axial}}}{V^{\text{radial}}}\right)^2$ is also provided.

	Transverse (V^{radial})		Longitudinal (V^{axial})	
	Mid diaphysis	Proximal-third	Mid diaphysis	Proximal-third
Mid diaphysis	-	0	-	1
Proximal third	0	-	1	-

Table 2.4: Null-hypothesis rejection analysis of radial and axial wave speed comparisons across measurement locations using the Kolmogorov-Smirnov test at a significance level of 5%

show significant differences between these two locations. This implies that radial wave speed from the two measurement sites can be combined, while axial wave speed cannot. This disparity may arise from differences in the precision of the estimated wave speed. Specifically, it suggests that the estimation of radial wave speed is less precise than that of axial wave speed. Consequently, for the remainder of the analysis, wave speed estimates from different sites are not combined.

In figure 2.9, the estimated radial and axial wave speed of each subject are shown.

No particularity is remarked. At the 5% significance level, the results of the Wilcoxon

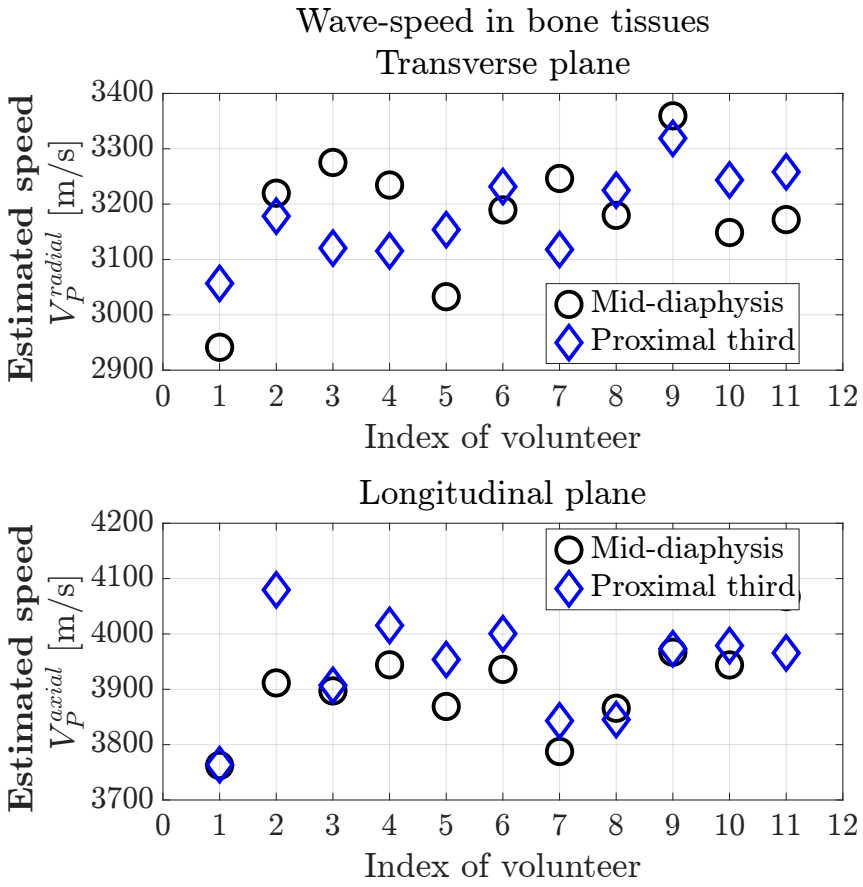

Figure 2.9: Estimated propagating wave speed in bone tissues

signed rank test is 0 for both the transverse and the longitudinal configuration indicating that the median of estimated wave speeds in the mid-diaphysis and the proximal one-third diaphysis do not significantly differ. This suggests that we can not conclude that wave speed measured in the mid-diaphysis is significantly greater (or lower) than wave speed estimated on proximal one-third diaphysis.

Estimated anisotropy form parameter in bone tissues ξ. In Table 2.3, the estimated anisotropy form parameter ξ for each subject and measurement location is presented. The results show variability in the anisotropy form parameter across subjects and measurement locations, with values ranging from 1 to 1.8 (Figure 2.10). These values are in concordance with those found by Renaud et al. [7] for the tibia bone of two healthy subjects, which were 1.4 ± 0.2 and 1.1 ± 0.2. We also computed the square root of the ratio between axial and radial wave speed $\left(\frac{V^{\text{axial}}}{V^{\text{radial}}}\right)^2$ and found values ranging from 1.4 to 1.7. This ratio corresponds to the anisotropy ratio between longitudinal coefficients of stiffness in the axial and radial directions C_{33}/C_{11}. These values are comparable to those reported at the tibia diaphysis *ex vivo* , which range from 1.3 to 2.5 [15], with values smaller than 1.8 corresponding to high-density (low porosity) bone. This is consistent with the relatively young age of our volunteers since younger individuals are supposed to have denser bones.

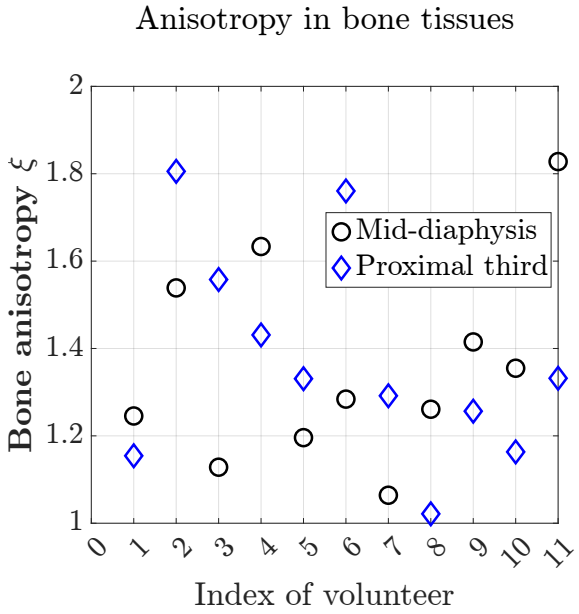

Figure 2.10: Estimated anisotropy form parameter ξ in cortical bone tissues for different subject at the two measurements locations.

2.3.2 Precision on the estimation of wave speed and bone anisotropy form parameter

Subject-specific precision in cutaneous tissues. Figure 2.11 and Table 2.5 present the relative precision CV_i of wave speed measurements in cutaneous tissues for each subject i at two different measurement locations (mid-diaphysis and proximal third) and for two probe orientations (transverse and longitudinal). The precision values are computed using Equation 2.11 where σ_i is given by Equation 2.10.

The precision values range from 0.1% to 1.4% across all measurements, indicating variability in measurement repeatability across subjects. On average, the precision ranges from 0.5% to 0.7%, suggesting relatively consistent repeatability across the dataset.

	Mid-diaphysis		Proximal third	
	Transverse	Longitudinal	Transverse	Longitudinal
MIN	0.2	0.1	0.2	0.2
MAX	1.1	0.9	1.4	1.2
Average	0.5	0.5	0.6	0.7

Table 2.5: Minimum, maximum and average subject-specific relative precision CV_i of wave speed in cutaneous tissues expressed in %.

Subject-specific precision in cortical bone. Precision on radial and axial wave speed are shown in Figure 2.12 and Table 2.6. Precisions are higher than those estimated for cutaneous tissues. The table and the figure reveal variability in precision across probe orientations. On average, the precision of wave speed in the radial direction is twice higher than that in the axial direction. This is confirmed by the Wilcoxon test. It indicates that the median of the precisions estimated in the transverse plane is significantly higher than those estimated in the longitudinal direction for both the middle and the proximal third of the diaphysis.

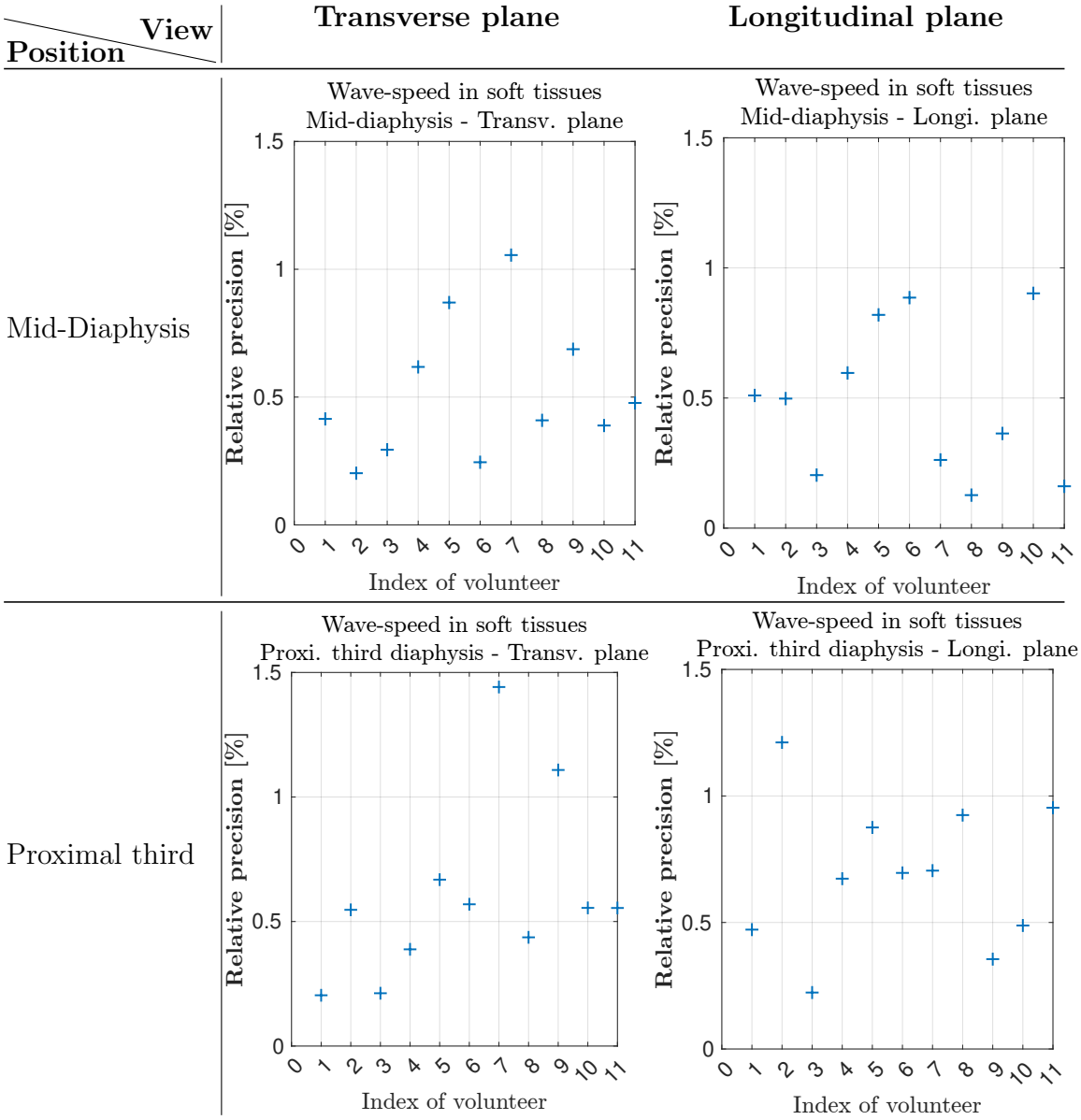

Figure 2.11: Subject-specific relative precision CV_i of wave speed V_0 in cutaneous tissues

	Mid-diaphysis		Proximal third	
	Transverse	Longitudinal	Transverse	Longitudinal
MIN	0.5	0.2	0.3	0.1
MAX	4.1	2.3	3.6	1.7
Average	2.1	0.9	1.5	0.8

Table 2.6: Minimum, maximum and average subject-specific relative precision CV_i (in %) of wave speed in bone tissues

Table 2.7 and figure 2.13 present the relative precision CV_i of the bone anisotropy form parameter ξ. The precision values exhibit variability across subjects and measurement locations, ranging from 5.1% to 18.1% at the mid-diaphysis and from 2.2% to 20.4% at the proximal third.

Precision of the technique. The absolute (in m/s) and relative precision (in %) of the technique is obtained from Equation 2.12 and 2.14 respectively by combining

View	**Transverse plane** Precision on radial wave speed	**Longitudinal plane** Precision on axial wave speed

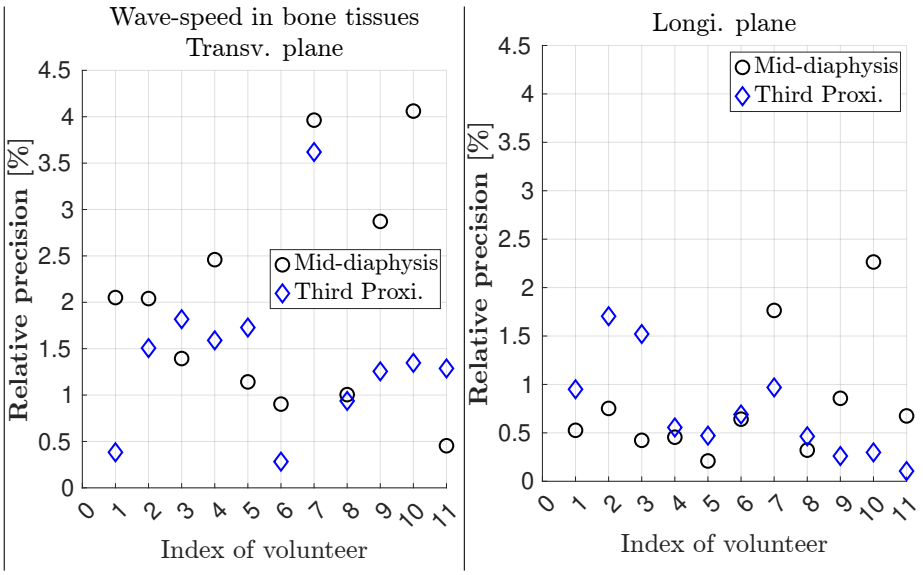

Figure 2.12: Precision on the estimation of radial and axial wave speed V^{radial} and V^{axial}.

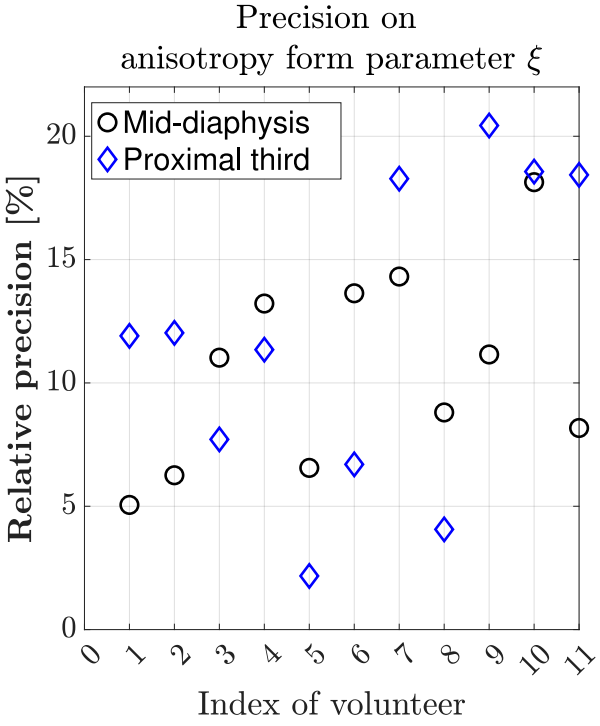

Figure 2.13: Subject-specific relative precision CV_i on the estimation of bone anisotropy form parameter ξ

the measurements for all subjects.

Table 2.8 present summaries of wave speed and anisotropy precision with 95% confidence intervals denoted as [L U], where L represents the lower bound and U represents the upper bound of the interval.

	Mid-diaphysis		Proximal third	
	Transverse	Longitudinal	Transverse	Longitudinal
MIN	-	5.1	-	2.2
MAX	-	18.1	-	20.4
Average	-	10.7	-	11.9

Table 2.7: Minimum, maximum and average subject-specific precision CV_i of bone anisotropy form parameter ξ expressed in %.

		Mid-diaphysis	Proximal third
V^{radial}	[m/s]	75 ([62.1 94.7])	52 ([43.4 66.2])
	[%]	2.4 ([2 3])	1.6 ([1.4 2.1])
V^{axial}	[m/s]	39 ([32.6 49.7])	34 ([27.9 42.9])
	[%]	1 ([0.8 1.3])	0.86 ([0.7 1.1])
ξ	[unitless]	0.15 ([0.1 0.2])	0.18 ([0.1 0.2])
	[%]	11 ([9.3 14.2])	13 ([10.5 16.3])

Table 2.8: Summary of absolute precision σ and relative precision CV on the estimation of wave speed and anisotropy form parameter with 95% confidence intervals

2.4 Discussion

In this *in vivo* study, we report the radial and axial wave speeds and anisotropy form parameter of cortical bone in the tibia of 11 healthy volunteers using bone ultrasound imaging with a phased array probe operating at a center frequency of 2.5 MHz. To our knowledge, this is the first study using this technique involving a significant number of subjects that reports bulk wave speeds in both cutaneous and cortical bone tissues at the diaphysis of the tibia. The main originality of this study lies in its reporting of precision measures for ultrasonic wave speed in both the axial and radial directions of the tibia.

Wave speed in the axial and radial direction. The values of V^{radial} range from 2941 to 3359 m/s for the mid-diaphysis and from 3057 to 3319 m/s for the one-third diaphysis. Renaud et al. [7] reported comparable values of radial wave speed, measuring 3240 and 3270 m/s on the tibia of two healthy subjects using a similar technique, which involved five measurements with repositioning. It is worth noting that ultrasonic radial wave speed in cortical bone has not been extensively studied *in vivo*. The values found in this study align with *ex vivo* studies. Except for subject 1 (which had a low radial wave speed), all of the subjects had radial wave speed greater than 3100 m/s. According to previous *ex vivo* studies, wave speeds larger than 3100 m/s correspond to low to moderate porosities (lower than 11%) [18, 1]. This aligns well with the age of the subjects, who were all young and assumed healthy.

In this study, thanks to imaging, we know the location of the external interface (segmentation of the periosteal interface) of the cortex and the wave speed in cutaneous tissues (V_0 estimated from autofocus). Therefore, the estimated value V^{axial} corresponds to the headwave velocity hence the axial bulk wave velocity. However, currently available clinical QUS devices provide the velocity of the first arriving

signal (FAS). This velocity is the speed of sound of a guided wave, which depends not only on the bulk wave velocity V^{axial} but also on cortical bone thickness. The FAS velocity is representative of bulk longitudinal wave velocity for a thick bone ([19]) but for cortical thickness comparable to the wavelength, the FAS velocity decreases with thickness. However, these are the only reported values of *in vivo* axial wave speeds. We found values of V^{axial} ranging from 3762 to 4067 m/s for the mid-diaphysis and from 3764 to 4080 m/s for the proximal one-third diaphysis. These values are comparable with reported FAS velocities. Knapp et al. [20] reported values of 3943 ± 101.12 at the mid-diaphysis of the tibia for a subgroup involving 42 young healthy subjects in a similar age range (20-29). Similar results were also reported by [21] at the midshaft tibia of 3929±143 in a subgroup of 109 subjects in age range of 20-29. Values from this present study appear to be higher than those reported by Schneider et al. [22], which ranged between 3838 and 3965 m/s for 15 subjects. One possible explanation for this discrepancy could be the difference in the age range of the participants between the two studies. In this study, the age range is 24-32, whereas in Schneider et al., the age range is 37-65. Age is known to be a significant factor affecting bone properties, including bone density and stiffness. It is plausible that the younger age range in this study may contribute to higher wave speed values, as bone properties tend to change with age. Additionally, Schneider et al. measured the FAS wave speed which is the wave speed of the first arrival signal which is not the head-wave when the cortex is too thin.

Even though all subjects were young, wave speed seems to increase with age (see Figure 2.14). The Spearman correlation coefficients indicate a positive correlation

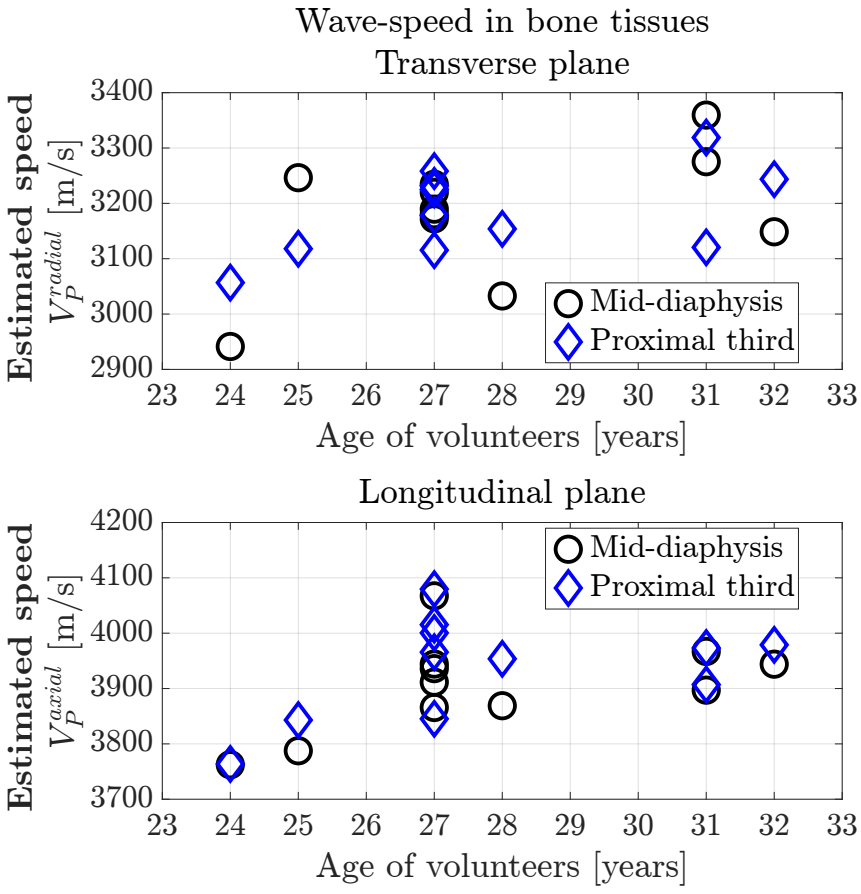

Figure 2.14: Estimated propagating wave speed in bone tissues as a function of age

between age and both radial and axial wave speed at both the middle and proximal one-third diaphysis. Specifically, the correlation coefficient between radial wave

speed and the age of subjects is 0.49 with a p-value of 0.019, while for axial wave speed, the correlation coefficient is 0.44 with a p-value of 0.041. These results suggest that as age increases, there is a tendency for wave speed to increase as well. These findings are consistent with previous studies. Drake et al. [21] reported that the peak FAS wave speed estimated with the Omnisense device tends to increase with age until the age of 40, with maximum mean values of 3928 m/s and a plateau between ages 32 and 44. Similar results were obtained at the radius by Talmant et al. [23]. However, it is important to note that the relatively small number of subjects in this study limits the generalizability of the findings. Further research with a broader age range, particularly including older individuals with osteoporosis, would be necessary to draw conclusions about age-related changes specifically related to osteoporosis.

Precision of wave speed in the axial direction. Most literature studies are based on measuring the time of flight of the first arriving signal (FAS) using devices operating at frequencies generally lower than 1.5 MHz. This wave speed does not always correspond to that of the head-wave, especially if the cortex is too thin compared to the propagating wavelength. In this study, we are operating at a center frequency of 2.5 MHz, which ensures that the wavelength is sufficiently short to accurately capture the head-wave propagation in bone tissue. Besides, thanks to imaging, the position of the periosteal interface and the wave speed in cutaneous tissues are determined priorly, making the probing of the head-wave more reliable.

The precision reported in this study aligns well with findings from the literature. We achieved precisions of 0.86% at the mid-diaphysis and 1% at the proximal third of the tibia using ultrasound imaging at a center frequency of 2.5 MHz. Previous studies, such as [22, 23, 21, 20, 24, 25], have reported precision for FAS velocity ranging between 0.4% and 1.7% at various skeletal sites including the tibia.

For instance, Schneider et al. [22], operating at a center frequency of 500 kHz, reported a precision of 25.8 m/s (0.7%) for the FAS velocity at the proximal one-third tibia of 15 patients with an average age of 51 $\pm$ 14 years. Similarly, Talmant et al. [23] reported precision error of 0.4% and 0.5% (15 and 20 m/s) at the radius with a center frequency of 1 MHz.

Drake et al. [21] reported a precision of 0.46% with a 95% confidence interval of [0.36, 0.56] when operating at a center frequency of 1.25 MHz at the mid-diaphysis of the tibia in 15 young healthy subjects with 3 repetitions.

Despite these differences in technology, methodology, and sometimes the region of interest, the precision of axial wave speed measurements achieved in this study remains comparable, with a maximum precision of 1.3% at a 95% confidence level, with nearly the same degree of freedom ($df = 53$ in this study compared to df ranging on average between 40 and 60 in the literature). This suggests the robustness and reliability of the ultrasound imaging approach employed in this study for assessing wave speed in the axial direction of bone. Our hypothesis is that the visual feedback obtained in real time is essential to ensure reliability of the repositioning.

Precision of wave speed in the radial direction. When analyzing the confidence intervals in Table 2.8, we observe that wave speed measurements in bone tissues exhibit less good precision in the transverse plane compared to the longitudinal plane. Few *in vivo* studies have estimated radial wave speed in cortical bone [7, 8, 26]. To our knowledge, this is the first *in vivo* study to report the precision of ultrasonic wave speed in the radial direction of the tibia.

The higher precision value observed in radial wave speed measurements could be attributed to several factors. Firstly, the estimation of axial wave speed V^{axial} relies

on maximizing the semblance of the raw received RF signals based on the equation of the receive time of flight of the head-wave (Equation 2.6). In contrast, the estimation of the radial wave speed V^{radial} is based on maximizing quality metrics computed on the reconstructed image of the bone cortex. Hence, the estimation of radial wave speed is sensitive to the beamforming process, which includes the reconstruction of the image.

Secondly, the propagation of the head-wave, which travels along the bone surface, may be less affected by pore scattering compared to the radial wave speed. The radial wave speed is sensitive to the heterogeneity of the cortex and also depends on the rugosity of the endosteal interface. This could contribute to the enhanced precision observed in radial measurements, as the head-wave encounters fewer obstacles or variations in the bone microstructure.

Finally, in the transverse configuration, there is a supplementary difficulty to find the plane of isotropy.

Precision of anisotropy form parameter ξ. It is noteworthy that the estimated precisions for the anisotropy form parameter are much higher than those for the axial and radial wave speed. This discrepancy might be attributed to the fact that the estimation of ξ is the last step and it utilizes the estimated values of both V^{radial} and V^{axial} (see Equation 2.5). This can potentially propagate measurement errors, leading to worse precision.

2.5 Perspectives

Based on the upper bound of the 95% confidence interval given in Table 2.8 for wave speed estimation using ultrasound imaging, we can conclude the following:

- For cutaneous tissues of the tibia, the autofocus approach can estimate the propagating wave speed with a precision of less than 1% of the mean wave speed (95% confidence level).
- For cortical bone, ultrasound imaging can estimate the propagating wave speed in both the radial and axial directions with good precision. Specifically, the precision is less than 3% of the mean wave speed for the radial direction and less than 1.3% for the axial direction (95% confidence level).
- Furthermore, the bone anisotropy form parameter can be estimated with a precision of less than 16% of the mean value (95% confidence level).

What does this precision represent for bone health. Peralta et al. [1] reported that an increase in cortical porosity of 5% is associated to a decrease in bulk radial wave speed of 100 m/s. This corresponds to a relative variation of around 3.3% of mean radial wave speed and around 2.6% of mean axial wave speed. Furthermore, Clinical studies have reported that the mean FAS wave speed at the cortex of the radius for non-fractured individuals is higher than those of fractured individuals by 150-200 m/s [24, 27]. This corresponds to a relative variation of around 5% of mean FAS wave speed. Furthermore, during adulthood (from 40 to 80 year old), the FAS wave speed declines on average by 186 m/s corresponding to 5% [21].

Therefore, the precision values found in this study suggest that ultrasound imaging can provide robustness in monitoring changes in bone mechanical quality and in

discriminating osteoporotic bone from healthy bone. However, the responsiveness of the method to changes between osteoporotic and normal patients has not been studied yet. In this regard, a natural progression of this study is to extend it to a clinical context.

Expected precision for osteoporotic bones. This study was conducted on young and healthy volunteers. The precision values reported here might differ for osteoporotic bones. In osteoporotic bones, the cortex can become thinner, and a gradient of porosity toward the internal surface may be observed, potentially affecting the estimation of V^{radial}. Consequently, the precision of V^{radial} is expected to worsen. The same holds for ξ.

On the other hand, the estimation of V^{axial} is expected to be less affected by changes in bone microstructure. The head-wave, which is used to determine V^{axial}, primarily travels along the longitudinal axis of the bone and is less influenced by variations in cortical thickness or porosity. Therefore, while there may be some impact on the precision of V^{radial} in osteoporotic bones, it is likely to be less pronounced compared to V^{axial}.

Bibliography

[1] Laura Peralta, Juan Deyo Maeztu Redin, Fan Fan, Xiran Cai, Pascal Laugier, Johannes Schneider, Kay Raum, and Quentin Grimal. Bulk wave velocities in cortical bone reflect porosity and compression strength. *Ultrasound in Medicine & Biology*, 47(3):799–808, 2021.

[2] Pascal Laugier and Quentin Grimal. *Bone Quantitative Ultrasound: New Horizons*. Number 1364 in Advances in Experimental Medicine and Biology. Springer International Publishing, 1st ed. 2022 edition, April 2022.

[3] Huong Nguyen Minh, Juan Du, and Kay Raum. Estimation of Thickness and Speed of Sound in Cortical Bone Using Multifocus Pulse-Echo Ultrasound. *IEEE transactions on ultrasonics, ferroelectrics, and frequency control*, 67(3):568–579, 2020.

[4] Sébastien Salles, Jami Shepherd, Hendrik J. Vos, and Guillaume Renaud. Revealing Intraosseous Blood Flow in the Human Tibia With Ultrasound. *JBMR Plus*, 5(11):e10543, 2021. _eprint: https://onlinelibrary.wiley.com/doi/pdf/10.1002/jbm4.10543.

[5] M. Karaman, Pai-Chi Li, and M. O'Donnell. Synthetic aperture imaging for small scale systems. *IEEE Transactions on Ultrasonics, Ferroelectrics, and Frequency Control*, 42(3):429–442, May 1995. Conference Name: IEEE Transactions on Ultrasonics, Ferroelectrics, and Frequency Control.

[6] Jørgen Arendt Jensen, Svetoslav Ivanov Nikolov, Kim Løkke Gammelmark, and Morten Høgholm Pedersen. Synthetic aperture ultrasound imaging. *Ultrasonics*, 44:e5–e15, December 2006.

[7] Guillaume Renaud, Pieter Kruizinga, Didier Cassereau, and Pascal Laugier. In vivo ultrasound imaging of the bone cortex. *Physics in Medicine & Biology*, 63(12):125010, June 2018. Publisher: IOP Publishing.

[8] Guillaume Renaud, Pierre Clouzet, Didier Cassereau, and Maryline Talmant. Measuring anisotropy of elastic wave velocity with ultrasound imaging and an autofocus method: application to cortical bone. *Physics in Medicine & Biology*, 65(23):235016, November 2020.

[9] Bradley E. Treeby, Trond K. Varslot, Edward Z. Zhang, Jan G. Laufer, and Paul C. Beard. Automatic sound speed selection in photoacoustic image reconstruction using an autofocus approach. *Journal of Biomedical Optics*, 16(9):090501, September 2011. Publisher: SPIE.

[10] Guillaume Renaud and Sébastien Salles. Single-Sided Ultrasound Imaging of the Bone Cortex: Anatomy, Tissue Characterization and Blood Flow. In Pascal Laugier and Quentin Grimal, editors, *Bone Quantitative Ultrasound: New Horizons*, Advances in Experimental Medicine and Biology, pages 197–225. Springer International Publishing, Cham, 2022.

[11] Mathilde Granke, Quentin Grimal, Amena Saïed, Pierre Nauleau, Françoise Peyrin, and Pascal Laugier. Change in porosity is the major determinant of the variation of cortical bone elasticity at the millimeter scale in aged women. *Bone*, 49(5):1020–1026, November 2011.

[12] Quentin Grimal, Kay Raum, Alf Gerisch, and Pascal Laugier. A determination of the minimum sizes of representative volume elements for the prediction of cortical bone elastic properties. *Biomechanics and Modeling in Mechanobiology*, 10(6):925–937, December 2011.

[13] Leon Thomsen. Weak elastic anisotropy. *GEOPHYSICS*, 51(10):1954–1966, October 1986. Publisher: Society of Exploration Geophysicists.

[14] W. M. Telford, L. P. Geldart, and R. E. Sheriff. *Applied Geophysics*. Cambridge University Press, October 1990. Google-Books-ID: oRP5fZYjhXMC.

[15] Simon Bernard, Joannes Schneider, Peter Varga, Pascal Laugier, Kay Raum, and Quentin Grimal. Elasticity–density and viscoelasticity–density relationships at the tibia mid-diaphysis assessed from resonant ultrasound spectroscopy measurements. *Biomechanics and Modeling in Mechanobiology*, 15(1):97–109, February 2016.

[16] C. T. M. Eneh, M. K. H. Malo, J. P. Karjalainen, J. Liukkonen, J. Töyräs, and J. S. Jurvelin. Effect of porosity, tissue density, and mechanical properties on radial sound speed in human cortical bone. *Medical Physics*, 43(5):2030–2039, 2016. _eprint: https://onlinelibrary.wiley.com/doi/pdf/10.1118/1.4942808.

[17] C. C. Glüer, G. Blake, Y. Lu, B. A. Blunt1, M. Jergas1, and H. K. Genant1. Accurate assessment of precision errors: How to measure the reproducibility of bone densitometry techniques. *Osteoporosis International*, 5(4):262–270, July 1995.

[18] Xiran Cai, Hélène Follet, Laura Peralta, Marc Gardegaront, Delphine Farlay, Rémy Gauthier, Boliang Yu, Evelyne Gineyts, Cécile Olivier, Max Langer, Aurelien Gourrier, David Mitton, Françoise Peyrin, Quentin Grimal, and Pascal Laugier. Anisotropic elastic properties of human femoral cortical bone and relationships with composition and microstructure in elderly. *Acta Biomaterialia*, 90:254–266, May 2019.

[19] Emmanuel Bossy, Maryline Talmant, and Pascal Laugier. Effect of bone cortical thickness on velocity measurements using ultrasonic axial transmission: a 2D simulation study. *The Journal of the Acoustical Society of America*, 112(1):297–307, July 2002.

[20] K. M. Knapp, K. M. Knapp, G. M. Blake, T. D. Spector, and I. Fogelman. Multisite Quantitative Ultrasound: Precision, Age- and Menopause-Related Changes, Fracture Discrimination, and T-score Equivalence with Dual-Energy X-ray Absorptiometry. *Osteoporosis International*, 12(6):456–464, June 2001.

[21] William M. Drake, Michael McClung, Christopher F. Njeh, Harry K. Genant, Clifford Rosen, Nelson Watts, and David L. Kendler. Multisite Bone Ultrasound Measurement on North American Female Reference Population. *Journal of Clinical Densitometry*, 4(3):239–248, September 2001.

[22] Johannes Schneider, Donatien Ramiandrisoa, Gabriele Armbrecht, Zully Ritter, Dieter Felsenberg, Kay Raum, and Jean-Gabriel Minonzio. *In Vivo* Measurements of Cortical Thickness and Porosity at the Proximal Third of the Tibia Using Guided Waves: Comparison with Site-Matched Peripheral Quantitative Computed Tomography and Distal High-Resolution Peripheral Quantitative

Computed Tomography. *Ultrasound in Medicine & Biology*, 45(5):1234–1242, May 2019.

[23] M. Talmant, S. Kolta, Ch. Roux, D. Haguenauer, I. Vedel, B. Cassou, E. Bossy, and P. Laugier. In vivo Performance Evaluation of Bi-Directional Ultrasonic Axial Transmission for Cortical Bone Assessment. *Ultrasound in Medicine & Biology*, 35(6):912–919, June 2009.

[24] D. Dr. Hans, S. K. Srivastav, C. Singal, R. Barkmann, C. F. Njeh, E. Kantorovich, C. C. Glüer, and H. K. Genant. Does Combining the Results from Multiple Bone Sites Measured by a New Quantitative Ultrasound Device Improve Discrimination of Hip Fracture?*. *Journal of Bone and Mineral Research*, 14(4):644–651, April 1999.

[25] A. J. Foldes, A. Rimon, D. D. Keinan, and M. M. Popovtzer. Quantitative ultrasound of the tibia: A novel approach for assessment of bone status. *Bone*, 17(4):363–367, October 1995.

[26] Huong Nguyen Minh, Marie Muller, and Kay Raum. Estimation of Thickness and Speed of Sound for Transverse Cortical Bone Imaging Using Phase Aberration Correction Methods: An In Silico and Ex Vivo Validation Study. *Applied Sciences*, 12(10):5283, January 2022. Number: 10 Publisher: Multidisciplinary Digital Publishing Institute.

[27] Reinhard Barkmann, Edvard Kantorovich, Chaim Singal, Didier Hans, Harry K Genant, Martin Heller, and Claus-Christian Glüer. A New Method for Quantitative Ultrasound Measurements at Multiple Skeletal Sites: First Results of Precision and Fracture Discrimination. *Journal of Clinical Densitometry*, 3(1):1–7, March 2000.

Chapter 3

Simulation of elastic wave propagation in realistic cortical microstructure

This chapter is adapted from a research article by A. S. DIA, G. Renaud, A. Hejazi, Q. GRIMAL published *under the title* The influence of intracortical microstructure on contrast in ultrasound images of the cortex of long bones: A 2D simulation study *in the journal Ultrasonics (127:106831) in 2022.*

Contents

3.1 Introduction

Bone fragility associated with osteoporosis and the resulting increased risk of fracture is an important medical threat as nine million fragility fractures occur annually worldwide [1]. The prediction of fracture risk is based on clinical factors and, often, areal bone mineral density (aBMD) measured with dual energy X-ray absorptiometry (DXA). However, many individuals who are at high risk of fracture are not identified with aBMD assessed with DXA [2, 3]. Quantitative ultrasound (QUS) methods to characterize trabecular and cortical bone have been developed in the past three decades to overcome the limitations of DXA and provide a non ionizing, portable, and affordable diagnostic tool for osteoporosis [4, 5].

While ultrasound imaging can accurately image the outer surface of bones [6], current clinical ultrasound scanners fail to reveal their inner structure. Only recently, with adapted image reconstruction methods and research ultrasound scanners, it was shown that the cortex can be imaged *in vivo* [7, 8]. These methods have only been applied on a limited number of individuals and the measurement of the cortical

thickness, a key parameter for fracture risk assessment [9, 10], was only shown to be feasible in young healthy adult volunteers [7].

Bone loss occurring as part of the natural ageing process and accelerated in osteoporosis is associated with a degradation of cortical bone microstructure: unbalanced intracortical remodeling leaves cavities only partially filled with newly formed bone tissue and so-called giant pores due to the clustering of the remodeled cavities [11][12]. Porosity increases with age, e.g., in females from about 5% at 30 years old to 15% at 80 years old [13]. This is associated with an increase in pore diameter [14]. At the diaphysis of long bones, most of the cortical porosity is formed by so-called Haversian canals, which are roughly cylindrical and run nearly parallel to the bone axis. Previous studies have shown that the median pore diameter can vary from 40 to 200 µm between individuals, for cortical bone tissue with porosity ranging from 1 to 21% [15, 16, 11, 17].

Ultrasound echo signals reflected at the inner surface of the cortex (endosteum) are weak due to scattering by the microstructure and absorption in the viscoelastic mineralized collagen extracellular matrix [18, 19]. The amplitude of the echoes backscattered from the pores may be more important than that of echoes from the endosteal interface. As a consequence, a major challenge for bone ultrasound imaging is to image the endosteal interface despite strong attenuation and diffuse scattering by the pores. In the degraded bones of osteoporotic subjects, characterized by a higher porosity and larger pores, stronger diffuse scattering by the pores is expected compared to healthy individuals. For instance, in ultrasound images from *in vivo* measurements of an ongoing study, shown in Figure 3.1 for illustration, the endosteal interface is found to be more visible for a young volunteer (26 y.o) than for an older one (61 y.o). Because little research on bone ultrasound imaging has

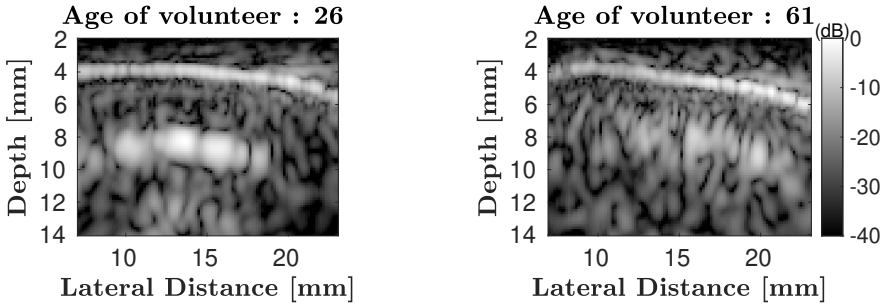

Figure 3.1: Illustration of degraded endosteal interface visibility with age on two subjects. Transverse ultrasound image of the tibia for two volunteers aged 26 (left) and 61 (right) are shown. The bright continuous line is the periosteal interface at a depth of about 4 mm which is perfectly visible for the two subjects. The endosteal interface at a depth of about 8 mm is more visible in the younger subject. Normalized gray scale dynamic range is given in dB. Images were obtained with a probe operating with a center ultrasound frequency of 2.5 MHz with a method similar to that described in [7]

been conducted until now, it is yet unknown to which extent it is possible to obtain an ultrasound image of the endosteal interface of human cortical bone, in particular in osteoporotic subjects.

The objective of this study was to quantify the influence of cortical bone microstructure on the identification of the endosteal interface in an ultrasound image in order to estimate the range of porosity and other microstructure variables, such as pore size, for which ultrasound imaging with a conventional beamformer would be

feasible. Synthetic data from two-dimensional numerical simulations using a large set of real cortical microstructures with porosity ranging from 2% to 24% were generated. Images were reconstructed using a delay-and-sum algorithm with optimized f-number and correction of refraction at the bone-soft tissue interface. A similar algorithm was previously used *in vivo* and enabled to determine the cortical thickness of young healthy individuals [7].

3.2 Materials and Methods

3.2.1 Models of bone cortex and soft tissues

The two-dimensional (2D) models of bone cortex used for the simulations were generated using synchrotron X-ray microcomputed tomography (SR-μCT) three-dimensional images of human bone from a previous study [20]. Briefly, samples were collected in the mid-diaphysis of the femur of 29 subjects (16 females and 13 males, age range: 50-95 years old). The femurs were provided by the Département Universitaire d'Anatomie Rockefeller (Lyon, France) through the French program on voluntary corpse donation to science. The tissue donors or their legal guardians provided informed written consent to give their tissue for investigations, in accord with legal clauses stated in the French Code of Public Health. For each femur, two cuboids specimens of nominal size $3 \times 4 \times 5$ mm^3 were extracted, one in the lateral and the other in the medial quadrant. Three specimens which contained trabecularized cortex were discarded, resulting in a collection of 55 specimens for this study. SR-μCT images of the specimens were obtained with isotropic voxel size of 6.5 µm performed on the beamline ID19 at the European Synchrotron Radiation Facility (ESRF, Grenoble, France). The image processing was described previously in [21]. Briefly, the 3D volume of each specimen was cropped to a perfect rectangular parallelepiped shape and slightly rotated so that the geometric coordinates coincide with the material coordinates defined by the faces of the specimen. Thereafter, axis 3 was approximately along the direction of osteons (and diaphysis axis) and axes 1 and 2 were perpendicular to osteons. The images were then binarized by single level thresholding to obtain two phases: pores and mineralized matrix with an output voxel size of 10 µm, Figure 3.2.

For the 2D simulations, a set of 105 2D images were created by randomly picking slices in the (1,2) plane from the 3D image stack (Figure 3.2) of the 55 specimens. The 2D images were sorted so that their porosity (pore surface to total surface ratio) was ranging from 2% to 24%. For the critical range of porosity (7 -15) % in which strong variations of the image contrast are expected, we selected 5 times more slices than for low ($< 7\%$) and high ($> 15\%$) porosities.

Each 2D image of microstructure was used to build a model for numerical simulations: a three-layer medium representing the configuration used for imaging the diaphysis of a long bone with an ultrasound transducer oriented perpendicular to the bone diaphysis (Figure 3.3). Since the original microstructure images were too small (approximately 2.7×3.5 mm^2) to perform a realistic simulation, the bone layer was created by duplicating and mirroring the microstructure of the original image in direction 2. A layer of soft tissue was placed above the cortical bone layer, to mimic the tissues between the probe and bone and a layer of marrow was placed below. The dimensions of the three-layer medium are given in Figure 3.3.

For the mineralized matrix of the cortical bone layer, the compressional and shear wave speeds used in the simulation were 3496 m.s^{-1} and 1645 m.s^{-1} respectively. These values were deduced from the elastic coefficients of the bone matrix [21] (see

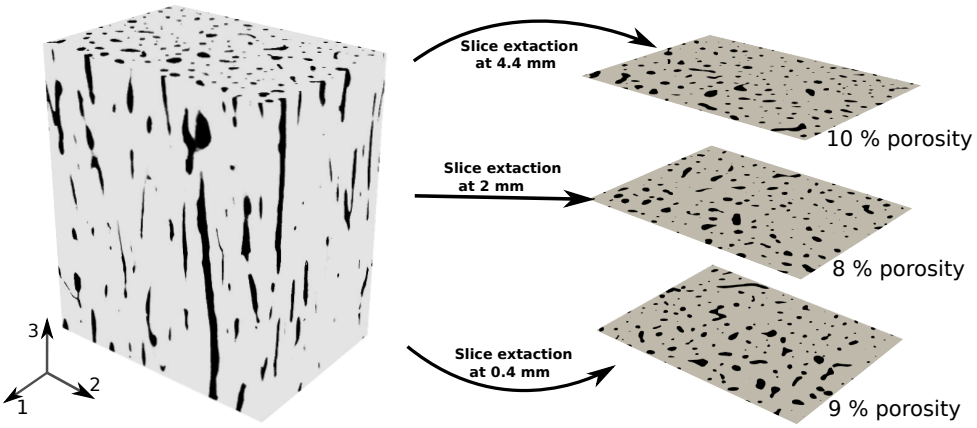

Figure 3.2: Binarized SR-μCT image of a cortical bone specimen of nominal dimensions $3 \times 4 \times 5$ mm^3 (original voxel size 6.5 µm). Black: vascular pores; light gray: mineralized matrix. Axis 1 corresponds to radial direction, axis 2 to the circumferential direction and axis 3 to the axial direction or diaphysis axis. For illustration, 3 slices extracted from the 3D volume, as used for 2D numerical simulations, are shown. 2D porosity values are given for each slice, illustrating the variable porosity in a 3D volume

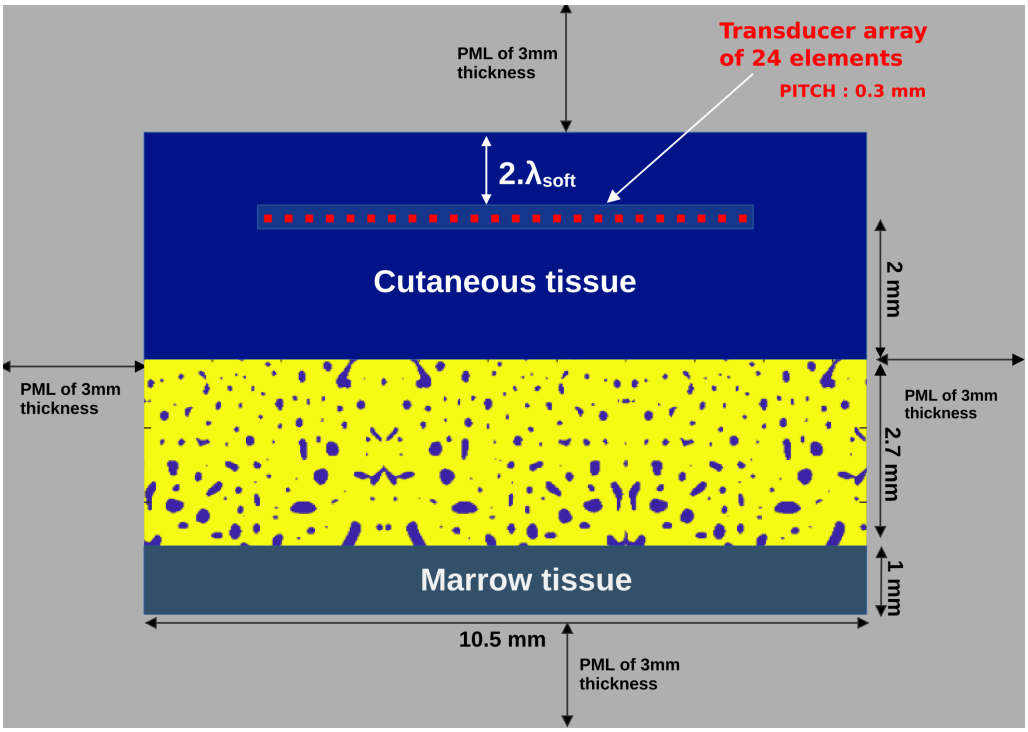

Figure 3.3: Three-layers model used for simulations: cutaneous tissue (blue), cortical bone tissue (yellow) and marrow tissue (bluish green) surrounded by Perfectly Matched Layers (PML, in gray).

Appendix A for details of the mass density and wave speed estimation).

The material within the pores was assumed to be a fluid. The compressional wave speed was 1610 m.s^{-1} for cutaneous tissue [22] and 1410 m.s^{-1} for marrow [23]. Ultrasound attenuation in cortical bone is due to a combination of absorption by dissipative mechanisms in particular in the mineralized matrix and scattering by the pores [24]. Following the models of Yousefian et al. [18, 25], a frequency-independent absorption within the bone matrix with an absorption coefficient of 19.0 dB/cm at 2.5 MHz was modeled.

3.2.2 Pores statistics

The microstructure for each model was characterized by cortical porosity (Ct.Por), cortical pore density (Ct.Po.Dn in pores/mm^2) and the distribution of pore diameters. These were calculated following the approach adopted by [26, 27]. Ct.Por was obtained by taking the ratio of the number of pixels associated with pores to the total number of pixels. Ct.Po.Dn was calculated as the number of pores divided by the total bone area. The diameter of each pore was calculated as the diameter of a disk of the same area. The distribution of pore diameters was characterized by the median value (Ct.Po.Dm); the 1^{st} (Dm.DC-1) and 9^{th} (Dm.DC-9) deciles; the average diameter of *small pores* (Sm.Po.Dm), i.e., of pore diameters smaller than Dm.DC-1; the average diameter of *large pores* (Lg.Po.Dm), i.e., of pore diameters larger than Dm.DC-9; the range of variation (Dm.Rng), i.e. the difference between the maximum and the minimum pore diameter; and the inter-decile range (Dm.IDRng).

In Figure 3.4 variations of Ct.Po.Dm and Ct.Po.Dn as a function of Ct.Por are plotted for the collection of microstructures used for the simulations.

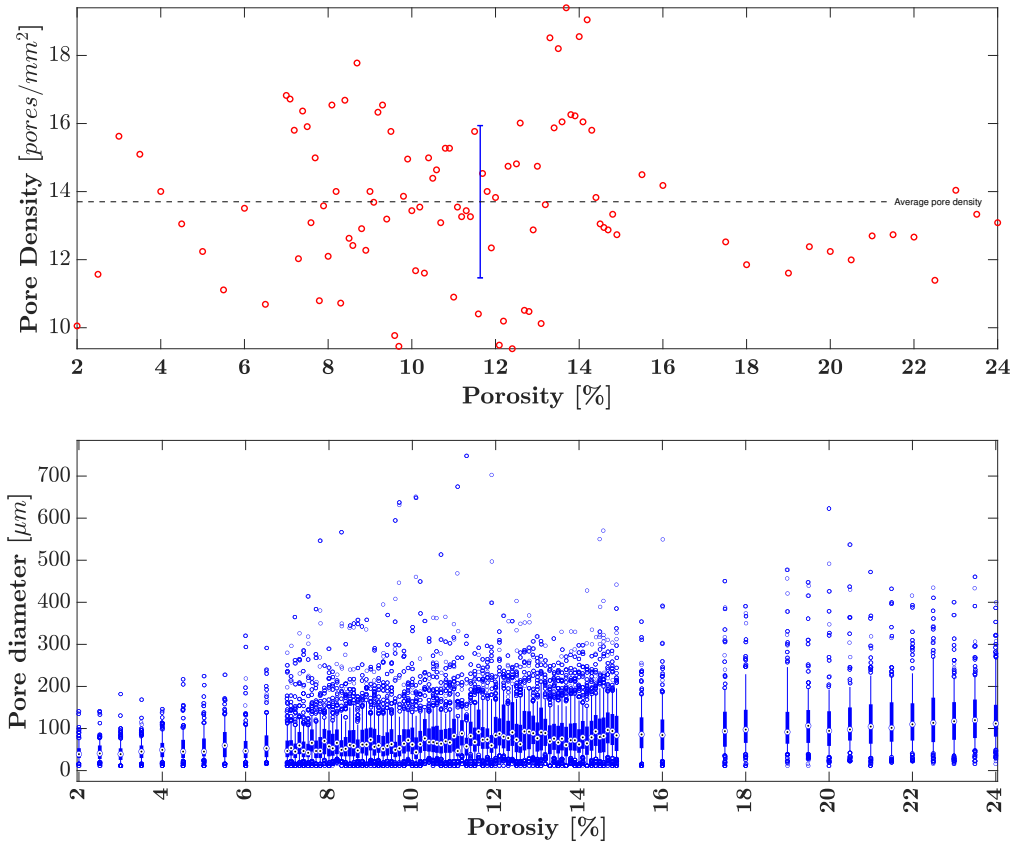

Figure 3.4: Pore statistics for each microstructure. Top: pore density (red circle) as a function of porosity; the black dashed line is the mean value and the standard deviation for the collection of microstructure is represented in blue. Bottom: stacked customized boxplots of pore diameter for each microstructure. Bottom and top of each box are respectively the first and last decile values, the circle in the middle of each box is the median pore diameter, the vertical line below each box extends from first decile to first quartile, the vertical line above each box extends from third quartile to ninth decile. Points below and above lines are respectively the values of diameters lower than the first decile and greater than the ninth decile

3.2.3 Simulation of the ultrasound imaging sequence

We simulated the experimental configuration and acquisition sequence in [7] where an ultrasound array is placed on the skin to image the radius or tibia in a transverse plane, that is, in a plane perpendicular to the diaphysis (and also perpendicular to the axis of the osteons). The simulated transducer mimicks the one used in the experiment except for the number of transducers. It is a 6.9 mm array with 24 elements and a pitch of 0.3 mm (element size of 10 µm, i.e. one grid step). The transducer is placed in the upper layer at a depth of 2 wavelengths to avoid border effects, and centered horizontally (Figure 3.3).
An acquisition scheme for synthetic aperture imaging was simulated: each individual element in the array successively transmitted a Gaussian-windowed tone burst with a central frequency of 2.5 MHz (3dB bandwidth= 1.33 MHz, see Figure 3.5). For each transmission, the backscattered signals were recorded by all the elements of the array. Therefore, for each bone microstructure, 24×24 backscattered synthetic signals were recorded.

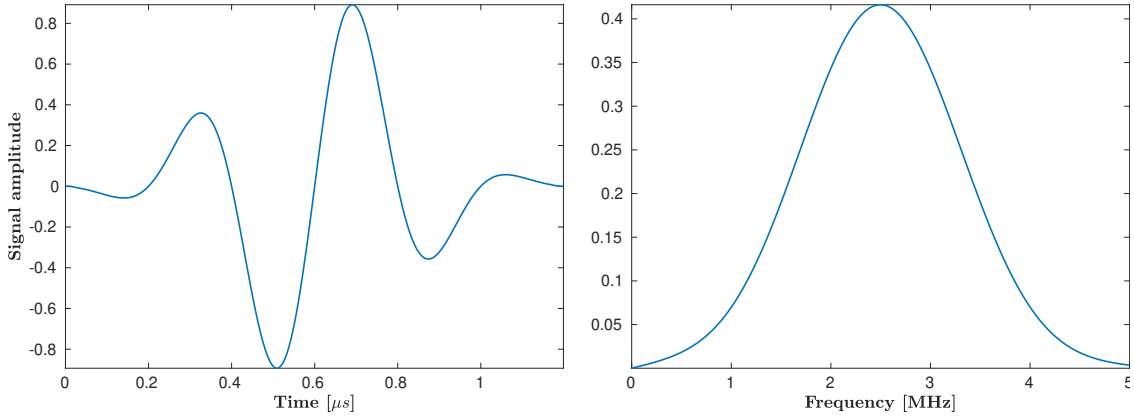

Figure 3.5: Emitted tone burst in temporal domain (left) and in frequency domain (right).

Elastic wave propagation in the three-layer medium was simulated with the Finite Difference Time-Domain (FDTD) open-source code SimSonic [28, 29]. To avoid reflections on the boundaries of the simulation domain, a Perfectly Matched Layer (PML) boundary condition (3 mm thickness, approximately 5 wavelengths in soft tissues) was set (Figure 3.3). The spatial grid size Δx for the FDTD simulation was equal to the microstructure image pixel size (10 µm). This leads to a mesh size equivalent to 56 points per wavelength in marrow at the center frequency, which is sufficient to model accurately the wave propagation with reasonably small numerical dispersion [30]. The simulation time step was chosen with respect to the Courant–Friedrichs–Lewy (CFL) stability conditions for 2D simulations. A constant value of $CFL = 0.99$ was used for these simulations.

3.2.4 Cortical bone wave speed estimation

The ultrasound wave speed in the bone layer (Figure 3.3) must be known to perform the refraction corrected image reconstruction as proposed in [7]. It is a priori unknown as it depends on the specific microstructure considered. Note that the combination of the isotropic elastic properties for the bone matrix with the quasi-random distribution of the pores in the plane $(1, 2)$, leads to isotropic properties in this plane at the scale of the wavelength, which is also the millimeter scale or mesoscale [31]. Additional simulations were performed in order to estimate this

wave speed. A plane wave at normal incidence was emitted by the array using the signal shown in Figure 3.5. Virtual receivers were placed inside bone along 5 equally spaced lines (spacing=0.5 mm) parallel to periosteal and endosteal interfaces. The waveforms recorded on each line of receivers were coherently summed and the time-of-flight was estimated from the first received signal peak. The wave speed in the cortical bone is finally obtained by linear regression of time-of-flights measured at the 5 different depths (see Figure B.1 in Appendix B). As an alternative method, the wave speed could be obtained by finding within a range of values, the wave speed that maximizes the focus quality at the endosteal interface as it was done in *in vivo* [7].

3.2.5 Image reconstruction with a refraction-corrected delay-and-sum algorithm

Delay-and-sum (DAS) algorithm with a constant f-number in receive throughout the image is used for image reconstruction [32]. DAS was chosen as it is the most extensively used beamforming algorithm, and also because it was used for the first *in vivo* imaging of the bone cortex in [7]. A hanning window was applied to the receiver sub-aperture. A preliminary study aimed to determine the optimal f-number that maximizes the image contrast for the detection of the endosteal interface, the optimal f-number was 1.9 (see Appendix C). This way, DAS is used at its highest potentiality as described by [32]. The synthetic aperture sequence led to 24 low resolution images which were coherently summed to get a high contrast image. The delays used in the DAS algorithm account for refraction at all the interfaces. The implementation described in [7] was used to calculate the delays: for each array element and image pixel, Fermat's principle is used to calculate the travel time through the multi-layered medium. Only the contribution of longitudinal waves were considered, i.e. the arrival times of wave contributions associated with the shear waves were disregarded. The ultrasound longitudinal wave speed used for the bone layer was different for each microstructure as explained in section 3.2.4.

3.2.6 Endosteal interface visibility quantification

To evaluate image quality, i.e., the visibility of interfaces, the relative interface contrast (C_{EP}) and the endosteal interface contrast (C_{EI}) were defined as follows:

$$C_{EP} = \frac{\mu_E}{\mu_P} \quad ; \quad C_{EI} = \frac{\mu_E}{\mu_I},$$

where μ_I, μ_E and μ_P are respectively the average image intensities in the center of the cortex, at the endosteal and periosteal interfaces. The regions of interest (ROI) used for the calculation of μ_I, μ_E and μ_P, are defined in Figure 3.6 where the red box represents the inner bone ROI, the yellow and blue boxes represent respectively the periosteal interface ROI and the endosteal interface ROI. Each ROI had a height of 0.8 mm and a width of 6.5 mm.

Because the amplitude of the reflection at the periosteal interface is only slightly influenced by the porosity, C_{EP} variations reflect the variations of the absolute visibility of the endosteal interface. C_{EI} evaluates how well the endosteal interface can be distinguished from the speckle inside the bone. On decibel scale, a positive value of C_{EI} means that endosteal interface is clearly visible while a negative value means that the endosteal interface is poorly visible.

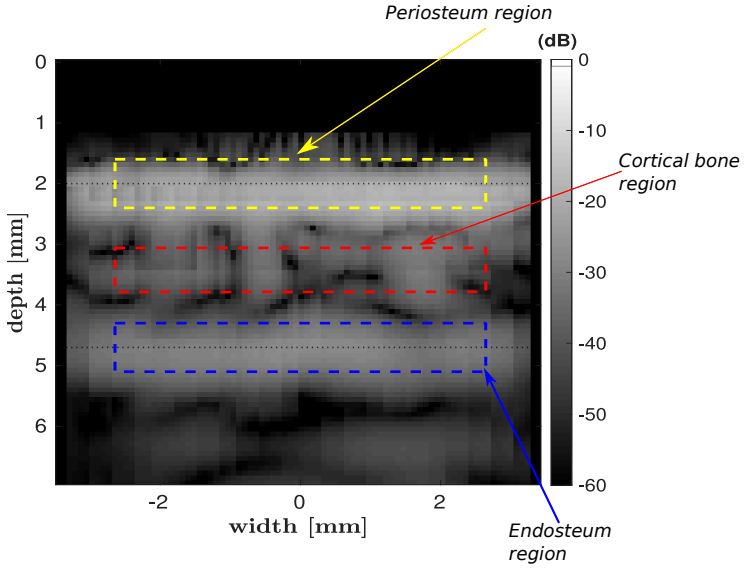

Figure 3.6: A typical reconstructed image for the simulation configuration shown in Figure 3.3. The yellow, red and blue ROIs were used to evaluate periosteum, inner bone, and endosteum contrasts, respectively

3.2.7 Data Analysis

A correlation analysis was conducted to identify the microstructure parameters defined in 3.2.2 of most important influence on endosteal interface visibility metrics (C_{EI} and C_{EP}). Normality of the distribution of the variables was evaluated using the Shapiro-Wilk test and we found that most of the variables were not normally distributed. Therefore, Spearman rank coefficients were used.

Correlations were considered statistically significant for $p < 0.05$. Statistical analyses were made using the Matlab 2018b Statistics Toolbox (Mathworks Inc., Natick, MA, USA). The patterns of variation of C_{EI} and C_{EP} with the three most important microstructure parameters were investigated. The purpose was to assess the range of values of the microstructure parameters, in particular porosity, for which the endosteal interface is visible.

Finally, the collection of images from all microstructure are analyzed and characteristic images to best illustrate the effect of the microstructure parameters on the appearance of the endosteal surface in the images were selected.

3.3 Results

3.3.1 Wave speed in cortical bone models

Figure 3.7 shows the wave speed in cortical bone estimated for each microstructure as a function of Ct.Por . Wave speed varied from about 2900 to 3400 m.s^{-1} as cortical porosity decreased from 24 to 2 %, that is a variation of wave speed of about 16%.

For comparison, experimental values that were deduced from experimental elastic coefficients obtained by Cai et al. [33] on the same collection of bone specimens (see in Appendix B the details on experimental wave speed determination) are also shown. Linear regression models between wave speed and Ct.Por for both experimental ($V_1^{exp} = 3404.5 - 23.83 \times Ct.Por$, $RMSE = 61.9$ m.s^{-1}) and synthetic

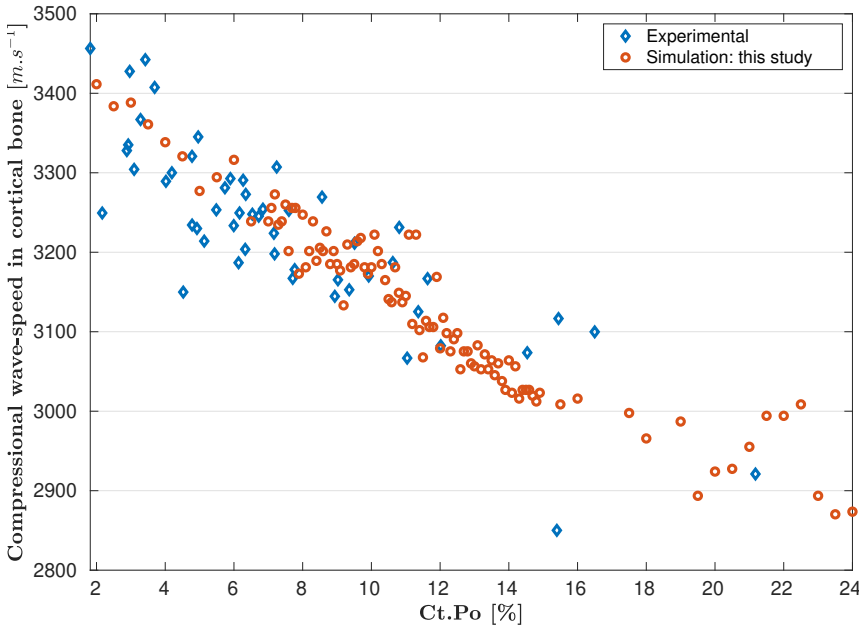

Figure 3.7: Simulated (red circles) and experimental (blue diamonds) wave speed against porosity (Ct.Por)

data ($V_1^{sim} = 3406.5 - 23.73 \times Ct.Por$, $RMSE = 37.8$ m.s^{-1}) had very close parameters and were in accordance with literature [34].

3.3.2 Descriptive statistics

The values of microstructural properties, wave speed in cortical bone and interface visibility metrics are summarized in Table 3.1

	Median	QT-1	QT-3	MIN	MAX
Ct.Por [µm]	11.19	8.57	13.83	2.00	24.00
Ct.Po.Dm. [µm]	67.70	57.26	84.81	39.09	119.95
Ct.Po.Dn. [pores/mm^2]	13.51	12.27	15.27	9.38	19.40
Dm.DC-1 [µm]	25.23	22.57	31.92	15.96	52.93
Dm.DC-9 [µm]	155.98	133.51	186.05	73.99	271.05
Lg.Po.Dm [µm]	213.01	186.06	238.79	97.95	337.39
Sm.Po.Dm [µm]	18.20	15.27	22.53	11.28	38.42
Dm.Rng [µm]	323.45	273.90	392.15	129.65	736.69
Dm.IDRng [µm]	132.62	106.56	154.74	54.04	229.13
V_1^{sim} [m.s^{-1}]	3137.13	3050.90	3210.75	2870.30	3411.42
C_{EI} [dB]	0.86	−0.59	3.33	−8.31	18.57
C_{EP} [dB]	−6.81	−8.15	−5.20	−11.35	−1.89

Table 3.1: The median, minimum value (MIN), maximum value (MAX), first (QT-1) and last (QT-3) quartile of the visibility metrics (C_{EI}, C_{EP}), the wave speed in cortical bone and the pore microstructural variables (defined in section 3.2.2)

3.3.3 Influence of microstructure on image contrasts

Spearman rank correlation coefficients between image quality metrics (C_{EI}, C_{EP}) and pore characteristics are given in Table 3.2. Ct.Po.Dn was not significantly corre-

Pore characteristics	C_{EI}	C_{EP}
Lg.Po.Dm	-0.71^{2}	-0.67^{2}
Ct.Por	-0.66^{2}	-0.63^{2}
Dm.IDRng	-0.65^{2}	-0.61^{2}
Dm.DC-9	-0.62^{2}	-0.59^{2}
Dm.Rng	-0.52^{2}	-0.48^{2}
Ct.Po.Dm	-0.50^{2}	-0.48^{2}
Dm.DC-1	-0.33^{1}	-0.29^{1}
Sm.Po.Dm	-0.27^{1}	-0.23^{1}
Ct.Po.Dn	$0.08^{n.s}$	$0.11^{n.s}$

Table 3.2: Spearman correlation coefficient r_s between image quality metrics and microstructural properties. C_{EI}: endosteal-interface contrast, C_{EP}: relative interface contrast . $^{n.s}$: not significant $p > 0.05$, ^{1} : $0.001 < p < 0.05$, ^{2} : $p < 0.001$

lated to the interface metrics, therefore it was discarded for the rest of the analysis. Negative correlations were found for the rest of the variables. Among all variables, the strongest correlation coefficients were for Lg.Po.Dm, Ct.Por, Dm.IDRng, and Dm.DC-9 (r_s from -0.61 to -0.71, $p < 0.001$). Correlation for Dm.Rng and Ct.Po.Dm were moderate (r_s from -0.48 to -0.52, $p < 0.001$). Smaller correlations for Dm.DC-1 and Sm.Po.Dm (r_s from -0.23 to -0.33, $0.001 < p < 0.05$) were found.

In figure 3.8, the variations of averaged pixel intensity in the three ROIs, C_{EI} and C_{EP} are shown for all microstructures as function of Lg.Po.Dm, Ct.Por, and Dm.IDRng which were found to be the most important variables (Table 3.2). Each point corresponds to a specific microstructure. First, we observe the relatively small variations of the periosteum mean intensity (blue curve) with respect to microstructure parameters. As a consequence, C_{EP} essentially evaluates endosteal interface contrast. As expected, this value is always negative because the endosteal surface is less visible than the periosteal surface.

Second, endosteal interface mean intensity (red curve) decreases while that of the internal bone speckle intensity (orange curve) increases for increasing values of microstructure parameters reflecting the degradation of bone microstructure. C_{EI}, which is by construction our metric best reflecting the visibility of the interface, varies between about -5 dB and 15 dB. Negative values correspond to speckle intensity inside bone larger than endosteal interface intensity. For small "large pore" size (Lg.Po.Dm < 200 µm), low cortical porosity (Ct.Por $<10\%$) and weak pore size dispersion (Dm.IDRng < 100 µm), C_{EI} is positive for most of the microstructures while it is negative for large "large pore" size (Lg.Po.Dm > 250 µm), high cortical porosity (Ct.Por $> 15\%$) and strong pore size dispersion (Dm.IDRng > 170 µm). For intermediate values, C_{EI} hovers around 0 dB.

The reconstructed images for all microstructures are provided in the supplementary material. In the following, a set of representative images are presented. Figure 3.9 shows a selection of images for different porosity values. Lg.Po.Dm and C_{EI} are given for each image. The periosteal interface is clearly visible as a bright zone centered at 2 mm-depth. The endosteal interface at 4.7 mm-depth is more or less visible depending on the microstructure. With increasing porosity, speckle intensity inside bone increases and endosteal interface visibility fades. On these images, for porosities of 2, 5, and 8% the endosteal interface stands out from inner cortical bone speckle and C_{EI} values are positive. For porosities of 13, 16 and 20 %, speckle

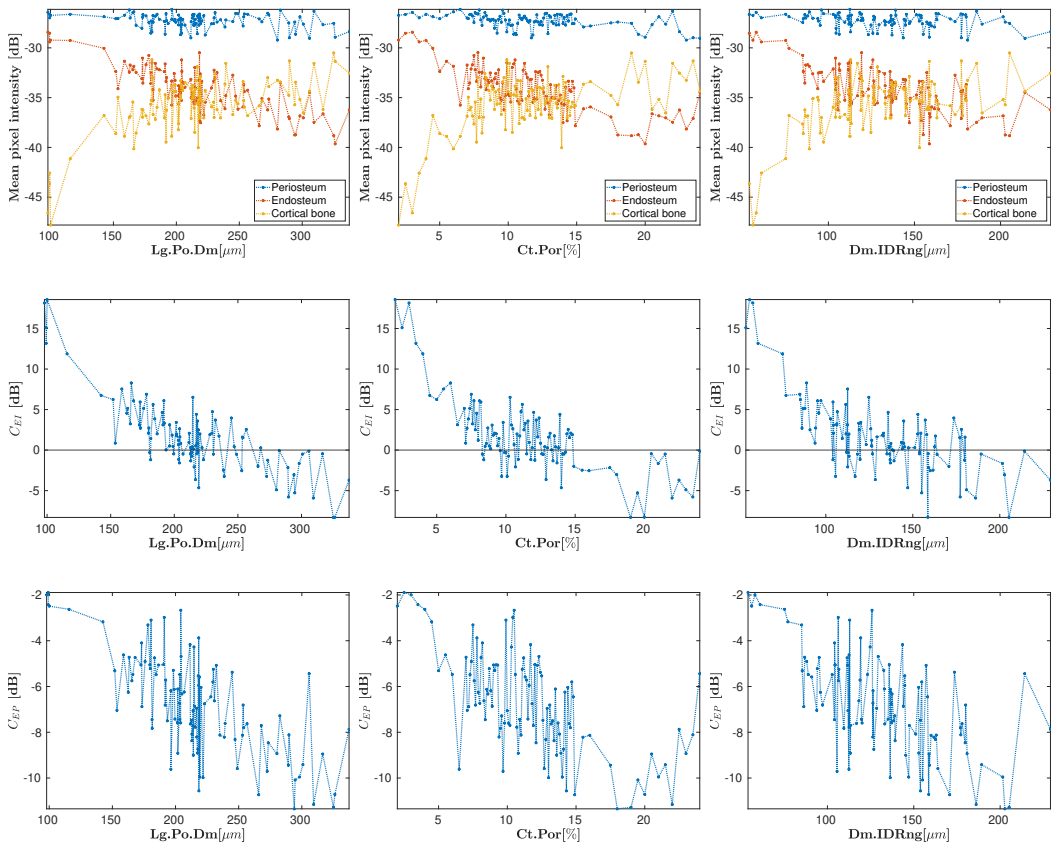

Figure 3.8: Average pixel intensity for the three ROIs (top), bone-endosteum contrast C_{EI} (middle) and interface contrast C_{EP} (bottom). The evolution of these variables for "large pores" size (Lg.Po.Dm), porosity (Ct.Por), and pore diameter dispersion (Dm.IDRng) are shown.

intensity inside the bone becomes dominant, the endosteal interface can hardly be distinguished, and C_{EI} values are negative.

As Lg.Po.Dm was found to be relatively strongly correlated to the image contrast, Figure 3.10 shows reconstructed images for microstructures with a similar porosity around 10.5% (±1%), and with increasing Lg.Po.Dm spanning the range 183 − 272 µm. For these microstructures, C_{EI} values decreased from 5.63 dB to −3.25 dB. Endosteal interface is visible for images on the first row whilst it is not for the images on the second row. As an example, figure 3.10 shows that the endosteal interface is perfectly detectable (C_{EI} = 5.63 dB) for 11.19 % porosity and Lg.Po.Dm= 183.3 µm and not visible (C_{EI} = −3.25 dB) for 10.09 % porosity and Lg.Po.Dm= 239.3 µm, illustrating a strong influence of the diameter of large pores on the image contrasts.

3.4 Discussion

3.4.1 Impact of the intra-cortical microstructure on image contrast

In this study, the effect of cortical bone microstructure on the quality of ultrasound images of the cortex is investigated. The contrast should be sufficient to allow the identification of the endosteal interface in order to assess cortical thickness, an important biomarker of bone health [5, 35]. Numerical simulations with a collection of

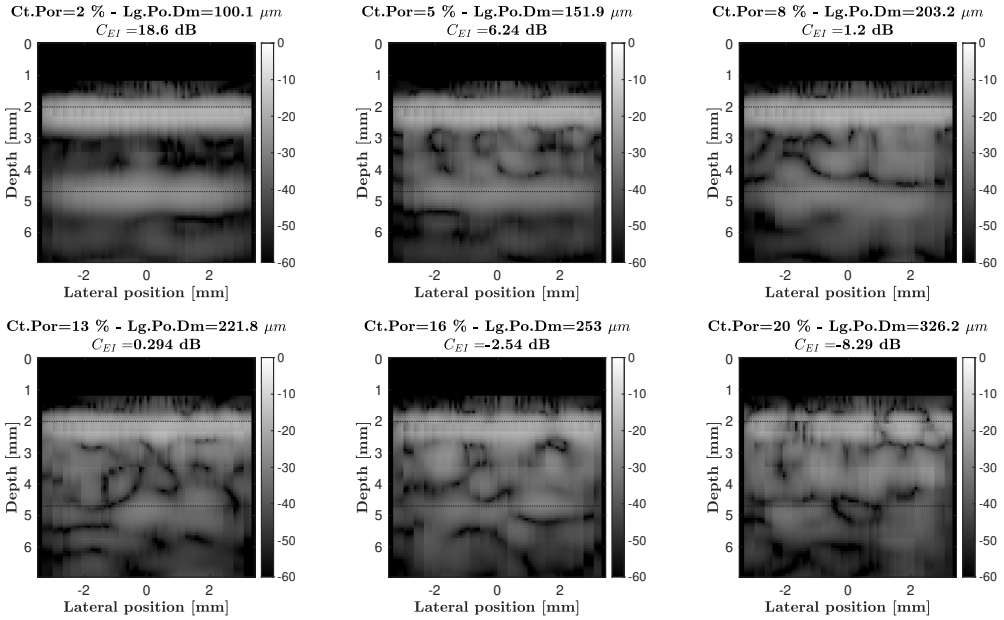

Figure 3.9: Reconstructed ultrasound images from simulated data for six microstructures for increasing porosties. 1^{st} row (from left to right): 2, 5 and 8 % porosity, 2^{nd} row: 13, 16 and 20% porosity. Lg.Po.Dm and C_{EI} are given for each image. The black dotted lines represent the true positions of the periosteal and endosteal interfaces. Each image is reconstructed using DAS with an optimized receive f-number of 1.9. The intensity is log-compressed and displayed with a dynamic range of 60 dB.

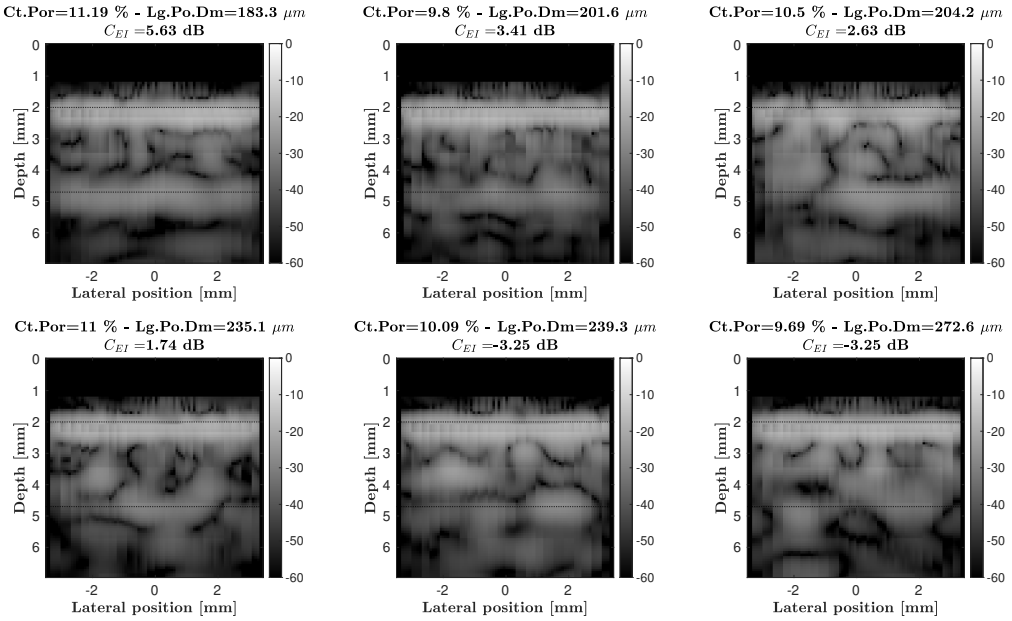

Figure 3.10: Reconstructed ultrasound images from simulated data for six microstructures with nearly equal porosity (around 10.5%) but increasing "large pore" size (Lg.Po.Dm). Ct.Por and C_{EI} are given for each image. The black dotted lines represent the true positions of the periosteal and endosteal interfaces. Each image is reconstructed using DAS with an optimized receive f-number of 1.9. The intensity is log-compressed and displayed with a dynamic range of 60 dB.

105 high-resolution images of microstructure (porosity ranging from 2 to 24%) were used in order to cover the diversity of porosity, pore size and pore distribution met in human cortical bone. Indeed, with ageing and osteoporosis, cortical bone porosity

and pore size increases. This degradation of the microstructure is challenging for ultrasound imaging.

The simulation framework was validated based on the excellent agreement found between experimental wave speed values and those recovered from numerical simulations (Figure 3.7 and Appendix B). Image reconstruction was performed using the state-of-the-art delay-and-sum image reconstruction with optimized receive f-number, correction of refraction at the soft tissue-bone interface and sample-specific wavespeed. A signal processing approach similar to the one adopted by [7] for *in vivo* imaging of the cortex of young adults were employed.

It is found that as Ct.Por increases, speckle intensity inside the bone cortex increases whereas the intensity of the signal from the endosteal interface decreases (Figure 3.8 and Figure 3.9). We found a reduction of approximately 18 dB in endosteal visibility metric (C_{EI}) from the denser bones to the most degraded microstructures. Interestingly, the presence of large pores (quantified by Lg.Po.Dm and Dm.DC-9) and the width of the distribution of pore size (Dm.IDRng) had a strong effect on image contrast (see Table 3.2). For similar porosities, a microstructure with larger "large pores" will be associated to lower visibility of the endosteal interface (Figure 3.10). This means that the sole augmentation of cortical porosity is not enough to explain the contrast deterioration (see figure 3.11 for illustration). Overall, the endosteal interface was visible ($C_{EI} > 0$ dB) for microstructures with

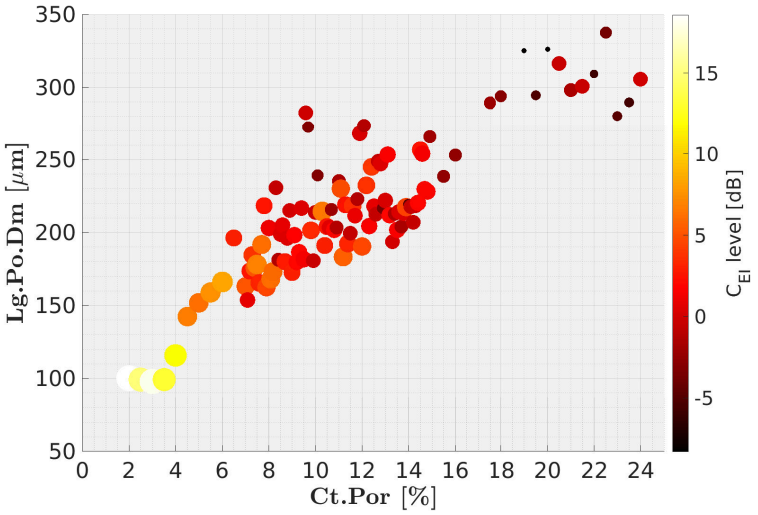

Figure 3.11: Scatter plot of endosteal interface contrast (C_{EI}) as a function of cortical porosity (Ct.Por) and diameter of large pore (Lg.Po.Dm). Size and color of each circle are proportional to the value of C_{EI}

moderate porosity (Ct.Por$\sim<$ 10%), small "large pore" size (Lg.Po.Dm $<$ 200 µm), and weak pore size dispersion (Dm.IDRng $<$ 100 µm). Endosteal interface was not visible ($C_{EI} < 0$ dB) for big "large pore" size (Lg.Po.Dm $>$ 250 µm), high cortical porosity (Ct.Por $>$ 15%) and wide pore size dispersion (Dm.IDRng $>$ 170 µm). These threshold values of the microstructure parameters are specific to our study as they are tied to the chosen central ultrasound frequency (2.5 MHz) used *in vivo* and cortical thickness (2.7 mm). For higher frequencies, ultrasound waves would experience stronger scattering by pores and higher attenuation resulting in lower threshold Ct.Por and Lg.Po.Dm values for a visible endosteum at the same depth.

3.4.2 Possible physical origins of contrast loss

The failure to observe the endosteal interface for degraded microstructures may be explained by several factors. The amplitude of the waves reflected at the endosteal interface decreases with increasing porosity because the effective acoustic impedance mismatch between bone and marrow is reduced. This can be quantified from the theoretical reflection coefficient (calculated for the acoustic power) which drops by 25% (corresponding to −1.2 dB in an image, see Appendix D) in the porosity range investigated. Therefore, the variations in the reflection coefficient cannot explain the 8 dB decrease in the intensity of the endosteal interface (Figure 3.8). Another factor is the attenuation that varies from about 20 dB/cm to 60 dB/cm in the investigated porosity range (see Appendix E). This corresponds to a decrease in the amplitude of backscattered echoes of about 20 dB if a round trip distance through the thickness of the cortex is considered. This value is larger than the observed 8 dB reduction of the amplitude at the endosteal interface. Because the proposed contrast metrics are calculated in the 0.8 mm-high regions of interest depicted in Figure 3.6, it is likely that our approach cannot accurately track further decrease in the amplitude of the specular reflection at the endosteal interface as the porosity increases. Indeed, because half the region of interest of the endosteal interface encompasses cortical bone, the amplitude at the endosteal interface shown in Figure 3.8 contains both specular reflection at the endosteal interface and diffuse scattering by the pores near the endosteal interface. The main reason for the loss of endosteal contrast could be the increase in the scattering strength from the inner microstructure of the cortex as porosity increases. For a porosity larger than 15 %, the amplitude of echo signals generated by the inner microstructure overcomes the amplitude of echo signals reflected at the endosteal interface. As a consequence, the endosteal interface is no longer visible. As shown in Figure 3.8, the speckle amplitude inside the cortex increases by about 10 dB (excluding extreme values) as the porosity increases. The product ka where k is the wavenumber at central frequency and for a wave speed of 3200 m/s, and a is the radius of the pores in the range 25 to 300 µm, varies from 0.12 to 1.5. Based on simulations similar to those of this study (but with monodisperse circular pores), Iori et al [36] found an increase of the backscatter intensity of about 5 dB as ka increased from 0.1 to 1, for ka between 1 and 1.5 a small decrease of about 2 dB was observed. This increase of pore backscatter intensity with ka supports the idea that the presence of large pores is the main cause of the loss of contrast at the endosteal interface.

3.4.3 Design of the numerical study: motivations and advantages

Our aim was to quantitatively assess the relationships between the bone microstructure and image contrast. This study was conducted with numerical simulation for several reasons. Firstly, this allowed us to investigate a large range of realistic microstructure types. This would not be possible in an *in vivo* study due to the limitations in X-ray imaging resolution *in vivo* , nor in an *ex vivo* study for which the number of samples and the control of their variability is an issue. One strength of the present study is to use high resolution images of human cortical bone obtained with SR-μCT, which reveal the realistic details of the microstructure of human cortical bone. Second, simulations of the imaging process are free of electronic noise and other experimental artifacts, resulting in a best-case imaging scenario. Finally, a plate-like cortical thickness with parallel interfaces was designed as the simplest

imaging configuration to isolate the effect of varying microstructure from those of varying thickness and interface curvature or interface tilt. Interface curvature and tilt can be accounted for with the refraction corrected image reconstruction algorithm used here [7].

3.4.4 Limitations of the study

The original microstructure images obtained with SR-μCT were relatively small (2.7×3.5 mm^2). Other high resolution imaging modalities could have been used to generate the model, such as scanning acoustic microscopy [37]. The advantage of using SR-μCT images was the high resolution (voxel size of 6.5 µm) and high contrast providing an accurate picture of the pores. Although the vast majority of simulations of ultrasound propagation in cortical bone has been conducted in 2D configurations in the plane transverse to osteons [8, 26], the validity of this configuration has not been investigated in detail. Haversian canals are not infinite cylinders as hypothesized here but their average length is in the range of 2-4 mm [38]. Volkmann canals, which run nearly perpendicular to Haversian canals, contribute to a part of the porosity and are not modeled in 2D configurations. Another three-dimensional feature not considered here is the spatial resolution in the elevation dimension of the probe which is finite and results in a summation of the backscattered signals over the height of the elements of the probe array. In cortical bone, attenuation due to pore scattering and absorption within the bone solid matrix both contribute to the total attenuation coefficient. In these simulations, a frequency-independent absorption within the bone matrix is modeled with an absorption coefficient of 19.0 dB/cm at 2.5 MHz following Yousefian et al. [18], [25]. This value leads to a total attenuation slightly higher than the values reported by Grimal et al [39] from *ex vivo* measurements of attenuation in human cortical bone specimens. They reported an attenuation of about 50 dB/cm at 4 MHz for specimens with a porosity around 10% while in the present simulation study we found an attenuation of 40 dB/cm at 2.5 MHz for the same porosity (see Appendix E). Some simulations were also conducted without absorption within the bone matrix (results not shown) and the results were found to be similar. Accordingly, we believe that the conclusions of this study are not sensitive to the choice of the absorption coefficient in the matrix. Finally, the heterogeneity of the distribution pore sizes was not fully considered. Specifically, a gradient of pore sizes through the cortex was only present in a few microstructure images, and the roughness of the endosteal interface due to the presence of large pores across the interface (trabecularization) [40] was not considered. The impact on image quality of this heterogeneity should be investigated in a separate study.

3.4.5 Conclusion and perspectives

The simulation results presented in this article suggest that the cortical thickness of individuals with low and moderate porosity can be successfully imaged at 2.5 MHz. This is in line with the *in vivo* results of Renaud et al. [7] on two young subjects for which the endosteal interface could be clearly identified at the radius and tibia. In contrast, our results suggest that imaging the cortical bone of some elderly subjects or osteoporotic subjects with a degraded microstructure (porosity larger than 10%, presence of large pores) [14] would be challenging. Specifically, we have found that the presence of large pores is detrimental to image quality. Such large pores are characteristic of degraded bone and were associated with weak femoral

strength *ex vivo* [35] and with fracture risk [41]. This may appear to be a major obstacle to bone imaging for some individuals with a high risk of fracture. A central frequency of 2.5 MHz like in *in vivo* measurements [7] is used. With a lower frequency, scattering and absorption may be reduced, however the spatial resolution in the ultrasound image may be not sufficient to clearly distinguish the endosteal interface from the periosteal and measure the cortical thickness. In this study we have used an optimally-implemented delay-and-sum image reconstruction algorithm, and demonstrated the limits of this approach. Advanced signal processing and image reconstruction could be considered to overcome this limitation, including data adaptive beamforming, specular beamforming, inverse problem and machine learning approaches [42, 43, 44, 45].

Bibliography

[1] C. Cooper and Serge Livio Ferrari. IOF Compendium of Osteoporosis. 2017. Publisher: International Osteoporosis Foundation (IOF).

[2] Ethel S. Siris, Ya-Ting Chen, Thomas A. Abbott, Elizabeth Barrett-Connor, Paul D. Miller, Lois E. Wehren, and Marc L. Berger. Bone Mineral Density Thresholds for Pharmacological Intervention to Prevent Fractures. *Archives of Internal Medicine*, 164(10):1108–1112, May 2004.

[3] Karine Briot, Simon Paternotte, Sami Kolta, Richard Eastell, Dieter Felsenberg, David M. Reid, Claus-C. Glüer, and Christian Roux. FRAX®: Prediction of Major Osteoporotic Fractures in Women from the General Population: The OPUS Study. *PLOS ONE*, 8(12):e83436, December 2013. Publisher: Public Library of Science.

[4] Pascal Laugier and Quentin Grimal. *Bone Quantitative Ultrasound: New Horizons*. Number 1364 in Advances in Experimental Medicine and Biology. Springer International Publishing, 1st ed. 2022 edition, April 2022.

[5] Q. Grimal and P. Laugier. Quantitative Ultrasound Assessment of Cortical Bone Properties Beyond Bone Mineral Density. *IRBM*, 40(1):16–24, February 2019.

[6] Valeria Beltrame, Roberto Stramare, Nicola Rebellato, Federico Angelini, Anna Chiara Frigo, and Leopoldo Rubaltelli. Sonographic evaluation of bone fractures: a reliable alternative in clinical practice? *Clinical Imaging*, 36(3):203–208, May 2012.

[7] Guillaume Renaud, Pieter Kruizinga, Didier Cassereau, and Pascal Laugier. In vivo ultrasound imaging of the bone cortex. *Physics in Medicine & Biology*, 63(12):125010, June 2018. Publisher: IOP Publishing.

[8] Huong Nguyen Minh, Juan Du, and Kay Raum. Estimation of Thickness and Speed of Sound in Cortical Bone Using Multifocus Pulse-Echo Ultrasound. *IEEE transactions on ultrasonics, ferroelectrics, and frequency control*, 67(3):568–579, 2020.

[9] Peter Augat and Sandra Schorlemmer. The role of cortical bone and its microstructure in bone strength. *Age and Ageing*, 35(suppl_2):ii27–ii31, September 2006.

[10] Yohann Bala, Roger Zebaze, and Ego Seeman. Role of cortical bone in bone fragility. *Current Opinion in Rheumatology*, 27(4):406–413, July 2015.

[11] K. L Bell, N Loveridge, J Power, N Garrahan, B. F Meggitt, and J Reeve. Regional differences in cortical porosity in the fractured femoral neck. *Bone*, 24(1):57–64, January 1999.

[12] Christina Møller Andreasen, Jean-Marie Delaisse, Bram CJ van der Eerden, Johannes PTM van Leeuwen, Ming Ding, and Thomas Levin Andersen. Understanding Age-Induced Cortical Porosity in Women: The Accumulation and Coalescence of Eroded Cavities Upon Existing Intracortical Canals Is the Main Contributor. *Journal of Bone and Mineral Research*, 33(4):606–620, 2018. _eprint: https://onlinelibrary.wiley.com/doi/pdf/10.1002/jbmr.3354.

[13] Valérie Bousson, Alain Meunier, Catherine Bergot, Éric Vicaut, Maria Augusta Rocha, Maria Helena Morais, Anne-Marie Laval-Jeantet, and Jean-Denis Laredo. Distribution of Intracortical Porosity in Human Midfemoral Cortex by Age and Gender. *Journal of Bone and Mineral Research*, 16(7):1308–1317, 2001.

[14] David M. L. Cooper, C. David L. Thomas, John G. Clement, Andrei L. Turinsky, Christoph W. Sensen, and Benedikt Hallgrímsson. Age-dependent change in the 3D structure of cortical porosity at the human femoral midshaft. *Bone*, 40(4):957–965, April 2007.

[15] C. Chappard, S. Bensalah, C. Olivier, P. J. Gouttenoire, A. Marchadier, C. Benhamou, and F. Peyrin. 3D characterization of pores in the cortical bone of human femur in the elderly at different locations as determined by synchrotron micro-computed tomography images. *Osteoporosis international: a journal established as result of cooperation between the European Foundation for Osteoporosis and the National Osteoporosis Foundation of the USA*, 24(3):1023–1033, March 2013.

[16] K. Raum, I. Leguerney, F. Chandelier, M. Talmant, A. Saïed, F. Peyrin, and P. Laugier. Site-matched assessment of structural and tissue properties of cortical bone using scanning acoustic microscopy and synchrotron radiation $\upmu$CT. *Physics in Medicine and Biology*, 51(3):733–746, January 2006. Publisher: IOP Publishing.

[17] M. S. Stein, S. A. Feik, C. D. L. Thomas, J. G. Clement, and J. D. Wark. An Automated Analysis of Intracortical Porosity in Human Femoral Bone Across Age. *Journal of Bone and Mineral Research*, 14(4):624–632, 1999. _eprint: https://onlinelibrary.wiley.com/doi/pdf/10.1359/jbmr.1999.14.4.624.

[18] Omid Yousefian, R. D. White, Yasamin Karbalaeisadegh, H. T. Banks, and Marie Muller. The effect of pore size and density on ultrasonic attenuation in porous structures with mono-disperse random pore distribution: A two-dimensional in-silico study. *The Journal of the Acoustical Society of America*, 144(2):709, August 2018.

[19] Maria Pia Zamorani and Maura Valle. Bone and Joint. In Stefano Bianchi and Carlo Martinoli, editors, *Ultrasound of the Musculoskeletal System*, Medical Radiology, pages 137–185. Springer, Berlin, Heidelberg, 2007.

[20] Xiran Cai, Hélène Follet, Laura Peralta, Marc Gardegaront, Delphine Farlay, Rémy Gauthier, Boliang Yu, Evelyne Gineyts, Cécile Olivier, Max Langer, Aurelien Gourrier, David Mitton, Françoise Peyrin, Quentin Grimal, and Pascal Laugier. Anisotropic elastic properties of human femoral cortical bone and relationships with composition and microstructure in elderly. *Acta Biomaterialia*, 90:254–266, May 2019.

[21] Xiran Cai, Renald Brenner, Laura Peralta, Cécile Olivier, Pierre-Jean Gouttenoire, Christine Chappard, Françoise Peyrin, Didier Cassereau, Pascal Laugier, and Quentin Grimal. Homogenization of cortical bone reveals that the organization and shape of pores marginally affect elasticity. *Journal of The Royal Society Interface*, 16(151):20180911, February 2019. Publisher: Royal Society.

[22] C. M. Moran, N. L. Bush, and J. C. Bamber. Ultrasonic propagation properties of excised human skin. *Ultrasound in Medicine & Biology*, 21(9):1177–1190, January 1995.

[23] Satoshi Kawasaki, Ryohei Ueda, Akihiko Hasegawa, Akifumi Fujita, Teruhisa Mihata, Mami Matsukawa, and Masashi Neo. Ultrasonic wave properties of human bone marrow in the femur and tibia. *The Journal of the Acoustical Society of America*, 138(1):EL83–EL87, July 2015.

[24] Roderic Lakes, Hyo Sub Yoon, and J. Lawrence Katz. Ultrasonic wave propagation and attenuation in wet bone. *Journal of Biomedical Engineering*, 8(2):143–148, April 1986.

[25] Omid Yousefian, Yasamin Karbalaeisadegh, and Marie Muller. Frequency-dependent analysis of ultrasound apparent absorption coefficient in multiple scattering porous media: application to cortical bone. *Physics in Medicine & Biology*, 66(3):035026, January 2021.

[26] Kaustav Mohanty, Omid Yousefian, Yasamin Karbalaeisadegh, Micah Ulrich, Quentin Grimal, and Marie Muller. Artificial neural network to estimate micro-architectural properties of cortical bone using ultrasonic attenuation: A 2-D numerical study. *Computers in Biology and Medicine*, 114:103457, November 2019.

[27] Yasamin Karbalaeisadegh, Omid Yousefian, Gianluca Iori, Kay Raum, and Marie Muller. Acoustic diffusion constant of cortical bone: Numerical simulation study of the effect of pore size and pore density on multiple scattering. *The Journal of the Acoustical Society of America*, 146(2):1015–1023, August 2019. Publisher: Acoustical Society of America.

[28] Emmanuel Bossy. SimSonic: free fdtd software for the simulation of ultrasonic waves propagation.

[29] Emmanuel Bossy, Frédéric Padilla, Françoise Peyrin, and Pascal Laugier. Three-dimensional simulation of ultrasound propagation through trabecular bone structures measured by synchrotron microtomography. *Physics in Medicine and Biology*, 50(23):5545–5556, November 2005. Publisher: IOP Publishing.

[30] Emmanuel Bossy and Quentin Grimal. Numerical Methods for Ultrasonic Bone Characterization. In Pascal Laugier and Guillaume Haïat, editors, *Bone Quantitative Ultrasound*, pages 181–228. Springer Netherlands, Dordrecht, 2011.

[31] Quentin Grimal, Kay Raum, Alf Gerisch, and Pascal Laugier. A determination of the minimum sizes of representative volume elements for the prediction of cortical bone elastic properties. *Biomechanics and Modeling in Mechanobiology*, 10(6):925–937, December 2011.

[32] Vincent Perrot, Maxime Polichetti, François Varray, and Damien Garcia. So you think you can DAS? A viewpoint on delay-and-sum beamforming. *Ultrasonics*, 111:106309, March 2021.

[33] Xiran Cai, Laura Peralta, Renald Brenner, Gianluca Iori, Didier Cassereau, Kay Raum, Pascal Laugier, and Quentin Grimal. Anisotropic elastic properties of human cortical bone tissue inferred from inverse homogenization and resonant ultrasound spectroscopy. *Materialia*, 11:100730, June 2020.

[34] Laura Peralta, Juan Deyo Maeztu Redin, Fan Fan, Xiran Cai, Pascal Laugier, Johannes Schneider, Kay Raum, and Quentin Grimal. Bulk wave velocities in cortical bone reflect porosity and compression strength. *Ultrasound in Medicine & Biology*, 47(3):799–808, 2021.

[35] Gianluca Iori, Johannes Schneider, Andreas Reisinger, Frans Heyer, Laura Peralta, Caroline Wyers, Melanie Gräsel, Reinhard Barkmann, Claus C. Glüer, J. P. van den Bergh, Dieter Pahr, and Kay Raum. Large cortical bone pores in the tibia are associated with proximal femur strength. *PLOS ONE*, 14(4):e0215405, April 2019. Publisher: Public Library of Science.

[36] G. Iori, J. Du, J. Hackenbeck, V. Kilappa, and K. Raum. Estimation of Cortical Bone Microstructure from Ultrasound Backscatter. *IEEE Transactions on Ultrasonics, Ferroelectrics, and Frequency Control*, pages 1–1, 2020. Conference Name: IEEE Transactions on Ultrasonics, Ferroelectrics, and Frequency Control.

[37] Quentin Grimal, Daniel Rohrbach, Julien Grondin, Reinhard Barkmann, Claus-C. Glüer, Kay Raum, and Pascal Laugier. Modeling of Femoral Neck Cortical Bone for the Numerical Simulation of Ultrasound Propagation. *Ultrasound in Medicine & Biology*, 40(5):1015–1026, May 2014.

[38] D. M. L. Cooper, C. E. Kawalilak, K. Harrison, B. D. Johnston, and J. D. Johnston. Cortical Bone Porosity: What Is It, Why Is It Important, and How Can We Detect It? *Current Osteoporosis Reports*, 14(5):187–198, October 2016.

[39] Quentin Grimal, Maryline Talmant, and Guillaume Renaud. Measurement of ultrasonic anisotropic attenuation of P-wave in millimetric-sized human cortical bone samples [abstract]. *International Symposium on Ultrasonic Characterisation of Bone*, page 1, June 2019, Villa-Clythia, Fréjus, France.

[40] Roger MD Zebaze, Ali Ghasem-Zadeh, Ann Bohte, Sandra Iuliano-Burns, Michiko Mirams, Roger Ian Price, Eleanor J Mackie, and Ego Seeman. Intracortical remodelling and porosity in the distal radius and post-mortem femurs of women: a cross-sectional study. *The Lancet*, 375(9727):1729–1736, May 2010.

[41] Gabriele Armbrecht, Huong Nguyen Minh, Jonas Massmann, and Kay Raum. Pore-Size Distribution and Frequency-Dependent Attenuation in Human Cortical Tibia Bone Discriminate Fragility Fractures in Postmenopausal Women With Low Bone Mineral Density. *JBMR Plus*, 5(11):e10536, 2021.

[42] H. Hasegawa. Recent Developments in Adaptive Beamforming. In *2019 IEEE International Ultrasonics Symposium (IUS)*, pages 1063–1066, October 2019. ISSN: 1948-5727.

[43] Alfonso Rodriguez-Molares, Ali Fatemi, Lasse Løvstakken, and Hans Torp. Specular Beamforming. *IEEE Transactions on Ultrasonics, Ferroelectrics, and Frequency Control*, 64(9):1285–1297, September 2017. Conference Name: IEEE Transactions on Ultrasonics, Ferroelectrics, and Frequency Control.

[44] R. Lavarello, F. Kamalabadi, and W.D. O'Brien. A regularized inverse approach to ultrasonic pulse-echo imaging. *IEEE Transactions on Medical Imaging*, 25(6):712–722, June 2006. Conference Name: IEEE Transactions on Medical Imaging.

[45] Shengfeng Liu, Yi Wang, Xin Yang, Baiying Lei, Li Liu, Shawn Xiang Li, Dong Ni, and Tianfu Wang. Deep Learning in Medical Ultrasound Analysis: A Review. *Engineering*, 5(2):261–275, April 2019.

Chapter 4

Ex vivo ultrasound imaging of human cortical bone: cortical thickness and speed of sound estimation

Contents

4.1 Introduction

Objectives of this study. In the previous chapter we studied the influence of cortical bone microstructure variables such as porosity and distribution of the pores, on the contrast of the endosteum in ultrasound images . However, this study was based on 2D simulation data with some limitations: small bone dimensions, small ultrasound probe and known speed-of-sound. Here, we performed *ex vivo* imaging of specimens from elderly human donors and compared US images to reference micro-computed tomography (μCT) images (high resolution). The objectives are to: (i) validate the estimation of cortical thickness in transverse ultrasound images of *ex vivo* human samples; (ii) investigate the determinants of ultrasound image quality in *ex vivo* human samples with moderate to high porosity; (iii) explore the relationship between wave speed estimated using the autofocus method and cortical porosity.

Only few *ex vivo* validation of QUS techniques have been performed in the past [1, 2, 3, 4, 5]. They are an essential step to validate the technique without some limitations of *in vivo*testing. In particular, in *ex vivo*experiments, the geometry of the microstructure of the specimens is known thanks to high-resolution microCT.

Limited testing of imaging techniques. Nguyen et al. [6] used refraction-corrected multifocus imaging and evaluated their method on bone phantoms and bovine tibia samples. Additionally, it was tested on only one human tibia [1], and the estimated cortical thickness was validated using high-resolution peripheral quantitative computed tomography (HR-pQCT).

In the technique developed by Renaud et al. [7], cortical thickness is measured based on the segmentation of ultrasound images obtained with refraction-corrected synthetic focus imaging, while the speed of sound and elastic anisotropy are determined using an autofocus approach. These measurements were validated *in vivo* at the tibia and radius in only two healthy volunteers by comparing ultrasound images and cortical thickness with high-resolution peripheral quantitative computed tomography (HR-pQCT).

4.2 Materials & methods

4.2.1 Sample extraction and preparation

Cortical bone samples were obtained from five human femoral shafts, selected from a dataset of ten femurs from female subjects aged between 66 and 98 years. This dataset was acquired from the Human Ethics Committee of the Centre du don des Corps at the University Paris Descartes (Paris, France), part of the French program for voluntary corpse donation for scientific research. Informed written consent was obtained from tissue donors or their legal guardians for research purposes, in accordance with the legal provisions outlined in the French Code of Public Health. This dataset was previously used in a study by Granke et al. (2011) [8].

The fresh bone material was carefully preserved by placing it in plastic bags, followed by freezing and storage at -20°C. Subsequently, most of the soft tissues were removed from the samples. For each femur, a half-cylinder of approximately 7 cm in length was then extracted along the femoral axis at the diaphysis, as shown in Figure 4.1. Unfortunately, during dissection of a femur, a lead projectile was discovered embedded inside. The lead projectile exhibited a cuboid shape, measuring approximately 1 cm on each side. The femur containing the lead is depicted in Figure 4.2.

Following extraction, the 5 bone samples underwent fixation using the alcoholic formalin-free fixative F13 [9] for a duration of 48 hours, as shown in Figure 4.3. F13 [9], a commonly used fixative in histology and medical diagnostics, consists of ethanol, methanol, polyethylene glycol, and water. Subsequent to fixation, the samples were immersed in distilled water for 6 hours in an ultrasonic bath to remove all remaining soft tissues. Despite the cleaning process, a portion of the lead residue remained on the sample and also diffused onto the other samples, as shown in panel (b) of Figure 4.3.

4.2.2 Experimental setup and ultrasound imaging

4.2.2.1 Degasing of the samples

We implemented a homemade degassing technique. Before ultrasound acquisitions, we implemented a protocol to eliminate any air present inside the bone microstructure, which could potentially interfere with the ultrasound reconstruction algorithm. The configuration is illustrated in Figure 4.4.

Figure 4.1: Extraction of half-cylinder bone samples from femoral shafts for analysis. Each sample, approximately 7 cm in length, was extracted along the femoral axis at the mid-diaphysis.

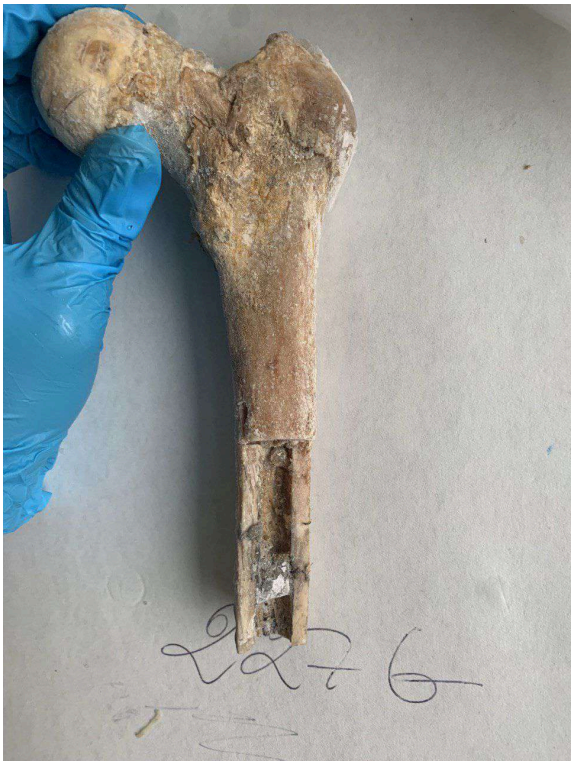

Figure 4.2: Lead-containing cuboid discovered within the femur during sample extraction. The cuboid-shaped lead measures approximately 1 cm on each side.

The cortical bone sample, a water bath, and a vibrating surface are placed within a vacuum bell connected to a pump. Magnets are employed to suspend the sample over the water bath, while the vibrating surface is brought into contact with the

(a) (b)

Figure 4.3: Cleaning process of bone samples after fixation using the alcoholic formalin-free fixative F13. Panel (a) shows the samples during cleaning, while panel (b) illustrates the samples after cleaning, with some lead residue visible on the samples.

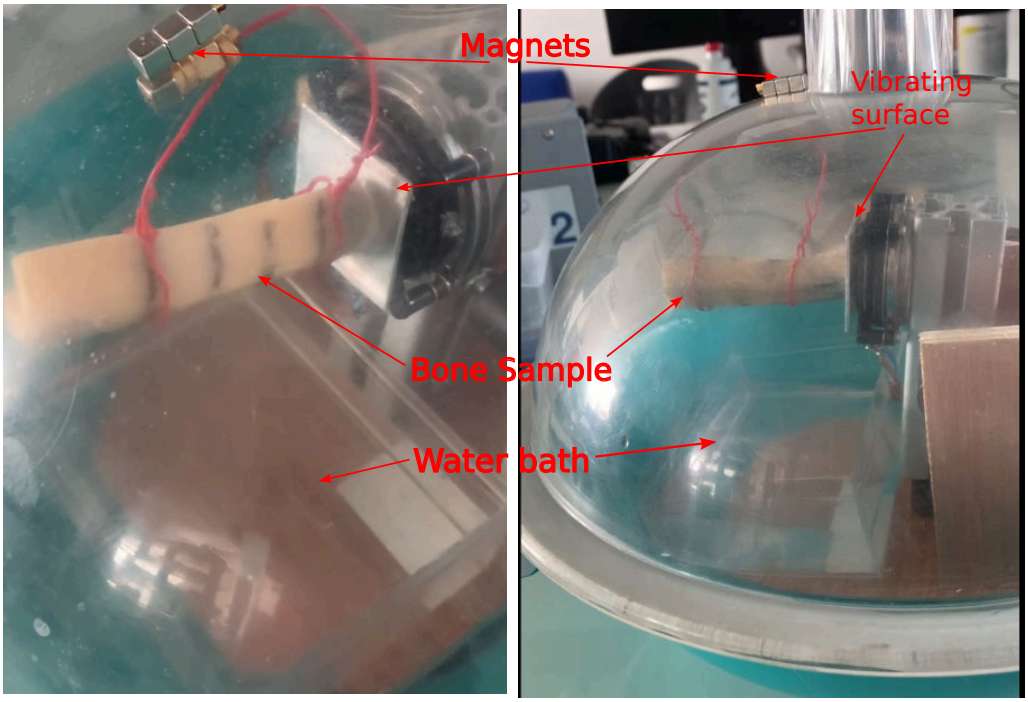

Figure 4.4: The homemade degassing setup implemented before ultrasound acquisitions to eliminate air from within the bone microstructure.

suspended sample.
For each sample, we applied a two-step process: an air removal phase followed by a water-filling phase. The air removal phase consists of three cycles, each involving active pumping with vibrations at 10 Hz followed by passive pumping with vibrations at 10 Hz. This process is aimed at evacuating air from the sample. Subsequently, during the water-filling phase, the sample is submerged in the water bath, and active pumping is conducted for 1 hour.

4.2.2.2 Ultrasound acquisitions

After degassing, the samples were immersed in water and scanned using a fully programmable ultrasound system (Vantage, Verasonics Inc., Redmond, WA, USA). The scanning scheme used a synthetic aperture protocol ([10, 11]) in which each element in the array was activated sequentially, followed by a full array recording of the received echo signals. A phased array ultrasound transducer with 96 elements operating at the central frequency of 2.5 MHz (P4-1 ATL/Philips, Bothell, WA, USA; pitch 0.295 mm) was used. The emitted pulse had a -6dB relative frequency bandwidth of 80%. A complete ultrasound acquisition resulted in a total of 96×96 pulse-echo signals.

The sample is approximately 7 cm long, while the elevation of the probe is around 1.5 cm. Therefore, the sample is divided into 4 equal subvolumes. The subdivision of the samples is illustrated in Figure 4.5.

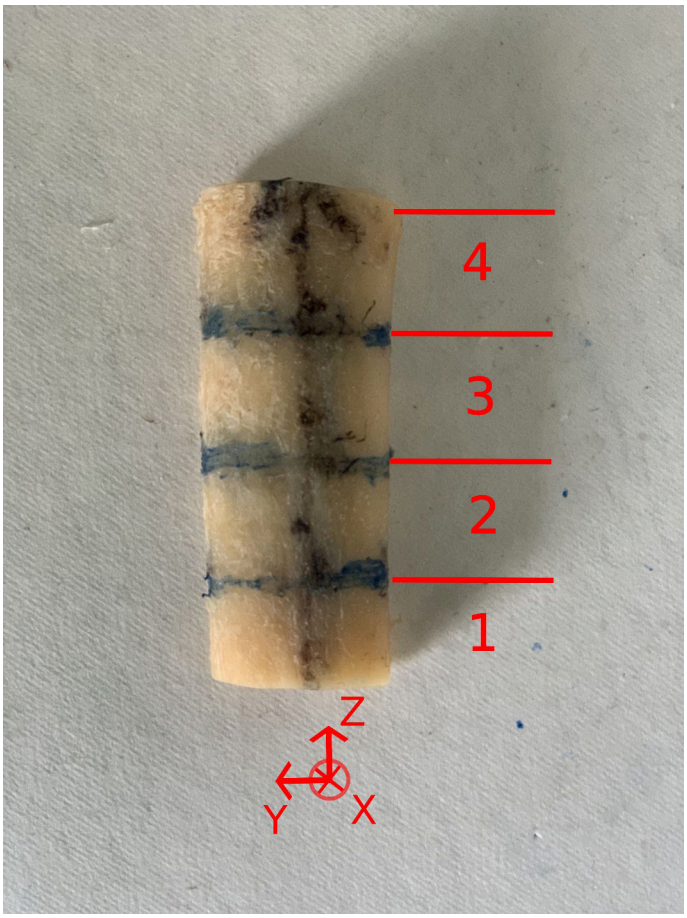

Figure 4.5: Subdivision of the samples into four subvolumes for ultrasound acquisitions. Each subvolume has a length of around 13 mm.

The sample will remain immersed during ultrasound acquisitions, and water will serve as a substitute for soft tissues. Ultrasound recordings were obtained for each subvolume of every sample, with the set-up illustrated in Figure 4.6. The probe was positioned in front of the sample and at the middle of each measurement zone, slightly submerged in water. Acquisitions were repeated 10 times with repositioning, guided by real-time visualization to accurately adjust the images. The objective of the repetitions was to obtain several acquisitions with various probe positions to select the one with the best probe alignment. When the probe is perfectly aligned with the sample, both the periosteal and endosteal interfaces are correctly visualized

in the ultrasound image. However, when the probe is not perfectly aligned, the periosteal interface appears doubled, showing two external interfaces.

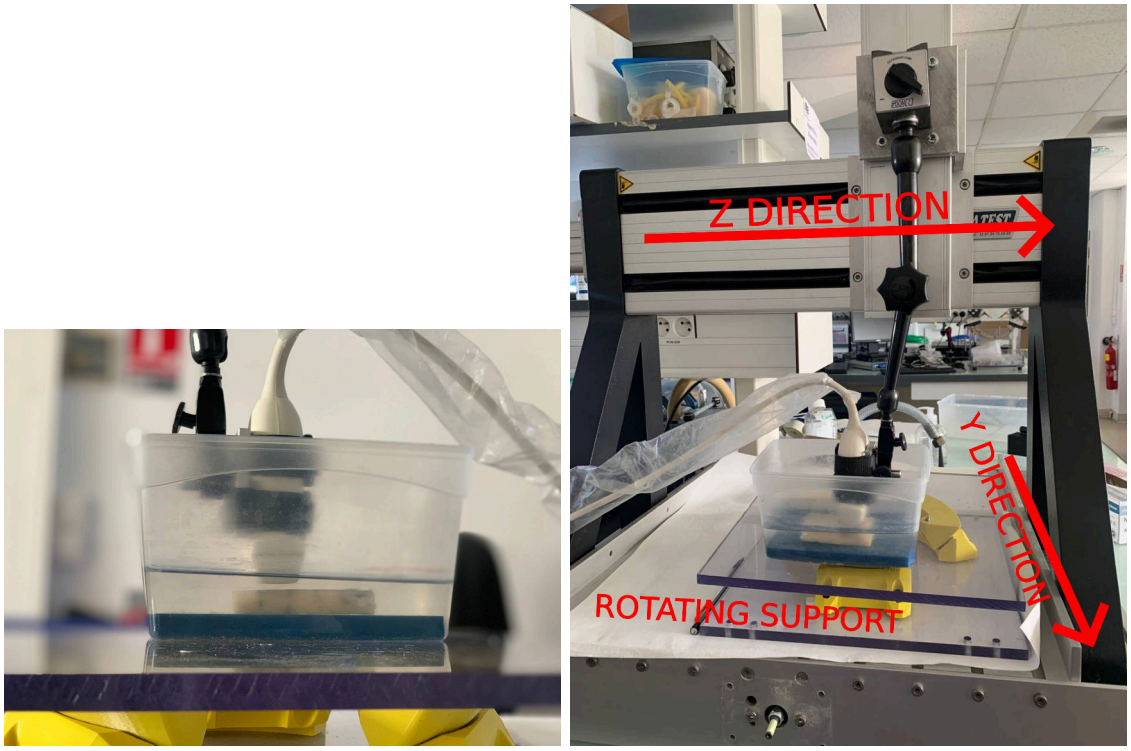

(a) (b)

Figure 4.6: Experimental setup for ultrasound acquisitions, with the probe positioned in front of the sample, slightly submerged in water (panel (a)). Acquisitions were repeated 10 times with repositioning for each measurement site using the rotating support and the translating device in panel (b).

4.2.2.3 Sample-specific speed of sound estimation for ultrasound imaging

The medium consists of two layers with distinct acoustical properties: a first layer of water simulating soft tissue and a layer of cortical bone. To reconstruct the image of this medium accurately, the ultrasound wave speed in each layer must be determined. In the first layer, the wave speed was estimated using the head wave propagating at the interface between the probe and water [12]. The estimated speed of sound ranged between 1480 and 1492 m/s. The water temperature was measured before acquiring each sample, ranging between 19 and 20 ° C. These estimated wave speed values correspond to the speed of sound in distilled water at these temperatures [13].

Regarding bone, the propagation speed in the cortex depends on the microstructure, particularly on the cortical porosity [8]. As observed in Tables 4.1 and 4.2 (on page 77), the samples exhibit highly heterogeneous porosity values, ranging from 5 to 17%. Therefore, sample-specific speed of sound was determined using an autofocus approach. This approach, described in detail in Chapter 2, was previously used by [7, 12] for determining the speed of sound model inside the cortical bone. In essence, the approach consists in searching for the ultrasound wave speed value that yields the best-reconstructed image in terms of image sharpness, global energy, and normalized variance of pixel intensities. This selected velocity serves as the best estimation of the true speed of sound [14]. In accordance with [8] and [15], the

algorithm was provided with a list of speeds ranging from 2500 to 3500 m/s, with a step of 25 m/s.

4.2.2.4 Ultrasound image reconstruction

The image reconstruction technique employed in this study follows the principles outlined in Chapter 1. In summary, the Delay-and-Sum (DAS) algorithm with a constant f-number in receive and constant receive angle was used [16]. DAS was chosen due to its widespread use in beamforming algorithms, and was previously used for the first *in vivo* image of the bone cortex [7]. A Hanning window was applied to the receiver sub-aperture, and the receive f-number was set to 1.9 and the receive angle was 0. The synthetic aperture sequence resulted in 96 low-resolution images (resulting from 96 successive single-element transmissions), which were coherently summed to generate a high-contrast image.

The delays incorporated into the DAS algorithm account for refraction at all interfaces. The delay calculation followed the implementation described in [7], where the Fermat principle is used to calculate the travel time through the multilayered medium for each element of the array and image pixel. It is important to note that only the contribution of longitudinal waves was considered and the arrival times associated with shear waves were ignored. Furthermore, the ultrasound longitudinal wave speed used for the bone layer was determined for each measurement zone of each sample and each repetition as explained above.

4.2.2.5 Segmentation of the bone interfaces

The segmentation of the periosteal and endosteal interfaces of the cortex is performed using Dijkstra's algorithm. For the periosteal interface, the algorithm searches for the shortest path extending across the entire lateral width of the ultrasound image that has the maximal intensity (see Figure 2.4). For the endosteal interface, the algorithm reduces the lateral width of the search area since the endosteal interface is less extended than the periosteal interface.

4.2.3 Imaging and microstructure analysis with X-ray micro-Computed Tomography

4.2.3.1 Imaging

Due to the unfortunate presence of lead in the samples, the micro-CT images were difficult to reconstruct, as the lead altered the pixel dynamics, making some images unusable. Consequently, the scans were performed a second time with adjusted parameters. The specimens were scanned using micro-computed tomography (micro-CT) in air done at IMOSAT (Université Paris descartes). We used a desktop micro-CT system (Skyscan 1176; SkyScan-Brücker, Kontich, Belgium) equipped with a scintillator coupled to a CCD Princeton camera with a pixel size of 12.53 µm and a depth of 16 bits. Scanning was performed at the maximum potential of 90 kV and 278 µA. The scanning trajectory used for micro-CT data acquisition was circular, with an angular rotation step of 0.3° and a total angular rotation of 197.10°. The total duration of the acquisition of the X-ray data ranged from 5 hours and 43 minutes to 6 hours and 12 minutes for different samples, with variations attributed to the use of different subvolumes for each bone sample.

Before analysis, we defined a Volume of Interest (VOI) in the 3D images of each measurement zone of each sample for (i) faster processing and (ii) better cor-

respondence with the dimensions of the ultrasonic probe (aperture and elevation) (Figure 4.7). First, we selected a subvolume. The delineation of the subvolumes, along with their corresponding indexes, is shown on a sample in the left part of Figure 4.7 and in Figure 4.5.

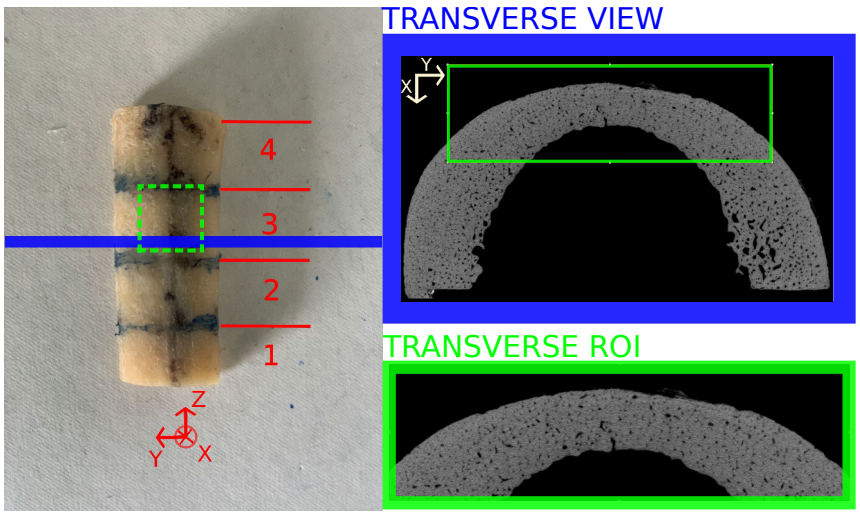

Figure 4.7: Illustration of the Volume of Interest (VOI) selection process. Each numbered region corresponds to a subvolume for ultrasound acquisitions (left part). Within each subvolume, a VOI of length 20 mm is selected (right part).

Within each subvolume, we then selected a rectangular cuboid with dimensions $D \times 20 \times 13$ mm^3. D corresponds to the radial depth of interest of the sample and is chosen to include the internal surface of the sample. The value of D ranged between 8 and 10 mm, depending on the diameter of the sample.

Three-dimensional images with a voxel size of 8.79 µm were reconstructed using a Feldkamp filtered back-projection algorithm provided with the manufacturer's reconstruction software NRecon (NRecon; SkyScan-Brücker, Kontich, Belgium) version 1.7.4.6. For each sample, appropriate beam hardening and ring artifact corrections were applied. Figure 4.10 displays a 2D image from each subvolume of each cortical bone sample in the transverse plane (x-y plane).

I would like to thank Christine Chappard for taking the time to help me with the micro-CT (scanning and reconstruction) of large bone samples.

4.2.3.2 Microstructure analysis

All the steps of microstructure analysis are summarized in Figure 4.8.

3D micro-CT image analysis was performed on each Volume of Interest (VOI) using CTAn software (CTAn; SkyScan-Brücker, Kontich, Belgium). In some samples, trabecularization was observed, resulting in the presence of two distinct zones: a cortical zone and a trabecular zone (see Figure 4.10). As this study focuses specifically on the cortical aspect of the bone, a preliminary treatment was necessary to eliminate the trabeculae and isolated bone regions. This involved employing kernel filtering (either Kuwahara or Uniform kernels with a radius of 2) and morphological operations to close all pores with diameters below a threshold value, thus generating a mask that excludes the trabecular regions. The specific kernel and parameters used varied across samples due to the high variability of the samples. Figure 4.9 presents a cross-section of a sample with trabeculae presence, illustrating the original image, the mask, and the binarized image. The pre-processed 3D reconstructed sub-volumes were binarized using the Otsu method.

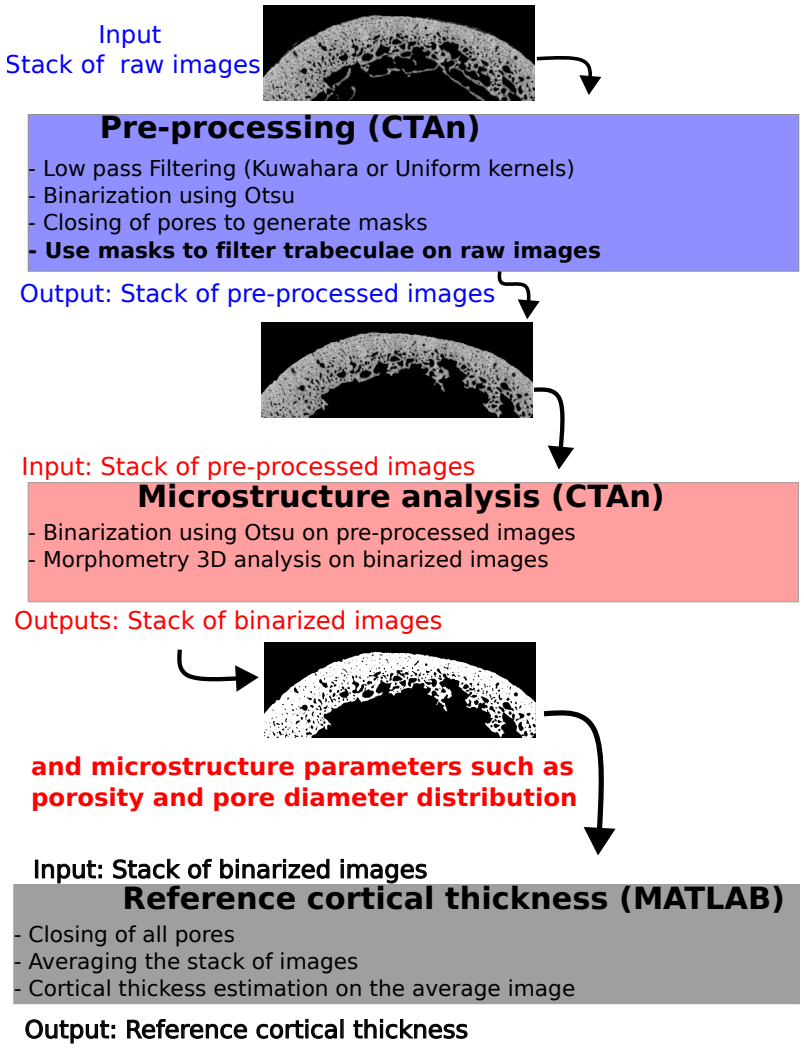

Figure 4.8: Summary of all the steps involved in the microstructure analysis and the determination of the reference cortical thickness.

(a) (b) (c)

Figure 4.9: Cross-section of a bone sample illustrating the original micro-CT image (a), the generated mask excluding trabecular regions (b), and the resulting binarized image after trabecular removal (c).

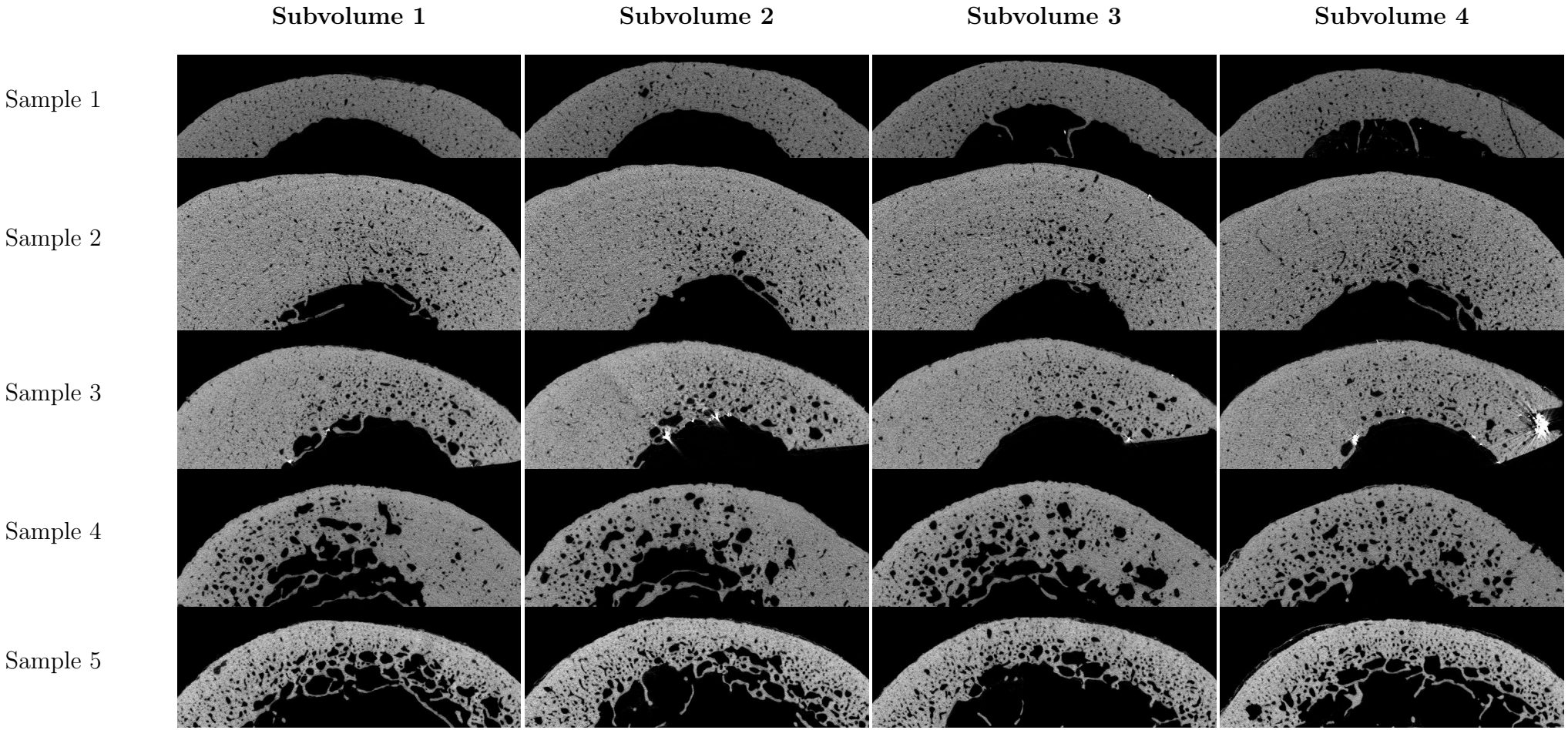

Figure 4.10: Reference X-ray images of all samples. An example slice is shown for each subvolume.

The binarized sub-volumes in 3D were used to extract pore characteristics through the advanced cortical 3D analysis method within the CTAn software. Subsequently, the cortical 3D porosity (Ct.Por), representing the percentage of pore volume over the total sub-sample volume, was deduced.

The microstructure was also characterized by cortical pore density (Ct.Po.Dn in pores/mm^3), and the distribution of pore diameters. Ct.Po.Dn was calculated as the number of pores divided by the total sub-sample volume. For the distribution of pore diameters, the analysis was performed in 2D space: in each cross-sectional slice (e.g., each slice of the xy plane) of a 3D binarized sub-volume, the diameter of each pore was calculated as the diameter of a disk with the same area using matlab. All pore diameters of all slices of a sub-volume were stacked together to obtain the pore distribution. From this point, the characterization of pore diameter distribution is the same as in the previous study [15] and in Chapter 3. The distribution of pore diameters was characterized by the median value (Ct.Po.Dm), the 1^{st} (Dm.DC-1) and 9^{th} deciles, the average diameter of small pores (Sm.Po.Dm) (all pores with a diameter smaller than Dm.DC-1), the average diameter of large pores (Lg.Po.Dm) (all pores with a diameter greater than Dm.DC-9), the range of variation (Dm.Rng), i.e., the difference between the maximum and minimum pore diameter, and the inter-decile range (Dm.IDRng). On page 77, all pore parameters of each sub-volume are summarized in Table 4.1 for lower porosity samples (e.g., samples 1, 2, and 3), and on Table 4.2 for higher porosity samples (e.g., samples 4 and 5).

4.2.4 Reference cortical thickness determination from micro-CT images

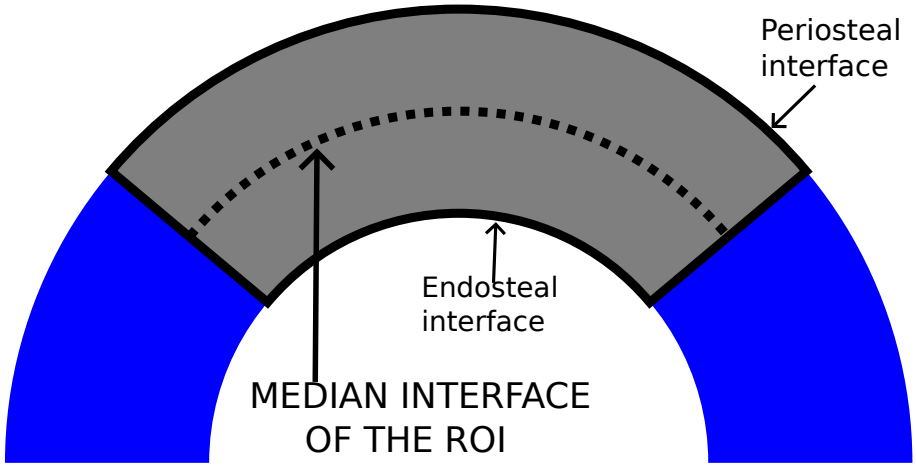

Figure 4.11: Illustration of the estimation of the cortical thickness. From the segmented periosteal and endosteal interface, a median interface is deduced. Cortical thickness is the ratio between the surface of the region-of-interest (the gray box) and the length of the median interface.

To estimate a reference cortical thickness for one measurement zone, the stack of binarized micro-CT images (depending on the sample a stack contains between 1365 and 1719 images) is processed by closing all pores in the stack. The resulting images are then averaged to produce a single 2D image. In Figure 4.12, panel (a) displays the average images of the first subvolume of each sample, illustrating the effect of averaging along the z-axis. To mitigate this effect, the average images are binarized (panel b of Figure 4.12). After binarization using Otsu method, contours

	Sample 1				Sample 2				Sample 3			
Property	Subv. 1	Subv. 2	Subv. 3	Subv. 4	Subv. 1	Subv. 2	Subv. 3	Subv. 4	Subv. 1	Subv. 2	Subv. 3	Subv. 4
Ct.Por(%)	4.96	6.45	6.15	6.42	5.6	12.35	10.93	7.03	11.54	12.35	10.93	7.03
Ct.Po.Dn (mm^{-3})	10.72	11.66	12.44	14.36	10.77	11.90	14.26	17.14	10.77	11.90	14.26	17.14
Ct.Po.Dm (μm)	56.14	57.01	55.26	51.57	57.01	53.44	53.44	49.62	57.01	53.44	53.44	49.62
Dm.DC-1 (μm)	24.31	26.26	26.26	24.31	26.26	26.26	26.26	24.31	26.26	26.26	26.26	24.31
Dm.DC-9 (μm)	115.31	127.09	119.91	111.40	160.64	154.70	140.35	134.25	160.64	154.70	140.35	134.25
Lg.Po.Dm (μm)	154.54	174.79	164.75	156.12	267.60	265.35	226.77	223.85	267.60	265.35	226.77	223.85
Sm.Po.Dm (μm)	23.07	23.88	23.89	23.11	24.08	24.03	24.06	23.15	24.08	24.03	24.06	23.15
Dm.Rng (μm)	1034.62	761.25	620.43	2994.06	2125.09	2079.84	1729.88	2385.07	2125.09	2079.84	1729.88	2385.07
Dm.IDRng (μm)	91.00	100.83	93.66	87.09	134.38	128.44	114.09	109.94	134.38	128.44	114.09	109.94

Table 4.1: Pore statitics for samples 1, 2 and 3.

	Sample 4				Sample 5			
Property	Subv. 1	Subv. 2	Subv. 3	Subv. 4	Subv. 1	Subv. 2	Subv. 3	Subv. 4
Ct.Por (%)	12.16	14.43	16.53	15.96	16.63	16.40	16.45	16.41
Ct.Po.Dn (mm^{-3})	8.02	7.09	6.75	7.88	12.47	13.03	12.81	13.09
Ct.Po.Dm (μm)	49.62	58.71	65.08	63.55	48.62	49.62	52.51	52.51
Dm.DC-1 (μm)	24.31	24.31	24.31	24.31	24.31	24.31	24.31	24.31
Dm.DC-9 (μm)	189.86	209.82	225.21	218.10	181.64	186.72	190.64	189.60
Lg.Po.Dm (μm)	333.57	382.79	422.71	382.85	307.04	302.44	303.39	299.81
Sm.Po.Dm (μm)	23.12	23.11	23.12	23.13	23.14	23.15	23.15	23.14
Dm.Rng (μm)	1698.95	1868.26	2415.22	1865.79	1919.21	1771.11	1835.63	1653.48
Dm.IDRng (μm)	165.55	185.51	200.90	193.80	157.33	162.41	166.33	165.29

Table 4.2: Pore statitics for samples 4 and 5.

are detected, and the periosteal and endosteal lines are deduced (panel (b) of Figure 4.12). These interfaces are approximated by parabolas. The median interface between the two segmented lines is then calculated (depicted by the blue dashed line in panel (b) of Figure 4.12).

The reference mean cortical thickness (Ct.Th) of the subvolume is the ratio between the bone surface and the length of the median interface (Figure 4.11. The

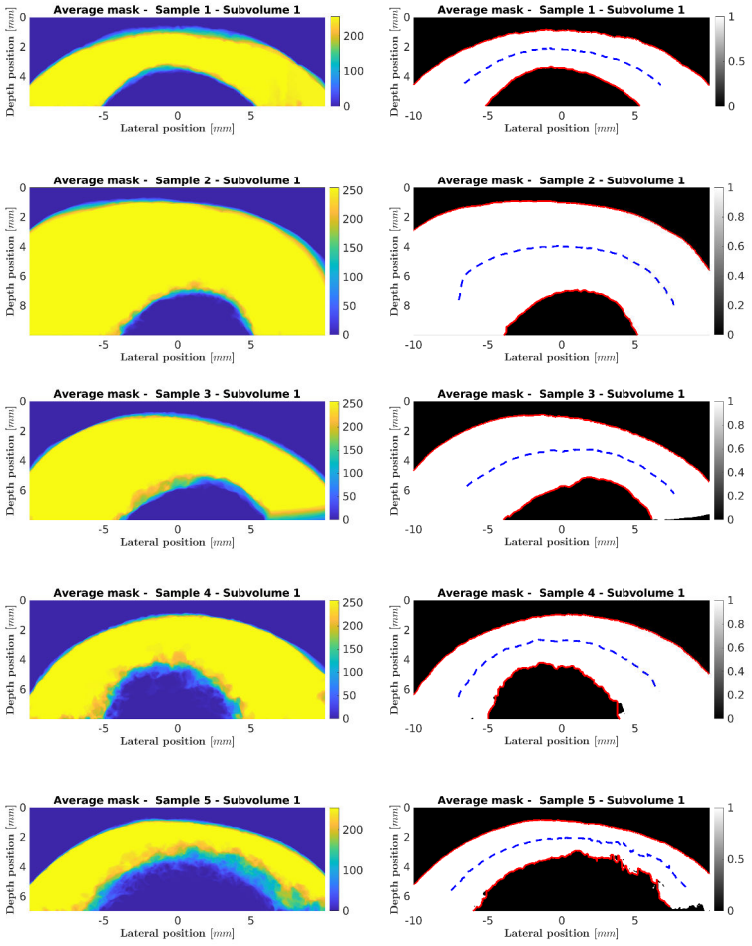

(a) (b)

Figure 4.12: Binarized average mask with interface delineation : the upper red line corresponds to the segmented periosteal interface, the lower red line corresponds to the segmented endosteal interface and the blue dashed-line is the median between the periosteum and the parabolic fit of the endosteum.

ground truth cortical thickness estimated from micro-CT images of all subvolumes are summarized in Table 4.3.

We estimate the cortical thickness in ultrasound image using the same procedure.

4.2.5 Alignment of ultrasound and X-ray images for comparative analysis

To facilitate a qualitative and visual comparison between ultrasound and X-ray images, we superimposed the X-ray images onto the ultrasound counterparts. Since the ultrasound images were not necessarily aligned with the X-ray images, a rotational adjustment was performed on the ultrasound images. This adjustment aimed

Subvolume	Estimated Cortical thickness (mm) from µ-CT images				
	Sample 1	Sample 2	Sample 3	Sample 4	Sample 5
Zone 1	2.69	6.29	4.36	3.86	2.23
Zone 2	2.89	6.29	4.50	3.82	2.25
Zone 3	2.69	6.29	4.65	3.97	2.41
Zone 4	2.54	6.29	4.67	3.62	2.25

Table 4.3: Estimated reference cortical thickness (Ct.Th) on each subvolume for all samples.

to achieve optimal alignment by aligning the raw segmented periosteal interfaces of the ultrasound images with the raw segmented periosteal interface from the X-ray reference image. To accomplish this, I determined the optimal rotation and translation matrices that minimize the least square errors [17] between the segmented periosteal interface from the X-ray images and the segmented periosteal interface from the ultrasound image. Subsequently, I applied this rotation and translation to the segmented periosteal interface from the ultrasound image.

4.3 Results & discussion

4.3.1 Descriptive statistics

4.3.2 Estimation of wave speed

wave speed results. The estimated wave speed of all samples are reported in Table 4.4. The results are summarized by the median and the range (MAX-MIN) of the wave speed across the ten repetitions.

Site	Sample 1	Sample 2	Sample 3	Sample 4	Sample 5
Zone 1	3299.1(188.5)	3335.2(213.5)	3207(218.9)	3160.3(224.8)	3021.7(151.8)
Zone 2	3230.7(144.3)	3372(197.0)	3159.4(127.4)	3236.6(596.4)	3198.8(173.8)
Zone 3	3249.9(203.4)	3373.9(233.4)	3141.6(193.9)	3196.6(396.6)	3099.2(195.8)
Zone 4	3344.9(235.9)	3280.1(185.0)	3208.3(151.2)	3330.2(558.9)	3218.1(167.4)
Average	3281.2	3340.3	3179.1	3230.9	3134.4

Table 4.4: A summary of the estimated wave speed (*median*(*range*)) in m/s using ultrasound for each measurement site of all samples over the repetitions. The average wave speed of the sample is provided in the last row.

Across all samples, there is variation in the estimated median wave speeds, ranging from approximately 3021.7 m/s to 3344.9 m/s. Sample 5 exhibits the lowest median wave speed, while sample 2 has the highest. Additionally, the range of wave speed values varies across samples, indicating differing degrees of variability in wave speed estimation. Overall, these results highlight the heterogeneity in wave speed within and across the studied bone samples. For sample 4, the range of wave speed values (224.8 m/s to 558.9 m/s) indicates significant fluctuations in wave speed estimates over the repetitions, highlighting the variability or complexity of this particular sample. This is further illustrated in Table 4.5, where the variations in wave speed estimation across repetitions for each measurement site of each

sample are presented. Relative Range (RR), calculated as the ratio of the range of variation over ten repetitions (*range*) to the median wave speed (*median*) expressed as a percentage, is used to quantify the variability. For all samples except sample

Site	Sample 1	Sample 2	Sample 3	Sample 4	Sample 5
Zone 1	5.7	6.4	6.8	7.1	5.0
Zone 2	4.5	5.8	4.0	18.4	5.4
Zone 3	6.3	6.9	6.2	12.4	6.3
Zone 4	7.1	5.6	4.7	16.8	5.2

Table 4.5: Relative range (RR in %) of estimated wave speed across repetitions.

4, the variation in wave speed is less than 10%. However, sample 4 exhibits high relative ranges (RR), ranging from 7.1% to 16.8%. This sample is the most heterogeneous, characterized by numerous large pores (refer to Table 4.2). Consequently, the autofocus method fails to provide an accurate estimate of the speed of sound in the cortex. Therefore, sample 4 will be excluded from further analysis. For the remaining samples, the maximum deviation from the median is 7.1%.

Note that these relative range variations are not comparable to the precision values reported in Chapter 2. In this current chapter, we conducted repositioning by slightly adjusting the lateral position of the probe without aiming to replicate the same measurement. The objective was to obtain multiple acquisitions and then select the one corresponding to the most optimal probe position.

Figure 4.13 presents the wave speed estimates for all measurement sites across all samples except sample 4. Error bars, defined by the interquartile range across repetitions, provide insight into the variability of the estimates.

Relationship between wave speed and porosity. Figure 4.14 illustrates the wave speed estimates for all measurement sites across all samples, plotted relative to sample porosity. Based on the measured wave speed, samples can be categorized into three porosity classes. Samples 1 and 2 exhibit high wave speed values ($>$ 3200 m/s) and can be considered as low porosity samples. Sample 3 is classified as a middle porosity sample, while sample 5 is categorized as a high porosity sample.

Additionally, the figure includes the radial wave speed derived in another study from Resonant Ultrasound Spectroscopy (RUS) [18] for comparison (depicted by black diamond points and a black line). RUS provides direct measurements of elastic coefficients and operates at frequencies around 100-600 kHz, whereas in this study, we operate at 2.5 MHz. Additionally, the cortical porosity during the RUS study was obtained using SR-microCT images with a voxel size of 6.5 µm. Despite these differences, we observe in Figure 4.14 that the dependency of wave speed with porosity observed in this study closely matches that observed during RUS measurements. The observed variation in wave speed ranges from approximately 3000 to 3400 m/s as cortical porosity decreases from 17 to 5%. This represents a variation in ultrasound wave speed of about 12.5%.

4.3.3 Ultrasound images

Comparative analysis of X-ray and ultrasound images. In Figure 4.15, only one representative ultrasound image for samples 1, 2, 3, and 5 are shown. We chose the image that has the best periosteal alignment with the X-ray image. For the images of each zone of each sample, please refer to Appendix G. The first row

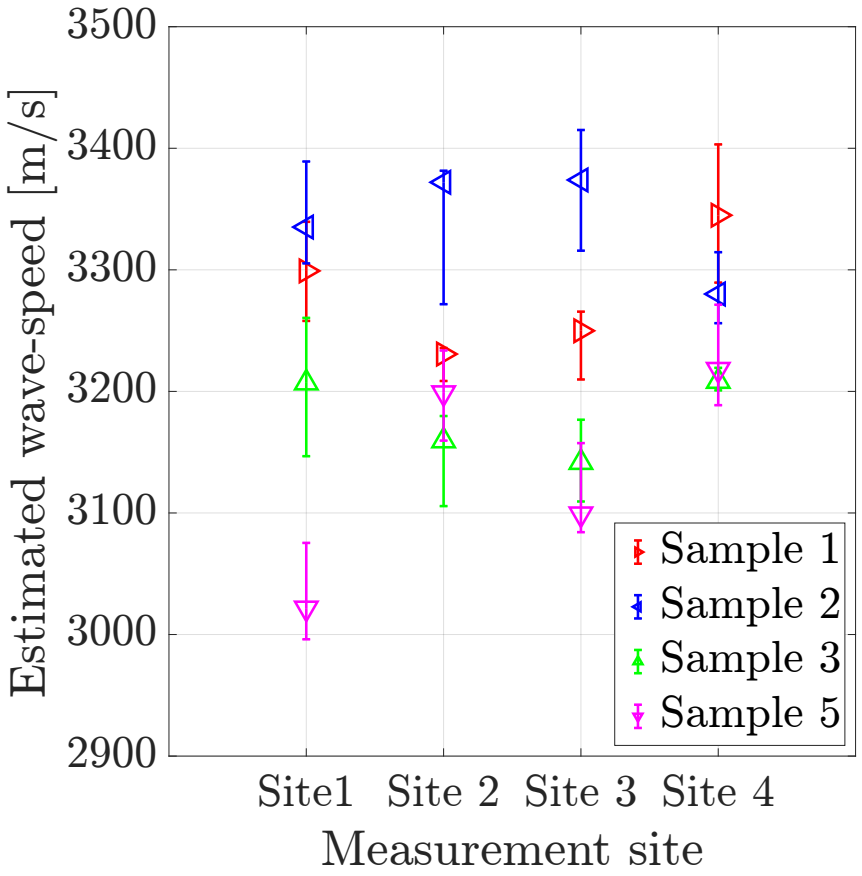

Figure 4.13: Wave speed estimates for all measurement sites across all samples except sample 4, with error bars representing the interquartile range over repetitions.

(panels (a), (d), (g) and (j)) displays the ground truth X-ray image, and the second row (panels (b), (e), (h), (k)) shows the ultrasound image. For each ultrasound image, the raw segmentation of the periosteal and endosteal interfaces of the cortex are displayed. In all ultrasound images, the detected periosteal interfaces are very bright. However, the brightness of the internal interface depends on the sample. The brightness of the endosteal interface of samples 1 and 2, which are low porosity samples, is higher than that of sample 3. For sample 5, which had the highest overall porosity, the brightness of the endosteal interface is very low. In the X-ray images (panels (a), (d), (g) and (j) of Figure 4.15), it can also be observed that samples 1 and 2 have a small number of large pores, while sample 3 has some large pores near the endosteal interface. Sample 5 is thinner than other samples and has a greater number of large pores near the endosteal interface. It is noteworthy that, despite the large thickness and complex geometry of sample 2, the endosteal interface is correctly visualized with high brightness in the ultrasound image. The last column is the superimposition of ultrasound and site-matched X-ray images. The images were combined using Inkscape software (Inkscape project, Inkscape version 0.92.5 [1]).

Impact of Sample Heterogeneity. Samples 1 and 2 (panel (c) and (f)) are homogeneous and exhibit a close match in bone geometry, with ultrasound images closely resembling high-resolution micro-CT images. This close resemblance ensures accurate cortical thickness estimation. For sample 3 (panel (i)), both the shape and position of the periosteal surface are correctly estimated in the ultrasound image.

[1] https://www.inkscape.org

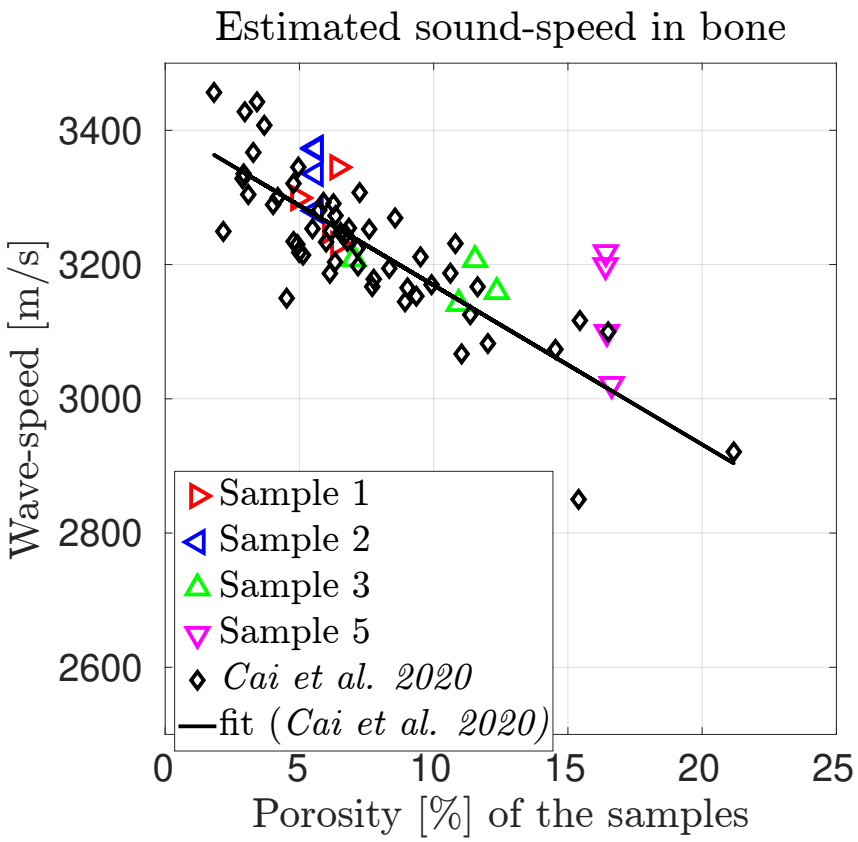

Figure 4.14: Wave speed estimates for all measurement sites across all samples, plotted relative to sample porosity. The plot includes the radial wave speed derived from Resonant Ultrasound Spectroscopy (RUS) [18] for comparison.

However, the endosteal surface is not correctly positioned, likely due to the sample's composition, which includes a dense part followed by a very porous part (panel (g)). Sample 5 (panel (l)) demonstrates a discrepancy in estimating the shape of the second interface, attributed to inaccurate wave speed estimation due to sample heterogeneity and difficulties in segmenting the interface caused by the presence of large pores. It is worth noting that the complex geometry and large thickness of sample 2 are correctly estimated, while the simple geometry and small thickness of sample 5 are not accurately estimated. This discrepancy is likely due to the homogeneity of sample 2.

Precision of periosteal surface segmentation. In the ultrasound image, the estimation of cortical thickness relies mostly on accurately estimating the wave speed and precisely segmenting the endosteal interface. In fact, the periosteal interface is correctly segmented in comparison to the reference x-ray segmentation. Table 4.6 provides details on the error of the segmented periosteum curve using ultrasound images compared to the reference segmented curve obtained with micro-CT images. It presents the minimum and maximum Root Mean Square Error (RMSE) over the ten repetitions. Across all samples, the error is smaller than 0.3 mm, corresponding to half a wavelength in water at 2.5 MHz (600 µm). Some ultrasound images achieve errors smaller than 100 µm.

4.3.4 Estimation of cortical thickness

In Figure 4.16, the measured cortical thickness using ultrasound at each measurement site for samples 1, 2, 3, and 5 is reported, with the corresponding cortical

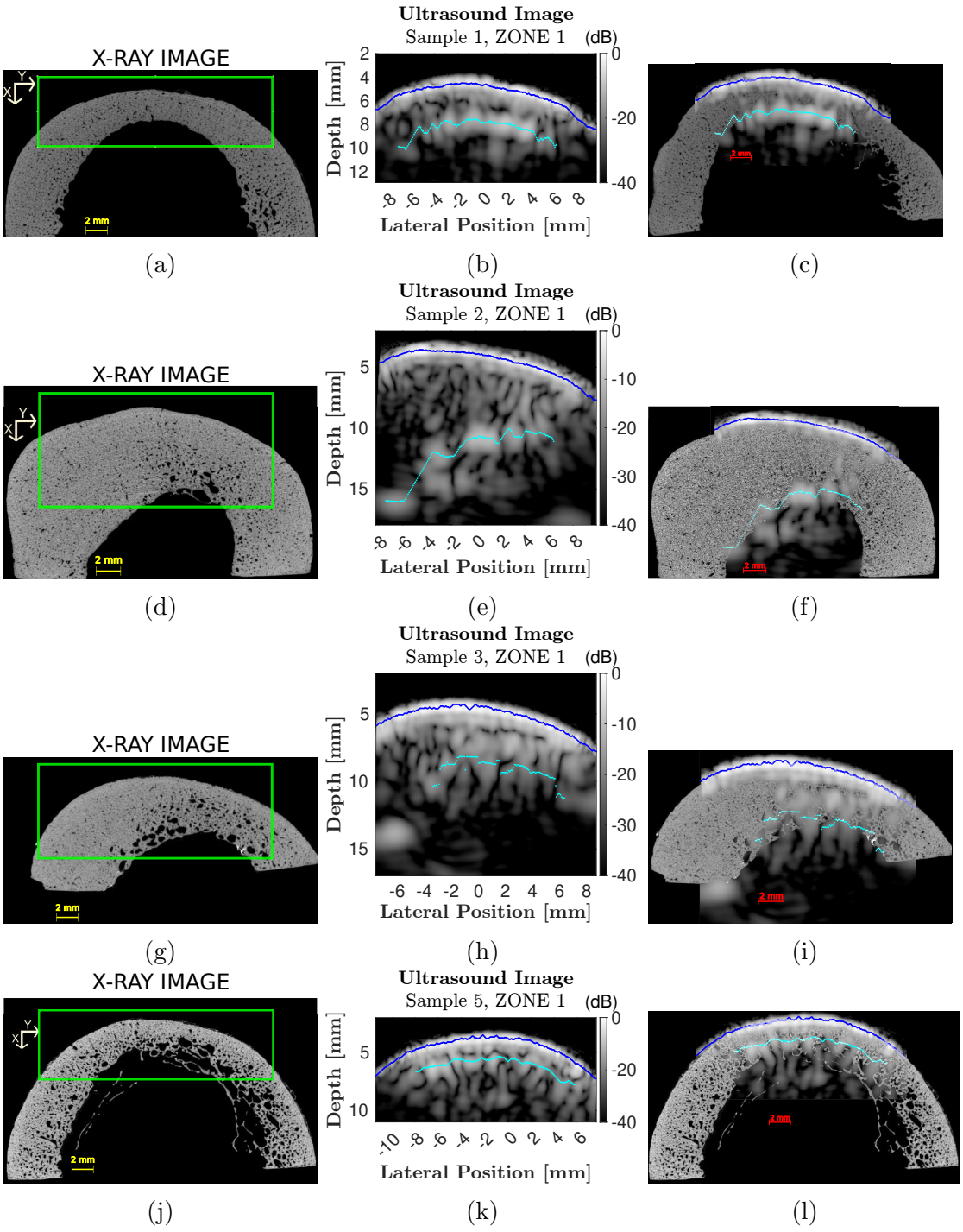

Figure 4.15: Comparison of X-ray and ultrasound images for representative samples. The first column displays X-ray images showing ground truth, the second column shows ultrasound images displaying raw segmentation of periosteal and endosteal interfaces, and the last column presents the superimposition of ultrasound and X-ray images. Brightness of interfaces varies with sample porosity.

thickness in the X-ray images (considered as ground truth). For sample 1 (indicated by the red right-pointing arrow), the estimated cortical thickness with ultrasound closely aligns with those measured by X-ray. Sample 2 (indicated by the blue left-pointing arrow) exhibits the greatest thickness, with the estimated cortical thickness around 6 mm, slightly exceeding the ground truth values. However, for sample 3 (indicated by the green up-pointing arrow), ultrasound tends to underestimate the cortical thickness, with values between 0.8 and 1.5 mm below the cortical thick-

	RMSE [MIN MAX] (mm)			
Measurement Sites	Sample 1	Sample 2	Sample 3	Sample 5
ZONE 1	[0.10 0.17]	[0.07 0.14]	[0.07 0.25]	[0.14 0.24]
ZONE 2	[0.16 0.26]	[0.12 0.19]	[0.10 0.19]	[0.19 0.28]
ZONE 3	[0.09 0.24]	[0.07 0.14]	[0.07 0.18]	[0.14 0.31]
ZONE 4	[0.18 0.24]	[0.12 0.19]	[0.07 0.25]	[0.05 0.17]

Table 4.6: Error analysis of periosteum segmentation in ultrasound imaging relative to X-ray images across various measurement sites and samples. The table displays the minimum and maximum Root Mean Square Error (RMSE) values, denoted as [MIN MAX], for each zone and sample.

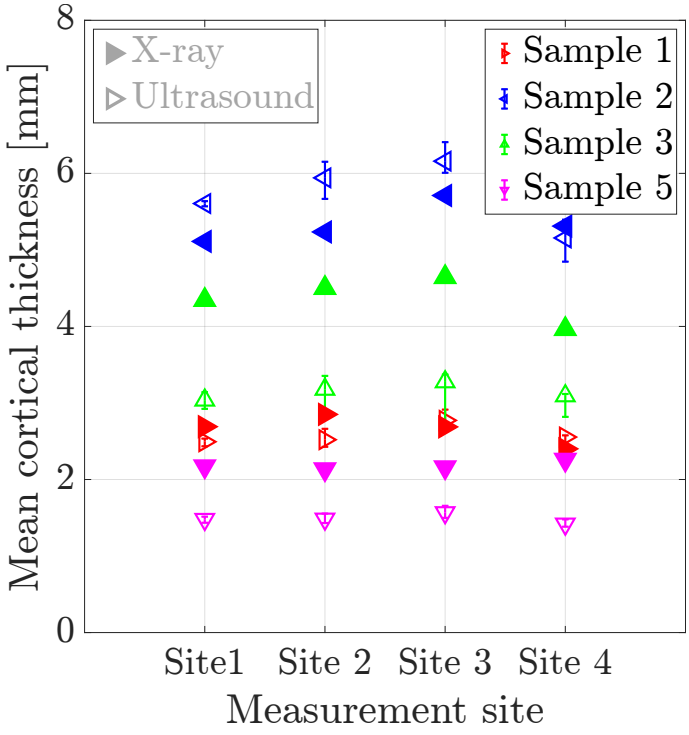

Figure 4.16: Estimated cortical thickness using ultrasound imaging (empty symbols) for each sample and each measurement site compared to reference cortical thickness estimated from X-ray images (filled symbols).

ness estimated in x-ray images. A similar, albeit less pronounced, underestimation is observed for sample 5 (indicated by the magenta down-pointing arrow). This discrepancy could be attributed to the presence of numerous large pores near the endosteal surface in samples 3 and 5, leading to non-uniform true wave speed distributions potentially rendering the endosteal surface unreachable. The combined factors of small thickness (less than 2 mm) and high heterogeneity in sample 5 could also contribute to the underestimation of the wave speed.

Results of cortical thickness estimation (Figure 4.16) suggest that ultrasound underestimates the cortical thickness determined in X-ray images of samples 3 and 5. However, it is essential to consider that when the endosteal surface becomes trabecularized, the estimated cortical thickness in the X-ray image may no longer be reliable. This is because obtaining a unique segmentation of the endosteal interface becomes challenging.

4.4 Summary & conclusion

This study represents the first attempt to estimate cortical thickness and radial wave speed on *ex vivo* human samples using ultrasound imaging. Ultrasound acquisitions were repeated 10 times with probe repositioning to search for the optimal probe alignment. An autofocus algorithm maximizing sharpness and intensity metrics was used to estimate radial wave speed. For a highly heterogeneous sample, the radial wave speed could not be properly estimated over the repetitions. The reconstructed images were used to segment external and internal surfaces of the cortex, from which an estimation of cortical thickness was provided. Estimated radial wave speed were compared to porosity and literature and cortical thickness were compared to values obtained with high-resolution x-ray images. The estimation of the periosteal surface was precise.

We performed ultrasound imaging of *ex vivo* human femurs that we compared to x-ray micro-CT images with a voxel size of 8.8 µm. The accuracy of bone geometry estimation was, for the first time, examined through the superimposition of ultrasound and X-ray images for various bone samples. The results suggest that ultrasound imaging of the human cortical can be used to successfully estimate the cortical thickness and the propagating wave speed of homogeneous bone cortex at a central frequency of 2.5 MHz. However, challenges arise for highly heterogeneous samples, where both wave speed estimation and segmentation become difficult. To address such cases, the utilization of a wave speed model that can describe a spatial gradient in wave speed from the periosteum to the endosteum and exploration of more bone geometry adapted reconstruction techniques are needed.

In the next chapter we will present a beamforming algorithm that enhances the visibility of specular interfaces.

Bibliography

[1] Huong Nguyen Minh, Marie Muller, and Kay Raum. Estimation of Thickness and Speed of Sound for Transverse Cortical Bone Imaging Using Phase Aberration Correction Methods: An In Silico and Ex Vivo Validation Study. *Applied Sciences*, 12(10):5283, January 2022. Number: 10 Publisher: Multidisciplinary Digital Publishing Institute.

[2] Johannes Schneider, Gianluca Iori, Donatien Ramiandrisoa, Maroua Hammami, Melanie Gräsel, Christine Chappard, Reinhard Barkmann, Pascal Laugier, Quentin Grimal, Jean-Gabriel Minonzio, and Kay Raum. Ex vivo cortical porosity and thickness predictions at the tibia using full-spectrum ultrasonic guided-wave analysis. *Archives of Osteoporosis*, 14(1):21, February 2019.

[3] David Mitton, Jean-Gabriel Minonzio, Maryline Talmant, Rafaa Ellouz, Frédéric Rongieras, Pascal Laugier, and Karine Bruyère-Garnier. Non-destructive assessment of human ribs mechanical properties using quantitative ultrasound. *Journal of Biomechanics*, 47(6):1548–1553, April 2014.

[4] Quentin Vallet, Nicolas Bochud, Christine Chappard, Pascal Laugier, and Jean-Gabriel Minonzio. In Vivo Characterization of Cortical Bone Using Guided Waves Measured by Axial Transmission. *IEEE Transactions on Ultrasonics, Ferroelectrics, and Frequency Control*, 63(9):1361–1371, September 2016. Conference Name: IEEE Transactions on Ultrasonics, Ferroelectrics, and Frequency Control.

[5] N. Bochud, Q. Vallet, Y. Bala, H. Follet, J.-G. Minonzio, and P. Laugier. Genetic algorithms-based inversion of multimode guided waves for cortical bone characterization. *Physics in Medicine & Biology*, 61(19):6953, September 2016. Publisher: IOP Publishing.

[6] Huong Nguyen Minh, Juan Du, and Kay Raum. Estimation of Thickness and Speed of Sound in Cortical Bone Using Multifocus Pulse-Echo Ultrasound. *IEEE transactions on ultrasonics, ferroelectrics, and frequency control*, 67(3):568–579, 2020.

[7] Guillaume Renaud, Pieter Kruizinga, Didier Cassereau, and Pascal Laugier. In vivo ultrasound imaging of the bone cortex. *Physics in Medicine & Biology*, 63(12):125010, June 2018. Publisher: IOP Publishing.

[8] Mathilde Granke, Quentin Grimal, Amena Saïed, Pierre Nauleau, Françoise Peyrin, and Pascal Laugier. Change in porosity is the major determinant of the variation of cortical bone elasticity at the millimeter scale in aged women. *Bone*, 49(5):1020–1026, November 2011.

[9] Detail - Morphisto, September 2019.

[10] M. Karaman, Pai-Chi Li, and M. O'Donnell. Synthetic aperture imaging for small scale systems. *IEEE Transactions on Ultrasonics, Ferroelectrics, and Frequency Control*, 42(3):429–442, May 1995. Conference Name: IEEE Transactions on Ultrasonics, Ferroelectrics, and Frequency Control.

[11] Jørgen Arendt Jensen, Svetoslav Ivanov Nikolov, Kim Løkke Gammelmark, and Morten Høgholm Pedersen. Synthetic aperture ultrasound imaging. *Ultrasonics*, 44:e5–e15, December 2006.

[12] Guillaume Renaud, Pierre Clouzet, Didier Cassereau, and Maryline Talmant. Measuring anisotropy of elastic wave velocity with ultrasound imaging and an autofocus method: application to cortical bone. *Physics in Medicine & Biology*, 65(23):235016, November 2020.

[13] Allan D. Pierce. The Wave Theory of Sound. In Allan D. Pierce, editor, *Acoustics: An Introduction to Its Physical Principles and Applications*, pages 1–60. Springer International Publishing, Cham, 2019.

[14] Bradley E. Treeby, Trond K. Varslot, Edward Z. Zhang, Jan G. Laufer, and Paul C. Beard. Automatic sound speed selection in photoacoustic image reconstruction using an autofocus approach. *Journal of Biomedical Optics*, 16(9):090501, September 2011. Publisher: SPIE.

[15] Amadou Sall Dia, Guillaume Renaud, Aida Hejazi Nooghabi, and Quentin Grimal. The influence of intra-cortical microstructure on the contrast in ultrasound images of the cortex of long bones: A 2D simulation study. *Ultrasonics*, 127:106831, January 2023.

[16] Vincent Perrot, Maxime Polichetti, François Varray, and Damien Garcia. So you think you can DAS? A viewpoint on delay-and-sum beamforming. *Ultrasonics*, 111:106309, March 2021.

[17] K. S. Arun, T. S. Huang, and S. D. Blostein. Least-Squares Fitting of Two 3-D Point Sets. *IEEE Transactions on Pattern Analysis and Machine Intelligence*, PAMI-9(5):698–700, September 1987. Conference Name: IEEE Transactions on Pattern Analysis and Machine Intelligence.

[18] Xiran Cai, Laura Peralta, Renald Brenner, Gianluca Iori, Didier Cassereau, Kay Raum, Pascal Laugier, and Quentin Grimal. Anisotropic elastic properties of human cortical bone tissue inferred from inverse homogenization and resonant ultrasound spectroscopy. *Materialia*, 11:100730, June 2020.

Chapter 5

Beamforming to enhance specular reflection from bone surfaces

Contents

5.1 Introduction

In medical ultrasound imaging, DELAY-AND-SUM (DAS) [1] is the most widely used beamformer for image reconstruction. Beamformers based on DAS assume a homogeneous medium composed only of point scatterers (small compared to the wavelength). For a diffusive point scatterer, the signal is backscattered uniformly in all directions. Therefore, maximum backscattered amplitude is recorded by the nearest element of the transducer array, because of diffraction loss (see Figure 5.1a). In a typically DAS implementation, the receive sub-aperture is chosen according to element directivity: it is independent of data.

DAS beamforming can yield good image quality for a nearly planar specular interface (much wider than wavelength) and nearly parallel to the surface of the ultrasound probe. However, when the interface is not parallel to the probe surface, maximum backscattered amplitude is not recorded by the nearest element of the probe array. The tilting angle of the interface determines the main direction of the reflected wavefront (Snell-Descartes' law). (see Figure 5.1b).

At 2.5 MHz (frequency previously used for *in vivo* measurements [2, 3]), there exists both specular and diffuse reflection of ultrasound inside cortical bone. In fact, on the external (periosteal) and internal (endosteal) surfaces of the cortex, the large impedance ratio between soft tissue and cortical bone tissue leads to specular reflection and cortical pores act as scatterers smaller than the wavelength. Therefore we expect a significant effect of specular reflection in bone ultrasound images.

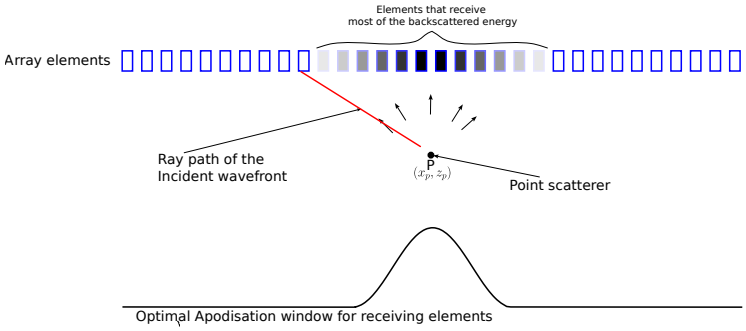

(a) Diffuse scatterer.

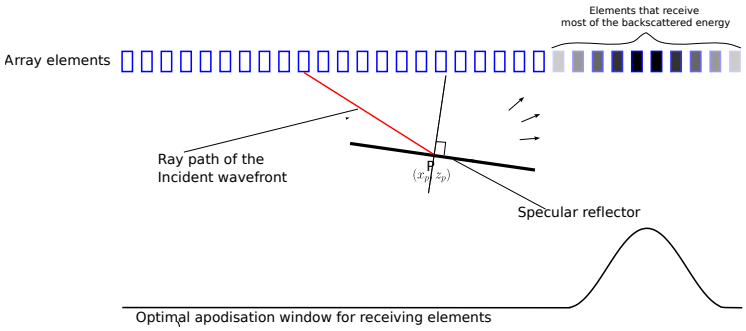

(b) Specular scatterer.

Figure 5.1: Illustration of the optimal receive sub-aperture for the reconstruction of pixel P. In (a) maximum backscattered amplitude is recorded by the nearest element of the transducer array. In (a) most of the back-scattered energy is concentrated to receivers around the lateral position of the scatterer. In (b), maximum backscattered amplitude is not recorded by the nearest element of the probe array.

As discussed in previous chapters, achieving a high-quality image of the cortex is crucial for clear visualization of the periosteal and endosteal surfaces. Specifically, Chapter 3 highlighted that during DAS beamforming, diffuse signals from the microstructure create speckle that may obscure the specular signal from the endosteal surface of the bone. An adaptive reconstruction technique could enhance signals from both the external and internal surfaces of cortical bone. We hypothesize that an optimal image reconstruction of bone cortex interfaces could be obtained with an adaptive receive sub-aperture determined based on the properties of specular reflection.

In this chapter, we present the principle of a beamforming algorithm tailored to the physics of specular reflection and refraction, with the specific goal of improving the visibility of the external and internal interfaces of the bone cortex, for instance to measure the cortical thickness.

In recent years, various approaches have been proposed for extracting specular information in medical ultrasound imaging. In 2008, *Vogt et al* [4] suggested using a single element transducer and exploiting the laws and properties of specular reflections, to reconstruct parametric images. Ultrasound data are acquired from different angular tilt and lateral positions of the transducer. The parametric images contain first-order statistics such as mean, standard deviation, maximum, and minimum of the envelope of received echo signals across all emission-reception events of specular reflections. By analyzing the parametric images, specular reflection could be effectively differentiated from diffuse scattering. Similarly, *Bandaru et al* [5] proposed using an array transducer to enhance reflections from specular interfaces. Instead of using the average, as in DAS methods, they took the standard deviation of received backscattered signals across the receive aperture. The orientation of the

specular interface was estimated based on the peak echo amplitude. This method was developed for conventional focusing in transmit.

In a preliminary study, *Nagaoka et al* [6] suggested the use of a data-independent apodization weight to highlight both diffuse scattering from small heterogeneities and specular reflection from flat interfaces.

Rodriguez-Molares et al [7] proposed a physical model-based technique of emphasizing specular reflection for needle tracking using a synthetic aperture sequence. Their technique, based on the source-image principle, involves developing a specular reflection model. They compared this model with the coherent compounding of received signals that follow Snell's law to obtain a matched filter maximizing the signal-to-noise ratio (SNR) of signals reflected by planar interfaces. This technique suppresses speckle and enhances the visualization of specular interfaces, such as an inserted needle.

More recently, *Malamal et al* [8] proposed an innovative approach involving the radon transform and plane wave imaging to identify the receiver index that maximizes the back-scattered energy from a specular interface. Then, a receive apodization window, centered around this optimized receiver index, is selected during Delay-and-Sum (DAS) beamforming. The same group [9] proposed to provide a real-time visual feedback mechanism for operators. They introduced a color-coded image containing a vectorized estimation of the reflection directivity within a defined region of interest. This allows the operator to reorient the probe or adjust the transmission sequence to align parallel to the surface of the reflector. Employing a plane wave imaging sequence, they applied this method to synthetic and experimental data for needle tracking and external bone surface imaging, effectively distinguishing fractured and smoothed regions of the periosteal surface of a bone. However, like conventional DAS algorithms, all these methods assume a homogeneous medium and a straight ray-path propagation hypothesis.

In this chapter, we implement specular beamforming according to [7] adapted to bone imaging. To emphasize the reflection of the external and internal surfaces of the bone, we propose to consider the physics of reflection and refraction.

The rest of the chapter is organized as follows. In section 5.2 we will explain the specular reflection principle for a flat interface in a homogeneous medium. In the next section 5.3, we will explain the principle of the method developed during the thesis for a multilayer medium with curved interfaces. Section 5.4 is the application of the developed method to synthetic ultrasound data and in section 5.5 we discuss the method and conclude. The method is used to process experimental data in Chapter 6.

5.2 Specular beamforming for homogeneous media

In this section we describe the principle of specular beamforming and the physics behind this principle as it is described by Rodriguez-Molares et al. [7].

5.2.1 Geometrical considerations

We will assume in the rest of the chapter that we are using a single element transmission technique with iT designating the index of the transmitting element and iR the index of the receiving element. The signals recorded by the elements are stored in the 3D-matrix $\mathbf{S}$. The dimensions of this matrix are $[N \times N_R \times N_T]$ where N is

the number of time samples, N_R is the number of receiving elements and N_T is the number of transmissions.

Let us consider a medium to be imaged containing a θ-oriented plane reflector passing through the pixel $P \equiv (x_P, z_P)$. The equation of this reflector is given by:

$$(D_s) : z = -\tan(\theta)(x - x_P) + z_P \tag{5.1}$$

An ultrasound probe is placed on the surface of the medium (at depth z=0). Suppose an ultrasound ray (T) originating from element $iT \equiv (x_t, z_t)$ of the probe, incident on point P of the interface and (R) is the reflected ray from P to receiving element $iR \equiv (x_r, z_r)$. According to the law of specular reflection, the reflected ray corresponding to a specular reflection (R_s) is symmetric to the incident ray iT from the normal interface. We note α_s the angle between the incident ray and the normal to the specular interface passing through P. Therefore, the angle between (R_s) and the normal of the specular interface is $-\alpha_s$ (see Panel 5.2b).

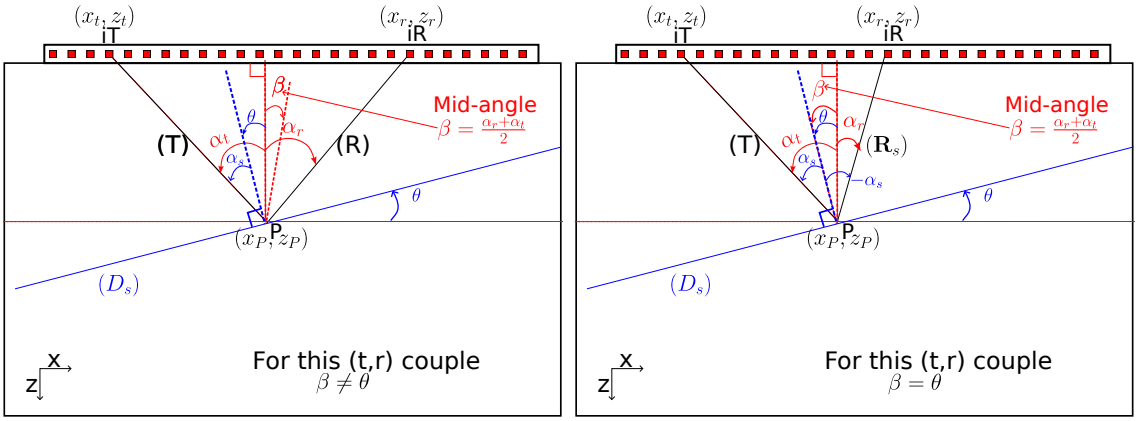

(a) (b)

Figure 5.2: Geometric illustration of specular reflection in a homogeneous medium with a θ-tilted reflector. The ultrasound ray from iT (T) hits the reflector at P. Element iR is recording all backscattered signals from the medium. In panel (a) elements iT and iR are chosen to satisfy laws of specular reflection. In panel (b) chosen receiving element iR does not satisfy specular reflection.

We define α_t as the angle between the incident ray (T) and the normal of the probe and α_r the angle between the reflected ultrasound ray travelling from point P to element iR (R) and the normal of the probe. If we choose (iT, iR) satisfying physical laws of specular reflection as in Figure 5.2b, we can write:

$$\begin{aligned} \alpha_s &= \alpha_t - \theta \\ -\alpha_s &= \alpha_r - \theta, \end{aligned} \tag{5.2}$$

yielding

$$\alpha_r + \alpha_t - 2\theta = 0. \tag{5.3}$$

Angular values α_r and α_t can be obtained from positions of iT, iR, and P using following trigonometric relationships (Figure 5.2):

$$\begin{aligned} &(iR, iT) \hookrightarrow (\alpha_r, \alpha_t) \\ &\alpha_r(P) = \arctan\left(\frac{x_P - x_r}{z_P - z_r}\right) \quad ; \quad \alpha_t(P) = \arctan\left(\frac{x_P - x_t}{z_P - z_t}\right) \end{aligned} \tag{5.4}$$

For the rest of the chapter, the dependency of α_t and α_r to P is omitted but the reader must bear in mind that α_r and α_t depend on the pixel as given in equation (5.4).
Let us identify β as the transmit-receive mid-angle ($\beta = \frac{\alpha_r+\alpha_t}{2}$). Then, equation (5.3) is equivalent to:

$$\beta - \theta = 0. \tag{5.5}$$

This means that when the transmit-receive mid-angle at point P equals the specular orientation θ of the object passing through P, the received back-scattered energy maximizes the specular energy reflected by the object. Therefore, we see as expected that the choice of the transmit-receiver pair that maximizes the back-scattered energy of a specular reflector depends on the specular orientation. If the pair (iT, iR) does not satisfy the equation (5.5), then the transmit-receive mid-angle is different from θ (depicted in Figure 5.2a).

The above relationship creates a signature specific to specular reflections. Rodriguez-Molares et al.[7] illustrated this signature with theoretical developments using the above equations and the image source principle. Following their work, in the next section, we will illustrate this signature in a set of simulations made with the MUST toolbox [10].

5.2.2 The specular signature

We simulated a linear array of 128 elements with a spacing of 300 µm. A synthetic transmit aperture sequence (SA) [11, 12] is simulated as acquisition scheme: each of the 128 elements of the probe emits a Gaussian-windowed tone burst with a central frequency of 2.5 MHz and all the elements of the probe record the back-scattered signals. This gives 128×128 back-scattered RF signals. We used 4 different configurations for the simulations. In all configurations, a fluid medium is considered with speed of sound $V_0 = 1540$ m/s.

- In the first configuration, we simulated a single diffuse point scatterer at position (0,20) mm in a homogeneous medium to illustrate diffuse reflection (Figure 5.3a).
- In the second configuration, we generated a pseudo random distribution of scatterers such that the mean distance between a scatterer and its nearest neighbor is approximately half of the wavelength at 2.5 MHz (300 µm). This configuration simulates speckle noise (Figure 5.3b).
- In the third configuration, a plane reflector tilted by $\theta = 10°$ passes through the pixel at coordinates (0,20) mm (Figure 5.3c).
- In the last configuration (see panel 5.3d), we generated a pseudo random distribution of scatterers as in the second configuration and added a plane reflector tilted by $\theta = 10°$ passing through the pixel at coordinates (0,20) mm (as in the third configuration).

Specular signature of specular objects. The delay corresponding to a wavefront emitted by the element iT of the probe to the scatterer P of coordinates (x_P, z_P) recorded by the probe at element iR is given by:

$$\tau_{iT,iR}(P) = \frac{1}{V_0}\left(\sqrt{(x_P - x_t)^2 + (z_P - z_t)^2} + \sqrt{(x_P - x_r)^2 + (z_P - z_r)^2}\right), \tag{5.6}$$

the first square root term of the equation is the incident travel time and the second term is the reflection travel time. $\tau_{iT,iR}(P)$ is called in the literature the two-way travel time.

Recorded signals from each focal point of the medium (corresponding to a pixel in the reconstructed image) can be written as a matrix S of RF signals consisting of 128 rows and 128 columns where each element of the matrix represents the back-scattered signal from pixel P recorded by element iR of the probe when the element iT is emitting $S(\tau_{iT,iR}(P), iR, iT)$. In Figure 5.3, we show the matrix of delayed signals for a focal point at (0,20) mm for each configuration.

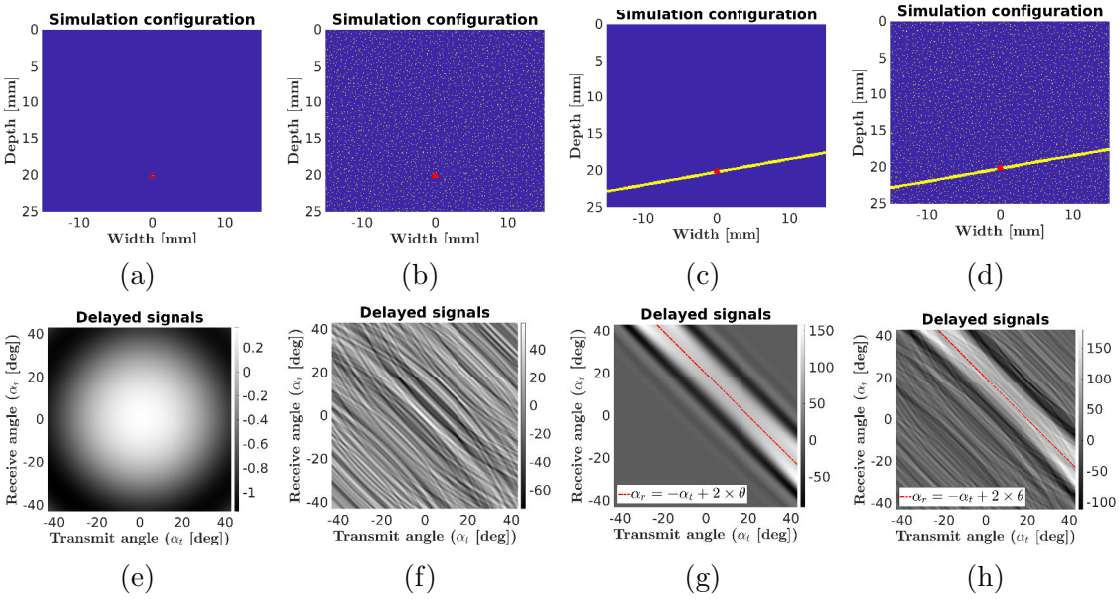

Figure 5.3: Illustration of received signal from a pixel located at depth (0,20)mm (red triangle in the top row images) for all different configuration. The top row images (panels (a), (b), (c) and (d)) are the simulation configuration and the bottom row images (panels (e), (f), (g) and (h)) are the corresponding delayed received signals with respect to receive and transmit angle. Panel (a): an homogeneous medium containing a single point-scatterer located at (0,20) mm. Panel (b): a medium where numerous point scatterers are randomly distributed such that the mean distance between two scatterers is 300 µm. Panel (c): a homogeneous medium containing a specular interface with orientation $\theta = 10°$ passing through $(0, 20)$ mm. Panel (d): a homogeneous medium containing numerous point scatterers as in (b) and a specular interface as in (c). The red lines in panels (g) and (h) are the plot of the specular reflection equation 5.3 for $\theta = 10°$.

For the first configuration (panel (a) of Figure 5.3), we see that the corresponding delayed signals (panel (e)) are uniformly distributed across all couples of elements. The radial decay of the signal's intensity from the center of the matrix ($\alpha_r = 0, \alpha_t = 0$) is due to the directivity of the simulated receiving elements and the diffraction loss of the propagation of a spherical wave as expected.

In the second configuration (panel (b) of Figure 5.3), the map of delayed signals at the focal point shows some randomness. This is principally due to the scattering of randomly located scatterers. This is what we refer as speckle noise.

We can see in the two last configurations that the corresponding received signals (panels 5.3g and 5.3h) present strong amplitude and similarity for couples satisfying equation (5.3) (e.g. in the direction $\alpha_r = -\alpha_t + 2 \times \theta$ corresponding to the red line in the panels). This is what we refer as specular signature. Specular beamforming consists of extracting this specular information out of speckle noise.

The results obtained in this simulation are the same as those of [7].

The specular transform. When performing DAS beamforming, an estimation of the reflectivity of pixel P is given by averaging delayed received signals. Classically, to mitigate off-axis signals and account for element directivity, an apodization window is chosen by setting a fixed transmit and receive f-number. Fixing the f-number is, in principle, equivalent to fixing the angular receive and transmit aperture [1]. The relationship between f-number ($f_\#$) and angular aperture Δ_α is given by:

$$f_\# = \frac{1}{2\tan\left(\frac{\Delta_\alpha}{2}\right)}. \tag{5.7}$$

For illustration, we choose here a receive and transmit f-number of 1 which corresponds to a fix receive aperture of $\pm 22°$. Therefore, the pixel value in a DAS image with these parameters is the average of delayed signals inside a square box centered around 0° and of width $\Delta_\alpha = 44°$. A diffuse point scatterer isotropically reflects the incident energy. We can see in Figure 5.4, where a blue box represents the averaging region, that most of the back-scattered energy is concentrated inside the blue box. Hence, the average of signals inside the box is a good estimate of the point reflectivity.

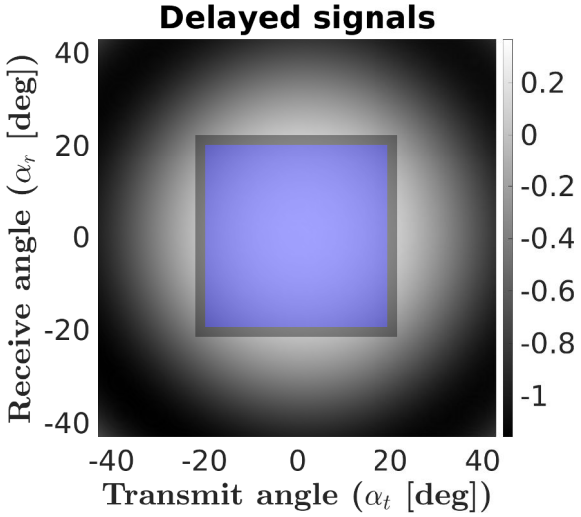

Figure 5.4: Delayed received signals from a diffuse point scatterer. The blue box centered around ($\alpha_t = \alpha_r = 0$) is the region of interest that DAS beamforming uses to average the signal to estimate the reflectivity of the pixel. This box represents a f-number of 1

For the case of a specular reflector, the back-scattered energy is no longer concentrated around the lateral position of the pixel, therefore the energy is not confined around a receive and transmit angle of 0°. Depending on the orientation of the specular interface, the box will only include part of the back-scattered energy along with destructive interferences. We illustrate this in Figure 5.5 for a specular object with different orientations θ: 0, 10 and 20 °. For the interface parallel to the probe surface (see panel 5.5a), the averaging region includes an important part of the specular reflection but also an important part of speckle noise. Although we are adding both constructive and destructive interference, averaging inside the blue box gives a good estimate of the specular reflection due to the fact that specular signal is much stronger than speckle noise. Hence, a DAS image gives good estimate of flat interfaces. However, with increasing absolute specular orientation, the part of

specular reflection will decrease (see panels 5.5b and 5.5c) and speckle contribution will increase. If the orientation of the specular object is greater than the maximum mid-angle of the transmit-receive aperture (blue box), then DAS will not detect the specular reflection. Therefore, DAS will fail to give a fair estimate of the reflectivity of pixel belonging to specular tilted objects.

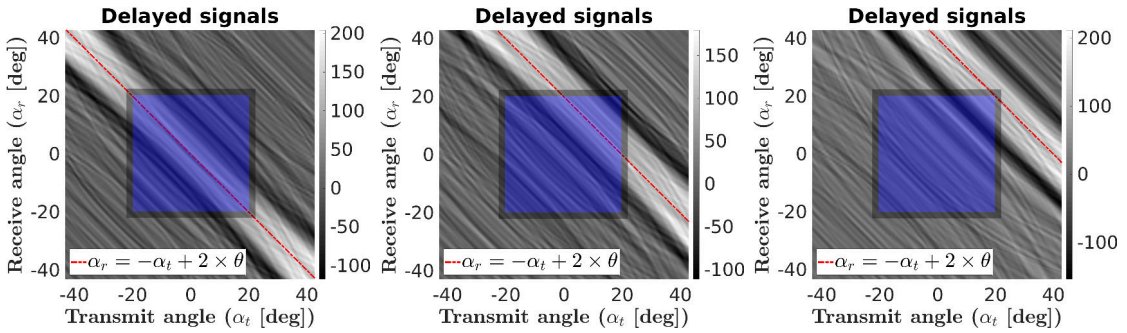

(a) (b) (c)

Figure 5.5: Delayed received signals from a point lying on a specular interface with different orientations. Panel (a): $\theta = 0°$, panel (b): $\theta = 10°$, and panel (c): $\theta = 20°$. The blue box centered around $(\alpha_t = 0, \alpha_r = 0)$ is the region of interest that DAS beamforming uses to average the signal to estimate the reflectivity of the pixel. This box represents a f-number of 1.

To overcome this poor estimation of tilted specular reflector, Rodriguez-Molares et al [7] proposed to transform the matrix of delayed signals into a so-called specular domain. The principle arises from Equation (5.5) which says that all transmitter-receiver pairs that share the same mid-angle β will maximize the back-scattered energy from a specular interface of orientation β. Therefore, signals of transceiver pairs associated with a common mid-angle (β) are summed to give a single signal. This means summing along each anti-diagonal of the matrix of delayed signals. Doing so, specular reflections add up constructively and diffuse scattering interferes randomly. The specular transform is a 1D signal that represents the contribution of all specular orientation:

$$f(\beta; P) = \sum_{iT=1}^{N_T} \mathbf{S}(\tau_{iT,iR}(P), \alpha_r, \alpha_t)|_{\frac{\alpha_r+\alpha_t}{2}=\beta} \tag{5.8}$$

This way of summing signals of transmit-receiver pairs that correspond to the same transmit-receive mid-angle has been used previously in compute ultrasound tomography in echo mode using Common Mid-Angle appellation by [13] to accurately predict the distribution of the phase of the received signals and provide an estimate of the speed-of-sound map of the medium.

Note that in this notation and in the rest of the chapter, we changed variables of $\mathbf{S}$ from (τ, iR, iT) to $(\tau, \alpha_r, \alpha_t)$.

Figure 5.6 shows the specular transform of received signals in configurations of panels 5.3b and 5.3d.

In a purely diffuse scattering regime, the specular transform presents randomness (see panel 5.6c). In the presence of a θ-oriented interface, the specular transform is maximum when the mid-angle $\beta = \theta$ and has a specific shape (see panel 5.6i and 5.6f). The red line in panels 5.6e and 5.6h corresponds to equation (5.3) and the red line in panels 5.6f and 5.6i corresponds to equation (5.5) where the orientation of the specular object θ equals 10°.

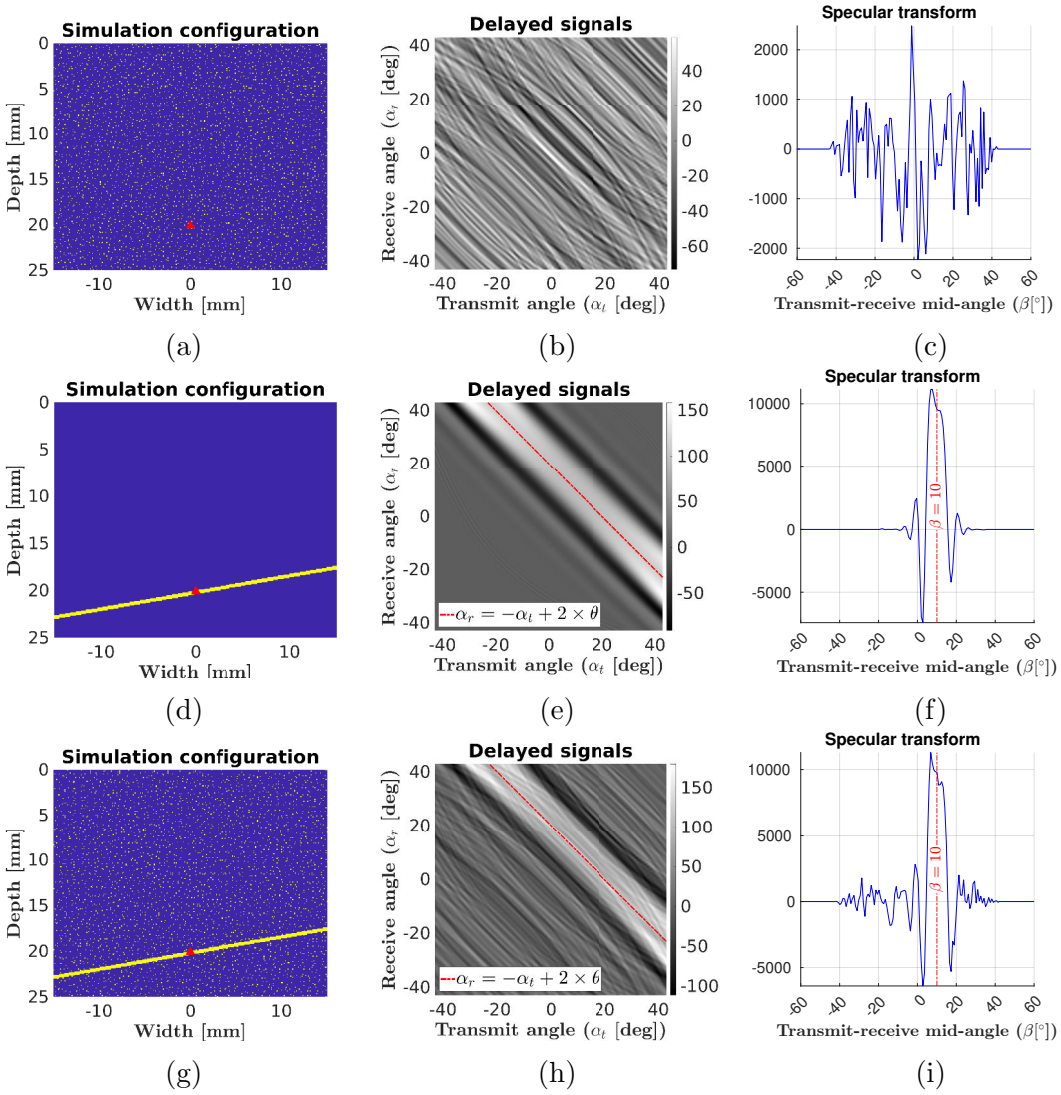

Figure 5.6: Illustration of the specular transform for a pixel located at (0,20)mm in different configurations. The first row correspond to the pure speckle configuration, the second row corresponds to pure specular interface with orientation 10° and the last row correspond to a configuration of specular interface surrounded with multiple point scatterers.

The specular transform contains information on: (i) the presence of a specular reflector (specularity) and (ii) the orientation of the reflector (specular orientation). Specularity can be obtained by observing the shape of the specular transform. For example, if the shape of the received signal is random as in Figure 5.6c we can deduce that the reflector is not specular. On the other hand, if the shape is similar to the specular transform of a specular reflector we can deduce that the reflector is a specular object. The transmit-receive mid-angle β that maximizes the specular energy is the specular orientation θ. For example this mid-angle is around 10° in panel 5.6i.

If we derive a model of a specular transform parting from the known emitted signal, we can formulate the estimation of the specularity as a situation where we have to maximize the energy of a known signal (specular reflection) drown into unwanted random signal (speckle noise).

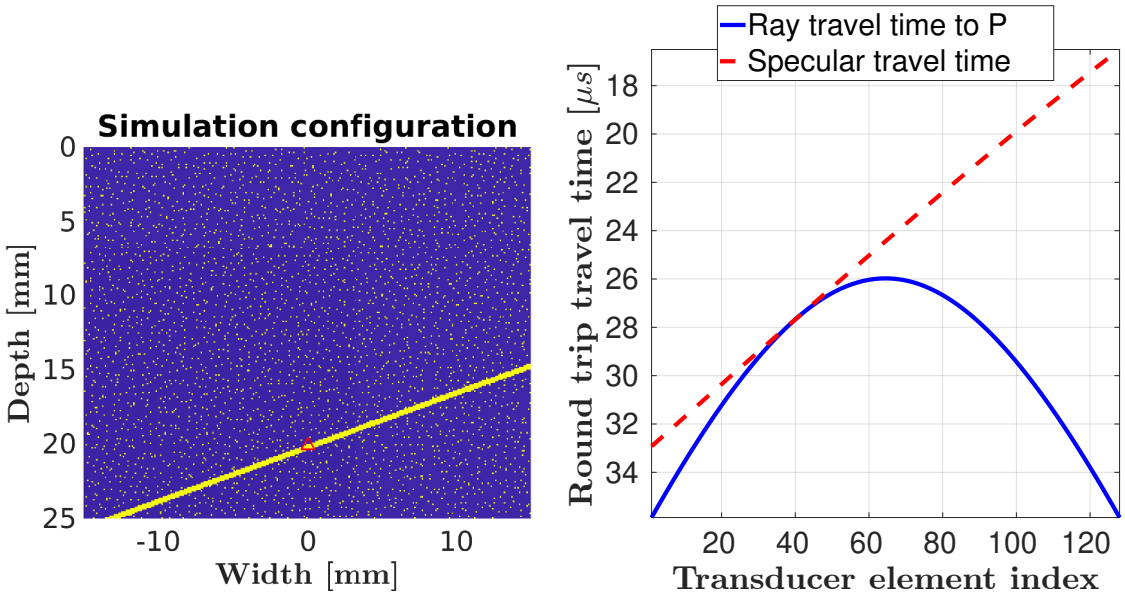

(a) (b)

Figure 5.7: Comparison of specular and diffuse travel time for a point lying on a tilted planar interface. Panel (a) is the simulation configuration and the red triangle corresponds to the point for which travel times are computed. In panel (b), the computed specular travel time is plotted as a red dashed-line and the diffuse ray travel time is plotted in plain blue line. To compute these values the transmitting element is also the receiving element (iT=iR).

5.2.3 Model of specular transform

In Figure 5.7, we show the specular and the diffuse travel time for a point belonging to a specular interface (the red pixel in panel 5.7a). We suppose that the transmitting element is the receiving elements (iT=iR). The red dashed line corresponds to the two-way travel time of the specular reflection at point P=(0,20) mm and the blue plain curve corresponds to the two-way travel time if we consider the pixel as a point scatterer (this correspond to the diffuse travel time given by equation 5.6). We can see that for a point scatterer, the shortest arrival time is recorded at the center of the probe (the blue plain curve is symmetrical and minimal around transducer elements 64 and 65). However, if we suppose a specular travel time with specular orientation $\theta = 20°$, the first arrival of the specular wavefront is recorded at the element closer to the specular interface (element 128 of the probe). Equal travel time is obtained for a point scatterer and a specular interface for element number 40. At this element, the transmit-receive mid-angle β equals the specular orientation θ.

Thus, our problem can be formulated as follows: we want to derive a model that gives the signal contribution from an orientation β (that corresponds to the transmit-receive mid-angle) knowing that the specular object has an actual orientation of θ.

A $\theta-$oriented plane interface passes through $P(x_P, z_P)$ as in figure 5.2. Signal emitted by the element iT is a Gaussian tone burst shown in the Figure 5.8 and denoted $e(t)$. When reaching the interface (D_s), the signal is reflected then recorded by element iR. Since the reflection at (D_s) is specular, there exists a unique point $Q \equiv (x_Q, z_Q)$ belonging to the interface, such that the pairs of transmit and receive angles at point Q $(\alpha_t(Q), \alpha_r(Q))$ given by the equation (5.4) will satisfy the law of specular reflection (equation (5.3)). This point Q is called the mirror point of the couple (iT, iR) (see Figure 5.9).

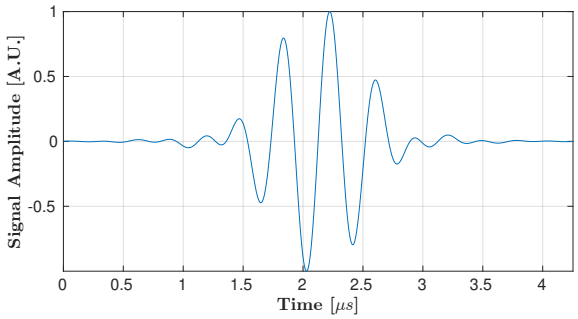

Figure 5.8: Emitted waveform e(t) by elements of the probe.

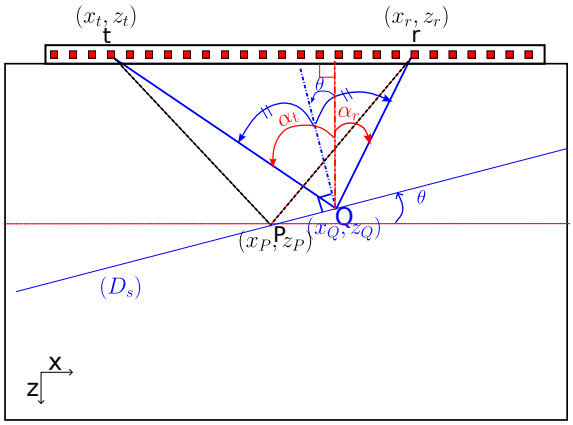

Figure 5.9: Geometric representation of specular reflection. Signal is emitted by iT and received by element iR. A θ-oriented interface is passing through pixel P. The corresponding mirror Point of this interface is Q and at this point $\alpha_r(Q) + \alpha_t(Q) - 2\theta = 0$. Ray path that follows Snell-Descartes law is in blue plain line whereas ray path is plotted in black dashed line.

We introduce the two way specular travel time as the time it takes to record with element iR, a wavefront emitted by the element iT and reflected by a specular interface passing through P. This specular travel time is equivalent to the diffuse two-way travel time (equation (5.6)) applied to the mirror point Q: $\tau_{iT,iR}(Q)$ (blue solid ray path in Figure 5.9). In ray theory, the first specular reflection will be recorded at this time. The ray travel time to point P is given by $\tau_{iT,iR}(P)$ (black dashed ray path in Figure 5.9). Hence, the specular contribution at point P is given by the value of the shifted echo: $e(\tau_{iT,iR}(P) - \tau_{iT,iR}(Q))$.

According to Snell's law of reflection, the transmit-receive mid-angle of the pair (iT, iR) at the mirror point Q equals the specular orientation θ. Therefore all pairs of (iT, iR) that share the same mid-angle θ will also share the same mirror point Q. Therefore, to take into account the multiplicity of the transmission, we can derive a model of specular signal at point P as:

$$h(\beta; P, \theta) = \sum_{iT=1}^{N_T} \sum_{r=1}^{N_R} e\left(\tau_{iT,iR}(P) - \tau_{iT,iR}(Q)\right), \tag{5.9}$$

in this notation Q means mirror point and depends on the position of the transmitting iT and receiving iR elements. This dependency is voluntary omitted for simplicity of notation.

Authors of [7] derived a model of specular transform for a homogeneous medium based on the image source principle. In this chapter the principle of mirror point is used to explain the development of the model but it is strictly equivalent to the image source principle.

Determination of the mirror point Q. We know that the mirror point Q belongs to the interface (D_s) and it also satisfies equation (5.3). This gives:

$$\begin{cases} z_Q = -\tan(\theta)(x_Q - x_P) + z_P \\ \alpha_r(Q) = 2\theta - \alpha_t(Q) \end{cases}$$

Using the trigonometric relationship of equation (5.4), we solve this system of two equations to find (x_Q, z_Q):

$$\begin{aligned} x_Q(iT, iR) &= \frac{b(1-a^2)(x_r + x_t) + 2a(x_r x_t - b^2)}{(a^2+1)[2b + a(x_r + x_t)]}, \\ z_Q(iT, iR) &= a x_Q(iT, iR) + b, \end{aligned} \tag{5.10}$$

with $a = -\tan(\theta)$ and $b = z_P + x_P \tan(\theta)$.

This analytical determination of the mirror point will allow us to get specular travel time from equation (5.6) and thus compute the specular model given by the expression in (5.9) for any specular orientation.

In figure 5.10, the specular model h is shown for different values of specular orientation θ: -20, -10, 0, 10 and 20 degrees.

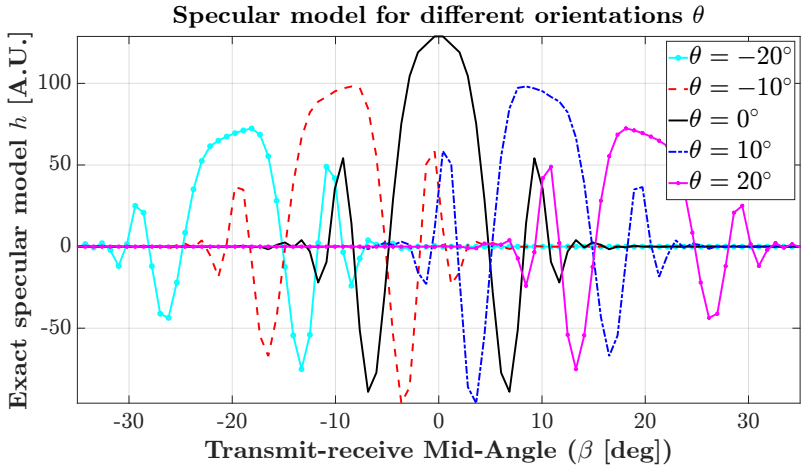

Figure 5.10: Models $h(\beta; P)$ of specular signal computed with equation (5.9). The model is shown for 5 different specular orientations: from -20 to +20°.

The maximum amplitude of the specular model is highest when the assumed specular interface is parallel to the probe ($\theta = 0°$) and decreases as $|\theta|$ increases. The slight asymmetry observed, depending on the sign of the specular orientation, is a result of the reduction in the number of transmitter-receiver pairs as the angle moves away from 0 degrees.

We observed in Figure 5.3 that delayed received signals exhibit symmetry concerning the Snell-Descartes equation (5.3). Specifically, for all pairs sharing the same mid-angle β, identical specular reflections are recorded. Since our focus is solely on the shape of the specular signal, we can derive a simplified model $h_0(\beta; P)$ by considering only one transmit-receiver pair for each β. We can limit our consideration along the axis $\alpha_r = \alpha_t$, corresponding to the diagonal of delayed signals in Figure 5.3:

$$h_0(\beta; P, \theta) = \sum_{iT=1}^{N_T} e\left(\tau_{iT,iT}(P) - \tau_{iT,iT}(Q)\right). \tag{5.11}$$

In figure 5.11, the simplified specular model h_0 is shown for different values of specular orientation θ: -20, -10, 0, 10 and 20 degrees.

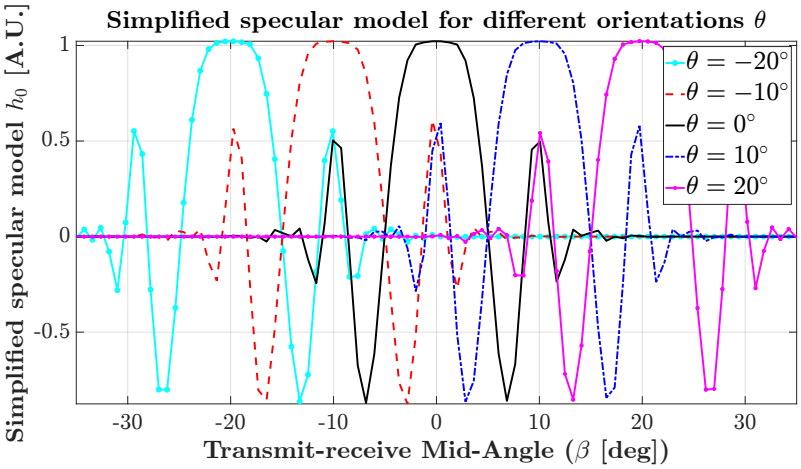

Figure 5.11: Models of specular signal computed with equation (5.11). The model is shown for 5 different specular orientations: from -20 to +20°

The expected signal maintains the same shape and reaches its maximum at the specular orientation θ. Notably, the simplified model remains invariant with respect to θ. Therefore, the specular model of a θ-oriented interface $h_0(\beta; P, \theta)$, can be approximated by the specular model of a flat interface $h_0(\beta; P, 0)$ translated by θ.

In the presence of a specular reflection, the known shape will be embedded in unwanted speckle. The objective is now to maximize the ratio of specular to unwanted speckle energy.

5.2.4 Model-based characterization of the specular reflection

Following Rodriguez-Molares et al., we define the specularity of a pixel as the probability that a specular interface exists at this pixel. To estimate the specularity of P, we calculate the normalized correlation between the model of specular signal $h_0(\beta; P, \theta = 0)$ and the specular transform of the received signals $f(\beta; P)$.

$$\chi(\theta; P) = \frac{\int_\beta f(\beta; P) \cdot h_0(\beta - \theta; P, 0) d\beta}{\sqrt{\int_\beta f(\beta; P)^2 d\beta \cdot \int_\beta h_0(\beta; P, 0)^2 d\beta}} \tag{5.12}$$

Normalizing the cross-correlation by the maximum correlation of a perfect match will give values between 0 and 1. A value close to 1 means that the two signals are nearly the same and a value close to 0 means the two signals are very different.

In Figure 5.12, we plot the normalized cross-correlation $\chi(\theta; P)$ for a pixel P when there is a specular reflector surrounded by numerous point scatterers (first column of the figure) and for a case where there is only speckle noise (second column of the figure).

We observe that even in the presence of speckle noise, the signal received from a specular interface is highly correlated with the specular model of a flat interface: we obtain a maximal value close to 1 (0.9) for $\theta = 20°$ (panel 5.12d). However when there is only speckle noise, the specular signal is poorly correlated to the specular model of a flat interface (panel 5.12e). Hence, one can deduce from these correlation results, an estimate of the specularity Ψ of a pixel as the maximum of the normalized cross-correlation $\chi(\theta; P)$.

$$\Psi(P) = \max(\|\chi(\theta; P)\|). \tag{5.13}$$

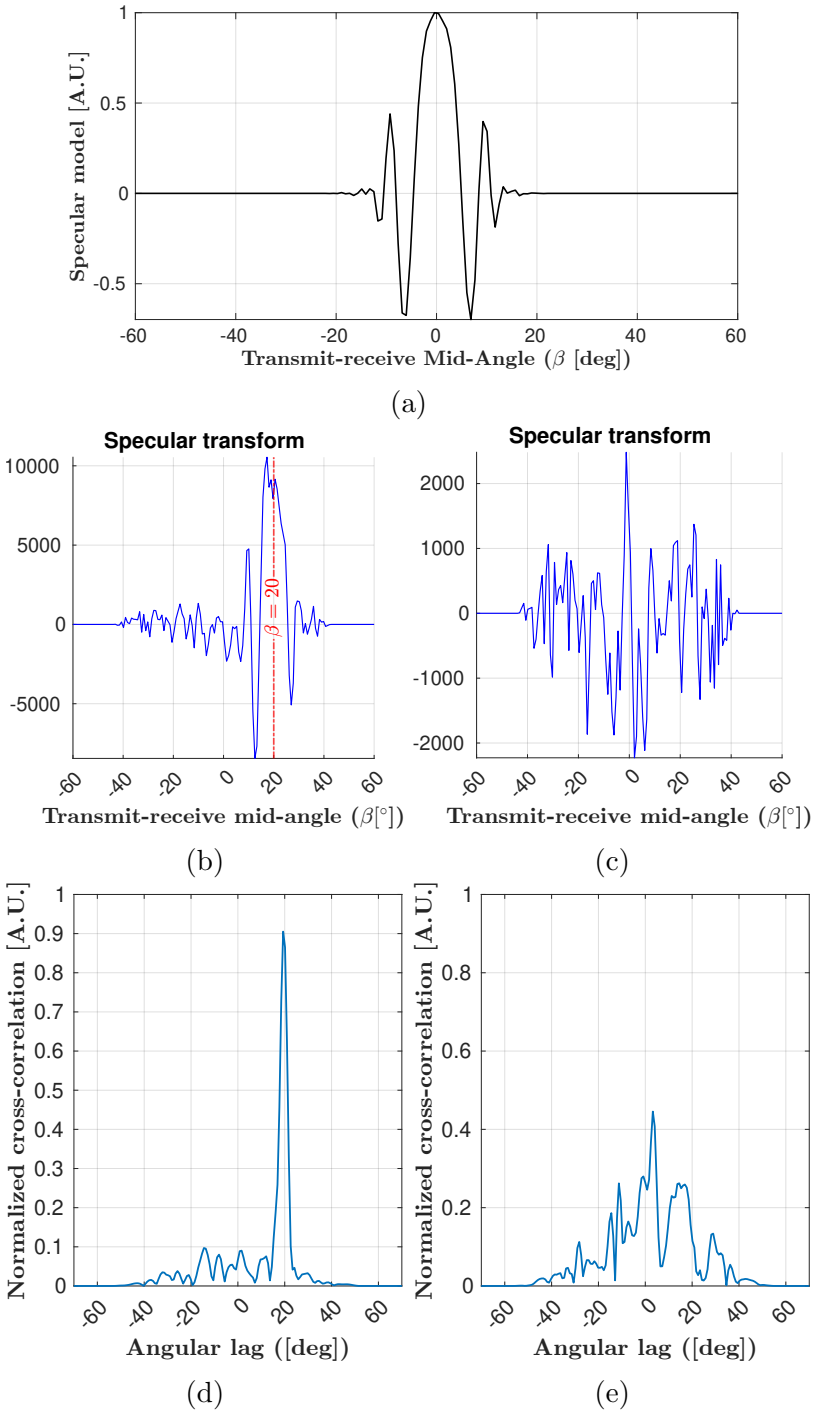

Figure 5.12: Illustration of correlation between a model of specular transform $h_0(\beta; P; \theta = 0)$ (panel (a)) and received specular transform $f(\beta; P)$. The first column (panels (b) and (d)) corresponds to a configuration of a specular interface surrounded by numerous point scatterers and second (panels (c) and (e)) corresponds to a configuration of randomly distributed point scatterers.

The angle that maximises this correlation gives an estimate of the orientation $\tilde{\Theta}(P)$ of the specular interface passing through P:

$$\tilde{\Theta}(P) = \arg\max_{\theta}(\|\chi(\theta; P)\|). \tag{5.14}$$

Finally, we obtain a specularity map Ψ which is an estimation of the specularity of objects inside the imaging medium and a map of orientation $\tilde{\Theta}$ which is an estimation of the orientation of the specular objects. In figure 5.13 we show the specularity maps

and the corresponding specular orientation of each pixel of a medium containing an interface with orientation $\theta = 20°$ surrounded by randomly distributed diffuse scatterers.

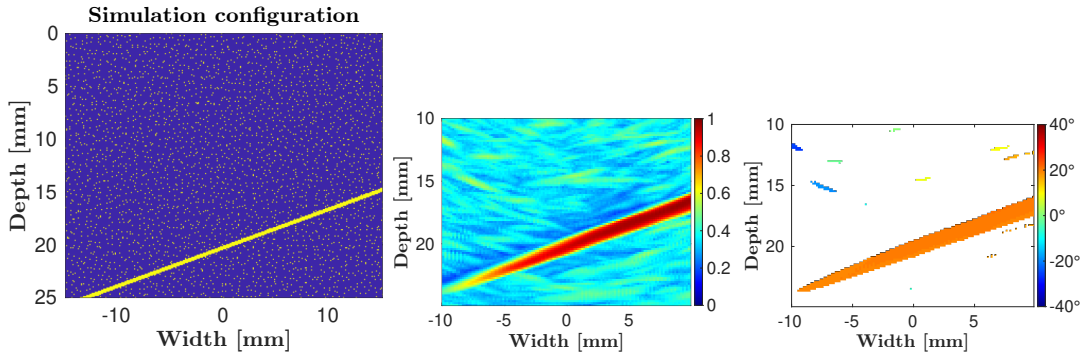

(a) (b) (c)

Figure 5.13: Characterization of specularity of a medium containing a specular interface with orientation $\theta = 10°$ drown into randomly distributed point scatterers. Panel (a) shows the medium configuration, panel (b) is the map of estimated specularity obtained equation 5.13 and panel (c) is the map of estimated specular orientation computed with equation 5.14 for pixels that have a specularity above 0.5.

Panel b of Figure 5.13 is the specularity map and panel (c) is the estimation of specular orientation for pixels with specularity greater than 0.5. We can see that the specularity is maximal and close to 1 at the object location (panel 5.13b) and low at other locations. The estimation of orientation of pixels having a good specularity (greater than 0.5) gives value close to 20° (see Figure 5.13c).

5.2.5 Image reconstruction

Beamforming with delay-and-sum algorithm When beamforming with DAS, a common practice is to use a fixed receive angle. Let us denote the corresponding lateral receive aperture Δ_r. Lateral aperture will depend on depth of the pixel. The relationship between lateral aperture and pixel's depth is obtained with f-number $f_\#$ definition [1]:

$$f_\# = \frac{z_P}{\Delta_r(P)}$$

The delays used to produce a low-resolution image are obtained from equation 5.6.

When a wavefront hits a diffuse point scatterer, it is isotropically radiated in all directions. Hence, the DAS consists of performing, for each transmission, a weighted sum over the delayed received signal. The window used here is a hann window centered on the lateral position of the pixel and its size is fixed by the receive f-number. Equation 5.15 gives the signal $(d(iT; P))$ obtained at focal point P with transmitting element number iT :

$$d(iT; P) = \sum_{iR=1}^{N_R} w(iR; P) \cdot \mathbf{S}(\tau_{iT,iR}(P), iR, iT), \tag{5.15}$$

where $w(iR; P)$ denotes the apodisation window used for pixel P (combination of

f-number and hann window centered at lateral pixel coordinates).

$$w(iR;P) = \begin{cases} \cos^2(\frac{\pi(x_r - x_P)}{\Delta_r}), & if\ |x_r - x_P| \leq \Delta_r(P) \\ 0, & if\ |x_r - x_P| > \Delta_r(P) \end{cases}$$

This transformation applied to all pixels leads to 96 (number of transmissions) low resolution images which are coherently summed to get one high resolution image. A DAS image is then obtained with :

$$I_{DAS}(P) = \sum_{iT=1}^{N_T} w(iT;P) \cdot d(iT;P). \tag{5.16}$$

Beamforming with specular algorithm The specular beamformed image is a weighted sum of specular-transformed signals $f(\beta;P)$. A hann window centered around the estimated specular orientation $\tilde{\Theta}_l$ is used. Value of the specularity of the pixel P is used to enhance specular structures and remove speckle, thus, the intensity of the specular beamformed signal denoted I_{SP} is given by:

$$I_{SP}(P) = \Psi(P) \cdot \sum_{\beta=\beta_{min}}^{\beta_{max}} w(\beta;\tilde{\Theta}_l(P)) \cdot f(\beta;P), \tag{5.17}$$

where $w(\beta;\tilde{\Theta}_l(P))$ denotes the apodisation window used for pixel P (a hann window centered around $\tilde{\Theta}_l(P)$):

$$w(\beta;\tilde{\Theta}_l(P)) = \begin{cases} \cos^2(\beta - \tilde{\Theta}_l(P)), & if\ |\beta - \tilde{\Theta}_l(P)| \leq \eta\frac{\pi}{2} \\ 0, & if\ |\beta - \tilde{\Theta}_l(P)| > \eta\frac{\pi}{2} \end{cases}, \tag{5.18}$$

here, η is introduced as the specular tolerance, ranging from 0 to 1. When $\eta = 0$, only the specular reflection from the orientation $\tilde{\Theta}_l$ is taken into account. As η increases, more specular signals with decreasing weights are considered and summed.

$d(iT;P)$ and $f(\beta;P)$ contain all the scattering information of the pixel but in different basis. The argument of the DAS output, iT and P, are respectively the position of the emitting element $(x_t, 0)$ and the position of the pixel P (x_P, z_P). The depth of the pixel is used to fix the receive aperture. The lateral position of the pixel fixes the value of the apodisation window. If the receiver and the pixel have same or close lateral position, the weight is close to 1 and when receiver's lateral position gets further away from the lateral position of the pixel, the smaller is its weight. Hence, the DAS operation can be seen as gathering information according to the lateral distance between receiving element iR and pixel P. The specular transform $f(\beta;P)$ gathers information according to the angular shift between the probe surface and a specular structure passing through P. Therefore, the main difference between these two algorithms lies in the summation basis and the apodization window used. They become equivalent when a rectangular window is used for both algorithms, a null f-number (full receive aperture) is used for DAS and a 100% specular tolerance ($\eta = 1$) is used for specular beamforming.

In Figure 5.14, we compare the images obtained using DAS Beamforming and specular beamforming for a medium containing a 20°-tilted specular object surrounded by numerous point scatterers. Visually, the specular object is better visualized in the specular beamformed image, and the speckle is significantly reduced compared to the DAS image.

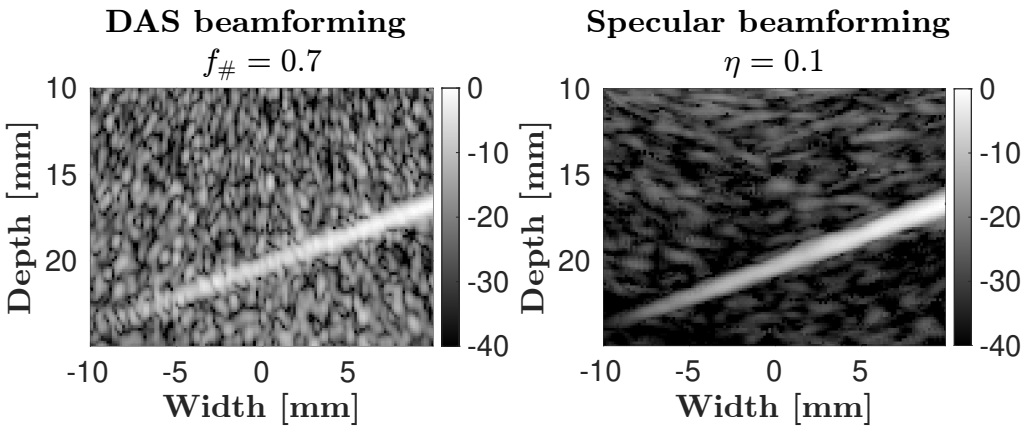

Figure 5.14: Comparison DAS beamforming (left panel) and specular beamforming (right panel). DAS beamforming (Equation 5.16) is performed with a receive f-number of 0.7 and specular beamforming (Equation 5.17) is performed with a tolerance angle $\eta = 0.1$.

5.3 Refraction-corrected specular beamforming for multi-layered media

All of the development above supposed a homogeneous medium in which ultrasound rays are straight lines. However we saw in previous chapters that the impedance of bone-tissue is at least twice higher than that of soft tissues. Therefore, the hypothesis of straight ray path is not a good approximation for the case of bone. In this section, we will illustrate refraction and specular reflection for a two-layers medium. We give a generalized model-based characterization of curved specular interfaces. In the scope of this chapter, we neglect lens of the probe.

5.3.1 Geometrical considerations

Refraction. We suppose a medium with two layers: a layer of cutaneous tissue on top of a layer of bone tissue. The interface between the two layers can be

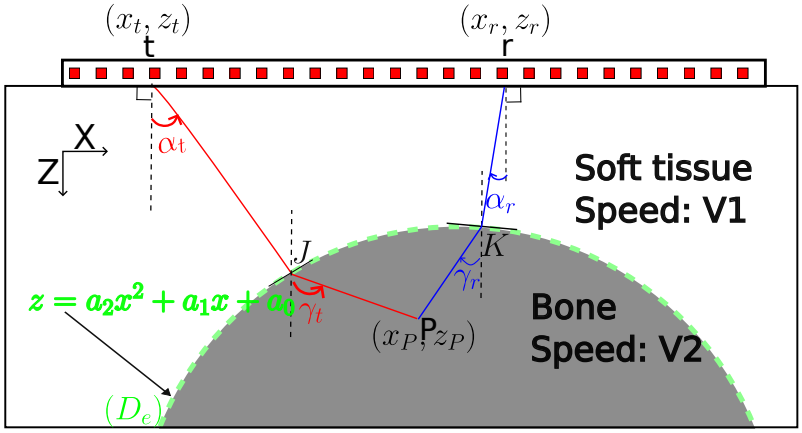

Figure 5.15: Illustration of refraction at the external interface of cortical bone.

approximated by a parabola with parameters a_0, a_1, a_2 :

$$(D_e) : z = a_0 + a_1 x + a_2 x^2, \tag{5.19}$$

where x and z are along the axes defined in Figure 5.15, V_1 and V_2 are the propagating wave speed inside cutaneous tissue and cortical bone respectively. We define α_t

(respectively α_r) as the angle of the incident ray parting (respectively the reflected ray) from element iT (respectively received at element iR) of the probe and γ_t (respectively γ_r) as the angle of the ray arriving at (respectively parting from) point P inside cortical bone (see Figure 5.15).

We define incident point J as the point of the interface through which the incident ray passes and incident point K as the point of the interface through which the reflected ray passes. Using these points above angles are given by:

$$\begin{cases} \alpha_t = \arctan(\frac{x_J - x_t}{z_J - z_t}) \\ \gamma_t = \arctan(\frac{x_P - x_J}{z_P - z_J}) \\ \alpha_r = \arctan(\frac{x_K - x_r}{z_K - z_r}) \\ \gamma_r = \arctan(\frac{x_P - x_K}{z_P - z_K}) \end{cases} \tag{5.20}$$

According to Snell-Descartes law of refraction for the transmitted ray from iT to P:

$$\frac{\sin(\alpha_t(P) + \arctan(2a_2x_J + a_1))}{V_1} = \frac{\sin(\gamma_t(P) + \arctan(2a_2x_J + a_1))}{V_2}. \tag{5.21}$$

The reflected ray from P to iR follows the same laws:

$$\frac{\sin(\alpha_r(P) + \arctan(2a_2x_K + a_1))}{V_1} = \frac{\sin(\gamma_r(P) + \arctan(2a_2x_K + a_1))}{V_2}, \tag{5.22}$$

where the arctan terms are the local orientations of the external interface at points J and K.

Let us denote $\sigma_{iT,iR}$(P) as the two-way travel time that considers refraction between layers. Hence, we obtain the relationship:

$$\begin{aligned} \sigma_{iT,iR}(P) = &\frac{\sqrt{(x_J - x_t)^2 + (z_J - z_t)^2} + \sqrt{(x_K - x_r)^2 + (z_K - z_r)^2}}{V_1} + \\ &\frac{\sqrt{(x_P - x_J)^2 + (z_P - z_J)^2} + \sqrt{(x_P - x_K)^2 + (z_P - z_K)^2}}{V_2}. \end{aligned} \tag{5.23}$$

Point J depends on both emitting element iT and focal point P, point K depends on both receiving element iR and focal point P. After angular transformation using equation (5.20), J and K can be obtained by finding the points that satisfy equations (5.21) and (5.22) respectively. If the external interface is planar, analytic developments give solutions for point J and K. However, if the external interface is not planar, solving these equations is not trivial. Solutions are found using numerical methods. We used MATLAB 2023a and its non-linear zero finding algorithm *fzero* Copyright 1984-2021 The MathWorks, Inc.

Specular reflection. Suppose that we have a curved reflector (D_i) inside the cortex as in Figure 5.16. The reflector can be approximated by a parabola with parameters b_0, b_1 and b_2:

$$(D_i) : z = b_0 + b_1x + b_2x^2 \tag{5.24}$$

We can apply the laws of specular reflection to a point P belonging to this interface. We can derive an equation similar to equation 5.3. This yields the same law:

$$\gamma_t + \gamma_r - 2\theta_l = 0, \tag{5.25}$$

where θ_l is the local orientation of the interface passing through focal point P and its value is given by $-\arctan(2b_2x_P + b_1)$.

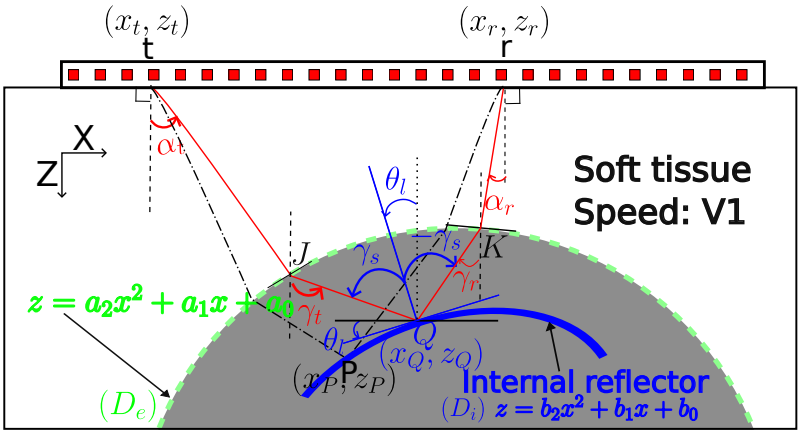

Figure 5.16: Illustration of specular reflection inside cortical bone.

5.3.2 The specular signature in presence of refraction

We consider a two-layer medium with the inclusion of different reflectors as in section 5.2 in the second layer. (see Figure 5.17 panel (a) to (d)).

We performed simulations with SimSonic software ([14]). A synthetic aperture imaging sequence with an array transducer (central frequency 2.5 MHz and a 3 dB bandwidth of 80%) of 128 elements of size 245 µm and with a spatial period (pitch) of 300 µm was simulated. The first layer is a homogeneous fluid medium with water speed of sound V_1=1540 m/s and the second layer is a homogeneous elastic medium with longitudinal wave speed of sound $V_2 = 3500\ m/s$ mimicking bone matrix. The simulated probe is immersed inside the first layer and the interface between two layers is at 10 mm depth from the probe surface. For this configuration 4 scenarios were considered:

- a scenario to illustrate diffuse scattering, a diffuse point scatterer is centered and placed at 20 mm depth, (Panel 5.17a)
- a scenario to illustrate pure speckle noise, numerous point scatterers are randomly placed in the second layer, (Panel 5.17b)
- a scenario to illustrate pure specular scattering, a specular object with an orientation $\theta = 10°$ is placed at 20 mm depth, (Panel 5.17c)
- a scenario to illustrate specular scattering drown into speckle noise, a specular object with an orientation $\theta = 10°$ is placed at 20 mm depth and is surrounded by numerous point scatterers randomly distributed, (Panel 5.17d)

Recorded signals from a focal point $P = (0, 20)$ mm for each configuration are shown in Figure 5.17 from panel (e) to panel (h). The same signature are observed as for an homogeneous medium (Figure 5.3). Signature of diffuse point scatterer in panel e is less marked in this case. In fact, the wavelength inside second layer is 1.4 mm instead of 0.6 mm giving a point scatterer more smaller compared to the wavelength. Therefore, the diffusion strength is smaller. Due to this small size of the scatterer, some numerical artifacts appear as we can see in the diagonal of the image in figure 5.17e.

In panels e to h of Figure 5.17, we observe in the upper left and lower right corners of the image the unwanted reflections from the external interface at 10 mm. These are the signals that follow an equivalent propagation path but do not originate from the wanted direction. These are contribution of secondary lobes and they can be eliminated with an appropriate f-number.

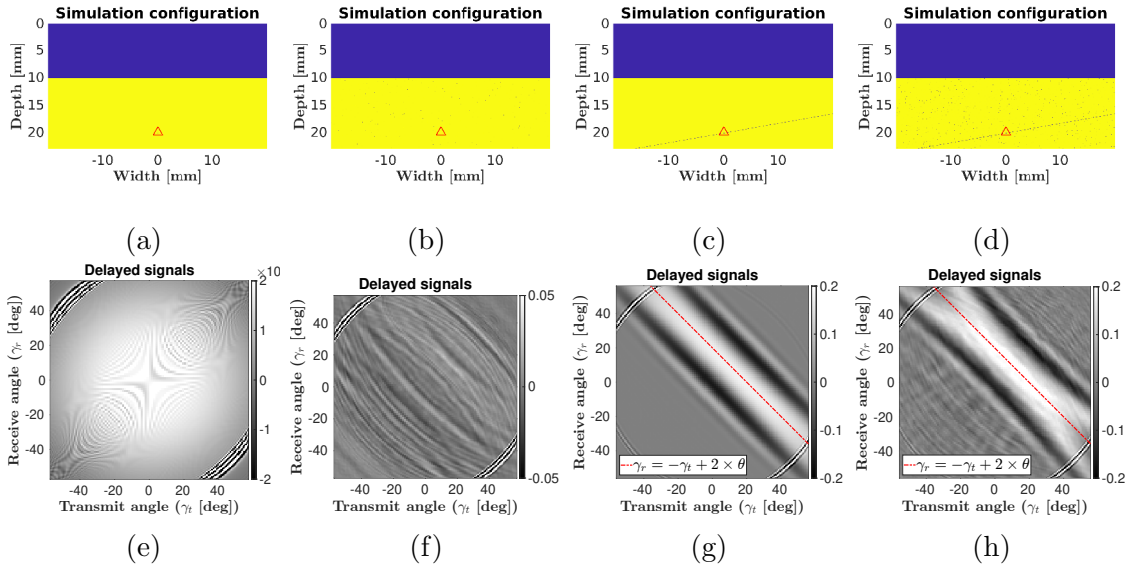

Figure 5.17: Delayed received signals from a pixel located at depth (0,20)mm inside the second layer (red triangle in the top row images) for all different configurations. The first layer is water with speed of sound of 1540 m/s and the second layer is bone matrix with speed of sound 3500 m/s. The top row images (panels (a), (b), (c) and (d)) are the simulation configuration as in Figure 5.3 and the bottom row images (panels (e), (f), (g) and (h)) are the corresponding delayed received signals with respect to receive and transmit angle at the pixel. The red lines in panels (e) and (h) are the plot of the specular reflection equation 5.25 for $\theta = 10°$.

Apart from these artifacts and noise, we obtain the same specular patterns as in section 5.2.

The specular transform. From the above results, specular signature does not change when refraction is considered appropriately. We can therefore use the specular transform by considering the receive and transmit angle at the pixel (γ_t, γ_r). Hence, the same transformation as in equation 5.8 translates the received signals in the specular domain through :

$$f(\beta; P) = \sum_{iT=1}^{N_T} \mathbf{S}(\sigma_{iT,iR}(P), \gamma_r, \gamma_t)|_{\frac{\gamma r+\gamma_t}{2}=\beta} \tag{5.26}$$

Figure 5.18 shows the specular transform of received signal for the configurations with pure speckle noise and for specular reflection with speckle noise.

As expected, specular transform exhibits the specular signature and the same shapes as in Figure 5.6. After transformation, speckle noise is random (panel (b)) and specular reflection exhibits a certain shape specific to specular reflector (panel (d)). Remark that the specular transform of panel 5.18d is wider than the specular transform of panel 5.6i. In fact, the full angular width at half maximum is around 7° for Figure 5.6g and around 15° for Figure 5.18d which corresponds to an increase of a factor of 2. This is due to the fact that the wavelength inside second layer (1.4 mm) is around twice higher than the wavelength inside water (600 µm).

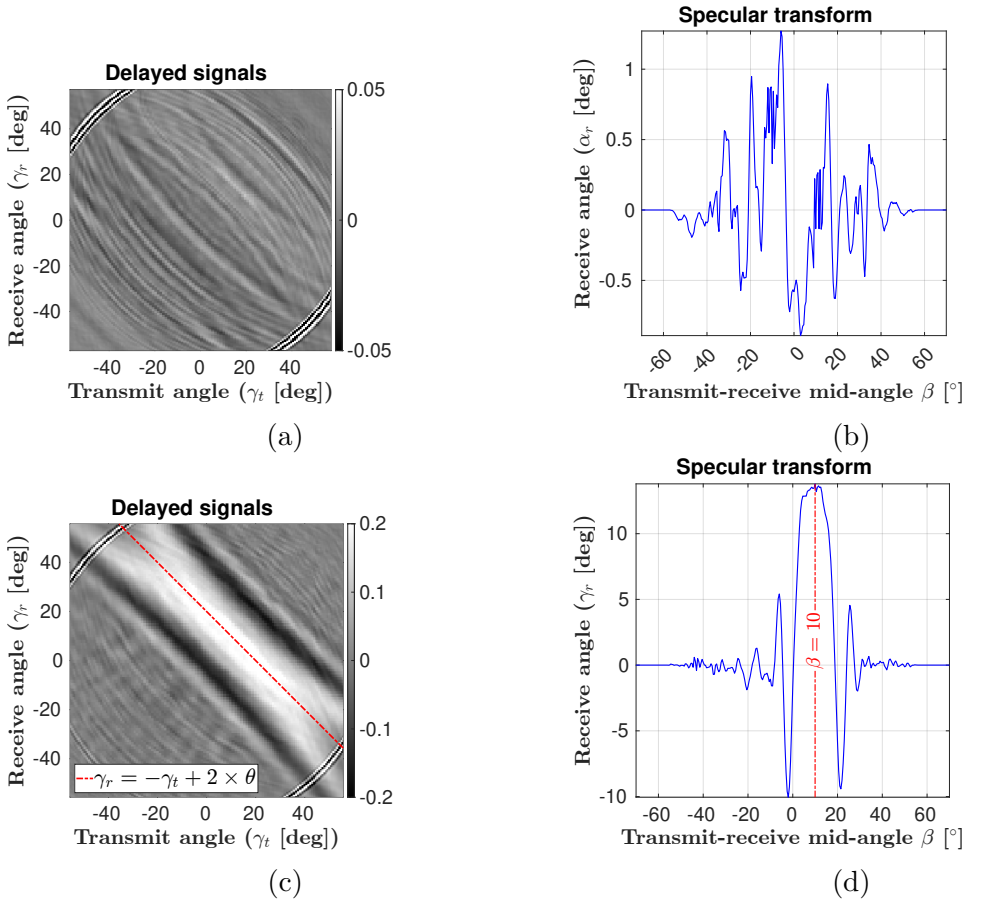

Figure 5.18: Illustration of the specular transform for a pixel located at (0,20)mm. First column: delayed received signals and last column corresponds to specular transforms. First row: pure speckle configuration (panels (a) and (b)), the second row: a specular interface surrounded by numerous point scatterers (panels (c) and (d)).

5.3.3 Model of specular transform

We derive a model of specular transform for a two-layered medium. Same principle as in section 5.2.3 is applied in the second layer but the travel time must consider refraction.

The reflector inside the second layer (D_i) is a parabola given by equation (5.24) (Figure 5.16). The parameter b_2 determines the curvature of the reflector. A positive value means a convex reflector and a negative value means a concave reflector. For the scope of this study, we will ignore concave reflectors and suppose that b_2 is always positive. If $b_2 = 0$, then we have a planar reflector with orientation $-\arctan(b_1)$. For non-null values of b_2, the curvature of the reflector increases with b_2. For this reason, b_2 is called the parameter of curvature and b_1 the parameter of local orientation.

When reaching the interface between the layers (D_e), part of the incident ray is reflected and another part is refracted inside bone cortex. At the reach of the specular reflector, the refracted ray is reflected and element iR records the back scattered signal after another refraction (black dashed ray path in figure 5.19). Therefore, there exists a unique point $Q \equiv (x_Q, z_Q)$ belonging to interface D_i such that the transmit and receive angles at point Q will satisfy the law of specular reflection and specular refraction given in equations (5.22), (5.21) and (5.25) (blue plain ray path in figure 5.19). This point noted Q is the mirror point (Figure 5.19).

Hence, the specular travel time that considers refraction is given to delay equa-

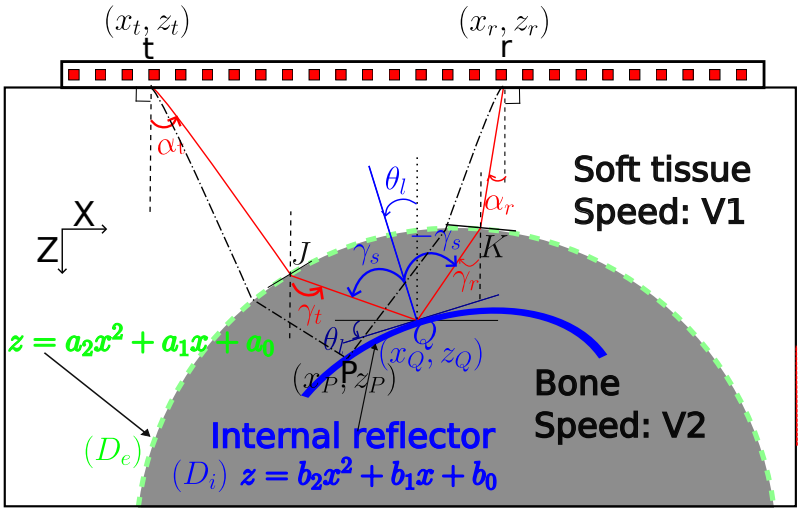

Figure 5.19: Geometrical illustration of specular reflection at the internal interface of the bone.

tion 5.23 applied to point Q: $\sigma_{iT,iR}(Q)$. Recording of specular reflection will start at this time. The ray travel time is given by $\sigma_{iT,iR}(P)$. In the same manner as in section 5.2, the specular contribution at point P is the shifted echo $e(\sigma_{iT,iR}(P) - \sigma_{iT,iR}(Q))$ and the model can thus be obtained by applying equation 5.9. Note that the travel time now also depends on the parameters of the external interface (a_0, a_1, a_2).

Determination of the mirror point Q. Applying the laws of specular reflection and refraction, we know that the coordinates of mirror point Q depends on the parameters of the external interface D_e, on the coordinates of the transmitting and receiving elements and it also belongs to the reflector D_i. Mathematically, this means:

$$\begin{cases} z_Q = b_0 + b_1 x_Q + b_2 x_Q^2 \\ \gamma_r(Q) = -2\arctan(2b_2x_Q + b_1) - \gamma_t(Q) \\ \frac{\sin(\alpha_t(P)+\arctan(2a_2x_J+a_1))}{V_1} = \frac{\sin(\gamma_t(P)+\arctan(2a_2x_J+a_1))}{V_2} \\ \frac{\sin(\alpha_r(P)+\arctan(2a_2x_K+a_1))}{V_1} = \frac{\sin(\gamma_r(P)+\arctan(2a_2x_K+a_1))}{V_2}, \end{cases} \tag{5.27}$$

where J and K are the incidents point of the incident and reflected wave respectively. Using the trigonometric relationship in equation 5.20, we can replace angles and solve the system 5.27. For the case of a single homogeneous medium and a planar reflector, analytical development of the coordinates of a mirror point could be found. In this present case of a multi-layer medium with curved specular interfaces, analytical developments are difficult to obtain. Hence, we use numerical computation to obtain x_Q and z_Q. We solved the non-linear system 5.27 using MATLAB 2023a and its non-linear zero finding algorithm *fzero* (Copyright 1984-2021 The MathWorks, Inc).

In figure 5.20, we plot the specular model obtained after computation of mirror points for 5 different local orientations ranging from -20 to +20° and fixed curvature parameter b_2 ($b_2 = 10\ \mathrm{m}^{-1}$). As expected, this model is similar to the model obtained for a planar interface in Figure 5.10.

In Figure 5.21, the local orientation of the specular interface is fixed to 10°, and specular models are plotted for 4 different curvatures of the reflector: $b_2 = 0\ \mathrm{m}^{-1}$, $b_2 = 20\ \mathrm{m}^{-1}$, $b_2 = 40\ \mathrm{m}^{-1}$ and $b_2 = 60\ \mathrm{m}^{-1}$.

We observe that the spread of the specular model increases with curvature, but

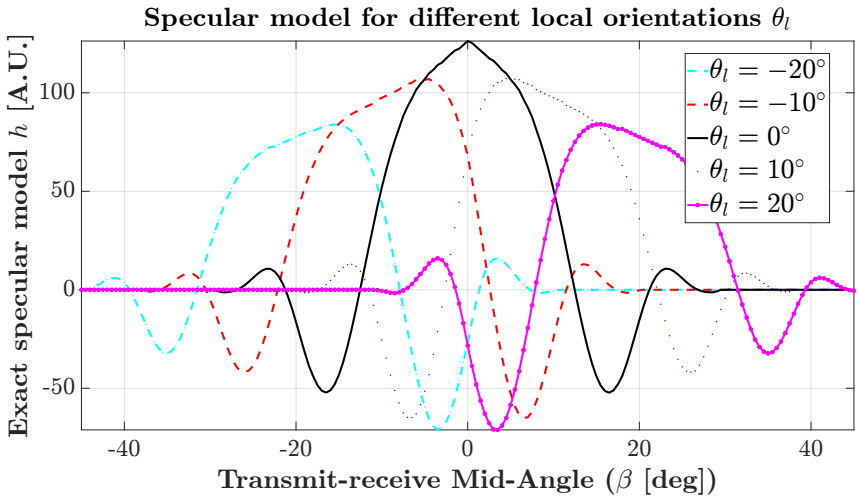

Figure 5.20: Specular model for a specular interface inside the cortex with fixed curvature ($b_2 = 30$ mm^{-1}) and varying local orientations θ_l. Parabolic parameters of the external interface are: $a_0 = 10$ mm, $a_1 = 0$, $a_2 = 30$mm^{-1}.

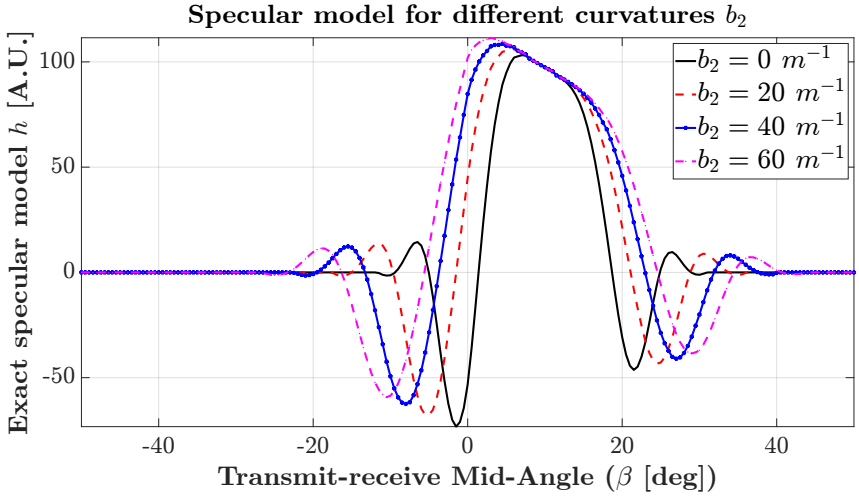

Figure 5.21: Specular model for a specular interface inside the cortex with fixed local orientation ($\theta_l = 10°$ corresponding to $b_1 = -0.17$) and varying curvatures b_2. Parabolic parameters of the external interface are: $a_0 = 10$ mm, $a_1 = 0$, $a_2 = 30$ mm^{-1}.

the center remains the same. Therefore, the curvature parameter b_2 alters the shape of the model. Similarly to the approach taken in section 5.2.3, we can derive an exact h and simplified h_0 specular model for a curved reflector with curvature b_2 and orientation b_1 passing through point P:

$$h(\beta; P, b_1, b_2) = \sum_{iT=1}^{N_T} \sum_{iR=1}^{N_R} e(\sigma_{iT,iR}(P) - \sigma_{iT,iR}(Q)). \tag{5.28}$$

$$h_0(\beta; P, b_1, b_2) = \sum_{iT=1}^{N_T} e(\sigma_{iT,iT}(P) - \sigma_{iT,iT}(Q)). \tag{5.29}$$

In Figure 5.22 and 5.23, the simplified specular models corresponding to exact specular models depicted in Figure 5.20 and 5.21, respectively, are plotted. The parameter b_1 only shifts the simplified model but does not change its shape and b_2 changes the shape of the model. Hence, h_0 is invariant to b_1. We can then

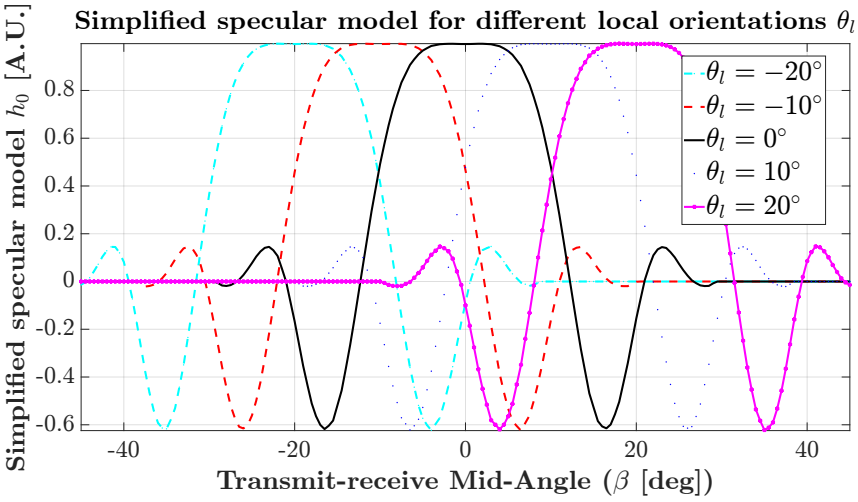

Figure 5.22: Simplified specular model for a specular interface inside the cortex with fixed curvature ($b_2 = 30$ mm^{-1}) and varying local orientations θ_l. Parabolic parameters of the external interface are: $a_0 = 10$ mm, $a_1 = 0$, $a_2 = 30$mm^{-1}

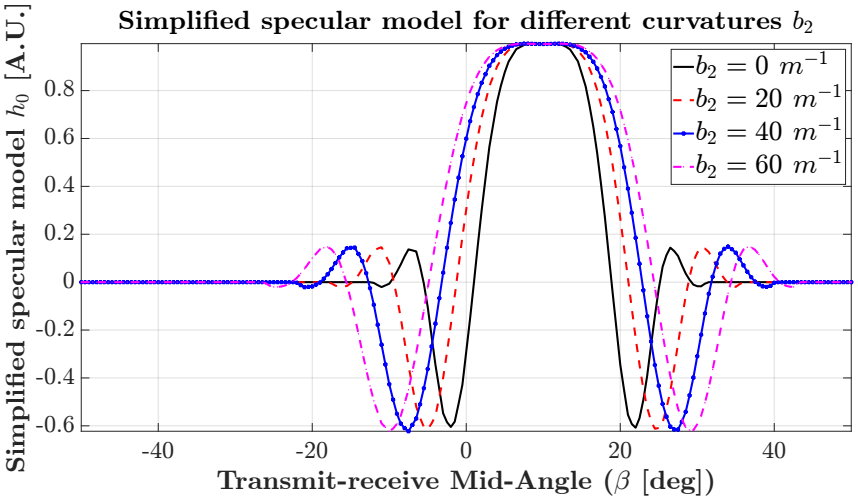

Figure 5.23: Simplified specular model for a specular interface inside the cortex with fixed local orientation ($\theta_l = 10°$) and varying curvatures b_2. Parabolic parameters of the external interface are: $a_0 = 10$ mm, $a_1 = 0$, $a_2 = 30$ mm^{-1}.

implement the matched filter by using the normalized cross-correlation between the model $h_0(\beta; P, b_1 = 0, b_2)$ and $f(\beta; P)$.

$$\chi(\theta_l; P, b_2) = \frac{\int_\beta f(\beta; P) \cdot h_0(\beta; P, 0, b_2) d\beta}{\sqrt{\int_\beta f(\beta; P)^2 d\beta \cdot \int_\beta h_0(\beta; P, 0, b_2)^2 d\beta}}. \tag{5.30}$$

We deduce the specularity by taking the maximum correlation :

$$\Psi(P) = \max(\|\chi(\theta_l; P, b_2)\|). \tag{5.31}$$

This maximum corresponds to a local orientation $\tilde{\theta_l}$ and a curvature $\tilde{b_2}$ given by :

$$[\tilde{b_2}, \tilde{\Theta_l}](P) = \arg\max_{b_2, \theta_l}(\|\chi(\theta_l; P, b_2)\|). \tag{5.32}$$

Estimate of the orientation parameter $\tilde{b_1}$ can be deduced from the relationship $\tan\tilde{\theta_l} = -(2\tilde{b_2}x_P + \tilde{b_1})$.

Similarly, one can generalize this procedure for a medium where the number of layers is above 2 and for other interfaces governed by higher degree polynomial. We then can get for any pixel, specular transform and a specular model that considers refraction. This allows to proceed to the model-based characterization of all reflections of the medium.

5.4 The impact of pore scattering on the contrast of specular images: a 2D simulation study

In sections 5.2 and 5.3, we explained how the laws of specular reflection and refraction can be utilized to classify and characterize reflections in a medium. These methods provide information on the specularity of the reflection and the orientation of the interface. While we illustrated the method with simulations of simple configurations where the specular interface is a needle-like object inserted into a homogeneous medium, these simulations are not representative of ultrasound imaging of cortical bone. In ultrasound imaging of cortical bone using delay-and-sum beamforming, pore scattering is known to be detrimental to image quality [15].

In this section, we investigate the influence of pore scattering on the contrast of specular images of the endosteal surface. We generate datasets that simulate various levels of diffuse scattering in a multi-layered media (Figure 5.24a). We explore both planar and curved geometries of bone surfaces. To simplify the study and emphasize the impact of pore size, we assume that all pores in each microstructure have the same diameter.

The technique outlined in section 5.3 is employed for the generated datasets, and the resulting images are compared with DAS images.

5.4.1 Materials & methods

Simulation of the ultrasound imaging sequence. We employed an elastic slab model to simulate the bone layer, incorporating randomly distributed pores with fixed diameters. Three pore diameters (10, 30, and 50 μm) were considered, each with three porosity levels (6%, 10%, and 14%) representing low, medium, and high porosity for human cortical bone, respectively. For each diameter-porosity combination, microstructures were generated with both flat and curved bone interface geometries (Figure 5.24b).

The bone layer was enveloped by a soft tissue-mimicking layer. For the soft tissue mimicking layers, a compressional wave speed of 1540 m/s was employed. Regarding the mineralized matrix within the cortical bone-mimicking layer, the compressional and shear wave speeds used in the simulations were 3500 m/s and 1800 m/s, respectively. The material within the pores was assumed to be the same as that in the soft tissue layer. We utilized the SimSonic open software [14] to generate ultrasound signals. To prevent reflections at the boundaries of the simulation domain, a Perfectly Matched Layer (PML) boundary condition was used.

Within the cortical bone mimicking layer, we modeled frequency-independent absorption within the bone matrix, with an absorption coefficient of 19.0 dB/cm at 2.5 MHz. The simulations were conducted with a grid size of 10 μm, and the corresponding time step was determined to maintain a constant value of CFL=0.99.

We simulated the same probe as used in experimental measurements, consisting of a linear array with 96 elements and a pitch of 300 μm. A synthetic transmit

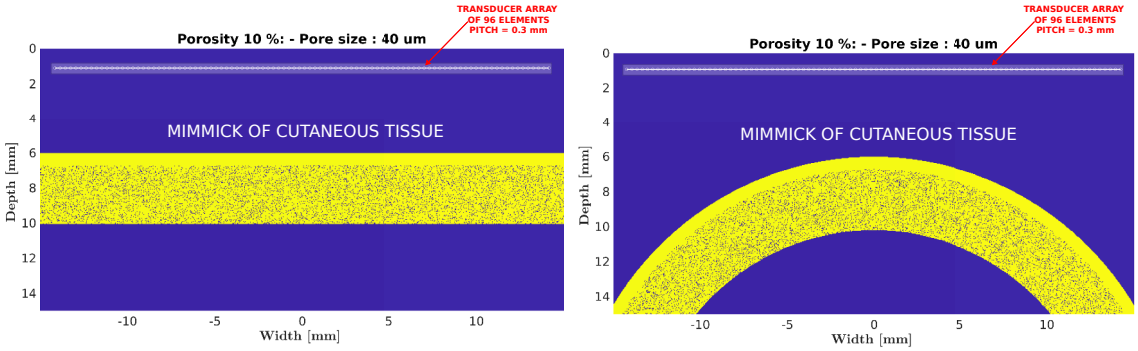

(a) (b)

Figure 5.24: Three-layers model used for simulations: two layers mimicking cutaneous tissue (blue) and one layer mimicking cortical bone tissue (yellow).Different geometries were generated: flat interfaces (left) and curved interfaces (right). The simulated probe is a linear array of 96 elements with a pitch of 300 μm.

aperture sequence was simulated. Each of the 96 elements emitted a Gaussian-windowed tone burst with a central frequency of 2.5 MHz (3dB bandwidth=1.33 MHz, Figure 5.25), and all the elements recorded the back-scattered signals. This resulted in a 96×96 matrix of back-scattered RF signals **S**.

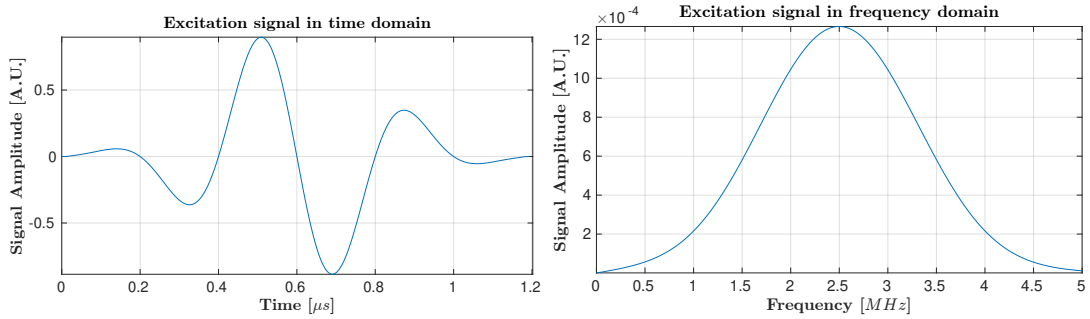

Figure 5.25: Emitted tone burst in temporal domain (left) and in frequency domain (right).Gaussian-windowed tone burst with a central frequency of 2.5 MHz and a 3 dB bandwidth of 1.33 MHz.

DAS Beamforming. DAS algorithm is used with a constant receive f-number of 0.5. This corresponds to a constant angular aperture at the transducer's elements of 45 degrees. Equation 5.16 is used for reconstruction.

Specular Beamforming. The specular algorithm produces three outputs: (1) a specularity map Ψ that is the probability to find a specular structure at each pixel, (2) an orientation map $\tilde{\Theta}_l$ that is an estimate of the most likely orientation of the specular structure and (3) an image that highlights specular structures and reduces speckle which we refer as specular beamformed image. Equation 5.17 is used with a tolerance angle η of 0.10 for planar interfaces and 0.25 for curved interfaces.

Speed of sound estimation. To perform beamforming, it is crucial to calculate travel times, which, in turn, requires knowledge of the speed of sound. While the propagating wave speed inside soft tissues is well-known, the porous nature of the cortical bone layer leads to variations in speed due to changes in porosity. Thus,

each layer is reconstructed sequentially using a specific sound speed for each microstructure.

We employ the autofocus principle, as outlined in Chapter 2, which suggests that among images generated with different velocity values, the optimal image in terms of brightness and sharpness is obtained when the velocity is closest to the velocity of the medium [2]. By utilizing various brightness and sharpness metrics, as detailed in Chapter 2, we determine the propagating wave speed in the cortical bone layer. In figure 5.26, the estimated speed values are reported for all configuration. In panel (a) we plot the speed values for configurations with flat bone surfaces and in panel (b) the values for configurations with curved bone surfaces.

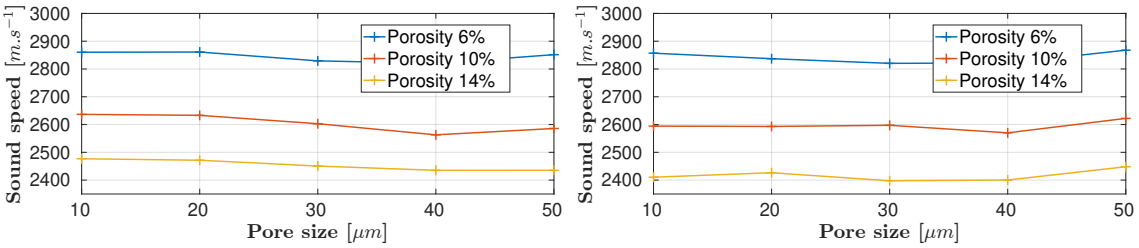

Figure 5.26: Speed of sound values in cortical bone obtained with autofocus approach for each cortical porosity and each individual pore size. Panel (a): flat bone interfaces. Panel (c): curved bone interfaces.

As expected, the wave speed values in cortical layer were found to decrease with respect to porosity. We also can remark that for a fixed porosity speed of sound slightly changes with pore size.

Endosteal interface visibility quantification. To evaluate the visibility of endosteal surface, we define the endosteal interface contrast (C_{EI}) as follows:

$$C_{EI} = \frac{\mu_E}{\mu_I}, \tag{5.33}$$

where μ_I and μ_E are respectively the average image intensities in the center of the cortex and at the endosteal interface. It is the same metric as the one defined in Chapter 3 but adapted to these geometries. The regions of interest (ROI) used for the computation of μ_I and μ_E all had a lateral extent from -5 to $+5$ mm. They are defined in Figure 5.27, where: the red box is the endosteal interface ROI, it has a height of one wavelength inside the bone layer and the yellow box is the inner cortex ROI, it extends from 1 mm after periosteal interface region to 1 mm before endosteal region.

C_{EI} evaluates how well the endosteal interface can be distinguished from the speckle inside the bone. On decibel scale, a positive value of C_{EI} means that endosteal interface is clearly visible while a negative value means that the endosteal interface is poorly visible.

5.4.2 Results

5.4.2.1 Parametric results on the presences of specular structures

Planar interfaces. Figures 5.28 display the maps of specularity Ψ and local orientation $\tilde{\theta}_l$ for configurations with planar bone interfaces and individual pore diameter

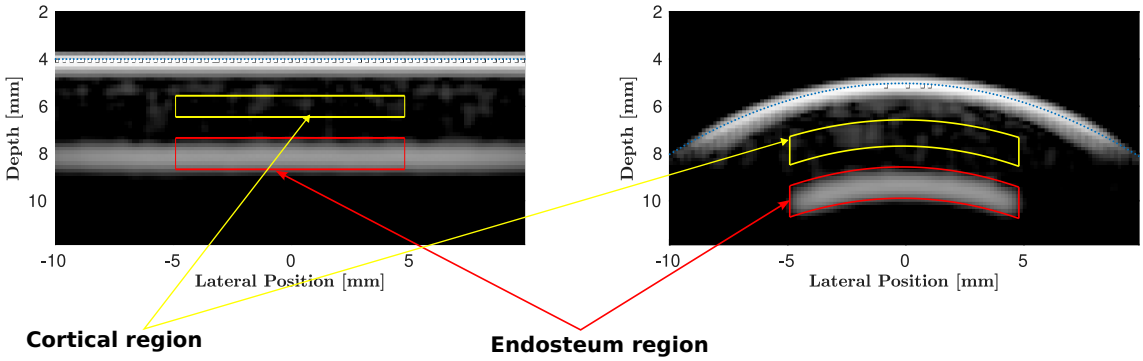

Figure 5.27: Region of interest to quantify endosteal interface visibility. Reconstructed images for a simulation configuration with flat interfaces (left) and configuration with curved interfaces (right). The yellow and red ROIs are used to evaluate inner bone cortex and endosteum contrasts, respectively

of 10 (panels (a)-(f)), 30 (panels (g)-(l)) and 50 µm (panels (m)-(r)). The configurations corresponding to same microstructures but with curved interfaces are displayed in Figure 5.29. In each subfigure, the panels of the top row corresponds to specularity map Ψ and panel of the bottom row corresponds to local orientation map $\tilde{\theta}_l$.

We observe in panels (a)-(f) of Figure 5.28 probability values close to 1 (between 0.92 and 0.99) at depth around 5 mm and 9 mm. The apparent thickness of the first interface is higher than that of the second interface due to larger wavelength inside bone. The specularity of the endosteal interface slightly changes with porosity. Inside the cortex, lower specularity values are found (values are lower than 0.4). This yields a good contrast between interfaces and the cortex: $C_{EI} = 11\ dB$. Specular orientation found for relevant pixels (with specularity ≥ 0.5, panel (d), e and f) correspond to flat interfaces.

In (g)-(l) of Figure 5.28 where individual pore diameter is 30 µm probability values at depth of bone interfaces are also close to 1 but lower than values found for configuration with pore diameter of 10 µm. Inside the cortex, some pixels have high specularity (values are greater than 0.5). This yields a lower contrast between interfaces and the endosteal surface: $C_{EI} = 6\ dB$. Specular orientation found for pixels of the interface correspond to flat interfaces but orientation for pixel inside the cortex are random.

For pore diameter of 50 µm ((m)-(r) of Figure 5.28), specularity of the internal interface decreases and number of "specular pixels" inside the cortex increases. Orientation of bone interface is accurately estimated and specular orientations inside the cortex are random. Visually, we observe a more pronounced decrease of the specularity of the endosteal interface with cortical porosity.

Curved interfaces. Similar results are obtained for specularity of curved interfaces. In Figure 5.29, specularity of pixels on the interfaces are very high ($\geq$0.9). The specularity map shows probability values ranging from 0.85 to 0.99 on the first bone interface. These values are nearly the same on the whole lateral extent of the interface from (e.g. for x varying from -10 to 10 mm). The corresponding specular orientation are ranging from -30 to 30 degrees. They correspond to the orientation of the local tangent at each point on the periosteal surface. The same variations are observed on the endosteal surface but with a lower lateral extent (from -7 mm to 7 mm). The narrower spread is due to the impossibility to retrieve backscattered echoes from some locations of the endosteal surface due to the high curvature of the

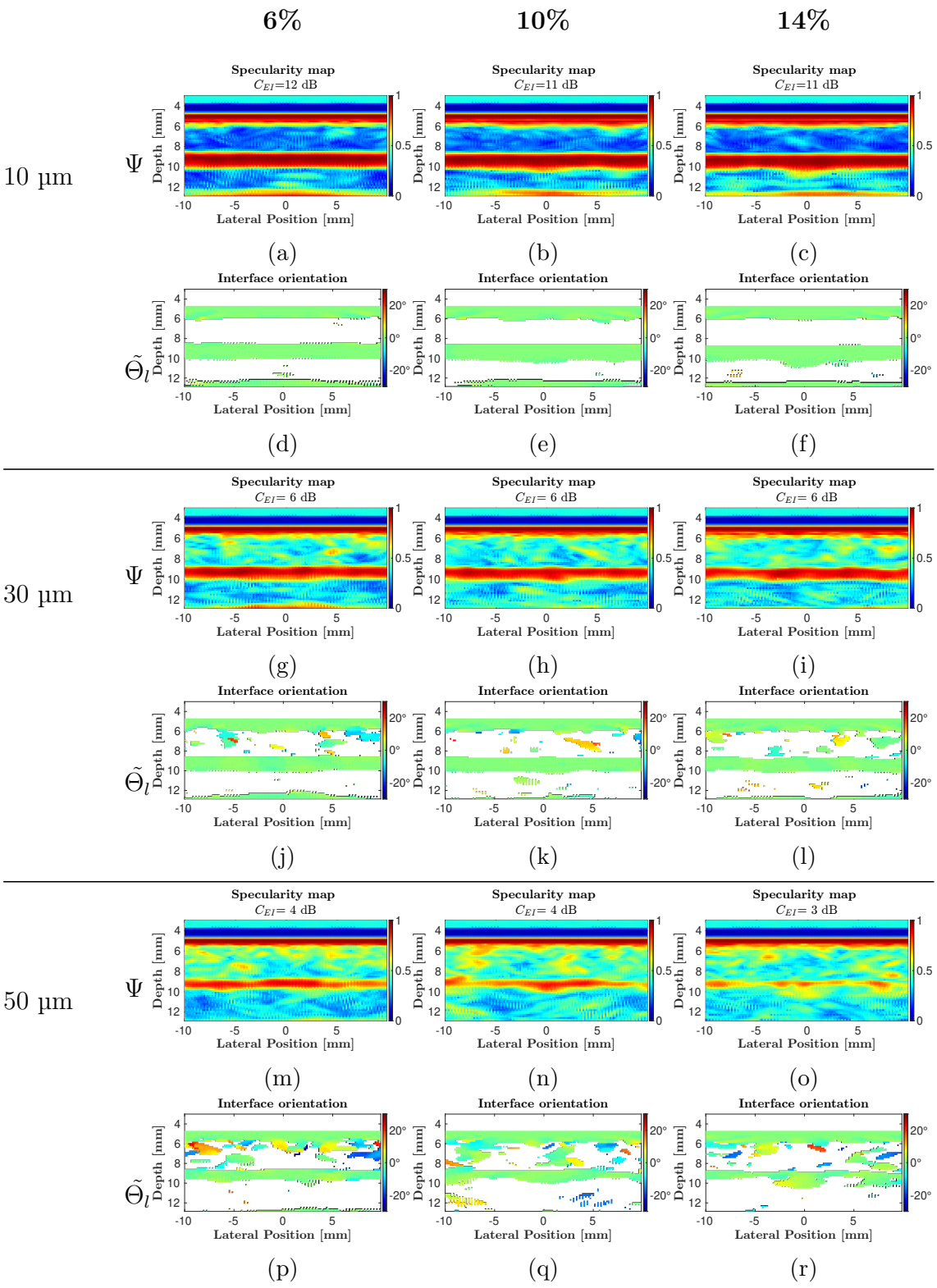

Figure 5.28: Specularity maps Ψ and corresponding thresholded orientation maps $\tilde{\Theta}_l$ for pixel with specularity greater than 0.5 for simulation configuration with flat bone interfaces. The diameter of the pores is 10 μm (panels (a) to (f)), 30 µm (panels (g) to (i)) and 50 µm (panels (m) to (r)). Cortical porosity: 6% (first column), 10% (second column) and 14% (last column). In each map of specularity C_{EI} is calculated.

interface increased by the refraction. This caused lower probability values. The corresponding specular orientations also range from -30 to 30 degrees. The estimated

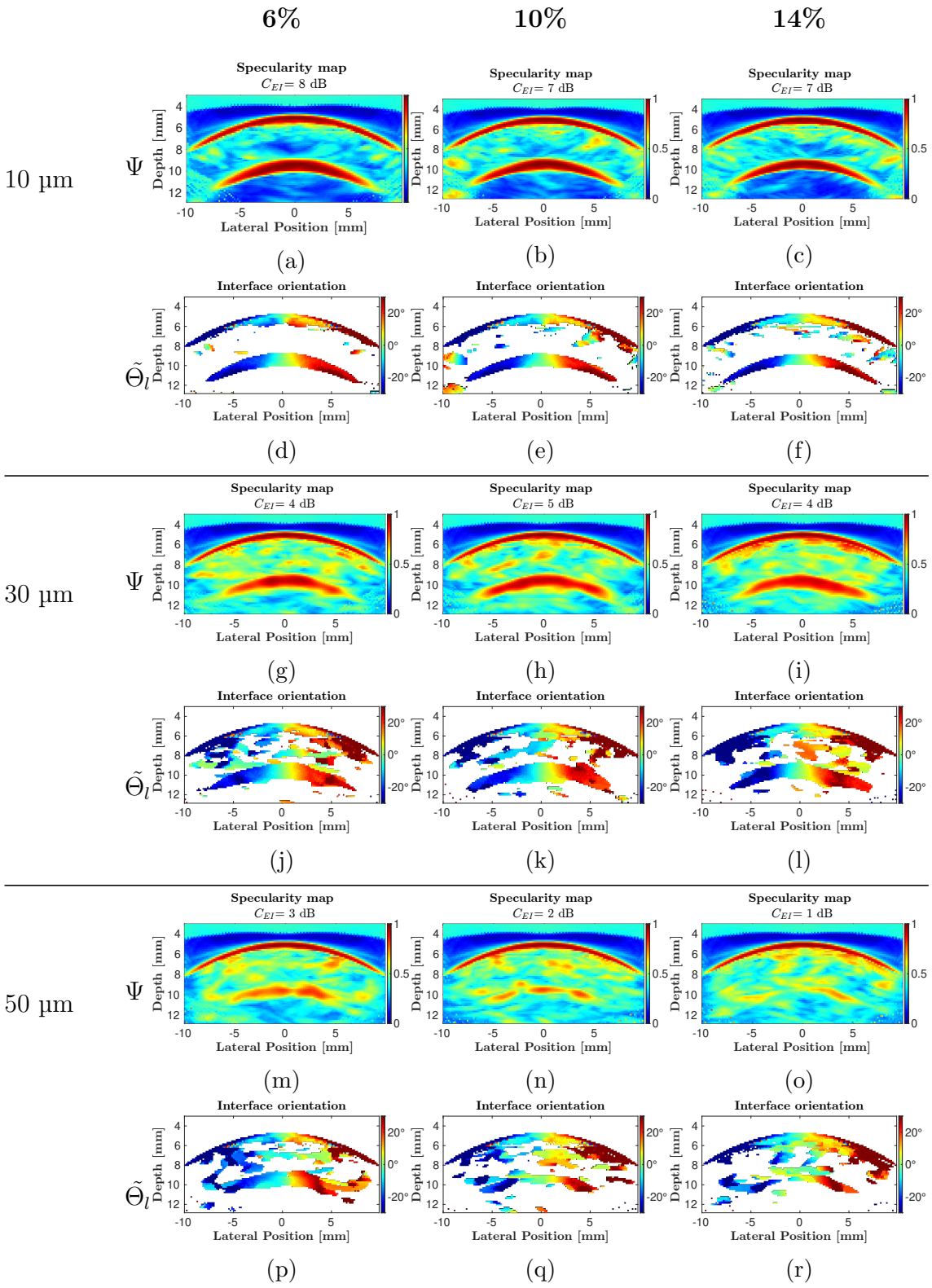

Figure 5.29: Specularity maps Ψ and corresponding thresholded orientation maps $\tilde{\Theta}_l$ for pixel with specularity greater than 0.5 for simulation configuration with curved bone interfaces. The diameter of the pores is 10 µm (panels (a) to (f)), 30 µm (panels (g) to (i)) and 50 µm (panels (m) to (r)). Cortical porosity: 6% (first column), 10% (second column) and 14% (last column). In each map of specularity C_{EI} is calculated

probability at the endosteal surface decreases slightly with porosity.
Within the cortical bone, probability values are low but higher than those found

for flat interfaces (at some spots values approaches 0.5). Specularity within cortical bone increases with porosity and at 10 and 14% porosity some bright spot are observed inside bone cortex. However, the extent of these particular spots does not allow us to highlight a specular structure. Furthermore, the randomness of the corresponding estimated specular orientation tell us that these values are strong speckle contributions. These values are consistent with the simulation configuration. Visibility of the endosteal surface is good: $C_{EI} = 7\ dB$ but lower than the corresponding configuration with flat interface. We can also remark that specularity of pixels below the internal interface are lower than specularity of pixels inside the cortex.

Specularity of the internal interface decreases with pore diameter. Specularity of pixels inside the cortex increases with pore diameter and for microstructure with pore diameter of 50 µm, we obtain low C_{EI} values : $C_{EI} = 2\ dB$ for porosities of 6 and 10 % and $C_{EI} = 1\ dB$ for porosity of 14% (panels (m)-(r) Figure 5.29).

5.4.2.2 Specular images compared to DAS image

Planar interfaces. Figure 5.30 shows the reconstructed images for all simulated configurations with flat interfaces. The images reconstructed with DAS beamforming are compared to the images reconstructed with specular beamforming. C_{EI} is given for each image. Qualitatively, we can see that with increasing porosity and individual pore diameter, speckle intensity inside bone increases and approaches the intensity of the endosteal interface.

For pore diameters of 10 µm (panels (a)-(c) of Figure 5.30), the endosteal interface is well distinguished from the inner bone cortex. For both beamforming algorithms, the periosteal and endosteal interfaces are clearly visible as bright zones centered respectively at 5 and 9 mm-depth as expected. C_{EI} values are ranging from 20.5 to 23.6 dB for DAS image and from 31.1 to 35.7 dB for specular images. C_{EI} values of specular images are always greater than those of DAS images. Specular beamforming improved the visibility of the endosteal interface by 10 dB. The texture of the interfaces is smoother in specular images and the speckle inside the cortex is lower.

For pore diameters of 30 µm (panels (d)-(f) of Figure 5.30), the endosteal interface is distinguished from the inner bone cortex. For both beamforming algorithms, the periosteal and endosteal interfaces are visible but the intensity of the speckle has increased. C_{EI} values are ranging from 10.6 to 12.3 dB for DAS images and from 16.5 to 18.7 dB for specular images. Here again, C_{EI} values of specular images are always greater than those of DAS images. Specular beamforming improved the visibility of the endosteal interface by 6 dB. In specular images, the texture of the interfaces is smoother and the speckle inside the cortex is lower.

For pore diameters of 50 µm (panels (g)-(i) of Figure 5.30), the endosteal interface is hardly distinguished from the inner bone cortex. For both beamforming algorithms, the periosteal interfaces are clearly visible but the intensity of the speckle increased and the endosteal interface vanished. For 6 and 10 % porosity, the interfaces are better defined in specular image but for 14% porosity, both DAS and specular images fail to reveal the endosteal surface. C_{EI} values are ranging from 3.2 to 5.8 dB for DAS images and from 5.1 to 9.5 dB for specular images.

Curved interfaces. Figures 5.31 shows the reconstructed images for configurations with curved interfaces.

For pore diameter of 10 µm (panels (a)-(c) of Figure 5.31), for both beamforming

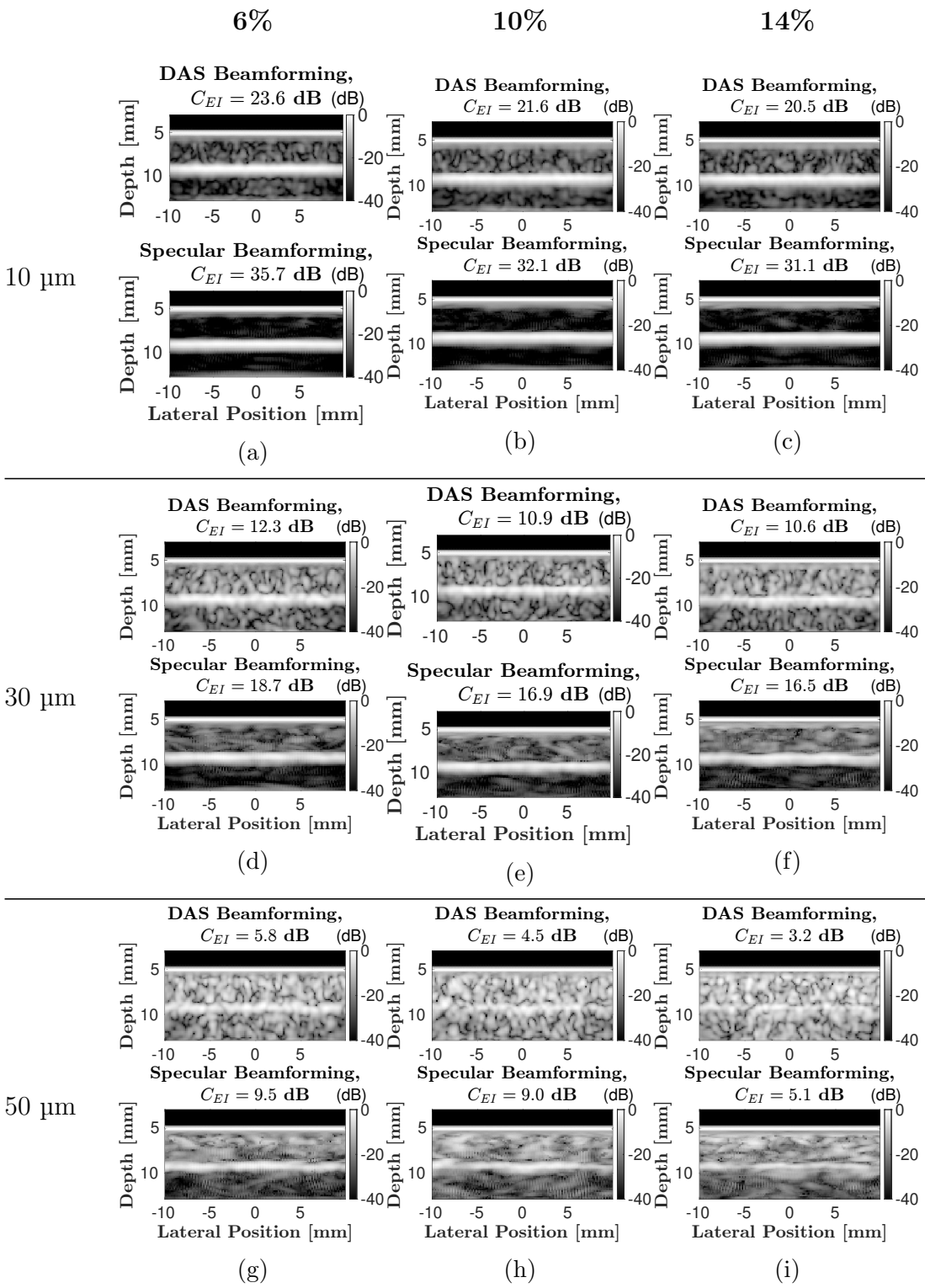

Figure 5.30: Reconstructed ultrasound images for simulated configurations with planar interfaces. Reconstruction was performed using a Delay-and-Sum (DAS) beamformer (top row images: panels a-c) and a specular beamformer (bottom row: panels d-f). The microstructure's pore diameter is 10 µm. Panels a and d correspond to a cortical porosity of 6%, panels b and e correspond to a cortical porosity of 10%, and panels c and f correspond to a cortical porosity of 14%. Each DAS image is reconstructed using an optimized receive f-number of 0.5. The intensity is log-compressed and displayed with a dynamic range of 40 dB.

algorithms, the periosteal and endosteal interfaces are clearly visible. With this geometry, due to the smaller transmitted energy of ultrasound at the periosteal

interface (critical angle), C_{EI} values are smaller than for flat interfaces: ranging 20-23 dB for DAS images and ranging 26-29 dB for specular images. Endosteal visibility metric is increased by 6 dB. For specular images, speckle within the cortex is very low compared to DAS images.

For individual pore diameter of 30 μm (panels (d)-(f) of Figure 5.31), for both beamforming algorithms, the periosteal and endosteal interfaces are visible. C_{EI} values are ranging from 8.8 to 11.6 dB for DAS images and from 11.8 to 15.6 dB for specular images. Specular beamforming increased endosteal visibility metric by 3-4 dB.

For individual pore diameter of 50 μm (panels (g)-(i) of Figure 5.31), C_{EI} values are ranging from 2.7 to 5 dB for DAS images and from 1.9 to 5 dB for specular images. For cortical porosity of 6 and 10%, specular beamforming gives same C_{EI} as DAS beamforming. However, we can see from panel (g) of Figure 5.31 that the endosteum is qualitatively more visible in the specular image than in the DAS image. At 14%, C_{EI} of DAS image (2.7 dB) is better than C_{EI} of specular image (2.3 dB). However, we can not say visually that DAS image is better than specular image. This is due to the fact that at 10 and 14% porosity, the level of noise is very high and speckle inside cortex is considered as specular reflections. This is consistent with the results on the specularity of the reflections in Figure 5.29.

5.4.3 Summary and discussion

Quantitative results regarding the endosteal interface visibility are summarized in Figure 5.32. For a constant porosity, C_{EI} values obtained from DAS images and specular images are plotted against the individual pore diameter of the simulation medium. In both beamforming algorithms, C_{EI} shows a decreasing trend with increasing pore diameter as expected from results of Chapter 3.

In the case of planar bone interfaces, specular beamforming consistently improves the C_{EI} contrast compared to DAS beamforming (panel 5.32a). For a pore diameter of 10 μm, there is an approximate 10 dB increase in contrast for all porosities. However, as the pore diameter increases, this enhancement diminishes, reaching nearly 3 dB at 50 μm. This diminishing trend is attributed to the correlation between speckle noise and the specular model. With a larger pore diameter, more speckle noise is considered as specular reflection (as observed in the increased specularity from panels (a)-(f) to panels (m)-(r) of Figure 5.30). Consequently, the speckle in specular images intensifies, resulting in a reduction in C_{EI}.
When bone interfaces are curved (panel 5.32b), the contrast improvement is smaller. For a pore diameter of 10 μm, there is an approximately 6 dB increase across all porosities and no increase for a pore diameter of 50 μm. This is attributed to a curved external interface reducing transmitted power and a curved internal interface decreasing power recorded by the probe.

We introduced the parameter η in Equation 5.17 and 5.18 as the specular tolerance and experimented with various values. As illustrated in figure 5.33, when η is too close to zero, it results in high noise levels, leading to poor interface contrast. Conversely, if η is too close to 1, the specular signal from the true specular orientation Θ_l interferes destructively with off-axis signals, resembling a Delay-and-Sum (DAS) image. Therefore, choosing an appropriate tolerance is crucial. The optimal values determined for η were 0.1 for planar bone surfaces and 0.25 for curved bone surfaces. The higher value for curved geometry is due to the wider spread of the specular transform of a curved reflector compared to that of a planar reflector.

Maps of specularity (Ψ) and specular orientation ($\tilde{\Theta}_l$) provide valuable infor-

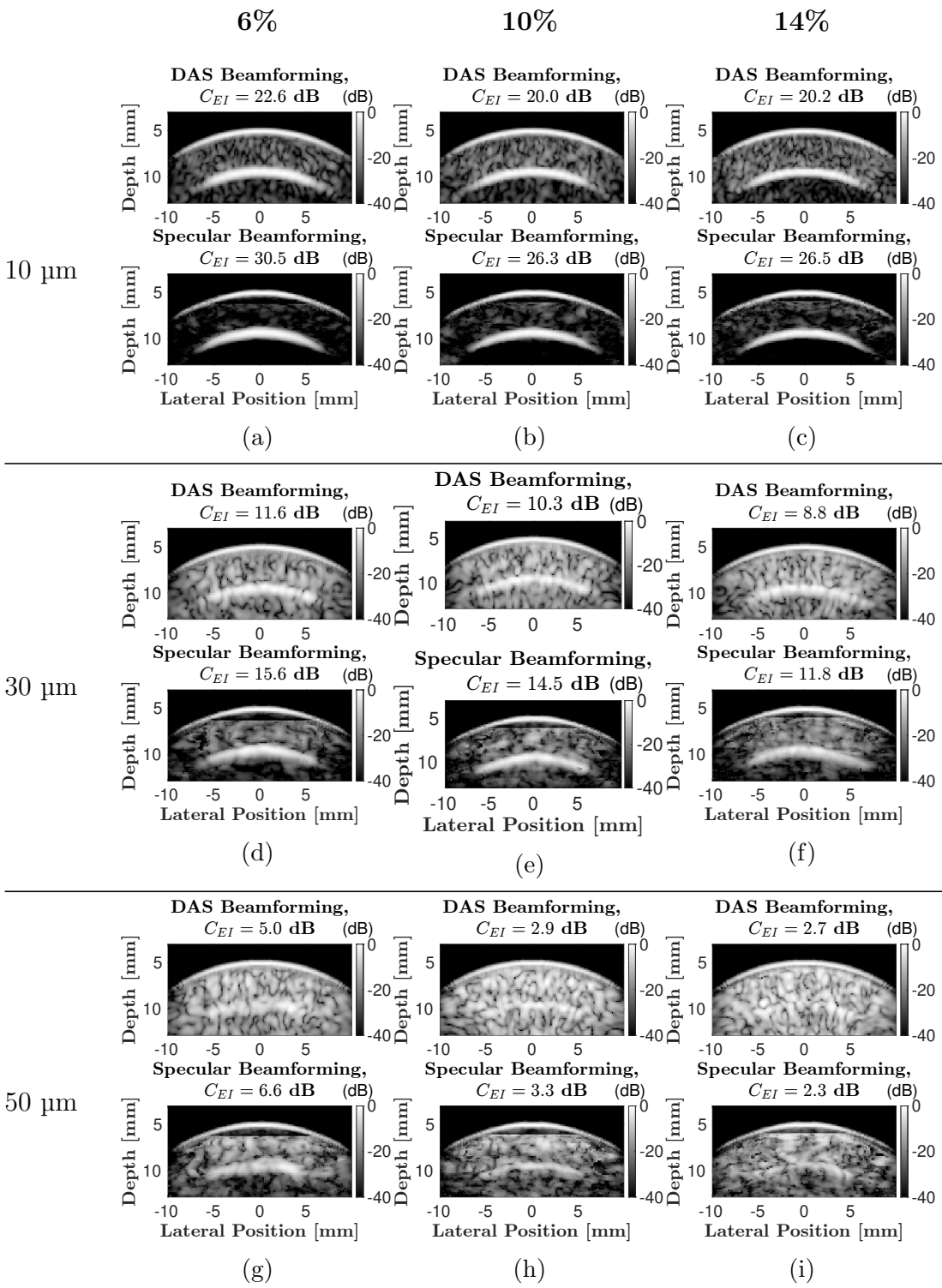

Figure 5.31: Reconstructed ultrasound images for simulated configurations with curved interfaces. Reconstructions were performed using a Delay-and-Sum (DAS) beamformer (top row images: panels a-c) and a specular beamformer (bottom row: panels d-f). The microstructure's pore diameter is 10 μm. Panels a and d correspond to a cortical porosity of 6%, panels b and e correspond to a cortical porosity of 10%, and panels c and f correspond to a cortical porosity of 14%. Each DAS image is reconstructed using an optimized receive f-number of 0.5. The intensity is log-compressed and displayed with a dynamic range of 40 dB

mation into the nature of reflectors within the medium, offering information about their physical parameters. These maps are useful for detecting and characterizing

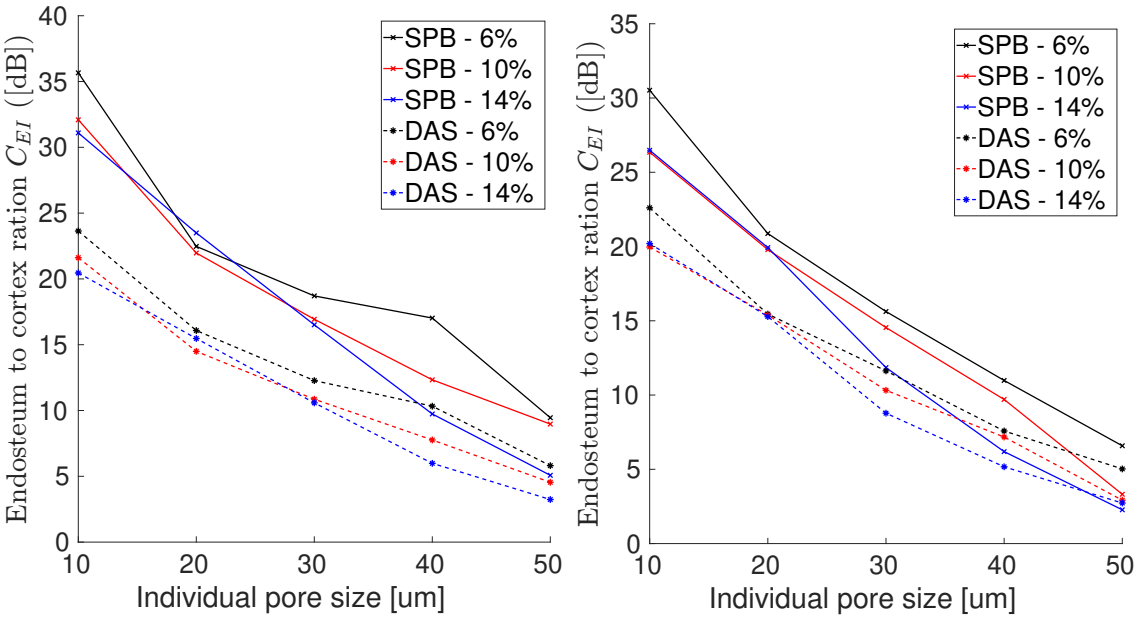

(a) Planar interfaces. (b) Curved interfaces.

Figure 5.32: Comparison of endosteal interface visibility (C_{EI}) obtained with Delay-and-Sum (DAS) beamforming and specular beamforming. The metrics are plotted for each porosity considering individual pore size. Panel (a) illustrates the comparison for planar interfaces, while panel (b) shows the comparison for curved interfaces.

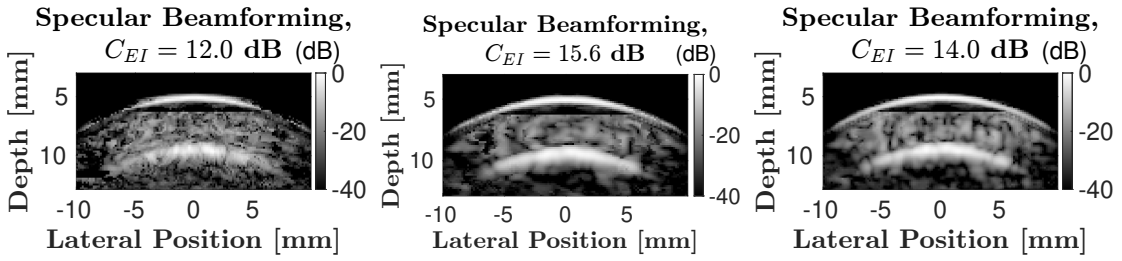

(a) (b) (c)

Figure 5.33: Demonstration of the impact of the parameter η on reconstructed ultrasound images. Three panels display images reconstructed with different η values: $\eta = 0$ in panel (a), $\eta = 0.25$ in panel (b), and $\eta = 0.5$ in panel (c). Each image corresponds to a pore size of 30 μm, with a cortical porosity of 6%.

specular structures. However, it is crucial to acknowledge that the resulting images may not be directly comparable to anatomical images, primarily due to the high specularity of non-specular structures (Ψ ranges from 0.2 to 0.5). Therefore, the use of I_{sp} provides a more natural ultrasound image at which signal-to-noise ratio is optimum.

In this simulation study, we simplified the representation of the bone layer by assuming homogeneity with pores having a single pore size. However, in reality, cortical microstructure is more complex, consisting of pores with various sizes. The objective of this chapter was to explore the influence of different pore sizes on specular imaging, considering diameters ranging from 10 to 50 µm. It is worth noting that for larger pore diameters, the cumulative scattering by all pores becomes excessive, posing challenges in obtaining clear ultrasound images of the cortex. For the application of specular beamforming to more realistic bone datasets, we turn to the next chapter, where the method is applied to *ex vivo* and *in vivo* bone ultrasound

data.

5.5 Conclusion

In this chapter, we presented a beamforming algorithm grounded in the principles of reflection and refraction to enhance specular structures. Previous works illustrated that incorporating the physics of specular reflection in beamforming improves the visibility of planar specular objects within a homogeneous medium. The originality of this present work was to address curved specular objects in a multi-layer heterogeneous medium, taking into account refraction. The goal was to decrease intra-cortical speckle noise and enhance specular reflections from the bone-soft tissues interfaces.

The algorithm was implemented and tested on simulated bone datasets designed to replicate cortical bone with varying microstructures. We introduced a metric, denoted as C_{EI}, to quantify the visibility of the endosteal interface. Comparative analyses were conducted between the specular images generated using our algorithm and those obtained through DAS imaging. Notably, specular images exhibited enhanced visibility for microstructures characterized by pore diameters smaller than 50 µm.

Bibliography

[1] Vincent Perrot, Maxime Polichetti, François Varray, and Damien Garcia. So you think you can DAS? A viewpoint on delay-and-sum beamforming. *Ultrasonics*, 111:106309, March 2021.

[2] Guillaume Renaud, Pieter Kruizinga, Didier Cassereau, and Pascal Laugier. In vivo ultrasound imaging of the bone cortex. *Physics in Medicine & Biology*, 63(12):125010, June 2018. Publisher: IOP Publishing.

[3] Sébastien Salles, Jami Shepherd, Hendrik J. Vos, and Guillaume Renaud. Revealing Intraosseous Blood Flow in the Human Tibia With Ultrasound. *JBMR Plus*, 5(11):e10543, 2021. _eprint: https://onlinelibrary.wiley.com/doi/pdf/10.1002/jbm4.10543.

[4] M. Vogt, J. Opretzka, and H. Ermert. Parametric imaging of specular reflections and diffuse scattering of tissue from multi-directional ultrasound echo signal data. In *2008 IEEE Ultrasonics Symposium*, pages 1963–1966, November 2008. ISSN: 1051-0117.

[5] Raja Sekhar Bandaru, Anders Rasmus Sornes, Jeroen Hermans, Eigil Samset, and Jan D'hooge. Delay and Standard Deviation Beamforming to Enhance Specular Reflections in Ultrasound Imaging. *IEEE Transactions on Ultrasonics, Ferroelectrics, and Frequency Control*, 63(12):2057–2068, December 2016. Conference Name: IEEE Transactions on Ultrasonics, Ferroelectrics, and Frequency Control.

[6] Ryo Nagaoka, Jens E. Wilhjelm, and Hideyuki Hasegawa. Preliminary study on the separation of specular reflection and backscattering components using synthetic aperture beamforming. *Journal of Medical Ultrasonics*, 47(4):493–500, October 2020.

[7] Alfonso Rodriguez-Molares, Ali Fatemi, Lasse Løvstakken, and Hans Torp. Specular Beamforming. *IEEE Transactions on Ultrasonics, Ferroelectrics, and Frequency Control*, 64(9):1285–1297, September 2017. Conference Name: IEEE Transactions on Ultrasonics, Ferroelectrics, and Frequency Control.

[8] Gayathri Malamal, Hans-Martin Schwab, and Mahesh Raveendranatha Panicker. Enhanced Needle Visualization With Reflection Tuned Apodization Based on the Radon Transform for Ultrasound Imaging. *IEEE Transactions on Ultrasonics, Ferroelectrics, and Frequency Control*, 70(11):1482–1493, November 2023. Conference Name: IEEE Transactions on Ultrasonics, Ferroelectrics, and Frequency Control.

[9] Gayathri Malamal and Mahesh Raveendranatha Panicker. On the physics of ultrasound transmission for in-plane needle tracking in guided interventions. *Biomedical Physics & Engineering Express*, 9(3):035018, March 2023. Publisher: IOP Publishing.

[10] Damien Garcia. Make the most of MUST, an open-source Matlab UltraSound Toolbox. In *2021 IEEE International Ultrasonics Symposium (IUS)*, pages 1–4, September 2021. ISSN: 1948-5727.

[11] M. Karaman, Pai-Chi Li, and M. O'Donnell. Synthetic aperture imaging for small scale systems. *IEEE Transactions on Ultrasonics, Ferroelectrics, and Frequency Control*, 42(3):429–442, May 1995. Conference Name: IEEE Transactions on Ultrasonics, Ferroelectrics, and Frequency Control.

[12] Jørgen Arendt Jensen, Svetoslav Ivanov Nikolov, Kim Løkke Gammelmark, and Morten Høgholm Pedersen. Synthetic aperture ultrasound imaging. *Ultrasonics*, 44:e5–e15, December 2006.

[13] Patrick Stähli, Maju Kuriakose, Martin Frenz, and Michael Jaeger. Improved forward model for quantitative pulse-echo speed-of-sound imaging. *Ultrasonics*, 108:106168, December 2020.

[14] Emmanuel Bossy. SimSonic: free fdtd software for the simulation of ultrasonic waves propagation.

[15] Amadou Sall Dia, Guillaume Renaud, Aida Hejazi Nooghabi, and Quentin Grimal. The influence of intra-cortical microstructure on the contrast in ultrasound images of the cortex of long bones: A 2D simulation study. *Ultrasonics*, 127:106831, January 2023.

Chapter 6

Applications of specular beamforming

Contents

6.1 Introduction

In chapter 5, we introduced specular beamforming for a multi-layer medium and tested its performance on synthetic dataset designed to replicate cortical speckle with varying microstructures. We demonstrated that the algorithm compared to DAS yields better endosteal interface visibility for microstructures characterized by pore diameters smaller than 50 µm.

The objective of this present chapter is to evaluate the efficacy of specular beamforming in improving the visualization of bone geometry using both *ex vivo* and *in vivo* data. In the *ex vivo* datasets, we have reference high resolution X-ray images and the geometry is fully known. The *in vivo* data were obtained under conditions closely resembling those encountered in clinical settings. The images obtained with the specular algorithm are compared to DAS algorithm.

6.2 Materials & methods

6.2.1 Data acquisitions

6.2.1.1 *Ex vivo* data

We used *ex vivo* data described in Chapter 4. Briefly, cortical bone samples were extracted from five human femoral shafts selected from a dataset comprising ten femurs obtained from female subjects aged between 66 and 98 years. The samples

were immersed in water and scanned using a fully programmable ultrasound system (Vantage, Verasonics Inc., Redmond, WA, USA). The scanning scheme employed a synthetic aperture protocol ([1, 2]) in which each element in the array was sequentially activated, followed by a full array recording of the received echo signals. A phased-array ultrasound transducer with 96 elements operating at the central frequency of 2.5 MHz (P4-1 ATL/Philips, Bothell, WA, USA; pitch 0.295 mm) was used. The emitted pulse had a -3dB bandwidth of 1.33 MHz. A complete ultrasound acquisition resulted in a total of 96×96 pulse-echo signals.

The samples are approximately 7 cm long, while the elevation of the probe is around 1.5 cm. Therefore, the sample is divided into 4 equal subvolumes along bone axis. Ultrasound recordings were obtained for a subvolume of every sample, with the setup illustrated in Figure 6.1. The probe was positioned in front of the sample, slightly submerged in water. Acquisitions were repeated 10 times with repositioning, guided by real-time visualization to adjust the images accurately. Sample 4 from Chapter 4 was excluded from this study due to its high heterogeneity, posing challenges in estimating ultrasonic wave speed.

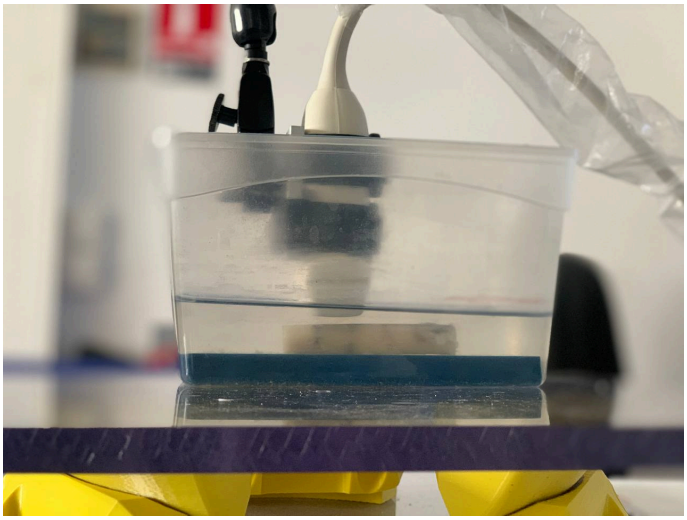

Figure 6.1: Experimental setup for ultrasound data acquisitions *ex vivo* , with the probe positioned in front of the sample, slightly submerged in water

6.2.1.2 *In vivo* data

We used *in vivo* data presented in Chapter 2. Briefly, the study involved 11 healthy male participants aged between 24 and 31 years. Informed written consent was obtained from each participant for research purposes in compliance with the legal requirements of the French Code of Public Health. Data was acquired from the middle of the tibia (mid-diaphysis) and the one-third proximal tibia (proximal third). The length of the tibia was considered as the distance between the apex of the medial malleolus and the distal patellar apex.

The same ultrasound system and phased array used in the *ex vivo* study were employed for the *in vivo* measurements. The scanning scheme also used a synthetic aperture. Acquisitions were repeated at each site five times with repositioning, guided by real-time visualization to ensure accurate adjustment of the images (Fig(ure 6.2). This resulted in 20 ultrasound acquisitions per subject. In this Chapter, we choose the ultrasound image corresponding to the first ultrasound acquisition obtained at the proximal-third tibia.

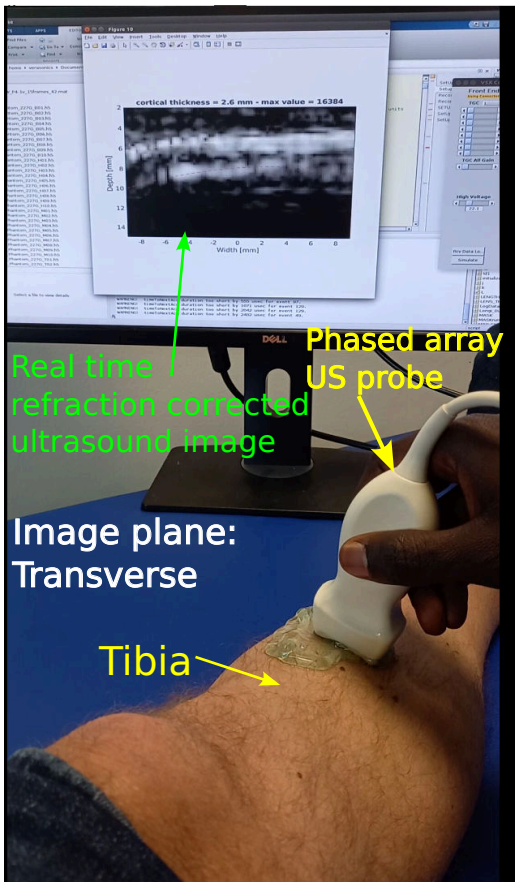

Figure 6.2: Configuration for acquisition of ultrasound data *in vivo*. Probe is placed perpendicular to bone axis (transverse)

6.2.2 Ultrasound image reconstruction

The image reconstruction technique employed in this study follows the principles outlined in Chapters 1, 2 and 5.

Speed of sound estimation. For *in vivo* data, the wave speeds in cutaneous tissues and in cortical bone estimated using an autofocus approach and reported in Chapter 2 are used. For *ex vivo* data, the wave speed in cutaneous tissues was estimated using the head wave propagating at the interface between the probe and water. The wave speed in cortical bone was estimated using autofocus, as described and reported in Chapter 4.

Beamforming with delay-and-sum algorithm. The DAS algorithm is used with a constant receive f-number of 0.5. This value was chosen after testing several f-numbers ranging from 0.1 to 2, with 0.5 providing the best image quality.

Beamforming with specular algorithm. For both *in vivo* and *ex vivo* data, the specular algorithm as detailed in Chapter 5 is used with an exact model h (obtained with Equation 5.28) and the approximation of planar specular interfaces.

For simulations in Chapter 5 a value of specular tolerance $\eta = 0.25$ was optimal. However, in this study, we determined that a specular tolerance η of 0.5 yielded optimal results for both *ex vivo* and *in vivo*. Lower values of η led to images with high levels of noise and noticeable discontinuities, while higher values did not significantly improve image quality. The effect of specular tolerance (η) on beamforming is

illustrated in Figure 6.3, where different values of η as introduced in Equation 5.18 are compared.

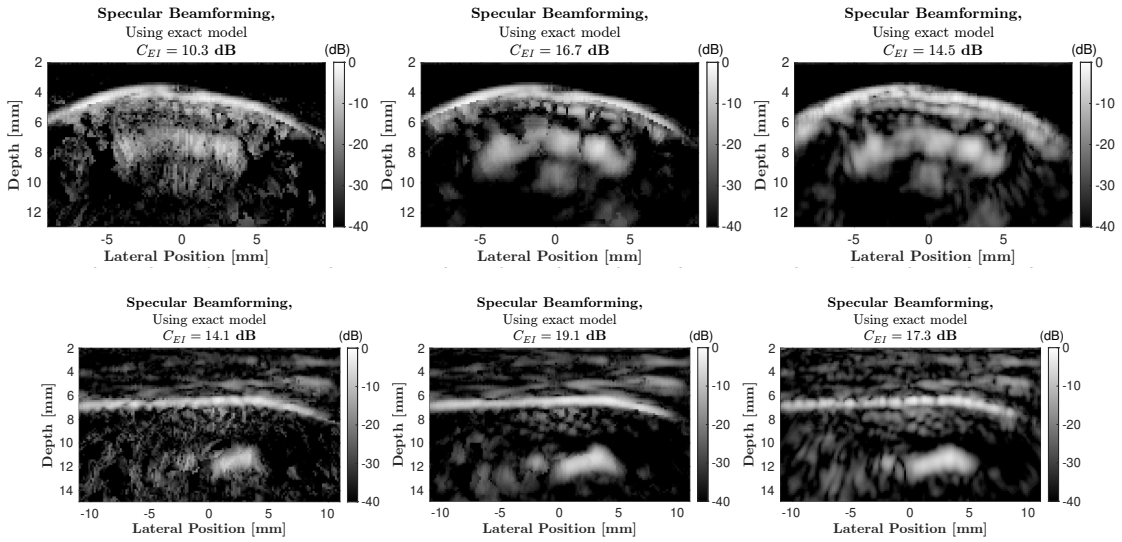

Figure 6.3: Illustration of the effect of specular tolerance (η) on beamforming. Top rows: *ex vivo* , bottom rows: *in vivo*. From left to right: $\eta = 0$, $\eta = 0.1$, $\eta = 0.5$

6.2.3 Endosteal interface visibility quantification

To evaluate the visibility of the endosteal surface, we use the endosteal interface contrast (C_{EI}) defined in Chapters 3 and 5, given by:

$$C_{EI} = \frac{\mu_E}{\mu_I}, \tag{6.1}$$

where μ_I and μ_E are the average image intensities in the center of the cortex and at the endosteal interface, respectively. The regions of interest (ROIs) used to quantify these contrasts are depicted in Figure 6.4.

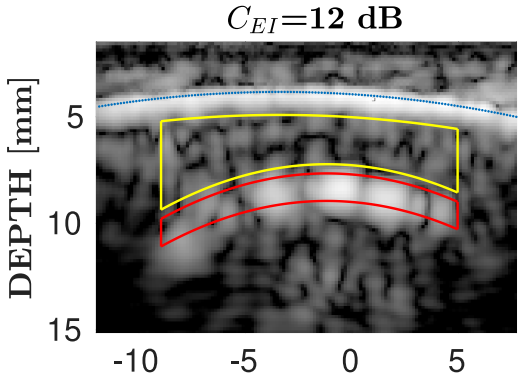

Figure 6.4: Region of interest to quantify endosteal interface visibility. Reconstructed image from *in vivo* data. The yellow and red ROIs are used to evaluate inner bone cortex and endosteum contrasts, respectively

It is important to note that the values of C_{EI} for both specular beamforming (BF) and Delay-And-Sum (DAS) images are computed from the segmentation of the external and internal interfaces performed on the ultrasound image produced by the DAS algorithm.

6.3 Results

6.3.1 *Ex vivo*

Figures 6.5, 6.6, 6.7, and 6.8 display the images obtained using Delay-and-Sum beamforming (DAS BF) and Specular beamforming (Specular BF) for each subvolume of samples 1, 2, 3, and 5, respectively. Each figure includes the following components for each subvolume:

- an example slice obtained with X-ray micro-CT
- an ultrasound image obtained with DAS beamforming
- an ultrasound image obtained with Specular BF
- a map of specularity
- a map of specular orientation for pixels with specularity greater than 0.4.

Table 6.1 provides a summary of the endosteal visibility metric (C_{EI}) computed for each sample and each subvolume, expressed in decibels (dB).

Sample	Beamformer	Subvol. 1	Subvol. 2	Subvol. 3	Subvol. 4	Mean(SD)
Sample 1	DAS BF	7.2	11.6	8.1	8.8	8.9(1.9)
	Specular BF	14.8	13.5	9.6	10.2	12.0(2.5)
	$C_{EI}^{sp} - C_{EI}^{das}$	7.6	1.9	1.5	1.4	3.1(3.0)
Sample 2	DAS BF	5.9	3.9	3.3	4.6	4.4(1.1)
	Specular BF	10.2	6.4	7.5	7.6	7.9(1.6)
	$C_{EI}^{sp} - C_{EI}^{das}$	4.3	2.5	4.2	3.0	3.5(0.9)
Sample 3	DAS BF	-0.7	-1.4	-1.1	-1.5	-1.2(0.4)
	Specular BF	-0.8	-1.0	1.4	0.4	-0.0(1.1)
	$C_{EI}^{sp} - C_{EI}^{das}$	-0.1	0.4	2.5	1.5	1.1(1.2)
Sample 5	DAS BF	-	-	-	-	-
	Specular BF	-	-	-	-	-
	$C_{EI}^{sp} - C_{EI}^{das}$	-	-	-	-	-

Table 6.1: Summary of endosteal visibility metric C_{EI} computed for each sample and each subvolume expressed in dB

For sample 1 (Figure 6.5), the endosteal interface is well observed for all subvolumes with DAS beamforming (C_{EI} ranging from 7.2 to 11.6 dB). Specular beamforming significantly increases the visibility of the endosteal interface, with C_{EI} ranging from 10.2 to 14.8 dB across the subvolumes. This corresponds to an increase ranging from 1.4 to 7.6 dB. Compared to DAS images, in specular beamforming images, the intra-cortical speckle is reduced, and the intensity of the endosteal interface is improved. Specularity maps display high specularities at the periosteal and endosteal interfaces (C_{EI} is 6 dB) and low specularities inside the cortex. The local orientation of the interface is retrieved with the map of specular orientations.

For sample 2 (Figure 6.6), the endosteal interface is also well observed for all subvolumes with DAS beamforming (C_{EI} ranging from 3.3 to 5.9 dB). Specular beamforming significantly increases the visibility of the endosteal interface, with C_{EI} ranging from 6.4 to 10.2 dB across the subvolumes. This corresponds to an increase ranging from 2.5 to 4.3 dB. Even for subvolumes with high porosities (subvolumes 2 and 3), the intra-cortical speckle is reduced in specular beamforming

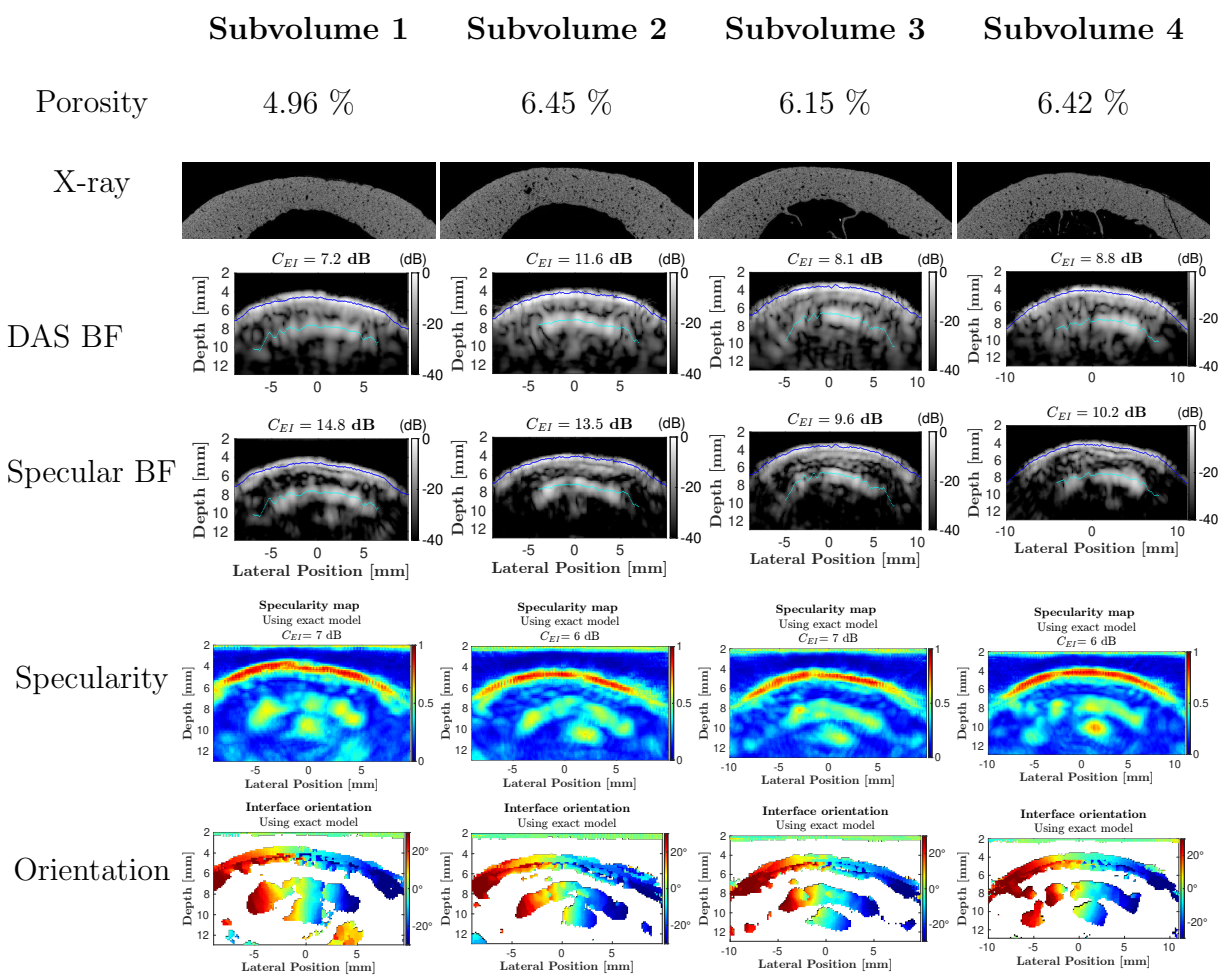

Figure 6.5: Comparison of ultrasound imaging techniques for each subvolume of sample 1. Each column corresponds to a subvolume, and each row from top to bottom displays the 3D porosity of the subvolume, the X-ray micro-CT slice, the ultrasound image obtained with Delay-and-Sum beamforming (DAS BF), the ultrasound image obtained with Specular beamforming (Specular BF), the specularity map (Ψ), and the orientation map for pixels with specularity greater than 0.4

images. In specularity maps, the intensity of the endosteal interface is highest for subvolumes with lower porosities (subvolumes 1 and 4) and moderate for higher porosities subvolumes. The local orientation of the interface is retrieved with the map of specular orientations.

For high porosity samples (sample 3 and 5), the endosteal interface does not exhibit significantly higher visibility than the intra-cortical speckle. For sample 3 (Figure 6.7) and subvolume 1, small negative C_{EI} values are found for both DAS and specular beamformed images. This means that the endosteal interface can be barely distinguished from the cortical speckle. Specular beamforming increases the intensity of the endosteal interface by approximately 0.4 to 2.5 dB for remaining subvolumes compared to DAS beamforming. The specularity maps exhibit moderate specularity values at the endosteal interface and inside the cortex.

For the most porous and most heterogeneous sample (sample 5), both DAS and specular BF fail to reveal the endosteal interface of the cortex. The image of the cortex is too thin, and the cortical thickness is less than the bone wavelength (Figure 6.8). Therefore, it is not possible to compute the metric of endosteal interface visibility (C_{EI}). However, we can observe in the reconstructed ultrasound images that the global speckle is highly reduced with specular BF compared to DAS BF.

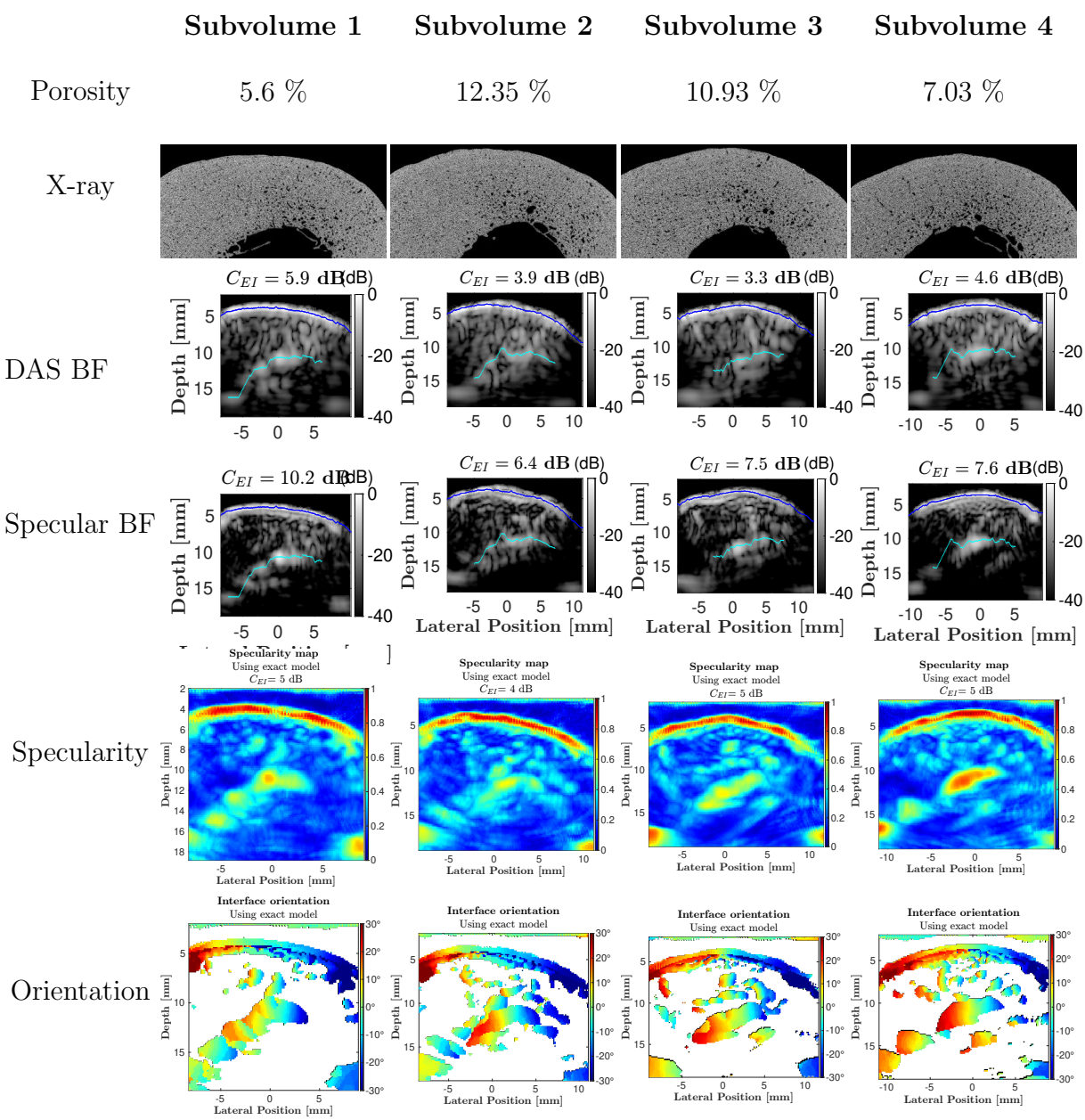

Figure 6.6: Same caption of Figure 6.5 applied to sample 2

The specularity map shows high specularities only at the periosteal interface and low specularities elsewhere.

Summary of the results. For all samples, the intra-cortical speckle is reduced with specular beamforming. The brightness of the endosteal interface of homogeneous samples (samples 1, 2 and 3) is increased with specular beamforming.

Exact model vs simplified model. In Chapter 5, we introduced specular beamforming with two different models of specular transform: an exact model h (obtained with Equation 5.28) and a simplified model h_0 (obtained with Equation 5.29). In Figure 6.9, a comparison between the images obtained with the two models is shown. Although the images obtained with the exact model yield less noise and better specular interface determination, the image obtained with the simplified model provides a good and comparable quality image. This suggests that the simplified model may offer a practical alternative in scenarios where computational efficiency or simplicity

	Subvolume 1	Subvolume 2	Subvolume 3	Subvolume 4
Porosity	11.54 %	12.35 %	10.93 %	7.03 %

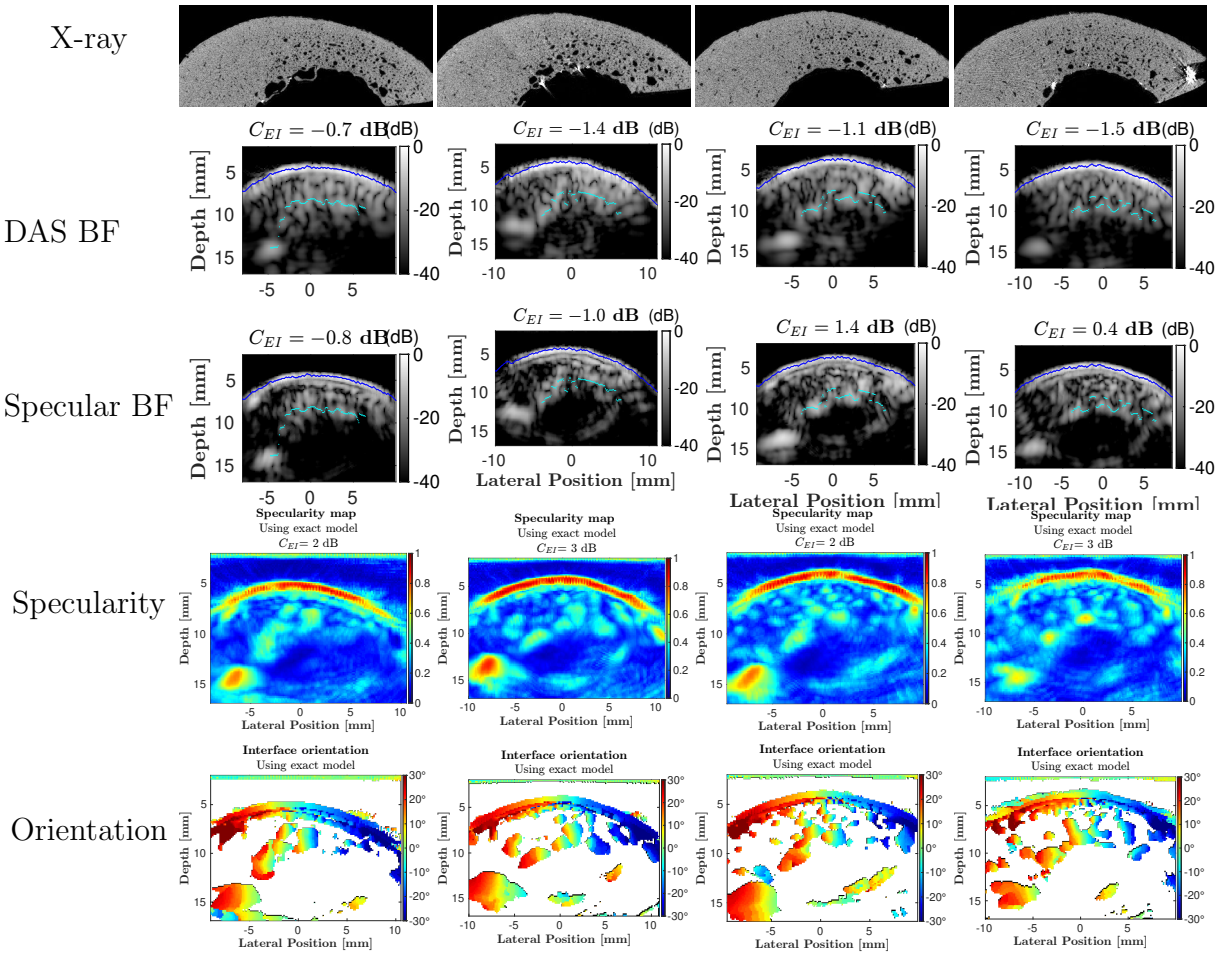

Figure 6.7: Same caption of Figure 6.5 applied to sample 3

is prioritized without sacrificing image quality significantly.

6.3.2 *In vivo*

In Figure 6.10, a comparison between DAS beamforming and Specular beamforming for *in vivo* data is presented. The reconstructed ultrasound images obtained with each beamforming algorithm are displayed for subjects 1 to 10 for only one representative measure per subject. DAS beamforming consistently yields images with good quality and good visibility of the endosteal interface across all subjects. However, within and after the cortex, there remains a significant presence of intra-cortical speckle.

On the other hand, Specular beamforming maintains good visibility of the endosteal interface while effectively reducing intra-cortical speckle compared to DAS beamforming. Over the 10 subjects, the DAS algorithm yields a mean and standard deviation (C_{EI}) of 10.1 dB (±3.9), while the Specular BF algorithm results in 13.0 dB (±5.3). This corresponds to an average increase of 3 dB.

Furthermore, an important effect of specular beamforming in the *in vivo* data, not always visible in the *ex vivo* images, is the reduction in speckle from the medullary cavity (after the endosteal interface) as well. This reduction in speckle both before and after the endosteal surface, while preserving a bright endosteal sur-

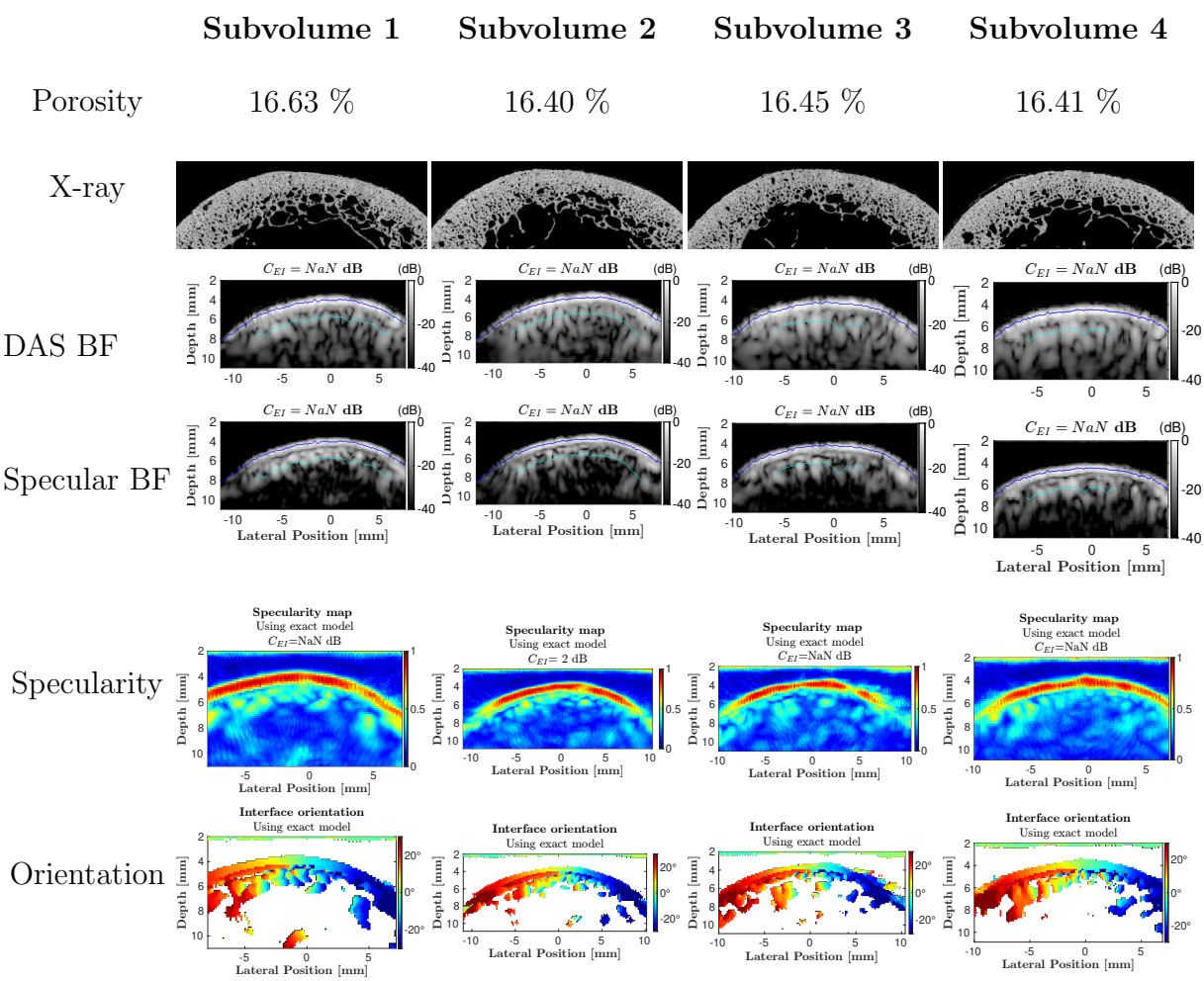

Figure 6.8: Same caption of Figure 6.5 applied to sample 5

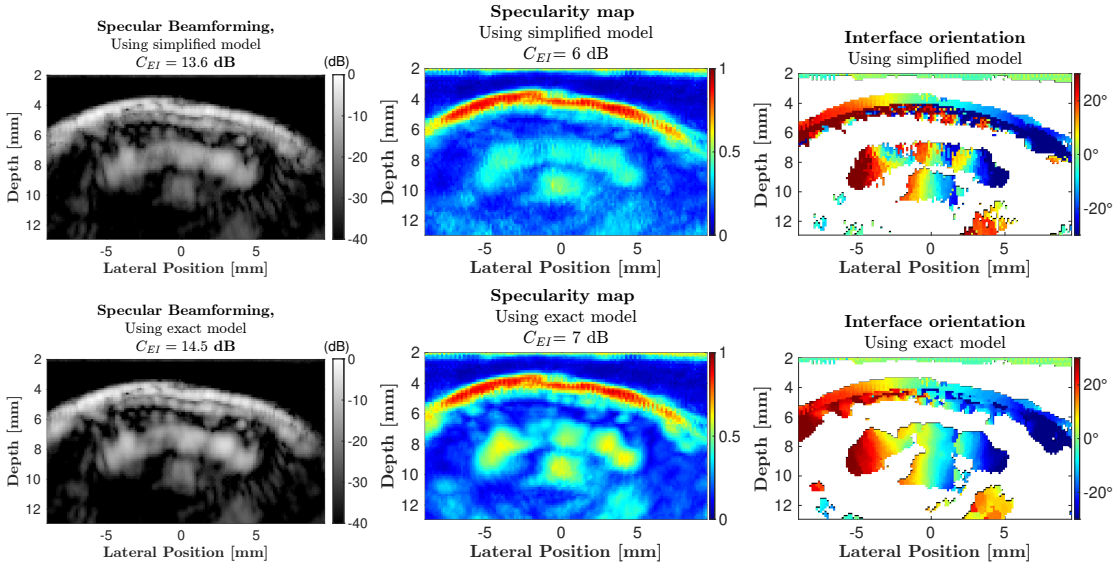

Figure 6.9: Comparison of images obtained using the simplified model (top row) and the exact model (bottom row) of specular transform. From left to right: Specular-only image, Specularity map, and Orientation map

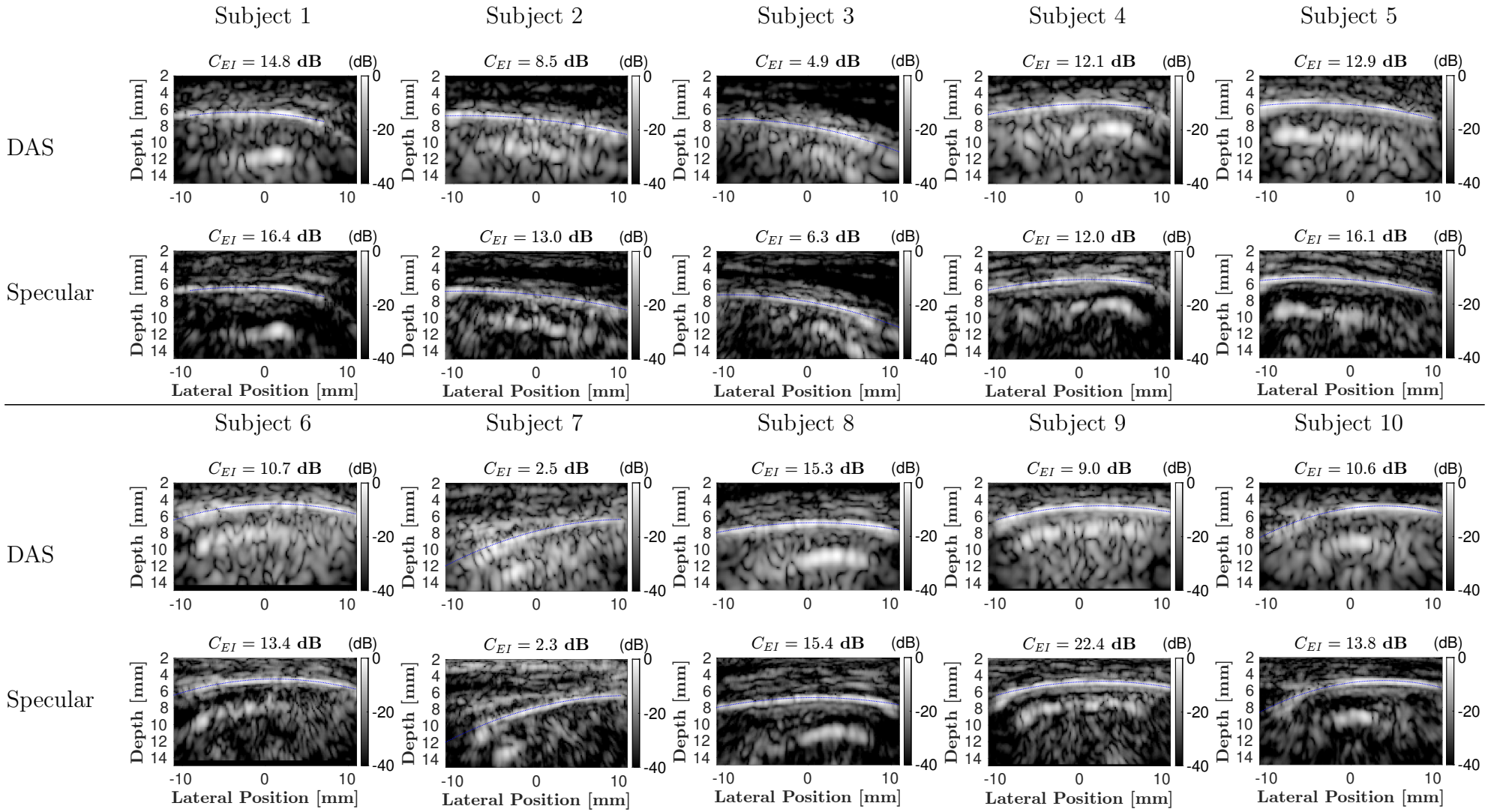

Figure 6.10: Comparison of DAS beamforming and specular beamforming for *in vivo* ultrasound imaging. Ultrasound images for subjects 1 to 10 are shown, with the blue dashed line representing the parabolic fit of the periosteal interface segmentation.

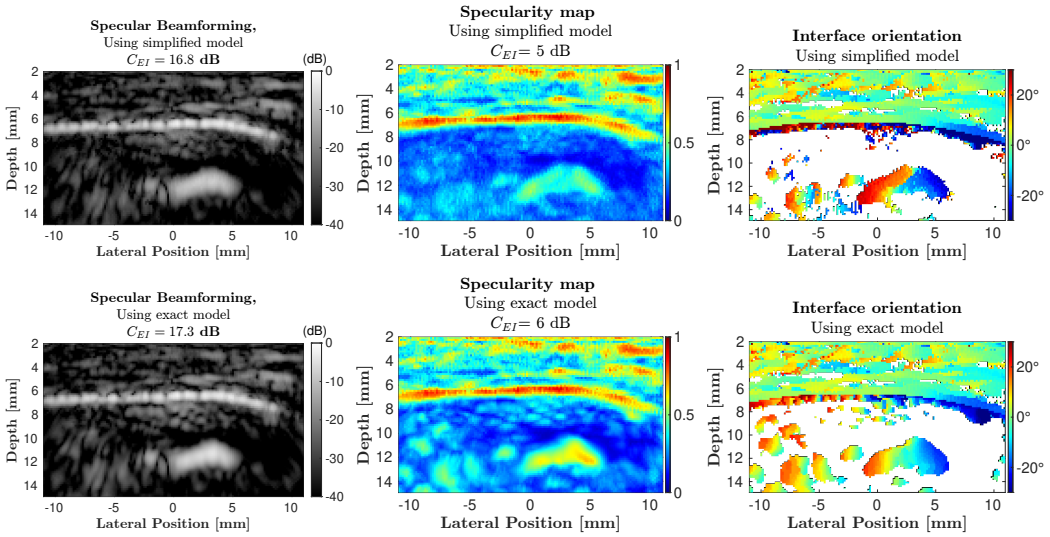

Figure 6.11: Comparison of *in vivo* images obtained using the simplified model (top row) and the exact model (bottom row) of specular transform. From left to right: Specular-only image, Specularity map, and Orientation map

face, enhances the overall contrast and image quality. However, it is worth noting that this improvement is not reflected in C_{EI}.

Despite the visual improvement observed with Specular beamforming, the metric of interface visibility (C_{EI}) may not accurately quantify this enhancement. There is significant variability in the degree of enhancement in C_{EI} observed from one subject to another, ranging from very high (e.g., 13 dB for subject 9) to very low (e.g. less than 1 dB for subjects 4, 7, and 8), despite the visually improved images obtained with Specular beamforming for these subjects. This suggests that C_{EI} might not be the most suitable metric for assessing the endosteal visibility, and alternative metrics may need to be considered to better evaluate the performance of Specular beamforming in *in vivo* ultrasound imaging.

Figure 6.12 presents the specularity (Ψ) and the local orientation maps ($\tilde{\Theta}_l$) of pixels with specularities greater than 0.4 for all subjects. For each subject, the top row displays the specularity maps, while the bottom row shows the corresponding local orientation maps.

The specularity of the periosteal interface appears consistently high across all subjects, with values exceeding 0.7, indicating robust specular reflections at this interface. Moderately high specularity values, exceeding 0.5, are observed at the endosteal interface, suggesting a notable specular reflection but to a lesser extent than the periosteal interface. Within the cortex, pixels with moderate specularity (greater than 0.5) are present but lack significant connectivity, implying that these areas may not represent genuine specular structures within the cortex.

The estimated local orientations align well with the observed geometry in the ultrasound images, indicating consistency between the specularity maps and the underlying bone structure.

In summary, the analysis of specularity combined with local orientation maps tells us that the bright interfaces present in the ultrasound images correspond to specular interface.

Exact model vs simplified model. In Figure 6.11, we show the images obtained with exact model compared to those obtained with simplified model. Beamformed images are of comparable quality but the specularity of the exact model is better.

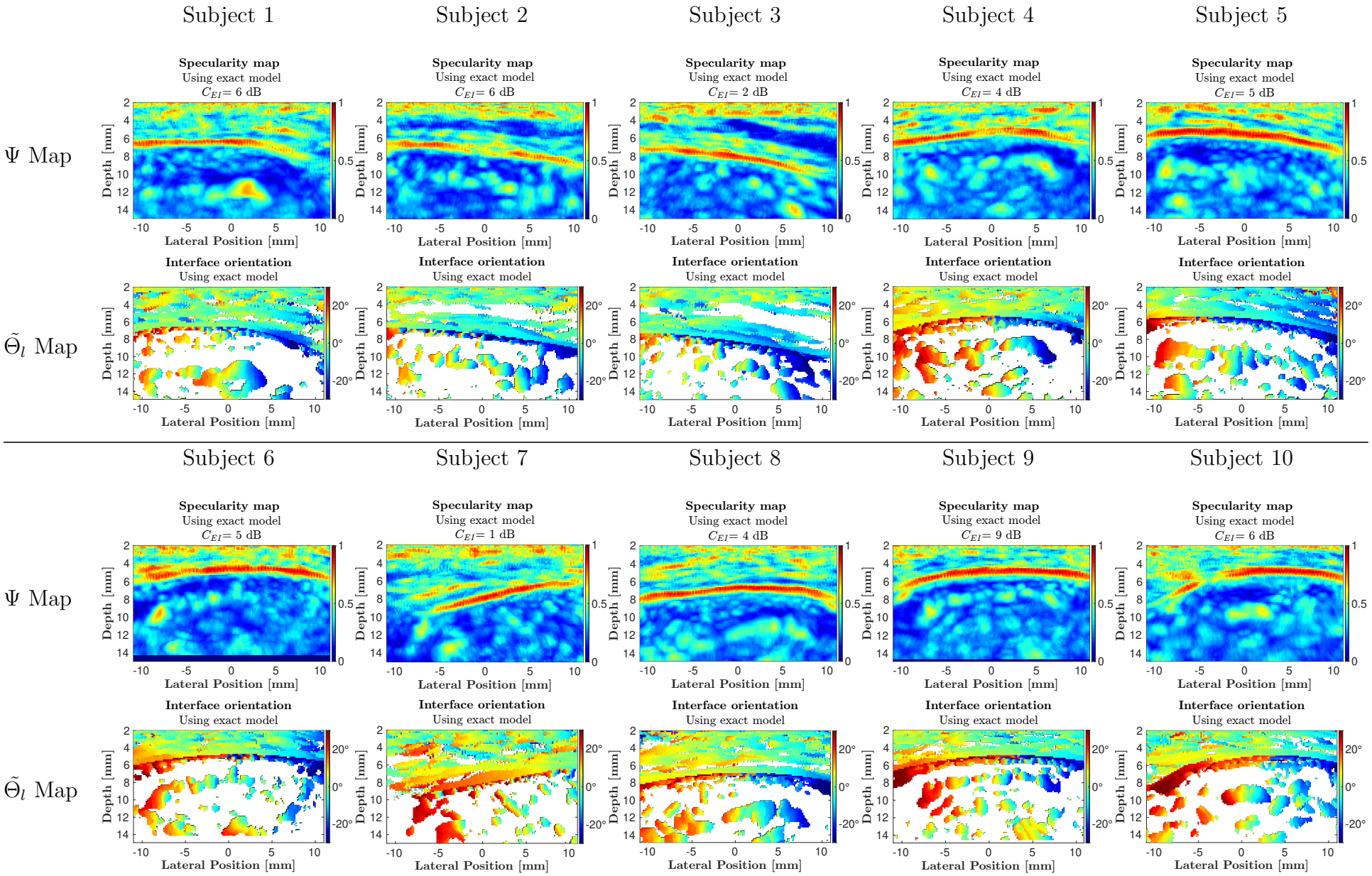

Figure 6.12: Specularities and corresponding specular orientation of *in vivo* ultrasound data. Images are shown for subject 1 to 10.

6.4 Conclusion & Discussion

In this chapter, we investigated the efficacy of considering the endosteal surface as a specular interface in enhancing its visibility in the ultrasound images. We applied specular beamforming to both *ex vivo* and *in vivo* human cortical bone. The images obtained are compared to those obtained using the beamforming method of Delay-And-Sum. A visibility metric for the interface was provided to quantify the improvements achieved.

Specular beamforming consistently enhances the visibility of the endosteal interface compared to DAS beamforming, as observed in both *ex vivo* and *in vivo* experiments. This enhancement is evidenced by higher endosteal visibility metric (C_{EI}) values obtained with specular beamforming. Notably, specular BF images exhibit significantly reduced speckle surrounding the endosteal interface while maintaining a bright interface, resulting in clearer images of bone geometry. The reduction of speckle from the marrow (medullary cavity) is particularly pronounced in the *in vivo* ultrasound images compared to the *ex vivo* images.

Despite improvements in image quality with specular beamforming, C_{EI} may not accurately quantify these improvements. C_{EI} does not consider the reduction of the speckle in the medullary cavity and in some *in vivo* cases, despite visual improvements in images obtained with specular beamforming, C_{EI} values may be lower.

Model curvature. In this chapter, we assumed planar specular interfaces in the computation of the model of specular transform. While this assumption simplifies the computational process, it becomes evident from the micro-CT images that the curvature of the samples is significant. As discussed in Chapter 5, this results in an underestimation of the specularity of the interface and inaccuracies in the specular orientation estimation. Therefore, although the assumption of a planar specular interface may be appropriate for certain applications where curvature effects are minimal or negligible, it is essential to acknowledge its limitations in this chapter.

Perspectives. Overall, the application of specular beamforming demonstrates promise for enhancing the quality of ultrasound imaging in bone tissue, offering improved visualization of endosteal interface and potentially aiding in improving the estimation of cortical thickness. However, further research is needed to optimize parameters, refine models, and develop more sensitive metrics to fully harness the benefits of specular beamforming in bone ultrasound imaging.

A combined analysis of specularity and local orientation maps can offer more information into the characteristics of the endosteal interface. By leveraging both outputs, it becomes possible to derive a novel quantity that assesses the roughness of the endosteal interface. This approach may provide a more comprehensive understanding of the interface's properties and enhance our ability to characterize bone microstructure accurately.

The wave speeds used for computing delays are obtained through an autofocus approach using a DAS algorithm applied by Renaud et al. to bone (see Chapter 2). However, employing this autofocus approach with a specular algorithm may lead to a more suitable and accurate estimation of the propagating wave speed. Additionally, the segmentation of periosteal and endosteal interfaces currently utilizes Dijkstra's algorithm on the DAS image. Considering the specific characteristics of specular beamforming, applying Dijkstra's algorithm directly to the specular BF image or to the specularity map may offer improved segmentation results.

The *in vivo* feasibility of real-time specular beamforming requires code optimization. Obtaining a DAS image is approximately 100 timesfaster than obtaining an specular BF with the exact model. The majority of the time for specular beamforming is dedicated to computing the specular model. Simplifying this model could lead to faster computation without significantly compromising image quality. Currently, the specular BF algorithm is fully implemented using MATLAB 2023.

The scope of this chapter is limited to analyzing the radial direction of bone (transverse) for both *in vivo* and *ex vivo* data. While it could be extended to include the longitudinal configuration, caution must be taken as the axial direction corresponds to the direction of the pores, potentially leading to specular structures inside the cortex.

Bibliography

[1] M. Karaman, Pai-Chi Li, and M. O'Donnell. Synthetic aperture imaging for small scale systems. *IEEE Transactions on Ultrasonics, Ferroelectrics, and Frequency Control*, 42(3):429–442, May 1995. Conference Name: IEEE Transactions on Ultrasonics, Ferroelectrics, and Frequency Control.

[2] Jørgen Arendt Jensen, Svetoslav Ivanov Nikolov, Kim Løkke Gammelmark, and Morten Høgholm Pedersen. Synthetic aperture ultrasound imaging. *Ultrasonics*, 44:e5–e15, December 2006.

Chapter 7

Conclusion

The global objective of this work was to test, further validate and improve intracortical bone ultrasound imaging, specifically for bones showing signs of osteoporosis. The achievement of this objective breaks down into three main points:

- Improve our understanding of the factors influencing the quality of bone ultrasound images, in particular the role of pores acting as scatterers and creating speckle.
- Complement the validation of the technique to measure material properties of bones of healthy subjects but also bones of older individuals.
- Explore the added value of using image reconstruction techniques tailored to the physics of wave propagation in bone, in particular specular reflections to improve contrast.

In Chapter 2, we introduced the estimation of the axial and radial wave speed (V^{axial} and V^{radial}) along with an anisotropy form parameter (ξ) of cortical bone using ultrasound imaging at the tibia of 11 healthy male volunteers. A model of weak transverse isotropy of the cortex was assumed, and the precision of the estimation is reported. Results show that ultrasound imaging can estimate the propagating wave speed with a precision error of a few percent for both the radial and axial directions of the bone.

In Chapter 3, through 2D numerical simulations, we studied the factors influencing the quality of bone ultrasound images. We used realistic cortical microstructure obtained from high-resolution Synchroton Radiation microcomputed tomography of the cortex of human femurs to simulate ultrasound wave propagation in the radial direction. The results suggested that with the increase of pore scattering, the speckle of the image increases, and at a certain level, the endosteal surface disappears from the images. Hence, high cortical porosity (typically larger than 10%) and the presence of large cortical pores are detrimental to image quality.

These findings were confirmed with an *ex vivo* study (Chapter 4). The same algorithm introduced in Chapter 2 was used to estimate V^{radial} and the cortical thickness. The ultrasound images were superimposed to reference x-ray micro-CT images. We found that the estimation of ultrasound wave speed, the reconstruction of the endosteal interface and the cortical thickness was successful for bones with homogeneous pore size distribution across the cortex. For degraded bone with prevalent large pores at the endosteal interface, these measurements were not accurate.

With this understanding gained from Chapter 3 and 4, we proposed to consider the endosteal interface as a specular reflector and to replace refraction-corrected DAS beamforming by a refraction-corrected specular beamforming. This algorithm is presented and detailed in Chapter 5 and tested on simulated bone datasets designed to replicate cortical bone with varying microstructures.

It is then applied to *ex vivo* and *in vivo* datasets in Chapter 6. A comparative analysis between the refraction-corrected DAS beamforming and the refraction-corrected specular beamforming showed that specular beamforming enhances the

brightness of the endosteal interface while significantly reducing the speckle inside bone and surrounding the endosteum.

In conclusion, this thesis confirmed that ultrasound imaging can be used to estimate cortical thickness and wave speed. The precision with which the radial and axial wave speeds are assessed seems sufficient to identify individuals with low cortical bone mechanical quality at risk of osteoporotic fracture. Our results suggest that the method can discriminate individuals with low, moderate and high porosity. This estimation should be extended to a clinical context to discriminate between osteoporotic and healthy patients. Furthermore, when incorporating the physics of specular reflection to the technique, it is possible to increase the quality of ultrasound images of the bone. This can help in (i) facilitating the measurement of cortical thickness in porous bones and (ii) improving the positioning of the probe during real-time acquisitions. Finally, this new algorithm gives information on the specularity of bone interfaces. As a perspective, we could use the full potentiality of this specularity for the derivation of a new measure that evaluates the roughness of the endosteal interface, thus giving a new marker of bone mechanical quality.

Despite these encouraging results, there is room for improvement. The limitation of the *ex vivo* study is the fact that it is limited to the transverse plane which is the plane of isotropy. A more complete *ex vivo* study should consider both the transverse and longitudinal planes for the estimation of cortical thickness and wave speed and the exploitation of the anisotropy of the bone.

Currently, the technique uses a probe with a linear array of transducers with an elevation of around 1.5 cm, and the received ultrasound data are averaged along the elevation. However, the contribution of the diffusion of pores is not the same across the elevation of the probe and bone surfaces might not be in the plane of elevation. Therefore, the use of a matrix array of transducers would benefit bone ultrasound imaging.

In this thesis, we only provided the measure of compressional wave speed and images produced are obtained with the compressional wave speed. However, bone being a solid material, both shear and compressional waves propagate. Exploring the wave speed of both compressional and shear wave could improve the classification of porous bones. Additionally, applying specular beamforming to mode-converted shear waves could yield different images that may offer a better bone image quality.

Appendix A

Estimating the bone matrix characteristics

The material properties of the bone matrix tissue used for the numerical simulations of the propagation of elastic waves were derived from experimental data as described below.

Mass density. The bone matrix mass density (ρ^m) was deduced from measurements of the apparent mass density (ρ) and cortical porosity (Ct.Por) of 55 cortical bone specimens from elderly donors [1] (the microstructures used in the present study came from the same samples). A linear regression between ρ and Ct.Por is determined:

$$\rho = \rho^m - 13.1 \times \text{Ct.Por}$$

where ρ^m is the intercept for a null porosity. The correlation between ρ and Ct.Por was strong: Adj-R^2 = 84.5 %, p= 2.43 10^{-23}, RMSE = 22.1 kg.m^{-3}. Finally, a value of 1996 kg.m^{-3} was found for ρ^m. Figure A.1 shows the values of ρ as a function of cortical porosity along with the linear fit.

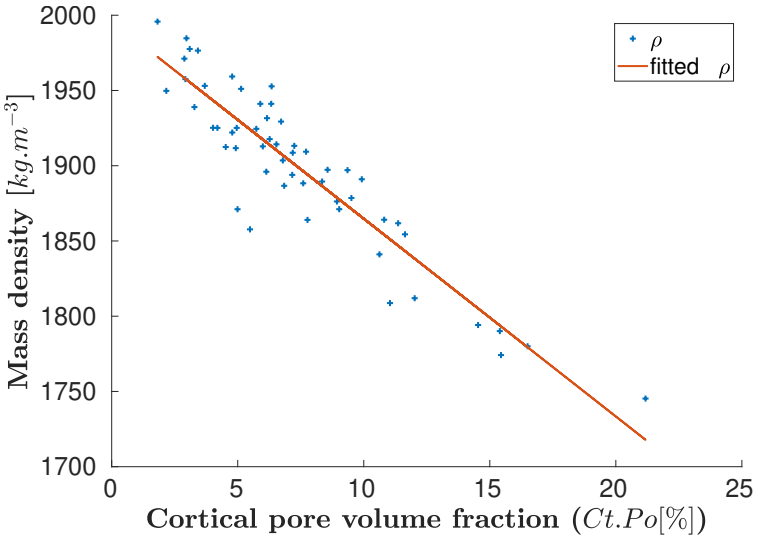

Figure A.1: Cortical bone apparent mass density (ρ) of the 55 human bone specimens of this study obtained by [1]. A regression linear model is fitted (red line).

Shear and compressional wave-speeds. Compressionnal and shear wave speeds in the bone matrix are deduced from ρ^m and experimental values of the matrix elastic coefficients C_{ij}^m (using Voigt notation, with $i, j = 1, 2, 3$) provided by Cai et al.[1] for the same bone specimens. For this study, V_1^m and V_{12}^m were used, they are respectively the velocities of longitudinal and compressional waves propagating in bone matrix in the plane perpendicular to the bone axis and with in-plane particle

motion. They are determined using:

$$V_1^m = \sqrt{\frac{C_{11}^m}{\rho^m}}, \quad \textit{and} \quad V_{12}^m = \sqrt{\frac{C_{66}^m}{\rho^m}}.$$

Cai et al. [1] reported $C_{11}^m = 24.5$ GPa and $C_{66}^m = 5.4$ GPa, from which values of 3496 m.s^{-1} and 1645 m.s^{-1} were deduced for V_1^m and V_{12}^m respectively.

Appendix B

Experimental ultrasonic velocity estimation for different cortical porosities

Cai et al [2] measured the stiffness tensor (C_{ij}), apparent mass density (ρ), and vascular porosity of cortical bone specimens from elderly donors. The compressional wave-speed for each specimen was calculated as $\sqrt{\frac{C_{11}}{\rho}}$, where C_{11} is the specimen-specific elastic coefficient corresponding to longitudinal deformation in the plane of isotropy. The obtained values of wave-speed in direction 1 (any direction normal to the symmetry axis of the microstructure) as a function of the intra-cortical porosity are shown in Figure 3.7 in blue diamonds. The red circles in Figure 3.7 represent the values of wave-speed estimated from this study using the method described in section 3.2.4 and the configuration of Figure B.1.

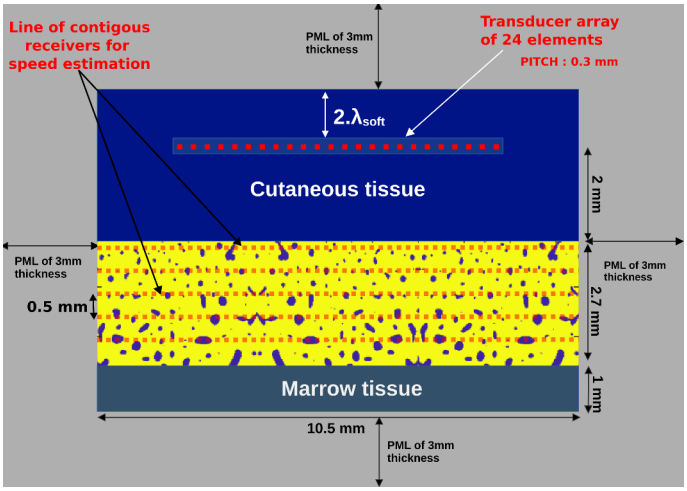

Figure B.1: Configuration model used for estimation of wave-speed in cortical bone. Virtual receivers are placed inside bone along 5 equally spaced (spacing=0.5 mm) lines (red dotted line inside cortical bone layer)

Appendix C

Determination of the optimal receive f-number for endosteal detection

In order to use the DAS algorithm optimally, the receive f-number was optimized as explained by Perrot et al. [3]. The interface visibility is evaluated for 25 different f-number values ranging from 0.2 to 2.6. The f-number was constant throughout the image, resulting in a different number of elements used for each point of the image. For a f-number greater than 2.6, less than 3 elements are used for the reconstruction of the endosteal interface, therefore the f-number was studied for values lower than 2.6. For a configuration without cortical pores (Ct.Por=0%), C_{EP} (defined in section 3.2.6) increases with f-number and reaches its maximum for a f-number close to 1.9 (increase of 8 dB). This is illustrated in Figure C.1.

Globally, the f-number that maximizes C_{EP} is close to 1.9. This value of f-number

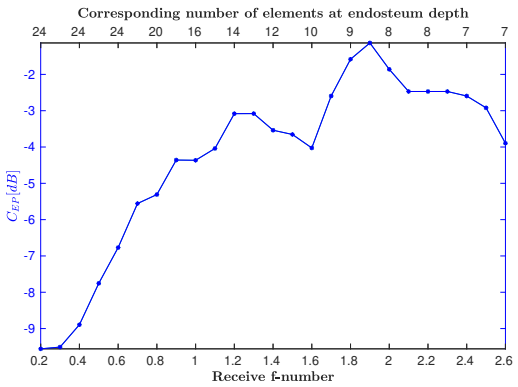

Figure C.1: Endosteum–Periosteum contrast for different values of f-number for a configuration without microstructure (i.e. porosity= 0%). The number of active elements is also given

corresponds to a receive aperture of 2.35 mm equivalent to 9 active elements for a focusing depth of 4.7 mm (i.e at the endosteal interface). For C_{EI}, the increase of contrast is smaller (increase of 3 dB), but the tendency is the same as for C_{EP} for almost all configurations. The f-number that maximizes C_{EI} is also close to 1.9. The metrics decrease for large f-number values.

Figure C.2 is an example plot of endosteal interface visibility against f-number for a configuration with a cortical porosity of 5.5%.

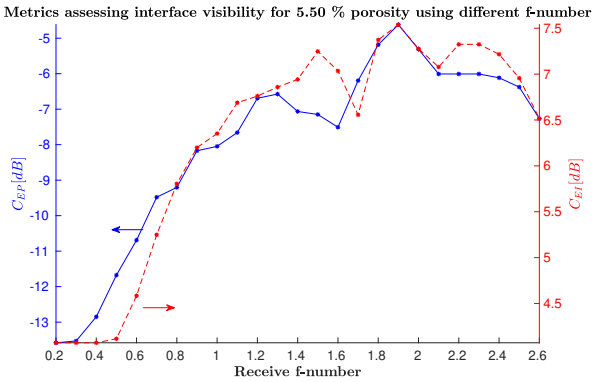

Figure C.2: Quantitative assessment of endosteal interface visibility as a function of the f-number, for a microstructure with a porosity of 5.5% porosity. The blue solid curve is relative interface contrast (C_{EP}) and the red dashed curve is endosteal interface contrast (C_{EI})

Appendix D

Power reflection coefficient at the endosteal surface

The amplitude of the specular reflection is important to interpret the appearance of the interfaces in the images of this study. Therefore the power reflection coefficient at the endosteal surface were calculated for different microstructure. As porosity increases, the speed of sound in cortical bone decreases leading to a drop of the power reflection coefficient at endosteal interface (R_{end}). The theoretical power reflection coefficient of plane waves is:

$$R_{end} = \left(\frac{Z_{marrow} - Z_{bone}}{Z_{marrow} + Z_{bone}} \right)^2,$$

where Z_{marrow} and Z_{bone} are the impedances of marrow and bone. In Figure D.1, reports R_{end} as a function of cortical porosity. In the porosity range 2-24 %, R_{end} decreases by 25 % of its value at 2 % porosity.

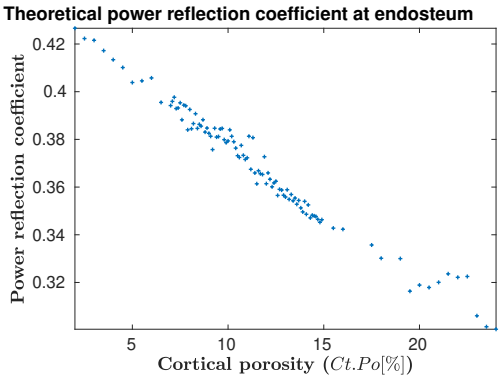

Figure D.1: Plane wave power reflection coefficient at the endosteal interface for each cortical microstructure

Appendix E

Attenuation coefficient

Estimation of the ultrasonic attenuation coefficient with numerical simulations. The attenuation value is important to interpret the ultrasound images of cortical bone obtained in this study. Therefore an analysis were conducted to document the variation of attenuation for our samples. Beside absorption inside the bone matrix, scattering due to pores contributes to the total amount of attenuation. To estimate the total attenuation coefficient in cortical bone additional simulation mimicking the substitution method commonly used for the experimental characterization of attenuation [4] were performed. For each model (i.e. each microstructure, see Figure 3.3), a plane wave at normal incidence is emitted by the transducer array and recorded after propagation through the layer of cortical bone by a line of virtual receivers positioned slightly below and parallel to the endosteal interface. To obtain a reference signal, the bone tissue is replaced with soft tissue. The attenuation coefficient in cortical bone was derived from the ratio of the magnitude spectrum of the signal received after propagation through bone ($|S(f)|$) to the magnitude spectrum of the reference signal ($|S_0(f)|$). Losses due to transmission through the two interfaces of the cortical bone layer were taken into account using the values of the plane wave transmission coefficients T_p (through the periosteal interface) and T_e (through the endosteal interface) calculated from the estimated compressional wave-speed (V_1) and apparent mass density (ρ). The attenuation coefficient α_{dB} in cortical bone expressed in dB/cm is obtained from:

$$\alpha_{dB}(f) = \frac{20}{\ln(10)} \frac{1}{Ct.Th} \ln\left(\frac{|S_0(f)|T_pT_e}{|S(f)|}\right)$$

, where Ct.Th is the thickness of the cortical bone layer in cm (0.27 cm).

Two sets of simulation were performed: with and without absorption in the bone matrix. Absorption in the bone matrix was set to 19.05 dB/cm as explained in Materials and Methods. Figure E.1 shows the obtained attenuation coefficient values as a function of porosity.

Relationship with microstructure. The difference between attenuation coefficients for simulations with and without bone matrix absorption is close to 19 dB/cm as expected. In fact, in this study, the maximum normalized frequency calculated as the product of sample wavenumber(k) and sample median pore diameter (Ct.Po.Dm) is 0.66 (moderate scattering regime), therefore, total attenuation is expected to be a linear summation of the bone matrix absorption and attenuation due to scattering [5].

Scattering attenuation coefficient is highly influenced by cortical microstructure. In the porosity range (2-24 %), attenuation coefficient increased by 40 dB/cm (Figure E.1). Spearman rank correlation coefficient between attenuation and microstructure variables were evaluated. There was strong positive correlation coefficient (r_s) for large pore size ($r_s = 0.92$), porosity ($r_s = 0.89$) and 9^{th} decile of diameters ($r_s = 0.83$) (see Table E.1). These statistics suggest that scattering magnitude increases with pore size and is dominated by scattering caused by large pores.

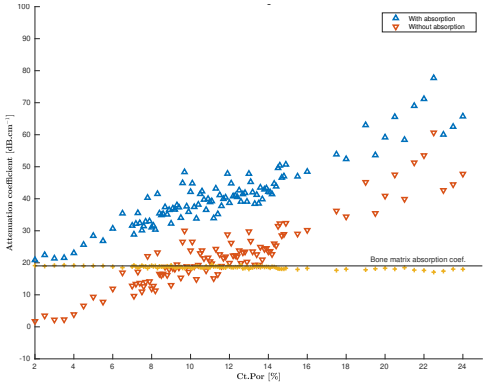

Figure E.1: Ultrasonic attenuation coefficient at 2.5 MHz in cortical bone as a function of porosity for simulations with absorption in bone matrix (blue upward pointing triangles) and simulations without absorption (red downward pointing triangles). The difference between these two data sets is also shown as yellow crosses

	Lg.Po.Dm	Ct.Por	Dm.DC-9	Dm.IDRng	Ct.Po.Dm	Dm.Rng	Dm.DC-1	Sm.Po.Dm	Ct.Po.Dn
Attenuation coefficient	0.92^{2}	0.89^{2}	0.83^{2}	0.82^{2}	0.70^{2}	0.67^{1}	0.54^{2}	0.46^{2}	$-0.21^{n.s}$

Table E.1: Spearman correlation coefficient r_s between attenuation coefficient and microstructure properties (see 3.2.2 for the definition of variables). $^{n.s}$: not significant $p > 0.05$, ^{1} : $0.001 < p < 0.05$, ^{2} : $p < 0.001$

Appendix F

Large pore influence on the visibility of the endosteal interface

Figure F.1 illustrates pore size effect on the visibility of the endosteal interface. The SR-µCT images of microstructures correspond to the reconstructed images of Figure 3.10. In the leftmost image, the microstructure does not contain

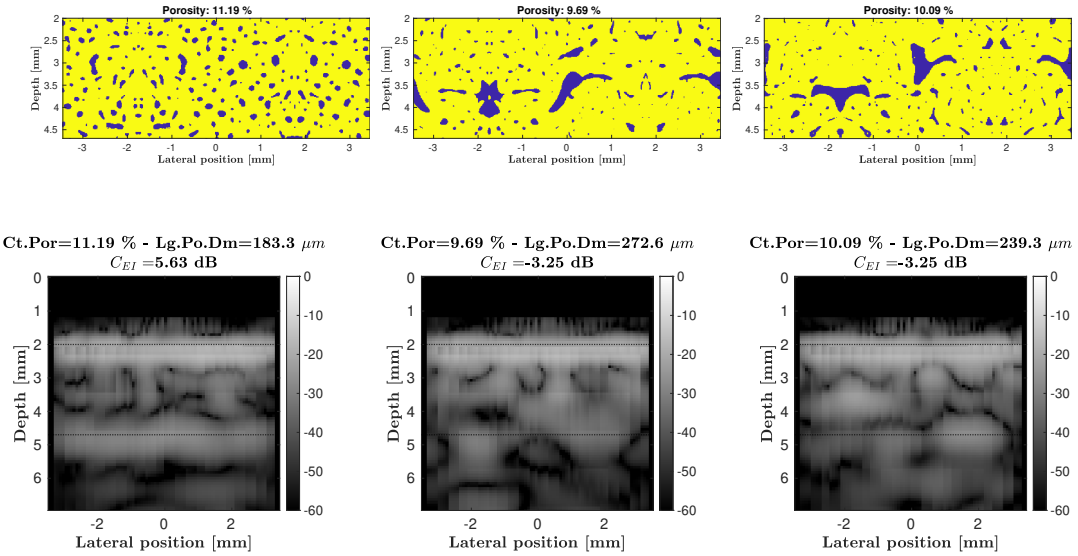

Figure F.1: Binarized SR-µCT image of microstructure with similar porosities (top) but increasing large pore size and their corresponding reconstructed ultrasound images (down)

pores with large diameter (Lg.Po.Dm=183.3 µm) and the endosteal interface is clearly visible (C_{EI} = 5.63 dB) while in the two following images some large pores (Lg.Po.Dm=272.6 µm and Lg.Po.Dm=239.3 µm) are observed and the endosteal interface is not visible (C_{EI} = −3.25 dB for both).

Appendix G

All ultrasound images *ex vivo*

In this appendix, ultrasound images of each measurement zone for each sample are presented, along with a representative slice of an X-ray image for each sample.

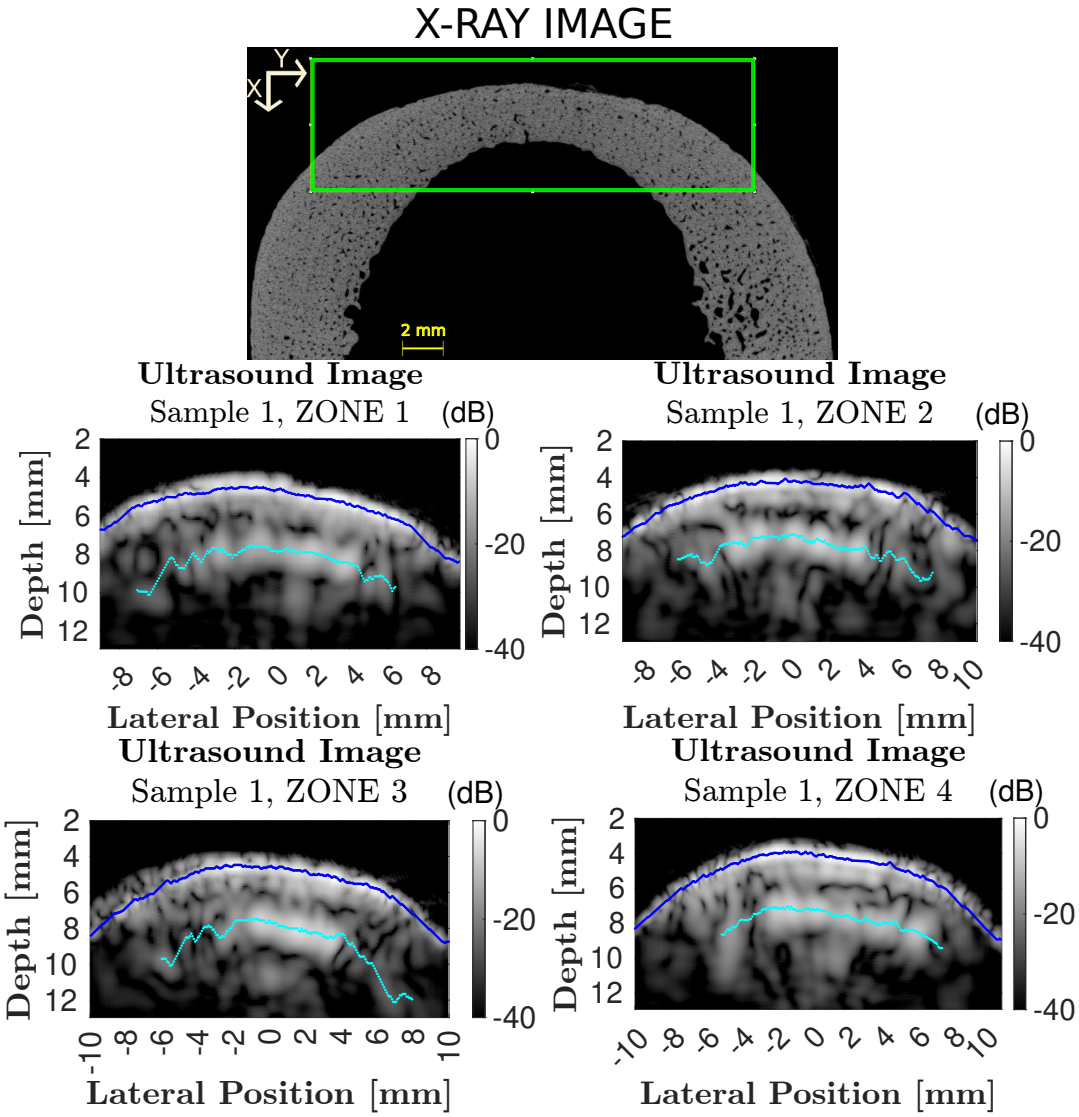

Figure G.1: Ultrasound images of each measurement zone of Sample 1.

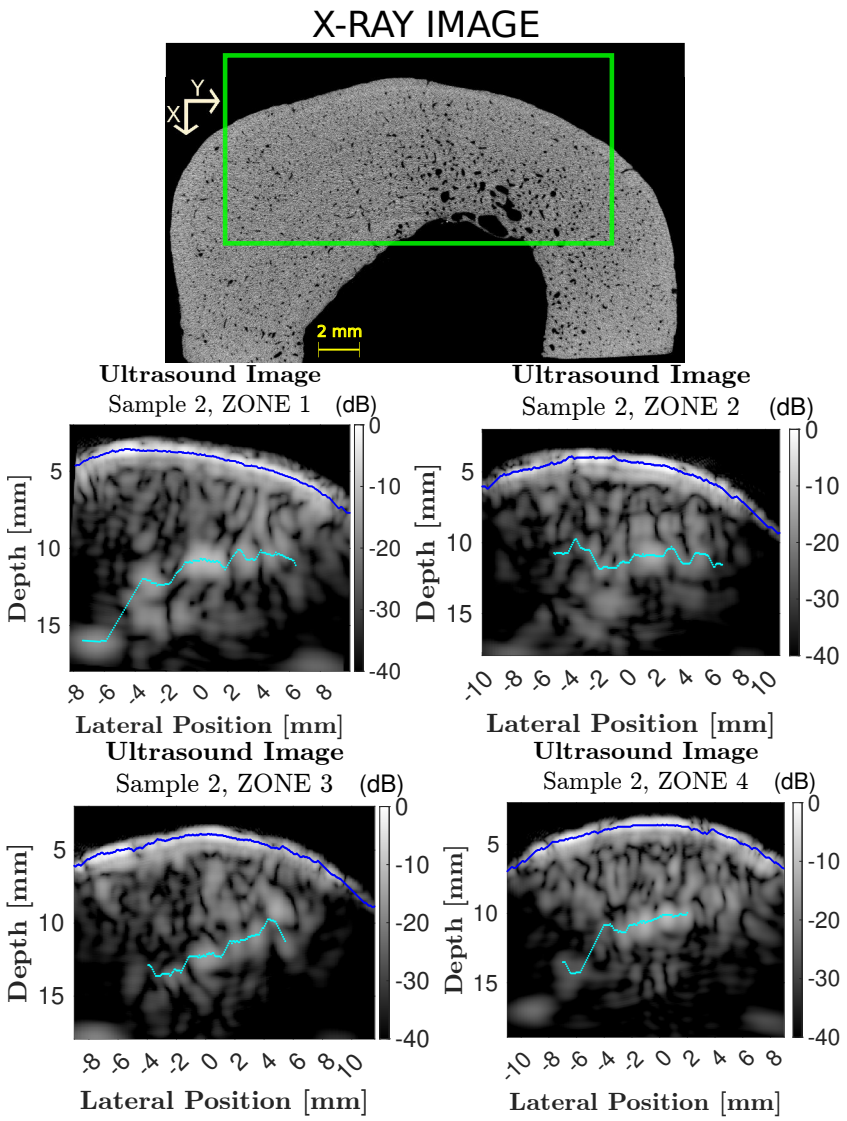

Figure G.2: Ultrasound images of each measurement zone of Sample 2.

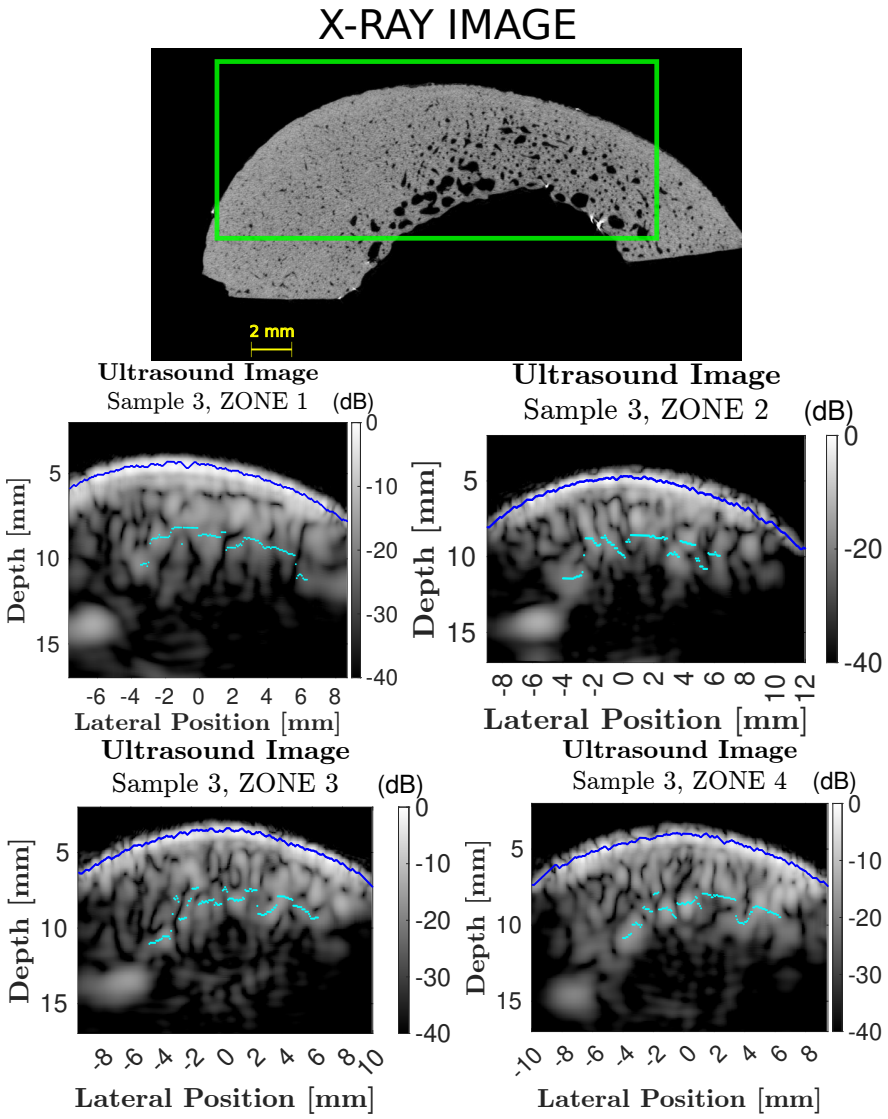

Figure G.3: Ultrasound images of each measurement zone of Sample 3.

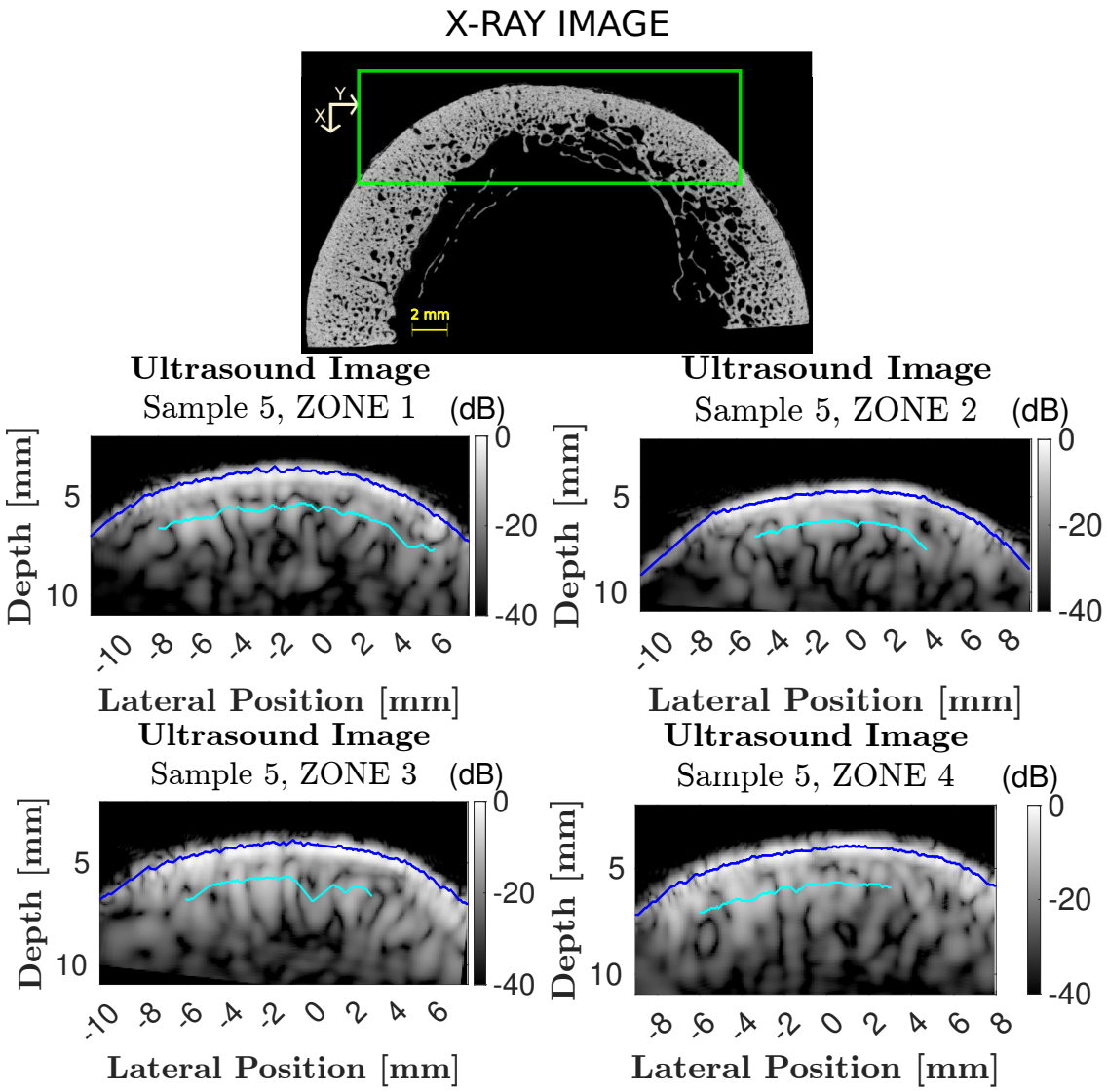

Figure G.4: Ultrasound images of each measurement zone of Sample 5.

Bibliography

[1] Xiran Cai, Laura Peralta, Renald Brenner, Gianluca Iori, Didier Cassereau, Kay Raum, Pascal Laugier, and Quentin Grimal. Anisotropic elastic properties of human cortical bone tissue inferred from inverse homogenization and resonant ultrasound spectroscopy. *Materialia*, 11:100730, June 2020.

[2] Xiran Cai, Hélène Follet, Laura Peralta, Marc Gardegaront, Delphine Farlay, Rémy Gauthier, Boliang Yu, Evelyne Gineyts, Cécile Olivier, Max Langer, Aurelien Gourrier, David Mitton, Françoise Peyrin, Quentin Grimal, and Pascal Laugier. Anisotropic elastic properties of human femoral cortical bone and relationships with composition and microstructure in elderly. *Acta Biomaterialia*, 90:254–266, May 2019.

[3] Vincent Perrot, Maxime Polichetti, François Varray, and Damien Garcia. So you think you can DAS? A viewpoint on delay-and-sum beamforming. *Ultrasonics*, 111:106309, March 2021.

[4] Magali Sasso, Guillaume Haïat, Yu Yamato, Salah Naili, and Mami Matsukawa. Frequency Dependence of Ultrasonic Attenuation in Bovine Cortical Bone: An In Vitro Study. *Ultrasound in Medicine & Biology*, 33(12):1933–1942, December 2007.

[5] Omid Yousefian, Yasamin Karbalaeisadegh, and Marie Muller. Frequency-dependent analysis of ultrasound apparent absorption coefficient in multiple scattering porous media: application to cortical bone. *Physics in Medicine & Biology*, 66(3):035026, January 2021.